FIELD-MEDIATED INTERACTION IN ACTIVE MATTER

A Dissertation
Presented to
The Academic Faculty

By

Shengkai Li

In Partial Fulfillment
of the Requirements for the Degree
Doctor of Philosophy in the
School of Physics
College of Sciences

Georgia Institute of Technology

May 2022

FIELD-MEDIATED INTERACTION IN ACTIVE MATTER

Thesis committee:

Dr. Daniel I. Goldman
School of Physics
Georgia Institute of Technology

Dr. Predrag Cvitanovic
School of Physics
Georgia Institute of Technology

Dr. Pablo Laguna
Department of Physics
The University of Texas at Austin

Dr. Dana Randall
College of Computing
Georgia Institute of Technology

Dr. Kurt Wiesenfeld
School of Physics
Georgia Institute of Technology

Dr. David Zeb Rocklin
School of Physics
Georgia Institute of Technology

Date approved: April 25, 2022

To family and friends.

ACKNOWLEDGMENTS

Before introducing the exciting research of my Ph.D. years, I would like to thank everyone that has made it all possible.

First, I would like to extend my deepest gratitude to my advisor, Prof. Daniel Goldman. My achievements today are indebted to his efforts in helping me pursue the fascinating problems he had chosen for me. These include but are not limited to: teaching me valuable skills such as scientific communication and how to seek important scientific questions; introducing me to amazing collaborators and resources; providing numerous opportunities, such as the various conferences to train my skills; encouraging me when I am down (like when I receive rejections from journals); and overall being very supportive of my career.

The assistance from my committee members has also been indispensable. I would like to thank Prof. Pablo Laguna for his extraordinarily patient babysitting of my general relativity (GR) skills, Prof. Dana Randall for her invaluable help in bridging physics and theoretical computer science, Prof. Zeb Rocklin for his help in creatively tackling hard problems in physics modeling, Prof. Kurt Wiesenfeld for helping me think deeply about the pros and cons of my research and his fascinating statistical mechanics course, and Prof. Predrag Cvitanovic for starting the GR project and his insightful nonlinear dynamics course. Last but not least, I would like to thank Prof. Robert Austin (Uncle Bob) for his introduction to the mind-blowing world of robotic ecology systems and showing me the way to and around Princeton with Dr. Chan.

I would also like to thank many other professors in School of Physics. I would like to thank Prof. Gongjie Li for her valuable advice on the GR project, Prof. Deirdre Shoemaker for teaching me the essentials of GR, Prof. Zangwill for his fascinating condensed matter course that prepared me with the skills to treat robot swarms from the condensed matter point of view, Prof. Sabetta Matsumoto for the 3D printing course which enjoyably taught me the essentials of solid object modelling. I would like to thank Prof. Markus Kinder-

mann, Prof. Brian Kennedy, Prof. Michael Pustilnik, Prof. Alberto Fernandez-Nieves, Prof. Roman Grigoriev for the general training of physics, and Dr. Emily Alicea-Muñoz for teaching me how to be a good teaching assistant.

I would also like to thank Prof. Sung Ha Kang in the School of Mathematics for her great classes and enthusiasm in helping me develop scientific computation skills. These were very helpful for my numerical simulations in research. I would also like to thank my former advisor, Prof. Hepeng Zhang for his encouragement.

I would like to thank my dear lab mates and friends in CRAB lab. I have benefited greatly in having met them all: Rida Abbas, Jeff Aguilar, Kehinde Aina, Henry Astley, Ram Avinery, Yasemin Ozkan-Aydin, Enes Aydin, Hosain Bagheri, Andrew Brown, Joseph Brunner, Grace Cassidy, Baxi Chong, Kelimar Diaz Cruz, Camila Dominguez, Bahnisikha Dutta, Noah Egan, Eva Erickson, Alia Gilbert, Jonathan Gosyne, Hussain Gynai, Madison Hales, Christian Hubicki, Andy Karsai, Deniz Kerimoglu, Venny Kojouharov, Bo Lin, Olivia Lofaro, Marine Maisonneuve, Erin McCaskey, Daria Monaenkova, Margot Paez, Jungsoo Park, Christopher Pierce, Feifei Qian, Aradhya Rajanala, Jennifer Rieser, Tommie Robinson, William Savoie, Perrin Schiebel, Max Seidel, Zhexin 'Jeff' Shen, Siddharth Shrivastava, Ella Small, Steven Tarr, Akash Vardhan, Tianyu Wang, Ross Warkentin, Charlie Xiao, Xiaobin Xiong, and Tingnan Zhang. I would like to especially thank my buddy Andras 'Andy' Karsai, who was always ready to help me on engineering problems with his ingenious skills and always tries his best to make sure I take a breath by arranging many fun events. I'd like to thank Will Savoie, Yasemin Ozkan-Aydin, Enes Aydin, Hussain Gynai, Steven Tarr, Bahnisikha Dutta, Ram Avinery, Tianyu Wang, Venny Kojouharov, and Jeff Shen for the amazing robots and teaching me how to do experiments. I would like to thank Olivia Lofaro, Charlie Xiao, Ella Small, Alia Gilbert, Andrew Brown, Camila Dominguez for their assistance in experiments. I would like to thank Baxi Chong for introducing me to many amazing problems in Geometric Mechanics, Bo Lin for the help in mathematics in a variety of fields, Steven Tarr, Kelimar Diaz Cruz for the great help in writing, Chris Pierce

and Hosain Bagheri for proofreading, and Akash Vardhan and Daniel Soto for enthusiastic discussion on research. Last but not least, I would like to thank my graduate student and postdoc mentors from when I first came to CRAB lab for their patient guidance, including Jeff Aguilar, Daria Monaenkova, Tingnan Zhang, and Feifei Qian.

There are also many friends and professors outside of the CRAB lab I would like to thank. I would like to thank Trung 'Average' Phan for his enthusiastic invitation to the amazing robotic ecology world with Uncle Bob, Dr. Liyu Liu, and Gao Wang. I would like to thank Prof. Andrea Richa and Josh Daymude for the indispensable help on BOBbots. I would like to thank all my friends and professors from MURI in addition to the ones above, including Prof. Michael Strano, Prof. Todd Murphey, Prof. Jeremy England, Hridesh Kedia, Jingfan Yang, Tommy Berruta, Joseph Briones, Tianxiang 'Albert' Liu, Allan Brooks, Jamison Weber, and Shunhao Oh. I would like to thank Hungtang Ko and James McInerney for sharing their great projects with me, and Shengnan Huang for his encouraging chats when I was down.

I would like to thank many friends for their effort to prevent me from burning out too much. I would like to thank Guanlin Li for taking me out to eat some delicious food, Tianyu, Baxi, Bangyuan 'Benny' Liu, and Juntao He for teaching me how to play different board games. I would like to thank Haoxiang Huang, Petro Milan Junior, Daoxun Sun, and Jiahao Xie for helping me survive the challenging coursework at Georgia Tech.

I would also like to thank my friends outside academia. I would like to thank Aunt Fang An and Uncle Zhang Qin for their food support so I could worry less about cooking, Uncle Jerry Chen and Aunt Karen for their encouragement over the years, Yuxiang Jiang and Xiaoxi Wang for taking me out for fun, Lutian Zhao for his extremely useful help in life and math, Fangzhou Zhao for his refreshing chats and good accompany at the APS meetings, Dong Xu and Lingquan Ding for their good company, and Siyu Ge for always encouraging me to go after my dreams. I also need to thank my furry friend Melon Chong for his *purrfect* company while his mom and dad were out of town.

Finally, I would like to thank the indispensable love and help from family. I would like to thank my mom Danlin Ge and dad Qiang Li for their remote support and my uncle Yuankai Ge and aunt Xiaohe Song for their local support. These have minimized my worries about life so I can focus as much as possible on research.

TABLE OF CONTENTS

LIST OF FIGURES

SUMMARY

Like most physical systems, the interaction characteristics among agents play an important role in active matter. For example, the extent of attraction can switch a collective of particles from a homogeneous mixture to phase-separated clusters; particle concavity in shape-changing active systems can change interactions from repulsive to attractive. The way that the force transmits can also be important. While many interactions transmit through direct or short-ranged contact (e.g., collisions or magnetic attraction), there are interactions that require the full description of the force-generating field to describe motion. These interactions can bring interesting features such as time delays, the coexistence of multiple length scales, and non-reciprocity, which are less common in short-ranged interacting systems. In this thesis, I will use several examples from my Ph.D. work to show the rich dynamics of active matter interacting through a field. Examples include active locomotors mimicking motion in curved space-time when driving on an elastic membrane, and resource-consuming agents driven by resource depletion that form different states of matter. Through these studies, I will also show how the connection between field-mediated interactions and classical fields allows us to explain and explore emergent phenomena in active matter using inspiration and tools from field theory. In addition to the study of field-mediated interactions, other studies of active matter with short-ranged interactions are presented in the later chapters. These include shape-changing active matter, the role of substrate curvature in active matter, and the analogy between attractive interaction in active matter and surface tension.

CHAPTER 1
INTRODUCTION

1.1 Active matter

Active matter is a kind of matter that has both internal energy input and dissipation. The study of systems composed of internally driven agents has long been the domain of biology [1, 2, 3] and robotics [4, 5, 6, 7] but it is coming into vogue in physics in the field of active matter [8, 9, 10]. Individual active agents display novel dynamics with their persistent motion [11] and control [12]. Active collectives display fascinating properties. For example, collectives can exhibit phase transitions [13] and an individual consuming ambient resource can drive itself through resource depletion [14]. Active matter is ubiquitous in our everyday life. Since any object subjected to internal energy input and dissipation is considered active matter, all living systems are active matter. In addition, driven and damped non-living systems, such as robots are also active matter as they take in energy to perform tasks and dissipate energy due to friction. Given its ubiquity, active matter has attracted interest in many fields.

Physics

Active matter attracts the attention of physicists due to its non-equilibrium feature. For equilibrium systems, there are straightforward methodologies such as obtaining thermodynamic properties from the partition function[15]. For non-equilibrium systems, the past three decades have seen much progress. For examples, Jarzynski equality[16] has connected free energy differences between two states with the work in irreversible process. The low rattling principle[10] has provided an understanding of the probability of steady states in non-equilibrium systems. Nonetheless, there has been no general principle like

what we have for equilibrium systems yet. To probe the physics of non-equilibrium systems, active matter provides many good experiment platforms with relatively easy access. Researchers can synthesize artificial active matter[17, 18], harness living systems[19, 20], or even create more customized robotic active matter[21, 10] to query specific scientific problems. In this way, active matter has helped us explore many non-equilibrium versions of well-known phenomena equilibrium systems, such as topological defects[19], motility-induced phase separation [18, 22], glassy state[20]. Additionally, active matter has enabled exploration of phenomena not existed in equilibrium systems, such as nonreciprocal phase transitions[13] and entropy production[23] (Figure 1.1).

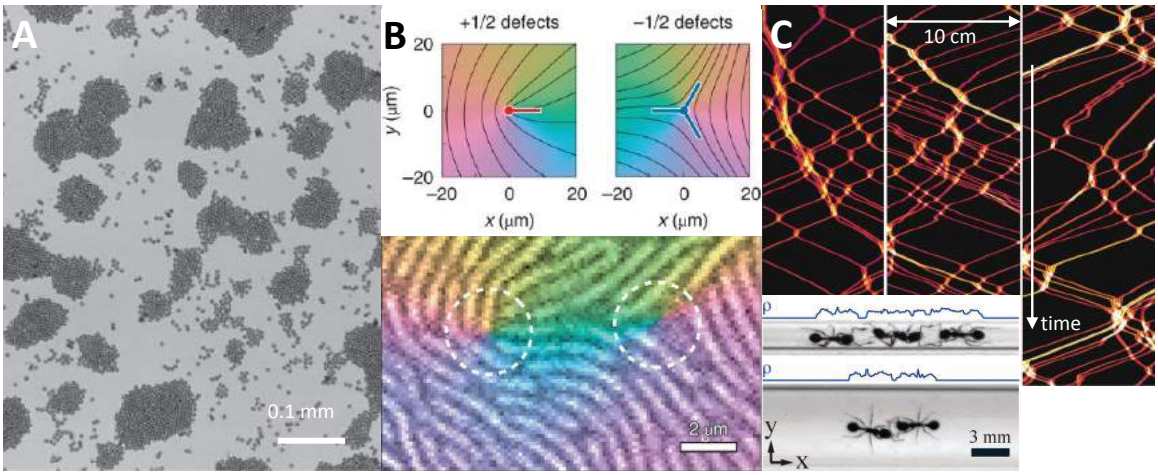

Figure 1.1: **Active matter extends the physics of passive systems.** (A) Aggregation of induced-charge electrophoretic self-propelled Janus colloids helps understand novel phase separations[18]. (B) Bacteria swarms help understand how topological defects could emerge from active motion. The white dashed lines encircle a $+1/2$ defect (left) and a $-1/2$ defect (right) of the nematic cell alignment[19]. (C) Space-time diagram of ants in a quasi-one-dimensional tunnel (see inset)[20]. The color represents the number density. The long vertical bright streaks show long interaction time. The dynamics' change with this time resembles a glass transition.

Biology

While physicists would develop artificial active matter (such as Janus particles[29]) to pursue the theoretical interests in non-equilibrium physics, the more natural contribution from active matter study is in living systems. These range from cell migration[24] to

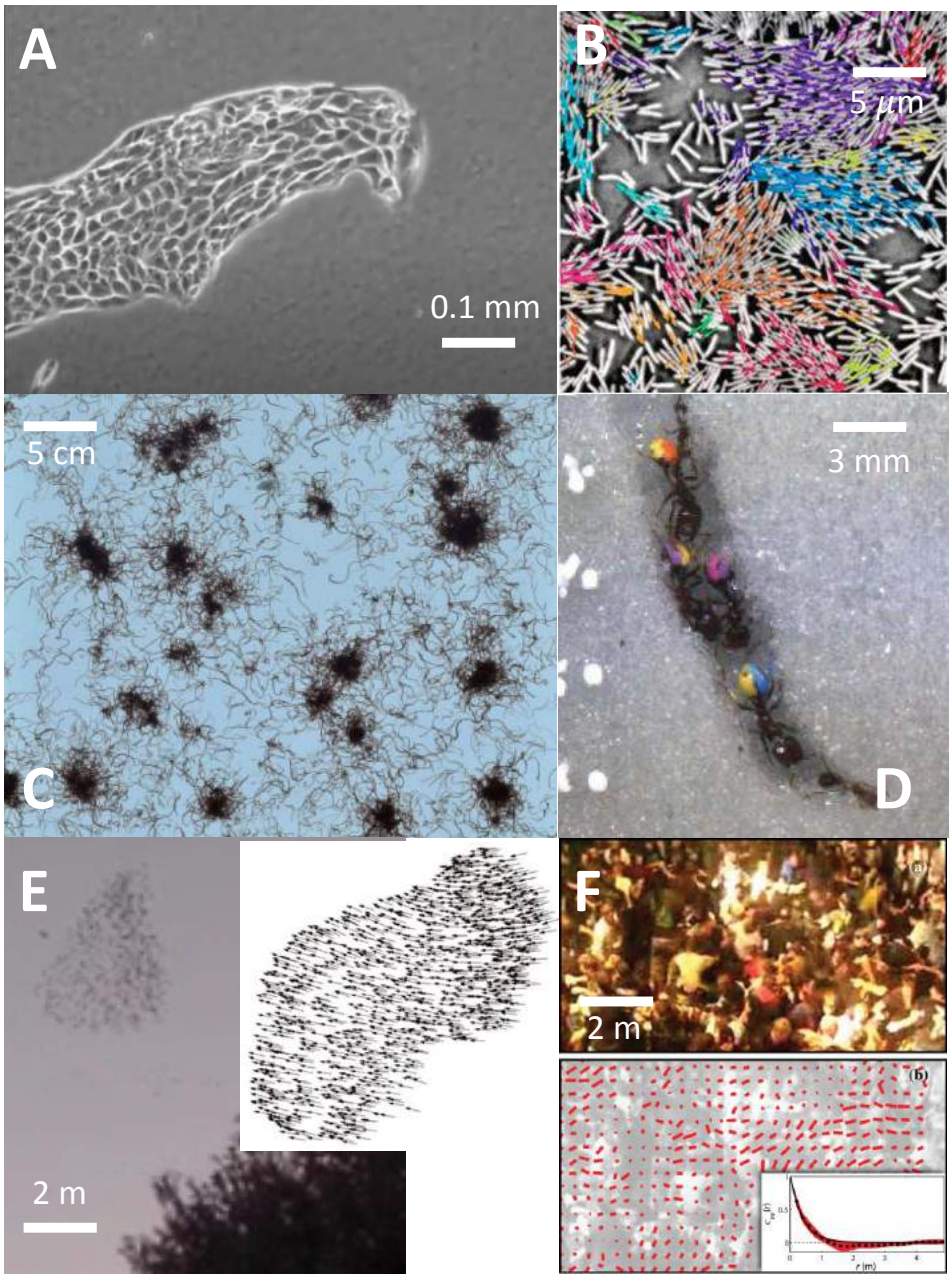

Figure 1.2: **All living systems, spanning many scales of size, are active matter.** (A) Migrating Madin-Darby canine kidney cells[24]. (B) Moving clusters of *Bacillus subtilis* with bacteria in the same dynamic cluster shown in velocity arrow with the same color[25]. (C) Initially homogeneous distributed *T. tubifex* show phase separation after 9.5 minutes[26]. (D) Painted *S. invicta* workers excavating a single tunnel along the wall of a transparent container with 0.25-mm-diameter wet glass particles[9]. (E) A flock of starlings [27]. The inset shows a tracked velocity distribution. (F) A typical "mosh pit" and the same image with overlaid velocity field [28]. Picture credits by the cited journal articles listed after each panel.

bacteria swarms[25], to spontaneously formed clusters of animals[30], social behaviors of animals[9] and even of humans[28] (Figure 1.2). For instance, coherent clusters of animals are now understood as active agents following simple alignment with the neighbors[30]. Cellular automaton modeling of ants' digging tunnels [9] has taught us that some idleness of individuals and retreating are necessary for efficient motion in a limited space. Models that reproduce the dynamic pattern in a crowd of congested humans [31, 28] could potentially teach us how to avoid accidents when a crowd of people or animals panic. Designing control and devices using the inspirations of these living systems (biomimicry) is also one route to help swarm robotics.

Robotics

Besides using an active matter approach to study living systems to facilitate understanding in biology, roboticists can also benefit from active matter studies in the field of robotics. For instance, principles in collective motion of active matter can help us design the control of individuals in robotic swarms to achieve desired tasks. For instance, the neighbor-aligning model mentioned above[30] has inspired robotic swarms capable of forming desired two-dimensional shapes on land [32] and various motion patterns in water [33]. We will see more examples of how active matter concepts can be applied in robotics in the work in chapter 4 and chapter 6 of this thesis.

There is no priority among the three threads above, and they are not independent of each other, either. In fact, the results we learn from the physics of active matter could be helpful for biology and robotics. The understanding of cell migration from the active matter perspective can possibly help us understand wound healing [34] and cancer metastasis [35]. Besides the three threads mentioned above, the discoveries of active matter principles could contribute to many more disciplines, such as chemistry [36, 37], economics, politics[38], and sociology[39].

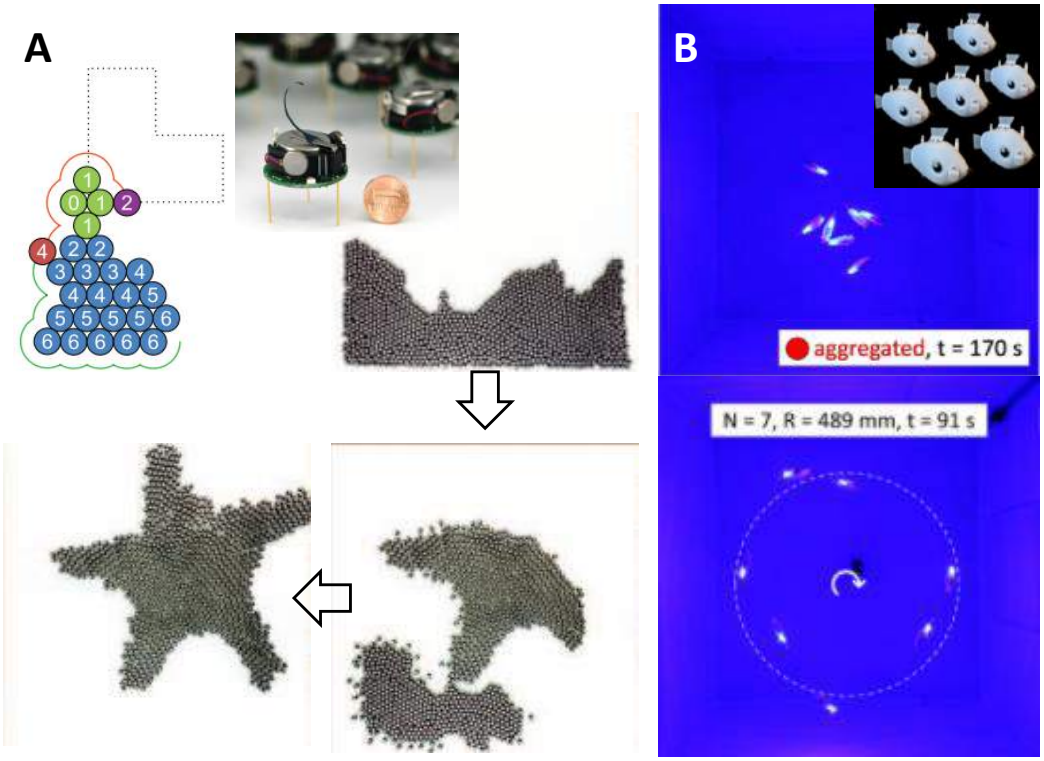

Figure 1.3: **Active matter connects to the designs of swarm robotics.** (A) By locating the position with the hints from the neighbors, a robotic swarm (kilobots) is able to form a desired shape [32]. By using a vision of the neighbors, fish-like robots are able to reproduce the aggregating and swirling (blueswarms[33]) behavior of fish schools.

1.2 Environment and the interaction in active matter

Active collectives can interact via physical and social forces [28]. Researchers have extensively explored the aerodynamic [41], hydrodynamic [42], and even terradynamic [43, 44] interactions and have increasingly understood their effects on agent locomotion such that we can build capable devices (like fast-moving robotic fish [45] and hawk-inspired drone [46]) and create capable swarms [47, 48, 4, 5, 6]. From these examples above, we have gained understanding of how the deformation of the environment would affect the agents individually. However, in addition to the individual environment-agent coupling, the environment can sometimes act as a medium to transmit inter-agent interactions. These interactions between agents that move on an environment which is highly, but not necessarily permanently, deformed by the agents are much less studied. In these systems, the

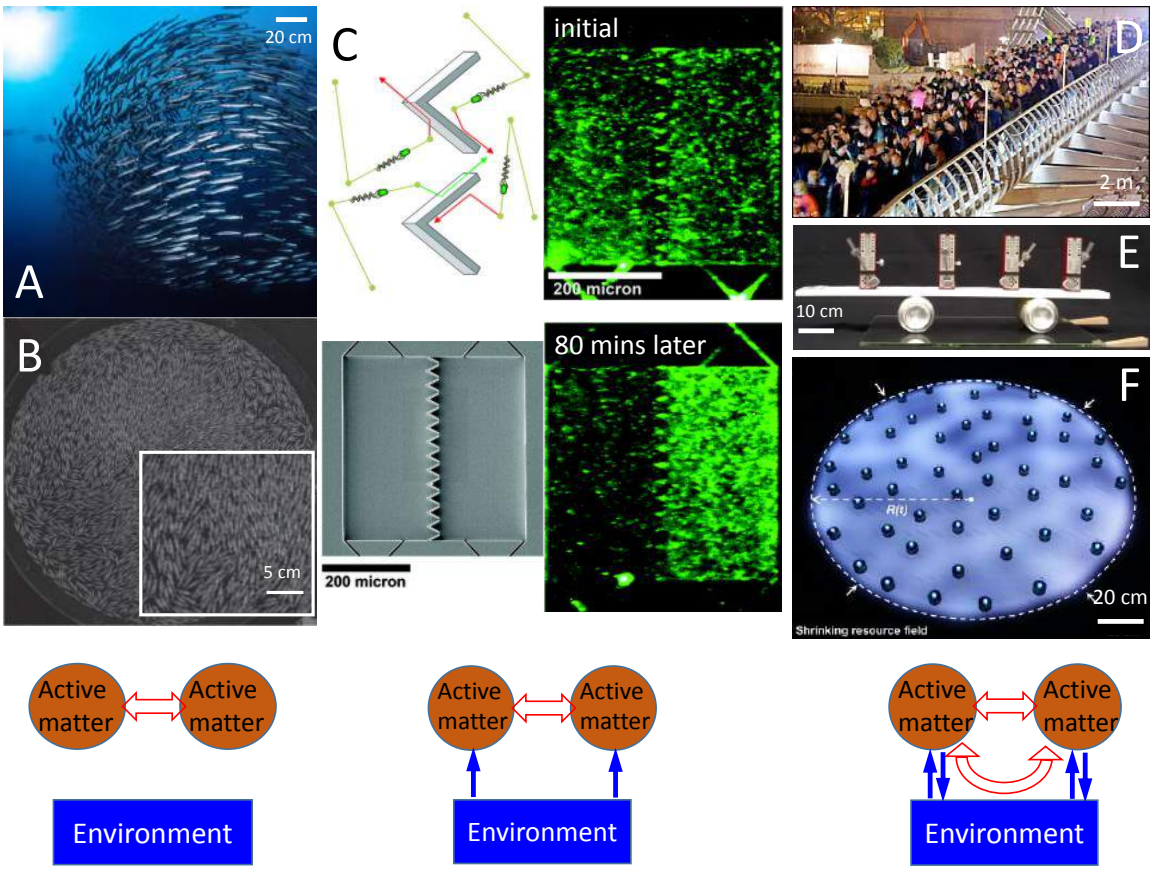

Figure 1.4: **Environment's role in active matter systems in three regimes.** I. When the environment does not effect the active matter: (A) A school of fish is formed by the alignment of neighboring fish. (B) A nematic order is formed by the alignment due to the sterical exclusion of rod-like particles (cut from 8-mm-diameter copper wires). II. When the environment affects the active matter: (C) A wall of funnels leads to the different concentration of bacteria on the two sides of the funnels[40]. III. When the environment shared by the active matter link them together: (D) Pedestrians walking on the Millennium Bridge wobbled the bridge by resonance. (E) The initially randomly-phased metronomes get synchronized on a shared loose platform (known as the Kuramoto oscillator). (F) Active agents consuming resources represented by LED light intensity and moving along the resource gradient show different states of matter depending on the number density and resource replenishing rate.

environmental deformation field plays an important role in the locomotion and non-contact interactions.

To gain insight into how the environment plays a role in active matter systems, here we do a brief survey by considering the interaction between the active matter and the environment in which it dwells. In an increasing order of the environment's involvement in

active matter systems, Figure 1.4 shows three distinct regimes with several representative examples. Although we want to show the effect of the environment, to have a systematic understanding, we will start with the regime where the environment plays a nominal role and see and go deeper into the unidirectional and, finally bidirectional case.

1.2.1 Scenario 1: Environment does not functionally affect active matter

In many active matter systems, there are no forces from the environment besides the forces constraining the object in the space of interest. The environment does not play a functional role on the active matter such that the agents only interact with themselves. While this case seems to be simple, the agent-agent interaction, even typically only affecting the neighboring objects, can create surprisingly rich phenomena. For instance, by visually aligning with the neighbors, fish and birds can collectively move together in schools and flocks (Figure 1.4A); nematic alignment of active granular rods shows up due to the sterical exclusion [49].

1.2.2 Scenario 2: Environment unidirectionally affects active matter

After reviewing the 'null regime', let us now consider a regime where the environment plays some meaningful role. In this regime, the environment affects the active matter while inversely the active matter is not strong enough to affect the environment. For instance, bacteria swimming around a wall of funnels have little effect on the funnels while the funnels can act as a ratchet to change the concentration of bacteria on the two sides [40, 50, 51] (Figure 1.4B). Other examples include snakes[52], propelled boats [53], and nematodes [54] colliding on and passing through vertical posts. In addition to these hard interactions, softer effects from the environment include active particles in electrical, magnetic, and acoustic [55] fields where the external field exerts force on the active matter while the field

is considered minimally disturbed. In these systems, the interaction is *unidirectional* in the sense that the effect from the environmental is so dominant that we can explain the phenomena by assuming the environment is static and the force from the environment acts individually on the active matter.

1.2.3 Scenario 3: Environment and active matter affect each other

While there are plenty of rich dynamics in the previous two regimes, even more interesting are situations where active agents modify their environment which *in return* modifies the dynamics of another active agent. This occurs when the active matter is strong enough to affect the environment reciprocally. For instance, when pedestrians were walking on the original Millennium Bridge, a 'wobbly' bridge in London, aside from the sterical exclusion between them that forbids penetration of pedestrians, additional forces were transmitted between every two pedestrians. In this case, each pedestrian transferred momentum to the bridge and the bridge back reacted to the other pedestrians given its mass was comparable to that of the pedestrians[56, 57]. Another similar though not active system that is extensively studied is the Kuramoto oscillator. In a Kuramoto oscillator, this coupling between the substrate and the object on top of it can leads to automatic synchronization[58].

In addition to the two examples above where the response of the environment (substrate) to the active matter is a simple motion as a rigid object without detailed structure, the environment can also change spatial-temporally like a field. For instance, Figure 1.4F and Figure 1.8B show a robophysical realization of mobile agents consuming virtual resources represented by the light intensity of the substrate. In this system, the environment changes over space and time, responds to the active agents as a result of consumption, and also exerts repulsion to the agents with the regions where the resource has run out. From this example, we can see that the spatio-temporally varying environment can act as a force field that mediates long-ranged indirect interaction of the agents in addition to the short-ranged

on-contact interactions, such as sterical exclusions (collisions between agents) mentioned in the previous two regimes. This can potentially create a two stage phase transition because there is more than one length scale. We will show an effect from this in chapter 3.

Resembling a more fundamental description of force that uses fields to transmit interaction in the microscopic world, systems in this third regime naturally possess the feature of non-reciprocity that the forces between two objects do not necessarily have the same magnitude and opposite signs as we have in Newton's third law. In addition to its existence in the microscopic world, non-reciprocal interaction also exists in many macroscopic systems. For instance, the speeds of the pursuer and the evader are different[59]; the phoretic response of enzyme A to the chemical produced by enzyme B is different from the that of B to the chemical produced by A[60]. Therefore, the interaction transmitted by the environment could be helpful to understand many emergent phenomena of macroscopic systems. We will refer to this kind of interactions as *field-mediated interaction* and discuss its features with more examples and in more detail in the next section.

1.3 Field-mediated interaction

1.3.1 Passive agents

Field-mediated interaction occurs in the agent-environment-coupled regime when the environment changes spatio-temporally with the agents moving above it. One of the most accessible phenomena in everyday life with field-mediated interactions is the Cheerios effect[62, 63]. As shown in Figure 1.5A, solid objects of light weight floating on a liquid can deform the liquid beneath and reciprocally the deformation could drive these floating objects together. As the deformation is made by all objects on the liquid surface collectively, the substrate acts as a media that can transmit long-ranged force to attract them together. Under this interplay between the objects (matter) and the substrate (space), the objects merge dynamically. Besides Cheerios themselves and similar solid objects floating on liq-

Figure 1.5: **Field-mediated interaction induced by the agent-environment coupling.** (A) Cheerios floating on milk attract to each other due to long-ranged fluidic forces[61]. (B) A drop of fluid is able to walk on a vibrating fluid instead of merging with the fluid beneath when the vibration frequency is higher than a threshold[11]. This fluidic droplet interacts with the substrate reciprocally. (C) A configuration composed of three such active droplets.

uid, many other scenarios with identical or similar underlying principles possess the same feature, such as coins floating on fluid and liquid droplets floating on a liquid substrate.

1.3.2 Active agents

While the Cheerios effect exists regardless if the objects are active or not, it is more interesting to investigate the cases where the objects are active agents. In these cases, locomotors can modify their environment which in turn modifies the dynamics of the locomotor (or another active agent). This is seen in organisms running on compliant membranes[64, 65], water walking organisms near menisci [66], macroscopic robots and insects walking on water surfaces [12, 67, 66, 68] and granular slopes [69], cellular motion on substrates [70, 71], locomoting agents that compete to consume spatially distributed resources [14], and walking droplets [72, 11]. Dynamics in such systems can display surprising features. For exam-

ple, in the walking droplet system the interaction of a droplet and its self-generated wave-field yields a hydrodynamic analog of "pilot wave" models of quantum mechanics [73, 74]. The system has also spurred inquiry into the foundations of quantum mechanics (see [75] for a recent review).

1.4 Perspective from field theory

1.4.1 Field description of active matter

In fluid mechanics, despite the fact that the fluid molecules have finite sizes, the Navier-Stokes equation, a field equation for continuum, well captures the fluid dynamics. Similarly, researchers have developed field theories for active matter with a finite size as well. For instance, Toner and Tu [76] developed a field theory that uses a velocity vector and a number density to describe active agents locally aligning with neighbors (Viscek model[30]). The Toner-Tu model provides theoretical support for the spontaneous formation of clusters with long temporal and spatial persistence in the Viscek model and explains the functional role of the local coupling in the flocking of active agents, such as birds and fish. Recently, by combining Toner-Tu's theory and the Swift-Hohenberg for pattern formation, researchers have formulated equations for a vector field to explain the different phases in the suspension of active polar and nematic particles[77, 78]. In chapter 6, we will see the Cahn-Hilliard equation, a field equation describing how surface tension gives rise to phase separation, can capture the cluster growth of spinning active matter[79].

1.4.2 General relativity

In systems with interactions mediated by the environment, the environment acts as a field. Therefore, a field description may help us understand the dynamics of active matter connected by the environment. We note that the interplay between the active matter and the environment recaps the famous aphorism on general relativity (GR) by Wheeler that 'the matter tells the spacetime how to curve and the spacetime tells the matter how to move.'

Therefore, I would like to ask what I can borrow from general relativity to understand active matter.

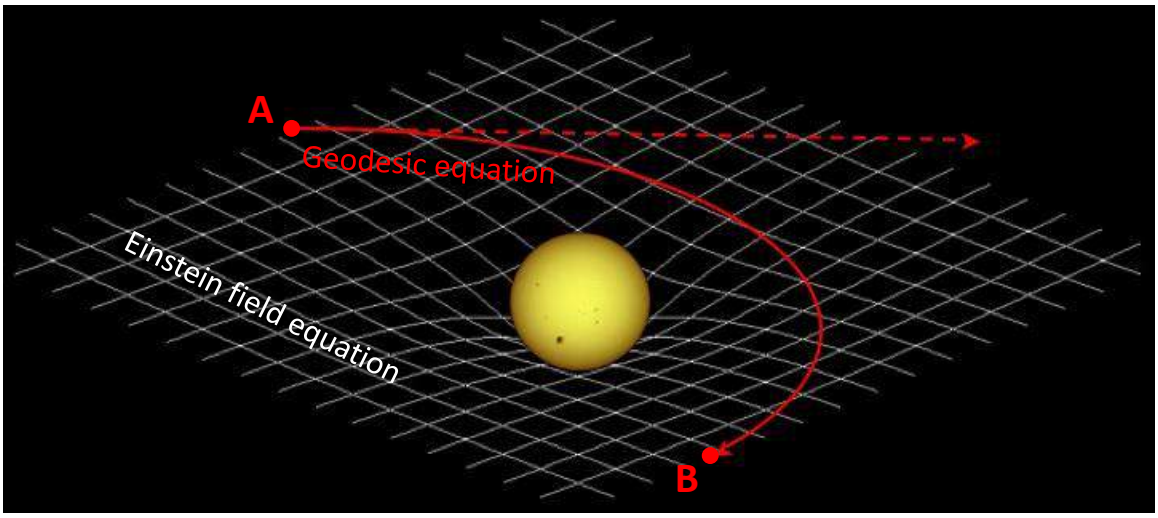

Figure 1.6: **Conceptual idea of general relativity.** The white mesh shows the spatial curvature of the spacetime curved by a mass (yellow sphere) in the center. For a low-mass particle at point A that does not further curve the spacetime, it will follow the geodesic (the red solid line, as opposed to the straight line on flat surface in red dotted line) on the curved spacetime to get to point B. The white mesh is a solution to the geodesic equation (Equation 1.2) and the red solid line is a solution to the Einstein field equation (Equation 1.3). The figure is adapted from relativity_curved_space.jpg on physicsoftheuniverse.com.

Spacetime tells matter how to move

Unlike the Newtonian (Galilean) view of space and time, GR views the space and time combined as a 4-dimensional continuum instead of separated coordinates. Mass moves along the shortest path (geodesics) in this continuum. To characterize the spacetime, we use the metric tensor, which describes how a line segment ds is composed of the spatial and temporal segments dx^μ:

$$ds^2 = g_{\mu\nu} dx^\mu dx^\nu \tag{1.1}$$

where the repeated indices denote summation (Einstein summation notation). For instance, here Equation 1.1 means $ds^2 = \Sigma_\mu \Sigma_\nu g_{\mu\nu} dx^\mu dx^\nu$ and $\mu, \nu = 0, 1, 2, 3$ where 0

denote the time and $1, 2, 3$ denote the three spatial coordinates. Throughout this thesis, we will use the Einstein summation for convenience.

In the metric, the metric tensor g_μ describes the curvature of spacetime. To understand this, we can use the example of Euclidean space where $g_{ab} = \delta_{ab}$. From Equation 1.1 we have $ds^2 = (dx^1)^2 + (dx^2)^2 + (dx^3)^2 = dx^2 + dy^2 + dz^2$. This is the familiar Pythagorean law. Nonetheless, in general spacetime is not flat and metric tensors are functions of all 4 coordinates. In Figure 1.6, the relatively flat mesh in the region far from the center has the spatial metric close to the $g_{ab} = \delta_{ab}(a, b = 1, 2, 3)$ while the more curved part around the center deviates from $g_{ab} = \delta_{ab}$. We will show a particular example of curved metric tensor in the next subsection.

The equation for the geodesics, the shortest path between two points in the spacetime reads

$$\frac{d^2x^\mu}{ds^2} + \Gamma^\mu_{\alpha\beta}\frac{dx^\alpha}{ds}\frac{dx^\beta}{ds} = 0 \tag{1.2}$$

where the Christoffel symbol $\Gamma^i_{kl} = \frac{1}{2}g^{im}(\frac{\partial g_{mk}}{\partial x^l} + \frac{\partial g_{ml}}{\partial x^k} - \frac{\partial g_{kl}}{\partial x^m})$ takes in the information of the spacetime curvature $g_{\mu\nu}$ and serves as the connection between different coordinates. s is an affine parameter for the curve parameterization.

Matter tells the spacetime how to curve

Now that we know how the matter moves in a given curved spacetime, we would like to ask how the spacetime is curved by the matter. The equation in GR describing this is the Einstein field equation:

$$G_{\mu\nu} + \Lambda g_{\mu\nu} = \kappa T_{\mu\nu} \tag{1.3}$$

On the left hand side, we have $G_{\mu\nu} = R_{\mu\nu} - \frac{1}{2}Rg_{\mu\nu}$ where $R_{\mu\nu}, R$ are the Ricci curvature and scalar curvature. Λ is the cosmological constant. On the right hand side, $T_{\mu\nu}$ is the stress-energy tensor and $\kappa = 8\pi G/c^4$ is the gravitational constant. $G_{\mu\nu}$ takes in the

spacetime curvature and represents the feature of spacetime. It is simply proportional to the stress-energy tensor if we neglect the comological term.

The spherically symmetric solution to this field equation with zero right hand side ($T_{\mu\nu}$), the so-called Schwarzschild metric, gives the gravitational field outside a spherical mass with zero electric charge of the mass, angular momentum of the mass:

$$ds^2 = (1 - \frac{r_s}{r})c^2dt^2 - (1 - \frac{r_s}{r})^{-1}dr^2 - r^2d\theta^2 - r^2\sin^2\theta d\varphi^2 \tag{1.4}$$

where $r_s = \frac{2GM}{c^2}$ is referred to as the Schwarzschild radius. Here M is the central mass and G is the gravitational constant.

This solution leads to an effective potential for a test particle with mass m orbiting around the central mass

$$V(r) = -\frac{GMm}{r} + \frac{L^2}{2\mu r^2} - \frac{G(M+m)L^2}{c^2\mu r^3}. \tag{1.5}$$

Here L is the angular momentum and μ is the reduced mass. The first two terms are the classical energies in Newtonian gravity. Now if we consider a tiny mass that insignificantly curves the spacetime, GR can reproduce the orbit of a planet around a star seen in Newtonian gravity (Figure 1.6).

Nonetheless, this picture assumes that the orbiting object has a very tiny mass so that we can view it as a test particle. For a scenario like the black hole mergers [80] where the objects deforming and traversing in the spacetime have comparable masses, one needs to iteratively solve how the field is curved by the matters after the matters update their new positions with the geodesic equation. This highly-coupled computation is typically very expensive given that the field equation is composed of ten partial differential equations.

1.4.3 Analog models

One may ask if it is possible to learn something by comparing the existing field theory and systems analogous to them. In fact, researchers in the field of analog gravity have developed diverse systems (fluid [81, 82], condensed matter [83], atomic, and optical [84, 85, 86]) to explore GR questions [81, 82, 84]. For instance, researchers have found hydrodynamic analog of damped resonances, which appears in the ringdown of black hole mergers, in bathtub vortices. This could provide insights into problems not understood in black hole mergers (Figure 1.7B).

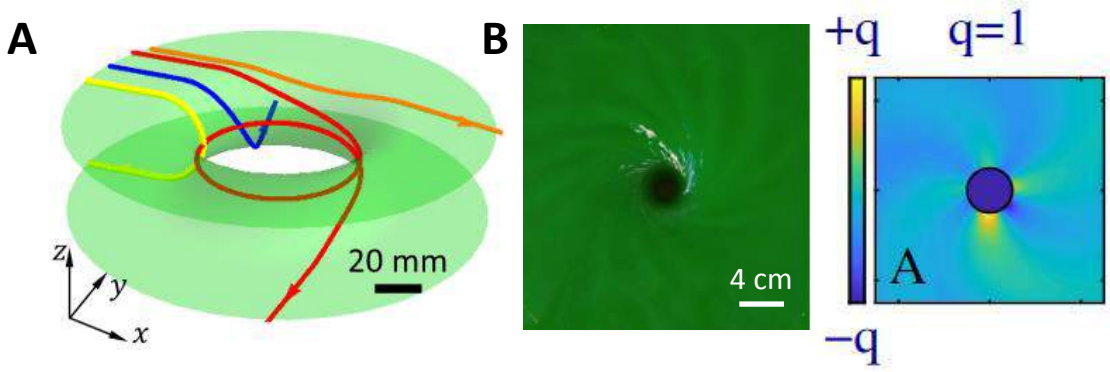

Figure 1.7: **Analog models of gravity.** (A) Light rays in a Transformation Optics device resemble tunneling through a wormhole. (B) Analogous to the ringdown spectrum that reveals many properties of the black hole, the spectrum of vortices in bath tub provides insights into rotating black holes.

In this thesis, we will explore the connections between active matter under field-mediated interactions and other fields in physics, such as general relativity, to show that we can learn something from different fields. For instance, we will show that we can benefit from the spacetime interpretation of the active matter dynamics to help design control schemes and alter the behaviors in robots and living systems. Additionally, considering the expensive numerical computation of field-agent-coupled systems, we posit that the analog models have the potential to provide insights into computationally-expensive problems. For instance, in a case where two masses interact through a field, if we can map the analog systems to the numerical results at the two extreme ends (very large and very small mass ratios), we could

turn to the experiments of the analog system for qualitative insights at intermediate mass ratio regime, which typically is the most challenging for computation.

1.5 Organization of the thesis

This thesis focuses on how field-mediated interactions lead to various phenomena in active matter, including

- Chapter 2, which investigates how active locomotors are affected by interactions mediated by an elastic membrane beneath (Figure 1.8A),
- Chapter 3, which shows that mobile agents driven by resource depletion can interact with each other through the mediation of the devoided resources (Figure 1.8B), and
- Chapter 4, which explores the collective behavior of shape-changing particles confined in a moveable ring (Figure 1.8C) and the individual motion on a flat ground by utilizing the friction.

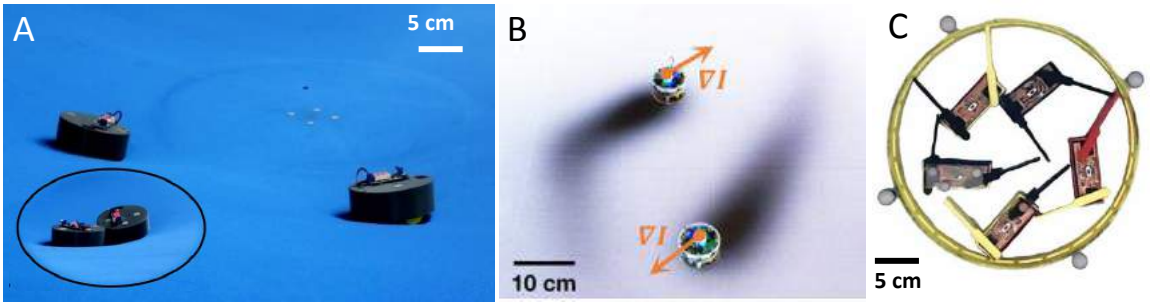

Figure 1.8: **Three field-mediated interactions presented in this thesis.** (A) Active vehicles moving on an elastic membrane are subjected to emergent attraction induced by the membrane deformation. (B) Individual active robots consuming and hunting for the resource would drive themselves due to resource completion. A collective of them would repel each other due to the depletion of the resource. (C) Shape-changing particles confined in a moveable ring show either diffusive or drifting motion depending on the activity homogeneity of the enclosed particles.

In addition to the field-mediated interactions, the latter chapters of this thesis explore interesting topics in the first two regimes, including

- Chapter 5, which shows how active matter moving in non-flat space can translate without conventionally defined forces, and

• Chapter 6, which shows how the attraction force acts as a surface tension in the clustering of active matter.

While the last two chapters are not directly related to field-mediated interaction, it will be interesting to extend them to field-mediated systems in the future. Notably, for the active matter moving in curved space (Chapter 5), the system would have field-mediated interaction if the curvature field can be affected by the active matter. In addition, if we could extend the short-ranged attractive force in Chapter 6 to a long-ranged field, it would be interesting to see what new physics will chime in.

CHAPTER 2

ACTIVE MOTION ON ELASTIC MEMBRANE

Systems consisting of spheres rolling on elastic membranes have been used as educational tools to introduce a core conceptual idea of General Relativity (GR): how curvature guides the movement of matter. However, previous studies have revealed that such schemes cannot accurately represent relativistic dynamics in the laboratory. Dissipative forces cause the initially GR-like dynamics to be transient and consequently restrict experimental study to only the beginnings of trajectories; dominance of Earth's gravity forbids the difference between spatial and temporal spacetime curvatures. Motivated by this limitation, we are curious to ask what will an active agent instead of a passive marble bring us with. Will it make the exact mapping to GR possible? What can we learn from the mapping if it works?

This chapter is devoted to answer these two questions. In section 2.1, We first show that one can extend the conventional passive pedagogical model with an active agent to map exactly onto GR. Next, in section 2.2, we show the tools from GR can help us understand the classical orbits and even manipulate the orbital feature of an individual agent on an elastic membrane. Finally, in section 2.3, we show the model generalized from the individual agent case can help us understand and control the collective behaviors of the active agents interacting through the membrane's mediation[1].

2.1 Programming spacetime dynamics with active vehicle

2.1.1 A classical pedagogical tool to introduce general relativity

Systems consisting of spheres rolling on curved surfaces [87, 88] are a well known non-hydrodynamic analog to gravity. In such readily accessible systems, researchers have made

[1]Part of this chapter is adapted from two arXiv preprints: 'Robophysical modeling of spacetime dynamics' (2202.04835) and 'Field-mediated locomotor dynamics on highly deformable surfaces' (2004.03549)

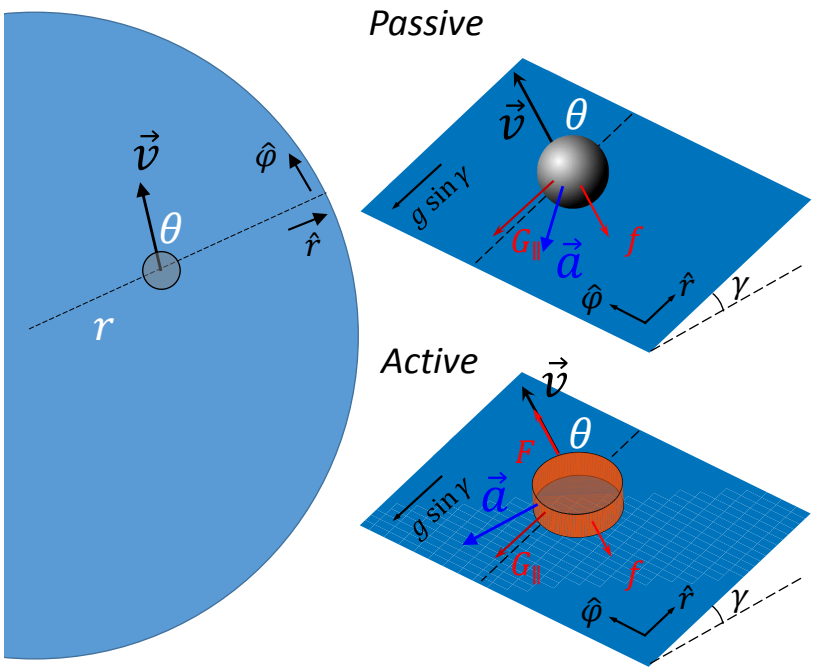

Figure 2.1: **A passive object versus an active object on a membrane.** While a passive marble is only subjected to friction and Earth's gravity that leads to energy dissipation as $\vec{F} \cdot \vec{v} \propto \vec{a} \cdot \vec{v} < 0$, an active object with an additional drive force can keep steady-state motion with prescribed speed as $\vec{a} \cdot \vec{v} = 0$.

intriguing connections to gravity such as Kepler-like laws, precession, and the stability of orbits. However, their studies have also found that these systems do not exactly mimic astrophysical gravity. For instance, the scaling between the period and radius is $T \propto r^{2/3}$ [89] instead of the $T \propto r^{3/2}$ in Kepler's law. Additionally, the sphere on the elastic is passive; as a result, not only do trajectories decay quickly, but also the tunable parameters are limited to only the boundary conditions and the mass of the marble [2].

We hypothesized that making the object "active" – an internally driven robot – would allow mechanical systems to better model GR in part because of the ability to study long time steady states. We further reasoned that the programmability and sensory capabilities of increasingly low-cost and powerful "robophysical" models [44, 90] could allow tuning of parameters that lead to inexact mimics of GR in passive systems. Indeed, our recent work

[2]This section is adapted from a first-authored arXiv preprint 'Robophysical modeling of spacetime dynamics' (2202.04835)

[91] built a framework to understand how the field-mediated dynamics of active agents on flexible membranes demonstrate in the words of Wheeler's famous aphorism: "matter tells spacetime how to curve and spacetime tells matter how to move" [92] as we have mentioned earlier. In particular, we show that the spacetime followed by an active object can be tuned by varying system parameters such as the membrane elasticity and the speed of the object.

Here we amplify on and extend the scheme introduced in [91] and demonstrate how the activity can lead to an exact mapping to GR. We first show how an active object with prescribed speed on an elastic membrane produces longer and more controllable trajectories compared with a passive marble. We then deduce the spacetime it follows, and subsequently show one can program the spacetime with a Schwarzschild orbit as an example. We posit that a future robot car controlled in the way we describe could mechanically mimic black holes dynamics in the laboratory, at low cost and with strong pedagogical value.

2.1.2 Longer trajectories and more control brought by an active object

We first consider an active object prescribed with a constant speed on a circular elastic membrane. Later, we will discuss the general case of time-varying speed. To prevent the object from simply following a near-straight-line spatial geodesic with a spatial curvature

$$ds^2 = \Psi^2 dr^2 + r^2 d\varphi^2 \tag{2.1}$$

where ds is a line segment on a curvature in a cylindrical coordinate system with radius, azimuthal angle and height denoted as r, φ, and z. Here, $\Psi^2 = 1 + z'^2$ and prime denotes the derivative with respect to r, we want the object to turn according to the instantaneous local curvature. To do so, we propel a vehicle with a differential drive that drives the center of mass of the vehicle with a prescribed speed while the speed difference between the two wheels depends on the local slope.

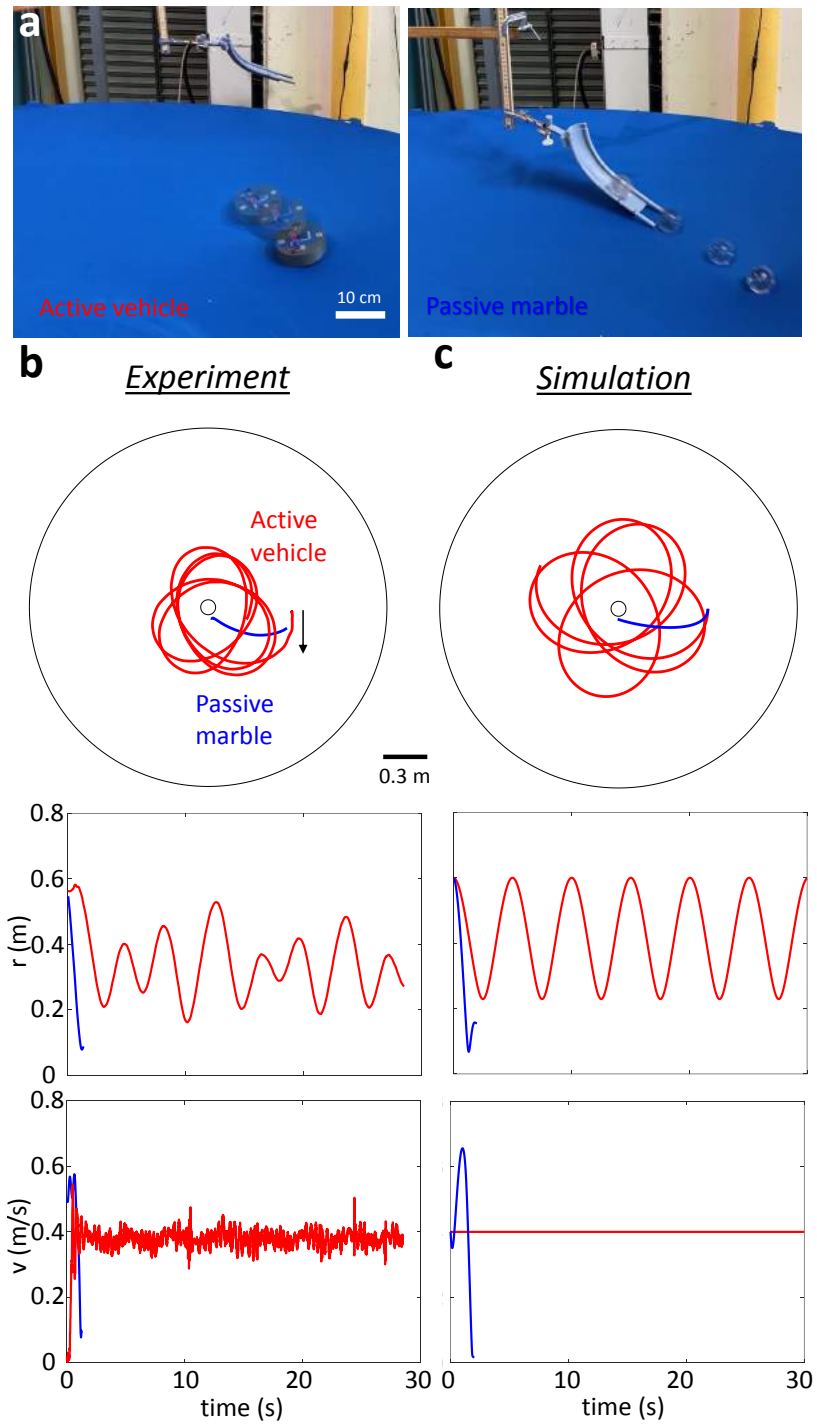

Figure 2.2: **Trajectories of passive and active objects on an elastic membrane.** (a) Sample perspective views of an active vehicle and a passive marble moving on a Spandex membrane. The time interval between two consecutive snapshots is 0.17 s. (b) The experimental trajectories, radius evolution, and speed evolution of the active (red) and the passive (blue) objects with the same mass (150 g) on the same membrane started from the same initial position and velocity on the same membrane. (c) The simulation counterparts of (b).

We first compare the trajectories of the active vehicle with those of a passive marble having the same mass as the vehicle. We released them with the same velocity on the same membrane individually. The speeds of the vehicle and marble are set by adjusting the voltage on the motor and the releasing height on the guiding track (Figure 2.2a) respectively. The trajectories collected from experiments showed that the active vehicle produced trajectories much more persistent (Figure 2.2c) than the passive marble which barely finished the first revolution (Figure 2.2b).

To understand these orbits, we follow the models in [91, 93]. While a passive marble dissipates energy as $\vec{a} \cdot \vec{v} < 0$ (Figure 2.1), an active object can conserve its speed when the driving force dynamically balances with the friction and exactly makes $\vec{a} \cdot \vec{v} = 0$ (Figure 2.3a). Therefore, the acceleration for a constant-speed motion can be written as

$$\frac{a_\varphi}{r} = \ddot{\varphi} + \frac{2\,\dot{r}\,\dot{\varphi}}{r} = \frac{a}{r}\cos\theta \tag{2.2}$$

$$a_r = \ddot{r} - \frac{r\,\dot{\varphi}^2}{\Psi^2} + \frac{\Psi'}{\Psi}\dot{r}^2 = -\frac{a}{\Psi}\sin\theta\,. \tag{2.3}$$

where θ is the heading angle between the radial direction and the velocity on an isotropic circular membrane.

Though the speed is constant, the change of the velocity (the scalar acceleration a) depends on the local slope γ (Figure 2.1). Since γ varies with radius (position) r, a is also a function of r. Additionally, a should also depend on velocity in general. However, given that the velocity has constant magnitude as the speed is constant, this dependence is reduced to one degree of freedom. For our convenience, we chose the direction of the velocity, θ. If we consider an active object without chiral bias such that its trajectory has a mirror symmetry, the dependence of a (thus a_φ) on θ should be anti-symmetric about $\theta = 0$, as otherwise the clockwise ($\theta(t = 0) = \theta_0$) and counterclockwise ($\theta(t = 0) = -\theta_0$) trajectories (Figure 2.3b) will not be mirror reflections with each other. A first-order approximation with this symmetry could be $a \propto k(r)\sin\theta$ where the $k(r)$ is the radial

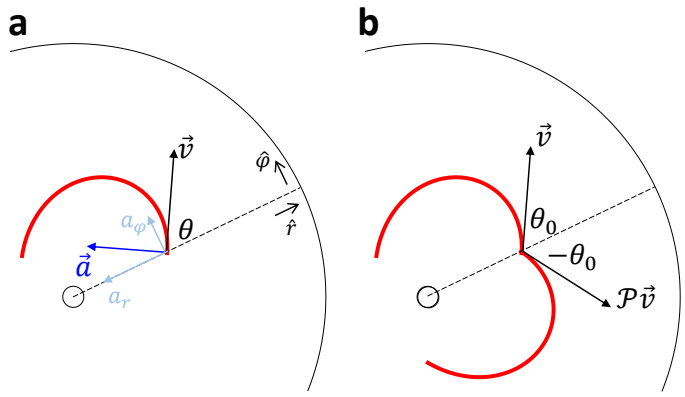

Figure 2.3: **Dynamics and symmetry of a non-chiral active vehicle.** (a) The acceleration of an active vehicle is perpendicular to its velocity $\vec{v}$. (b) A non-chiral vehicle with a mirror-reflected initial velocity $\mathcal{P}\vec{v}$ will produce a mirror-reflected trajectory.

dependence due to the local slope $\gamma(r)$ that changes with radius. One could imagine k increases with the local slope γ. The detail relation between k and γ would depend on the mechanical structure of the active object, but one could always Taylor expand this dependence. For preliminary study, here we assume linear dependence $k = C\gamma$.

While an active object follows equations Equation A.30a, Equation A.30b, a passive marble rolling on the membrane without slipping has a Lagrangian [93]

$$\mathcal{L} = \frac{7}{10} m \left((1 + z'(r)^2)\dot{r}^2 + r^2\dot{\varphi}^2 \right) - mgz(r). \tag{2.4}$$

If we consider the dissipation function to be an effective Coulomb rolling friction $D = -fv$ (See Sec. A of the Appendix) where $v = \sqrt{\dot{r}^2 + r^2\dot{\varphi}^2}$ and $f = \mu mg$, we arrive at a more realistic model by plugging the dissipation into the right hand side of the Euler-Lagrange equation $\frac{d}{dt}(\frac{\partial \mathcal{L}}{\partial \dot{q}}) - \frac{\partial \mathcal{L}}{\partial q} = -\frac{\partial D}{\partial \dot{q}}$ where q are r and φ.

$$(1 + z'^2)\ddot{r} + z'z''\dot{r}^2 - r\dot{\varphi}^2 + \frac{5}{7}gz' = -\frac{5}{7}\mu g\frac{\dot{r}}{v} \tag{2.5}$$

$$r^2\ddot{\varphi} + 2r\dot{r}\dot{\varphi} = -\frac{5}{7}\mu g\frac{r^2\dot{\varphi}}{v} \tag{2.6}$$

The left hand sides of the above equations are the same as the dynamical equations in

[87] while the right hand sides correspond to the friction force.

Integration of the above models for the active vehicle and passive marble (Figure 2.2c) shows qualitative agreement with the experiments. Figure 2.2c shows the integration of the active dynamics Equation A.30a, Equation A.30b and the passive dynamics Equation 2.5, Equation 2.6 on the same membrane measured from an experiment when the object started from the same position and velocity. The physical parameters are measured from experiments. The acceleration dependence on radius k for the active vehicle uses $k = C\gamma = C\partial_r z$ where $z(r)$ is measured from the height of the static vehicle placed at different radii r. The proportionality C uses the ratio between acceleration and the gradient $\partial_r z$ at the radius close to the edge of the elastic membrane. We probe the friction coefficient for the passive marble by measuring the dissipation of mechanical energy in a designed experiment (See Appendix section A.1).

2.1.3 A recipe for spacetime programming

To functionally understand the feature of the orbit of the active object so that we are able to program it, the spacetime of these orbits could provide us with insights. If we recognize similarity between the resultant spacetime metric and some known metrics, then we could understand how the orbital features depend on the system parameters.

In principle, the orbital dynamics we wish to map could be described by a diversity of metrics. But for simplicity, and to make the analogy with GR in the weak field limit, given the axi-symmetry of the system, we propose a metric of the form

$$ds^2 = -\alpha^2 dt^2 + \Phi^2(\Psi^2 dr^2 + r^2 d\varphi^2) \tag{2.7}$$

with $\alpha = \alpha(r)$, $\Phi = \Phi(r), \Psi^2 = 1 + z'^2$. Here, the elements of the metric $g_{\alpha\beta}$ are zero except $g_{tt} = -\alpha^2$, $g_{rr} = \Phi^2\Psi^2$ and $g_{\varphi\varphi} = \Phi^2 r^2$. Plug the $g_{\alpha\beta}$ into the Christoffel symbols

$\Gamma^{\mu}_{\alpha\beta}$ in the geodesic equations $\mathring{\ddot{x}}^{\mu} + \Gamma^{\mu}_{\alpha\beta}\mathring{x}_{\alpha}\mathring{x}_{\beta} = 0$, we arrive at

$$\mathring{\ddot{t}} + \frac{(\alpha^2)'}{\alpha^2}\mathring{t}\mathring{r} = \frac{1}{\alpha^2}\left(\alpha^2\mathring{t}\right)^{\circ} = 0 \tag{2.8}$$

$$\mathring{\ddot{\varphi}} + \frac{(\Phi^2\, r^2)'}{\Phi^2\, r^2}\mathring{\varphi}\mathring{r} = \frac{1}{\Phi^2\, r^2}\left(\Phi^2\, r^2\mathring{\varphi}\right)^{\circ} = 0 \tag{2.9}$$

$$\mathring{\ddot{r}} + \frac{(\alpha^2)'}{2\Phi^2\Psi^2}\mathring{t}^2 + \frac{(\Phi^2\Psi^2)'}{2\Phi^2\Psi^2}\mathring{r}^2 - \frac{(\Phi^2 r^2)'}{2\Phi^2\Psi^2}\mathring{\varphi}^2 = 0 \tag{2.10}$$

with λ as an affine parameter and $\mathring{q} = dq/d\lambda, \mathring{\ddot{q}} = d^2q/d\lambda^2$. From Equation 2.8,Equation 2.9, we have that

$$\alpha^2\mathring{t} = E = \text{constant}, \tag{2.11}$$

$$\Phi^2 r^2\mathring{\varphi} = L = \text{constant}, \tag{2.12}$$

both a consequence that conservation of energy and angular momentum holds.

With the help of $\mathring{q} = (dq/dt)(dt/d\lambda) = \mathring{t}\dot{q}$ (see Appendix section A.2 for details), the geodesic equations can be rewritten as

$$\ddot{\varphi} + \frac{2\dot{r}\dot{\varphi}}{r} = \left[\frac{(\alpha^2)'}{\alpha^2} - \frac{(\Phi^2)'}{\Phi^2}\right]\dot{r}\,\dot{\varphi} \tag{2.13}$$

$$\begin{aligned}\ddot{r} - \frac{r\dot{\varphi}^2}{\Psi^2} + \frac{\Psi'}{\Psi}\dot{r}^2 &= \left[\frac{(\alpha^2)'}{\alpha^2} - \frac{(\Phi^2)'}{\Phi^2}\right]\dot{r}^2 \\ &+ \frac{1}{2\,\Phi^2\Psi^2}\left[(\Phi^2)'v^2 - (\alpha^2)'\right]\end{aligned} \tag{2.14}$$

where primes denoting differentiation with respect to r.

Notice that the left hand side of Equation 2.13,Equation 2.14 are the components of the acceleration, a_{φ} and a_r respectively, in Equation A.30a,Equation A.30b. When we plug $\cos\theta = \dot{r}/v, \sin\theta = r\dot{\varphi}/v$ and $a = k\sin\theta$ into Equation A.30a,Equation A.30b, we have

$$\ddot{\varphi} + \frac{2\,\dot{r}\,\dot{\varphi}}{r} = \frac{k}{v^2}\dot{r}\dot{\varphi} \tag{2.15}$$

$$\ddot{r} - \frac{r\,\dot{\varphi}^2}{\Psi^2} + \frac{\Psi'}{\Psi}\dot{r}^2 = -\frac{k}{\Psi}\frac{r^2\dot{\varphi}^2}{v^2}. \tag{2.16}$$

Thus, comparing the right hand sides of Equation 2.13,Equation 2.14 and Equation A.30a,Equation A.3 and noticing $\dot{r}^2 + r^2\dot{\varphi}^2 = v^2$ in Equation 2.16 yield the following relationships between the metric functions α and Φ in terms of the speed of the vehicle and k.

$$\frac{(\alpha^2)'}{\alpha^2} = \frac{k\Psi}{v^2}\left[\frac{\Phi^2 v^2}{\alpha^2 - \Phi^2 v^2}\right] \tag{2.17}$$

$$\frac{(\Phi^2)'}{\Phi^2} = \frac{k\Psi}{v^2}\left[\frac{2\Phi^2 v^2 - \alpha^2}{\alpha^2 - \Phi^2 v^2}\right]. \tag{2.18}$$

Integration of the above equations yields

$$\alpha^2 = -\frac{1}{C_1 v^2} + C_2 \cdot e^{-K/v^2} \tag{2.19}$$

$$\Phi^2 = \frac{\alpha^2}{v^2} + C_1(\alpha^2)^2 \tag{2.20}$$

where $K = K(r) \equiv \int_0^r k(s)\Psi(s)ds$.

To determine the constants, we make use of the normalization condition and the fact that the metric should be flat at $k \to 0$.

The metric (Equation 2.7) gives us normalization condition $-1 = -\alpha^2\mathring{t}^2 + \Phi^2(\Psi^2\mathring{r}^2 + r^2\mathring{\varphi}^2)$. To exploit this condition, we want to eliminate the $d/d\lambda$ in $\mathring{r}$ like Equation 2.11, Equation 2.12. Using $\mathring{q} = (dq/dt)(dt/d\lambda) = \mathring{t}\dot{q}$, Equation 2.11, Equation 2.12, and the fact that $v^2 = r^2\dot{\varphi}^2 + \dot{r}^2$, we have

$$\begin{aligned}
\mathring{r}^2 &= \left(\frac{E}{\alpha^2}\dot{r}\right)^2 \\
&= \frac{E^2}{(\alpha^2)^2}\frac{1}{\Psi^2}(v^2 - r^2\dot{\varphi}^2) \\
&= \frac{E^2}{(\alpha^2)^2}\frac{1}{\Psi^2}\left[v^2 - r^2\left(\frac{\alpha^2}{E}\mathring{\varphi}\right)^2\right] \\
&= \frac{E^2}{(\alpha^2)^2}\frac{1}{\Psi^2}\left[v^2 - r^2\left(\frac{\alpha^2}{E}\frac{L}{\Phi^2 r^2}\right)^2\right].
\end{aligned} \tag{2.21}$$

Plug the $\mathring{t}, \mathring{r}, \mathring{\varphi}$ derived above into the normalization condition, we now have

$$-1 = -\frac{E^2}{\alpha^2} + \frac{\Phi^2 E^2 v^2}{(\alpha^2)^2}. \tag{2.22}$$

Plug in the α^2 and Φ^2 derived earlier (Equation 2.19,Equation 2.20), we have

$$-\frac{1}{E^2} = C_1 v^2. \tag{2.23}$$

Therefore $C_1 = -\frac{1}{v^2 E^2}$.

Another condition to determine the constants is that when $k = 0$, the metric is flat. In fact, $k(r) = 0$ indicates $K(r) = \int_{s=0}^{r} k(s)\Psi(s) = 0$. We set the lower limit of the integral to zero, without loss of generality, since otherwise the arbitrary constant will be absorbed by C_2. This limit reduces the metric to

$$\alpha_0^2 = -\frac{1}{C_1 v^2} + C_2$$
$$\Phi_0^2 = \frac{\alpha_0^2}{v^2} + C_1(\alpha_0^2)^2$$

where $\alpha_0 \equiv \lim_{k\to 0} \alpha$ and $\Phi_0 \equiv \lim_{k\to 0} \Phi$.

To satisfy the flatness that $\alpha_0 = \Phi_0$, we need

$$\begin{aligned} \alpha_0^2 &= \frac{\alpha_0^2}{v^2} + C_1(\alpha_0^2)^2 \\ 1 &= \frac{1}{v^2} + C_1(-\frac{1}{C_1 v^2} + C_2) \\ C_1 C_2 &= 1. \end{aligned} \tag{2.24}$$

Plug the conditions Equation 2.23,Equation 2.24 into the metric with undetermined

coefficients Equation 2.19,Equation 2.20, we finally arrive at

$$\alpha^2 = E^2(1 - v^2 e^{-K/v^2}) \tag{2.25}$$

$$\Phi^2 = E^2 e^{-K/v^2}(1 - v^2 e^{-K/v^2}). \tag{2.26}$$

The quantity E is a constant of motion (energy) associated with the fact that the metric is time-independent. The other constant of motion is L (angular momentum) associated with the metric's φ-symmetry.

Thus our formulation indeed reveals that the vehicle does not simply follow spatial geodesics of the membrane but instead follows geodesics in an emergent spacetime generated by the global curvature, the local curvature, the active dynamics, and the differential mechanism. The resultant dynamics can now be understood as those of a test particle in a new spacetime where the active feature of the real particle, such as a persistently controlled speed, generates a non-splittable effective spacetime for the test particle (i.e. g_{tt} is not constant). In the language of the work by Price [94], the effects of curvature are now not restricted to space [95]. That is, in general, the metric function g_{tt} could depend on both the coordinate time (t) as well as the spatial coordinates. For a static metric (i.e., the metric functions are independent of time), the spacetime becomes splittable when g_{tt} does not depend on the spatial coordinates. This leads to only spatial curvature. It was argued in [94] that the spatial curvature is different from the spacetime curvature as it is devoid of gravity, i.e., a free particle initially at rest will remain at rest.

The essential contribution from active drive is the persistent response to the local curvature, here particularly enabled by the controlled constant speed unseen in passive systems. In fact, when the response of the turning to the local slope vanishes at the limit $v \to \infty$ such that $\alpha^2 = \Phi^2 = E^2(1 - v^2)$, the metric Equation 2.7 with components Equation 2.25,Equation 2.26 reduces to a splittable (and flat) spacetime Equation 2.1. On the other hand, when v is finite and controllable, the active locomotion provides more flexibility

and programmability in fabricating the desired spacetime depicted by GR than the passive agents studied in the previous works such as the dissipative marbles [93, 87] rolling on a membrane. For instance, the conserved quantity directly led from the metric could show that a k increasing with r makes an orbit have a precession with a sign opposite to the orbit while a k decreasing with r makes an orbit have a precession with a sign same as the orbit [96].

2.1.4 Programming a Schwarzschild blackhole

The metric Equation 2.25,Equation 2.26 has shown us how the parameters of the system change the spacetime and thus the orbit. Now we want to see how we can do the inverse problem to program the desired spacetime with the system parameters (e.g., $k(r)$ and $v(r)$).

In metric Equation 2.25,Equation 2.26, we can tune the speed and membrane elasticity to change the spacetime of the orbits. However, here the spatial and radial metric are not completely disentangled yet. To have two degrees of freedom such that we can indeed program the spacetime arbitrarily, one could introduce another degree of freedom. For instance, if we allow the speed v to vary with the radius r (physical instantiation could be achieved by inferring the radius from the instantaneous tilting angle γ), Equation 2.17, Equation 2.18 with $\Psi^2 \approx 1$ give the requirement of mapping as

$$\frac{(\alpha^2)'}{\alpha^2} - \frac{(\Phi^2)'}{\Phi^2} = \frac{v'}{v} + \frac{k}{v^2} \tag{2.27}$$

$$\frac{(\Phi^2)'v^2 - (\alpha^2)'}{2\Phi^2} = -k. \tag{2.28}$$

These two equations above give us the recipe to create desired spacetime by changing the speed of the vehicle with radius. For a desired metric with spatial curvature $\Phi^2(r)$ and temporal curvature $\alpha^2(r)$, we can solve for the required membrane elasticity and object

speed by plugging in the curvatures into these to equations. The solution (see Appendix section A.3 for details) is

$$v(r)^2 = \left(\int_{r_1}^{r} f(r') \cdot \frac{(\alpha^2)'(r')}{\Phi^2(r')} dr' \right) / f(r) \tag{2.29}$$

where

$$f(r) = -e^{\int_{r_1}^{r} -2\frac{(\alpha^2)'(r')}{\alpha^2(r')} + \frac{(\Phi^2)'(r')}{\Phi^2(r')} dr'}. \tag{2.30}$$

For instance, if we plug in the Schwarzschild metric in isotropic coordinates $\alpha^2(r) = 1 - r_s/r, \Phi^2(r) = (1 - r_s/r)^{-1}$, we arrive at the prescription for the membrane elasticity $k(r)$ and active object speed $v(r)$ as shown in Figure 2.4a. Analytically,

$$v(r)^2 = r_s \frac{(r - r_s)^2}{r^3} + C \left(\frac{r - r_s}{r} \right)^3 \tag{2.31}$$

$$k(r) = \frac{r_s(r - r_s)(r + Cr + r_s - Cr_s)}{2r^4} \tag{2.32}$$

where

$$C = \frac{v_0^2 r_0^3}{(r_0 - r_s)^3} - \frac{r_s}{r_0 - r_s}. \tag{2.33}$$

Here, v_0 is the vehicle speed at r_0 as the boundary condition. One can use the inner radius as r_0 for instance.

Simulations using this prescription show features of Schwarzschild orbit such as the linear dependence of precession angle in terms of the inverse latus rectum. For Schwarzschild

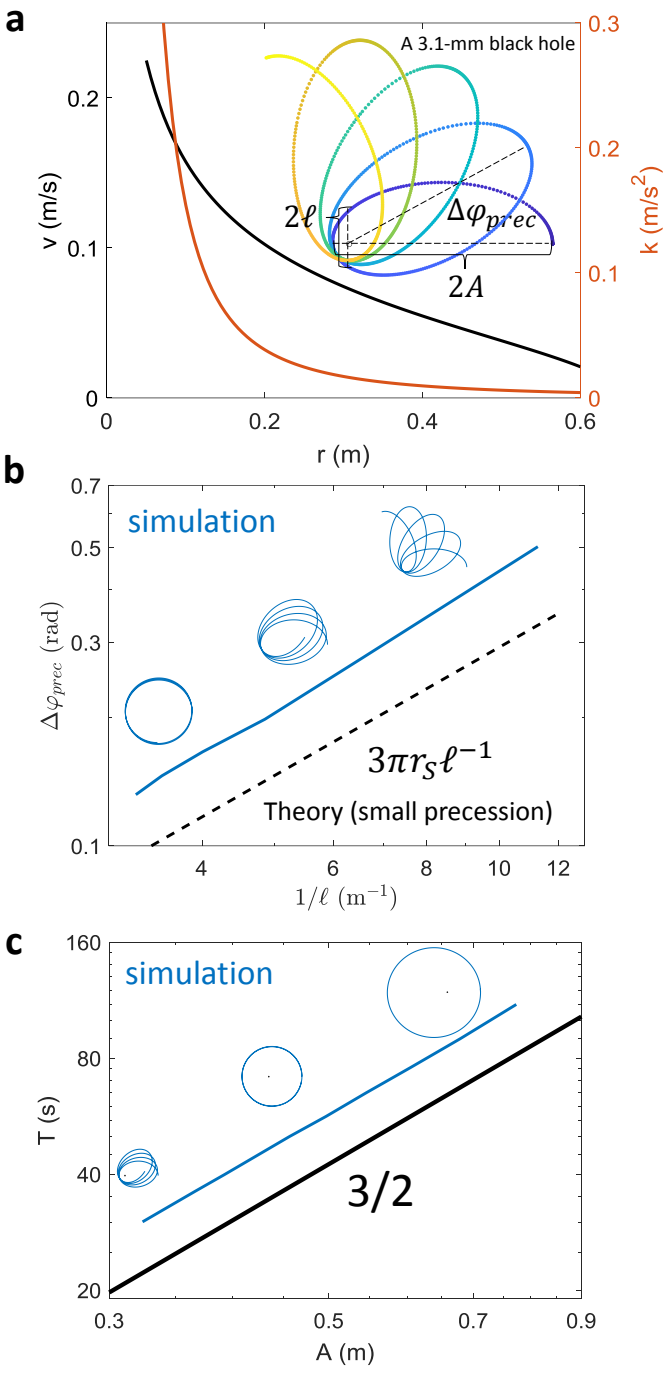

Figure 2.4: **Creating Schwarzschild orbit with speed varying particle.** (a) The speed and membrane elasticity's dependence on radius to create an Schwarzschild blackhole with $r_s = 3.1$ mm. The inset shows a precessing orbit with $A = 0.3$ m by using this prescription. (b) Precession angle $|\Delta\varphi_{\text{prec}}|$ as a function of inverse latus rectum. (c) The relation between the orbital period T and the semi major-axis A follows the Keplar's law as $T \propto A^{3/2}$. Insets in (b) and (c) show the trajectories around the data points.

orbits with small precession, the precession angle increases with the inverse latus rectum as $\Delta\varphi_{\text{prec}} = 6\pi G^2 M/(c^2 l) = 3\pi r_s \ell^{-1}$ where G is the gravitational constant, M is the mass of the star, c is the speed of light, and $\ell \equiv A\,(1-e^2)$ is the latus rectum. We evaluate the semi major-axis A and the eccentricity e using the minimum and maximum radii: $A = (r_{\text{max}} + r_{\text{min}})/2,\ e = (r_{\text{max}} - r_{\text{min}})/(r_{\text{max}} + r_{\text{min}})$. Figure 2.4b shows the precession angle $\Delta\varphi_{\text{prec}}$ as function of the inverse of the latus rectum ℓ^{-1} from simulations given $v_0 = v(r_0 = 0.05\text{m}) = 0.225$ m/s and $r_s = 0.0031$ m. The curve qualitatively follows the linear relationship, with small deviation from the theory due to the large precession angle. By changing (r_0, v_0), we can get larger angular momenta and thus larger orbits around the same blackhole. These orbits show a relation between period T and semi major-axis A following the Keplar's law (Figure 2.4c).

To achieve this in experiments, a vehicle must actively vary its speed with radius and a membrane must have a radial dependence of its elastic modulus. One possible solution for the vehicle is to attach a tilt sensor to infer the radius and change the speed. To program the membrane with radially varying profile $k(r) = Cg|\partial_r z|$, here we consider a membrane with linear elasticity following the Poisson Equation $\nabla \cdot E \nabla z = P$ where P is the unit load from the membrane gravity. One possible way is to obtain the desired $k(r)$ is to create an elastic material with a radially varying thickness $P = P(r)$. Another option is to fabricate a membrane with a radially varying modulus $E = E(r)$.

By developing a mapping between dynamics of a wheeled vehicle on a spandex membrane, we demonstrate that an active object that can prescribe its speed can not only obtain steady-state orbits, but also use the additional parameters such as speed to tune the orbits towards relativistic dynamics. Our mapping demonstrates how activity mixes space and time in a metric, shows how active particles do not necessarily follow geodesics in the real space but instead follow geodesics in a fiducial spacetime. The mapping further reveals how parameters such as the membrane elasticity and instantaneous speed allow programming a desired spacetime such as the Schwarzschild metric near a non-rotating black hole.

Given the flexibility in construction and programming vehicles, our system makes for an attractive target to push toward a mechanical analog GR system; while superficially our system resembles the educational tool used to motivate Einstein's view of spacetime curvature influencing matter trajectories [89, 93, 87], unlike such systems which are *not* good analogs of GR, the activity allows the dynamics of the vehicle to be dictated by the curvature of "spacetime", not just the curvature of space as in splittable spacetimes (g_{tt} is constant) [94]. Thus we posit that mechanical analog "robophysical" [44, 97] systems can complement existing fluid [81, 82], condensed matter [83], atomic, and optical [84, 85, 86] analog gravity systems [98] given the ability to create infinite types of spacetimes. Further, we might even generate analogies to wave-like systems [72, 11, 99]; for example, one could increase the speed of the vehicle to be comparable to disturbance propagation (such that the membrane would follow the wave equation).

Beyond its role as a mechanical analog for GR, this framework could also provide a new perspective to understand active matter undergoing field-mediated interactions [14, 96]. Our mapping and framework point the way to the possibility to create a robophysical analog gravity system in the laboratory at low cost and provide insights into active matter in deformable environments and robot exploration in complex landscapes. For instance, the spacetime metric of the agents' motion can both guide our choice of parameter values to alter orbital features like the precession sign and influence our design of control schemes that accomplish tasks like helping multiple agents avoid mergers on the membrane [96].

2.2 Dynamics of an individual agent

The previous section shows us the theoretical and preliminary support of the possibility to systematically understand and control the dynamics of an active agent on an elastic membrane. Now we try to see how this framework works for a systematic examination of the orbits[3].

[3]This section is adapted from a co-first-authored arXiv preprint 'Field-mediated locomotor dynamics on highly deformable surfaces' (2004.03549)

To avoid the time and space-dependent complexity of hydrodynamic and complex terradynamic surfaces (e.g. splashing and permanent deformation respectively), we chose the same model as the previous section. Specifically, we study the locomotion and field interaction of vehicles on highly deformable elastic environments via the study of two cases: a single vehicle in the presence of a fixed obstacle and multiple vehicles influencing each other. We find that the dynamics of even a single vehicle are interesting when influenced by a non-moving boundary via membrane curvature alone. Despite possessing neither sensing nor control, the vehicle orbits, collides with the center, or escapes from the membrane, analogous to how bodies orbit stars. In the next section, we will base on this model for individual agent and show how multiple vehicles generically display a substrate-mediated cohesion whose collision timescale depends on vehicle mass, which is reminiscent of the Cheerios effect [62].

2.2.1 Basic vehicle dynamics

We study the dynamics of a differential driven vehicle self-propelling on a deformable curved surface. The vehicle (Figure 2.5a,b) takes inspiration from many active matter experiments [100, 25, 101] and simulations [30, 102, 101] in that it moves straight in the absence of interaction with the other agents. Further, its mechanics are key elements of modern wheeled vehicles, which are deployed in diverse terradynamic scenarios, from paved roads to Martian landscapes [103, 104, 105]. The vehicle has two rear wheels and one front spherical caster for stability. A critical feature of the vehicle is a *differential* [106] which allows independent rotation of the wheels upon different load conditions by maintaining constant speed governed by motor rotation rate. If the load of the two wheels is equal, e.g. the vehicle is on level ground, both wheels turn at the same rate and the vehicle goes straight. If the load of one of the wheels increases (i.e. vehicle tilts) the corresponding wheel slows down and the opposite wheel speeds up, which results in turning motion around the slow wheel. While we have used a particular robot to perform the study, we note

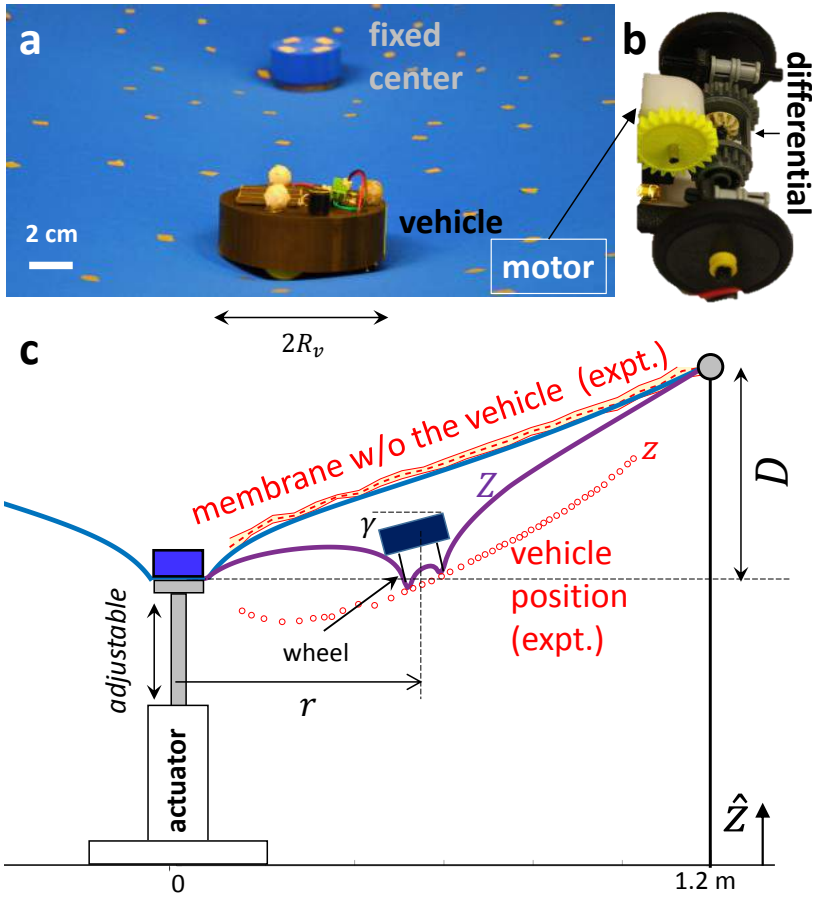

Figure 2.5: **Interaction induced by elastic substrate deformation.** (a) One vehicle transiting around a central depression. (b) Side view of the differential driven vehicle and side view of the drive mechanism; see also Figure 2.9a for more details. (c) Cross section of the experimental set-up with a depression D (z axis of the membrane is linearly stretched for visual clarity). The red dashed line denotes the measurement of the membrane shape in the absence of the vehicle, the red open dots show the contact positions of the vehicle with the membrane when it is placed at different radii. The vehicle's vertical position z relative to the confining outer membrane ring is approximated by the average of the membrane height Z around it: $z(\mathbf{r}) \approx \langle Z(\mathbf{r}')\rangle_{|\mathbf{r}'-\mathbf{r}|=R_v}$ where $\mathbf{r}$ and $\mathbf{r}'$ are the horizontal positions of the vehicle and the membrane around it. In the axi-symmetric case shown here, it can be further approximated by $z(r) \approx (Z(r-R_v)+Z(r+R_v))/2$.

that constant speed motion is a convenient starting point to study more general dynamics in such active systems.

Experiments were performed on a four-way stretchable spandex fabric (that stretches and recovers both width- and lengthwise) affixed unstretched to a circular metal frame (see Materials and Methods) with a radius of $R = 1.2$ m. In the first situation with a fixed center,

a linear actuator attached to the center of the membrane warps the fabric from underneath to allow adjustable central depression of depth D with a cap (radius $R_0 = 5$ cm) fastening the actuator to the fabric. A diagram of the experimental setup is given in Figure 2.5c. The membrane has a measured axi-symmetry such that the standard deviation of the membrane height at each radius is less than 5% of the central depression magnitude D (see Figure A.7 in the appendix).

Three aspects are important to understand the dynamics of the vehicle on the membrane. The first is that the vehicle dynamics are highly damped and inertia plays a minimal role: if the motor stops, the vehicle rapidly comes to rest (within a second). That is, there is no "rolling downhill". The second aspect is that the differential in the vehicle allows it to turn dynamically according to the local curvature instead of simply following the spatial geodesics of the membrane, which leads to almost straight trajectories given the shallow depressions of the membrane. The third important aspect is that, while the global shape of the membrane without the vehicle is important, due to the vehicle's mass, its local environment deviates from the unloaded shape of the membrane, introducing an additional local deformation of the membrane. This results in a vehicle tilting to an angle γ (between the normal of the vehicle surface and $\hat{z}$) depending on the vehicle's radial position in membrane as depicted in Figure 2.5c.

2.2.2 Precession dynamics

For simplicity, we first study the dynamics of a single vehicle moving at constant speed on the membrane (set by constant motor rotation rate and enforced by the differential mechanism). Experiments were conducted by setting the initial radius r (the distance between the center of the vehicle and the actuator) and heading angle θ (the angle between the radial direction and the velocity of the vehicle, Figure 2.6b). The trajectories of the vehicle were recorded for 2 minutes by a high-speed motion capture system (Optitrack, 120 Hz) posi-

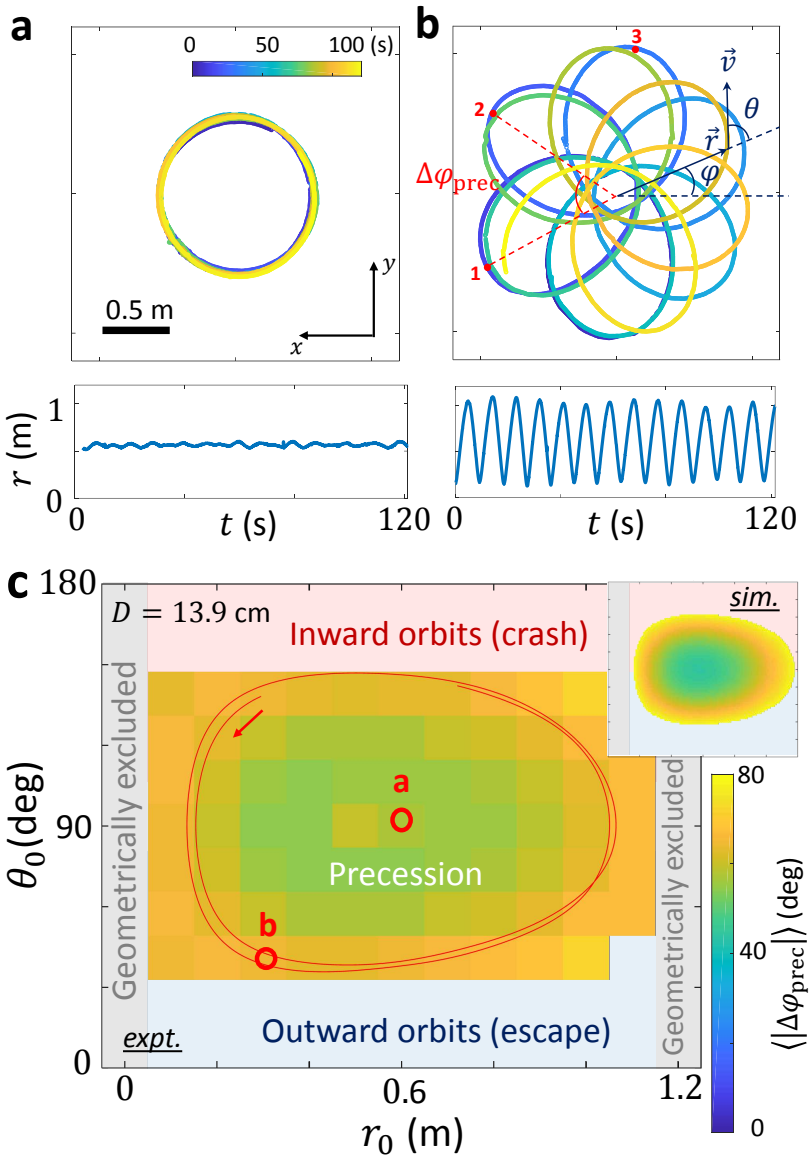

Figure 2.6: **Examples of bound vehicle trajectories.** An example (a) circular orbit and (b) eccentric orbit for the central depression $D = 13.9$ cm. In (b) the angle θ denotes the heading angle and φ denotes the azimuthal angle. The corresponding evolution of the radius over time are shown below. The eccentric orbit exhibits a precession of $|\Delta\varphi_{\mathrm{prec}}| \approx \pi/3$ evaluated from consecutive apoapsis or periapsis (peaks or valleys on the $r - t$ plots). (c) Precession angle's dependence on initial condition. The initial condition of the circular orbit (a) is indicated by a red circle. Any points on the trajectory of (b) can be considered as an initial condition of it. Two orbits of (b) are shown in a red curve. The inset shows the prediction from theory using (Equation A.30a) and (Equation A.30b); axes ranges are the same as those in main figure.

tioned above the membrane. Certain initial conditions (a particular radius $r_0 = r_c \approx 0.6$m and heading $\theta_0 \approx 90^\circ$) developed immediate circular orbits (Figure 2.6a). However, similar to orbiting droplets on a liquid surface curved by their weight [107], for a majority of (r_0, θ_0), we observed trajectories consisting of *retrograde* precessing ellipse-like orbits (Figure 2.6b) about the central depression, i.e. the maximum radius of the orbit does not return to the same azimuthal position but rather lags behind after an orbit.

The precessing dynamics can persist for many orbits until the vehicle's orbit either slowly increases or decreases its eccentricity. In the former case, the vehicle ultimately collides with the central cap or escapes to the boundary. In the latter case, the precession decays into an approximately circular orbit with a critical r_c radius depending on the central depression D. From analysis of the vehicle mechanism and dynamics (see section A.4 in the appendix), we attribute these behaviors to slight mechanical imperfections in the mass distribution in the vehicle, such as the deviation of the center of mass from the center-line, ΔB. The eccentricity evolves over orbits with a factor $e^{-\epsilon\varphi/2}$ where $\epsilon = -\Delta B/L_c$; the precessing dynamics can observed over longer timescales as the magnitude of imperfection decreases. Here L_c is the distance between the wheel axle and the center of mass, and R_v is the radius of the vehicle. Ideally, a perfect vehicle with $\Delta B = 0$ makes $e^{-\epsilon\varphi/2}$ remain at 1 and the orbit stays in the steady-state forever. The half-life $(2\log 2)/\epsilon$ characterizes how steady an orbit is; the sign of ΔB determines if the eccentricity will expand or decay.

Besides the slight chirality characterized by ΔB, the slight anisotropy of the membrane could be another contribution to the variability of trajectories by generating a perturbation with period 2π in the azimuthal angle. This has a larger effect on lighter vehicle since smaller mass is more susceptible to the same perturbation from anisotropy. Given the precession angle is $\Delta\varphi_{prec}$, the azimuthal angle that the orbit sweeps across in one precession is $\Delta\varphi(1) = 2\pi - \Delta\varphi_{prec}$. After N precessions, the angle swept by the orbit is $\Delta\varphi(N) = N(2\pi - \Delta\varphi_{prec})$. The smallest positive integer N that makes $\Delta\varphi(N)$ an integer multiple of 2π so that the car will return to the same position is $N = 2\pi/\Delta\varphi_{prec}$. This

gives $\Delta\varphi(N) = 2\pi(N-1)$. Fig.Figure 2.7 shows two examples with $N = 4$ and 5 that verify this argument.

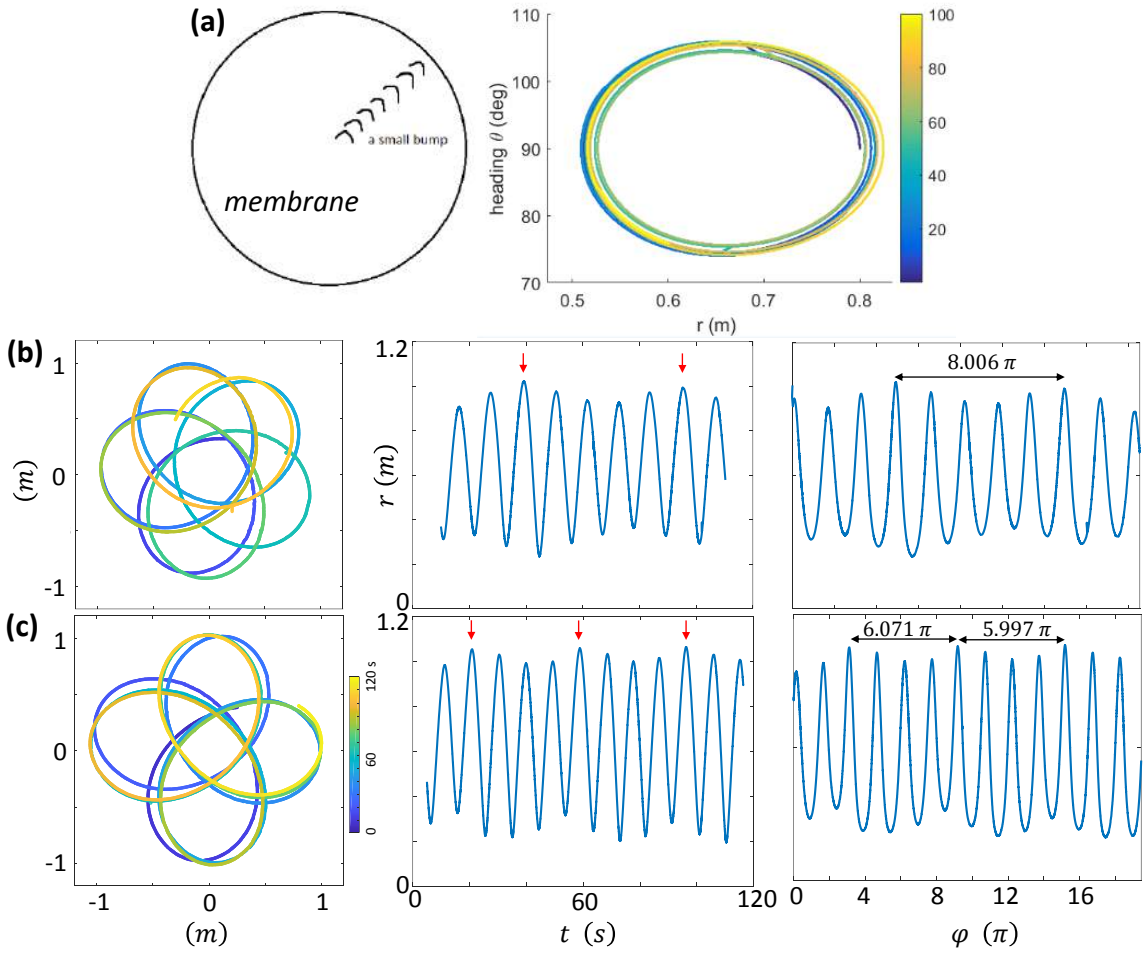

Figure 2.7: **Effect from membrane defects.** (a) When the membrane does not have a perfect axial symmetry, the orbit of a steady precession is not a perfect contour in the $r-\theta$ plane. Instead, it is an annulus with finite width. The period of the modulation is therefore $2\pi/\Delta\phi_{prec}$ precessions. Trajectories with N-fold symmetry has a modulation period of $2(N-1)\pi$. (b) experimental trajectory with $N = 5$. (c) experimental trajectory with $N = 4$.

Incorporating the transient decay from the chiral bias and the modulation from the , we can evaluate the precession, half life and other quantities using the model

$$r_{model}(\varphi; r_c, A_1, \varphi_1, A_2, \varphi_2, \omega_{\text{prec}}) \tag{2.34}$$

$$= r_c + e^{-\varphi/\tau}\left(A_1 \cos\left(\varphi + \varphi_1\right) + A_2 \cos\left(\omega_{\text{prec}}\varphi + \varphi_2\right)\right) \tag{2.35}$$

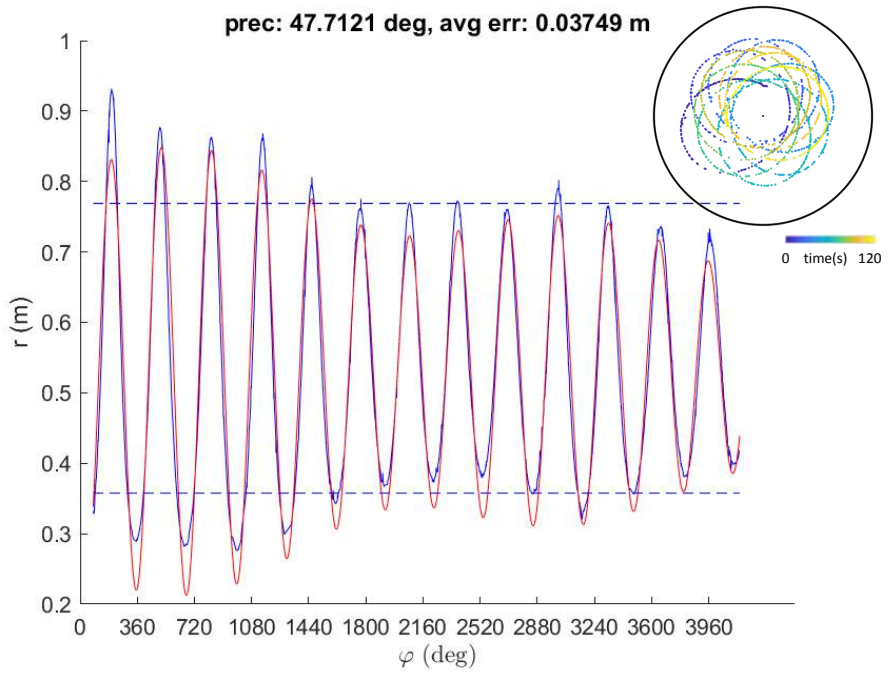

Figure 2.8: **An example of model fitting.** Experiment 25per_b1_r20_a80_3 with azimuthal period $T_\varphi = 312.28°$ (therefore $\Delta\varphi_{\text{prec}} = 360 - 312.28 = 47.72°$), precession amplitude $A_2 = 31.0$ cm and anisotropy defect amplitude $A_1 = 4.6$ cm, and half-life $\tau = 17.9$ revolutions. The blue curve shows the experimental data and the red curve shows the fit. The two dashed lines show the r_{max} and r_{min} evaluated as the median of the peaks in the experiment curve.

This model incorporates the precession ($A_2 \cos\left(\omega_{\text{prec}}\varphi + \varphi_2\right)$), the transient feature ($e^{-\varphi/\tau}$, cause shown in section A.5), and the membrane defect ($A_1 \cos\left(\varphi + \varphi_1\right)$), which has a period 2π. For a perfect trajectory made by a perfect vehicle, $\tau = \infty, A_1 = 0$.A figure of an experimental trajectory is shown in Fig.Figure 2.8.

We use fminsearch in MATLAB to find the best $(r_c, A_1, \varphi_1, A_2, \varphi_2, \omega_{\text{prec}})$ that minimizes the least square error between the model and experiment data.

To gain insight into the precessing dynamics, for bounded steady-state trajectories

with half-lives of eccentricity longer than 5 revolutions, we measured average precession $|\Delta\varphi_{\text{prec}}|$ as a function of initial conditions (r_0, θ_0) by evaluating the change in angular location of consecutive apoapsides or periapsides (e.g. between periapsis 1 and 2 in Figure 2.6b). A map of this is shown in Figure 2.6c in the $r - \theta$ space. We choose the heading angle θ rather than the azimuthal angle φ to reduce the redundant counting of the same trajectories shifted by just an azimuthal angle due to the axi-symmetry. We find the precession angle to be constant throughout the trajectory, therefore all the points sampled from a trajectory share a constant precession angle and each point's (r, θ) along this trajectory can be regarded as an effective initial condition in the trajectory $r - \theta$ space. Including these initial conditions, the map reveals that the precession is minimal when the vehicle is initiated at a particular radius r_c (≈ 0.6 m when the central depression $D = 13.9$ cm) and heading of 90°; $|\Delta\varphi_{\text{prec}}|$ increased as initial conditions deviated from this region. However, r_0 is restricted to the range 0.2 m $\leq r_0 \leq 1.1$ m to exclude the central cap in the membrane and to avoid starting the vehicle too close (less than 10 cm) to the outer ring. Initial headings which pointed approximately towards or away from central depression did not achieve a stable orbit. While the range of θ_0 that starts stable orbits varies with r_0, we approximated the boundary of stable orbits with uniform bounds of θ_0. That is, in experiments, for $\theta_0 < 30^\circ$ the vehicle collided with the outer boundary, and for $\theta_0 > 150^\circ$ the vehicle crashed into the central cap.

2.2.3 Understanding precession with differential geometry

To gain insight into how vehicle orbital dynamics emerge solely due to interaction with the curvature field generated by both the central depression and the vehicle's local depression field (Figure 2.5a), rather than solving a coupled membrane-vehicle interaction system of equations, we instead construct a minimal model which gives physical insight into how a such deformation fields influence the vehicle's dynamics. Since the vehicle moves at a

constant speed, this model requires that the acceleration is perpendicular to the velocity such that $\Psi^2 a_r v_r + a_\varphi v_\varphi = 0$ where the projected components of acceleration in r and φ directions are $a_r = -a\, v_\varphi/(\Psi\, v)$, $a_\varphi = a\Psi v_r/v$. Here $\Psi^2 \equiv 1 + z'^2$ with $z' \equiv \partial z/\partial r$ as the gradient of the vehicle's height z measured from the frame holding the spandex sheet. With the help of $\cos\theta = \Psi\, v_r/v = \Psi\, \dot{r}/v$ and $\sin\theta = v_\varphi/v = r\dot{\varphi}/v$, we have

$$\frac{a_\varphi}{r} = \ddot{\varphi} + \frac{2\,\dot{r}\,\dot{\varphi}}{r} = \frac{a}{r}\cos\theta \tag{2.36}$$

$$a_r = \ddot{r} - \frac{r\,\dot{\varphi}^2}{\Psi^2} + \frac{\Psi'}{\Psi}\dot{r}^2 = -\frac{a}{\Psi}\sin\theta\,. \tag{2.37}$$

with $a = [\Psi^2 (a_r)^2 + (a_\varphi)^2]^{1/2}$. Dots and primes denote differentiation with respect to t and r respectively. Our experiments reveal that, to a good approximation, the dependence of the vehicle's acceleration on the radius and heading is given by

$$a = k\, \sin\theta \tag{2.38}$$

where k (referred to as the acceleration strength below) is a function of r only (Figure 2.9c). We want to point out the form of $k \sin\theta$ can be regarded as the first order expansion of any $a(r, \theta)$ for any vehicles. Having $a \propto \sin\theta$ implies that, in this axi-symmetric case, the magnitude of the acceleration is proportional to that of the cross product between the velocity and the gradient of the terrain since the gradient of the terrain is aligned with the radial direction. We will later show that $a \propto |\mathbf{v} \times \nabla z|$ also holds for surfaces with arbitrary shapes.

We treat the vehicle with tilt angle γ from its level orientation as driving on a local incline with slope γ. From a theoretical analysis of how the constant-speed differentially driven vehicle pivots on a slope (Figure 2.9b, see appendix section A.4 for derivations), we found that the acceleration strength $k = C\, g\, \sin\gamma\, \cos\gamma \approx C\, g\, |\nabla z|$ with g Earth's gravity. The prefactor C is a mechanical constant related to the structure of the vehicle as

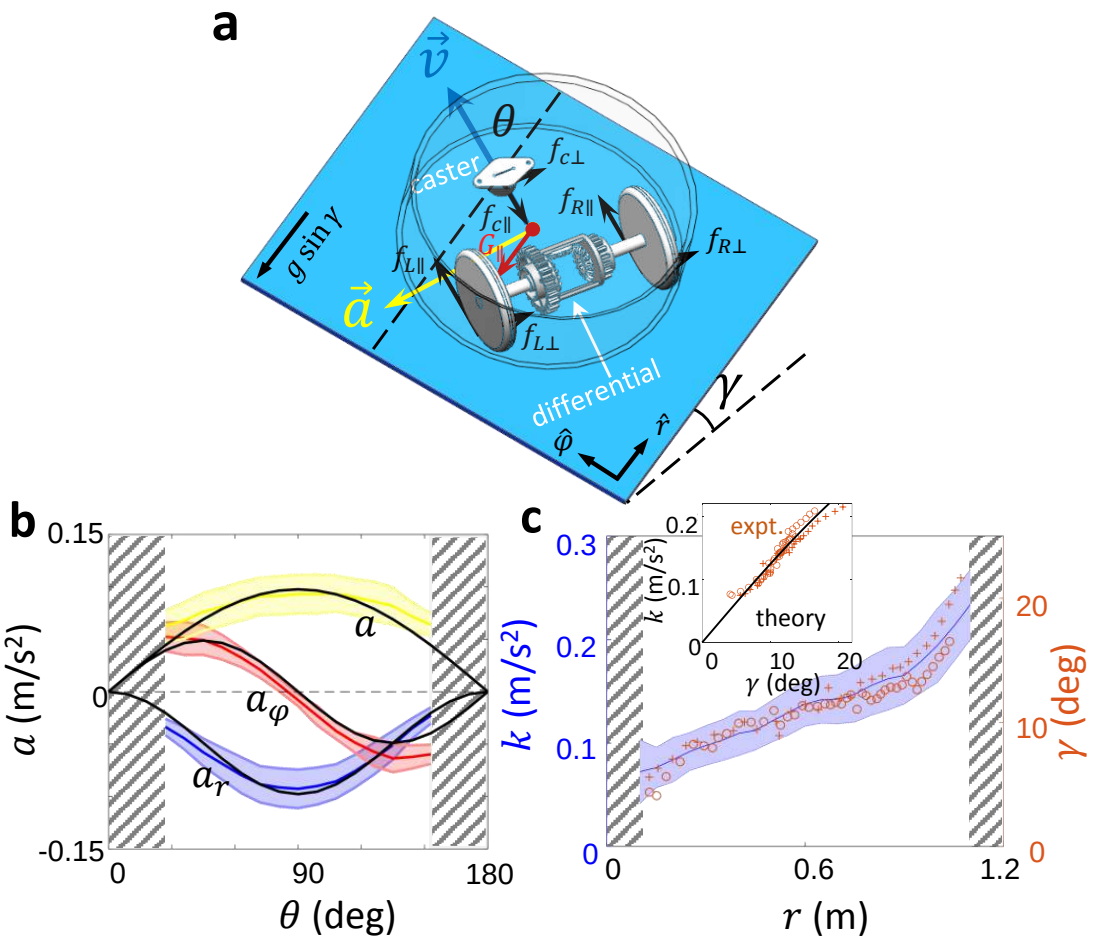

Figure 2.9: **Vehicle dynamics.** (a) Schematic of a vehicle moving on a piece of membrane and its force diagram. The dashed line on the incline shows the radial direction. The frictions on the wheels and the caster are shown in black and the component of Earth gravity along the slope is shown in red. (b) Magnitude of the acceleration a (yellow), and its components a_r (blue) and a_φ (red) as a function of the heading angle θ evaluated at $r = 0.3$ m (central depression $D = 9.6$ cm) obtained from 238 experiments. Black lines correspond to $a = k(0.3\text{m}) \cdot \sin\theta$, $a_r = -(a/\Psi)\sin\theta$, and $a_\varphi = a\cos\theta$ with $\Psi \approx 1$. The gray shaded regions indicate extreme headings that do not have steady trajectories. Data at other radii can be found in section A.4 of the appendix. (c) The acceleration strength k and vehicle tilt γ as a function of the radius r for $\theta = 90°$ with the solid blue line and shading denoting the mean and standard deviation of k obtained from 238 experiments. The red markers show the vehicle tilt γ measured from the experiment on two different azimuths separated by $90°$ with open circles and pluses respectively. Inset shows the relation between k and γ using the k data (mean) from the main figure and the theoretical curve $k = 0.074\, g \sin\gamma\cos\gamma$.

$C = L_c^2/(L_c^2 + \frac{1}{2}R_v^2)$ where $L_c \approx 1$ cm is the distance between the wheel axle and the center of mass (see appendix section A.4), and $R_v = 5$ cm is the radius of the vehicle. The theoretical value for C from the model is approximately 0.074, while the experimental fit

(Figure 2.9c inset) gives a value of 0.073 ± 0.001 (see appendix section A.4).

The model as described by (Equation A.30a) and (Equation A.30b) yields good agreement with experiments over a range of $v = 0.20 - 0.32$ m/s. The essential ingredient of the model is that the differential mechanism ensures torque balance on both wheels. In addition, the rolling friction on the caster is negligible compared to other contact forces (see Figure 2.9a for force diagram). The model indicates $k = a/\sin\theta$ should be the same for any θ for a balanced vehicle. The experimentally measured result shows a slight dependence on heading angle θ (appendix section A.5) that can be understood as weight imbalance, characterized by ΔB. Introduction of this bias into the analysis returns a correction in the form of $a_{bias}/\sin\theta = k \cdot (\Delta B/L_c)\cot\theta$. It vanishes when $\theta = \pi/2$ or $\Delta B = 0$ (perfectly balanced vehicle). Integration of (Equation A.30a) and (Equation A.30b) yields precession dynamics that quantitatively matches with the experiments for all different depressions (Figure 2.6c,Figure 2.11b).

An important aspect of the dynamics which is revealed by the model is that unexpectedly the vehicle does not follow spatial geodesics of the membrane (as in the museum demos of GR [108]) given by curves on curvatures with metric $ds^2 = \Psi^2 dr^2 + r^2 d\varphi^2$. These spatial-only geodesics are nearly straight lines in our setup (Figure 2.10).

We will later show that the essential ingredients that generate this difference are the deformation of membrane by the vehicle, and the active nature of the system shown in the vehicle's ability to change the direction of motion as a consequence of the local tilt of the vehicle. These two aspects are reflected respectively in the acceleration strength k governed by membrane deformation and θ, the heading angle of the vehicle.

To understand aspects of the system's dynamics (e.g. how substrate parameters can alter orbital properties of the active locomotor), we sought to obtain conserved quantities including an effective potential. While there are many ways to obtain these quantities, inspired by features of the dynamics resembling those found in astrophysical systems, we chose to use techniques from differential geometry, the mathematics relevant to situations

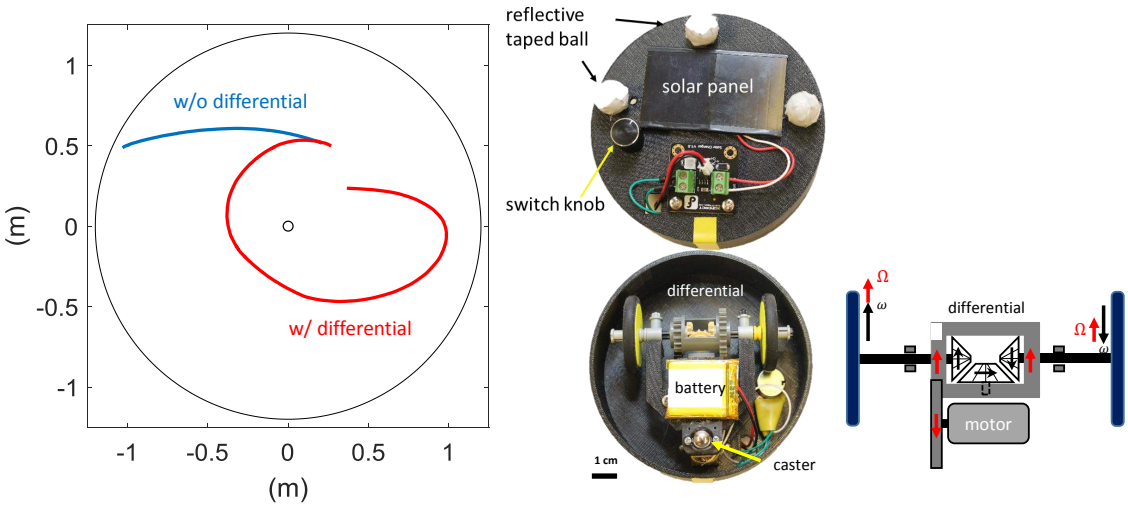

Figure 2.10: **Turning with the slope makes the trajectory deviate from the spatial-only geodesics.** Left: the top and bottom views of the vehicle. Middle: Comparison of the trajectories of the vehicle on the membrane when differential mechanism is applied and disabled. To disable the differential mechanism so that the two wheels are rigidly connected, the gears in the differential are glued. Right: top view of the differential mechanism.

described by Einstein's theory of General Relativity (GR). In a separate paper [109] we further expand on the connections of our robophysical system to GR.

Our scheme proceeds in analogy to GR: recall that in GR, test particles move in response to the curvature of spacetime by following the locally length-minimizing curves (i.e., geodesics). Thus, we must first obtain the "metric" of the effective spacetime, which describes the spacetime curvature. Following the metric and applying the variational principle, one could obtain the equation of motion for the test particles [e.g., 110]. For instance, the Minkowski metric in the flat spacetime is defined by the diagonal matrix $\eta_{\alpha\beta} = \{-1, 1, 1, 1\}$ in Cartesian coordinates. This specifies that the distances between close points in spacetime can be calculated as the following: $ds^2 = -dt^2 + dx^2 + dy^2 + dz^2$, and leads to the equation of motion $d^2x^\alpha/dt^2 = 0$ for test particles. By matching the geodesics equations of the metric with the equations of motion (Equation A.30a) and (Equation A.30b), one can find that the metric is

$$ds^2 = -\alpha^2 dt^2 + \Phi^2(\Psi^2 dr^2 + r^2 d\varphi^2) \tag{2.39}$$

where the curvatures are $\alpha^2 = E^2(1 - v^2 e^{-K/v^2})$ and $\Phi^2 = E^2 e^{-K/v^2}(1 - v^2 e^{-K/v^2})$. Here, $K = K(r) \equiv \int_0^r k(s)\Psi(s)ds$ and E is a constant of motion. The metric provides us with

$$1 = \frac{\Phi^2}{\alpha^2}\Psi^2\dot{r}^2 + \frac{1}{r^2}\frac{\alpha^2}{\Phi^2}\frac{L^2}{E^2} + \frac{\alpha^2}{E^2} \tag{2.40}$$

where L is another constant of motion. The details of derivation can be found in section A.6 of the appendix.

(Equation 2.40) can be rewritten in the following suggestive form: $\mathcal{E} = \frac{1}{2}m\,\dot{r}^2 + V$, with $\mathcal{E} = 1/2$, $m = \Phi^2\Psi^2/\alpha^2$ the effective mass, and $V = [\alpha^2\,\ell^2/(\Phi^2 r^2) + \alpha^2/E^2]/2$ the effective potential, where we have defined $\ell \equiv L/E$. Plugging in the α^2 and Φ^2 derived above, we finally arrive at the effective potential

$$V \;=\; \frac{1}{2}\left(\frac{\ell^2}{r^2}e^{K/v^2} + 1 - v^2 e^{-K/v^2}\right). \tag{2.41}$$

Note that the energy and angular momentum enter through the ratio $\ell = L/E$, which can be calculated from the initial conditions since $\ell = \Phi^2 r^2\dot{\varphi}/\alpha^2$. Figure 2.11a shows examples of the potential V for different values of ℓ with $\ell_{max} = v\; r_c \exp\left(-K(r_c)/v^2\right)$ (see section A.6 of the appendix). The dashed line at $1/2$ denotes $\mathcal{E}$, and the turning points where $\dot{r}$ changes sign when the potential energy reaches the maximum amount are given by the solution to $r_\pm = \ell\, e^{K_\pm/v^2}/v$, where we use the subscript $\pm$ to denote a quantity evaluated at the turning points. Circular orbits occur when the minimum of the potential matches $\mathcal{E}$. The minimum is found from $V' = 0$ and is located at $r_c = v^2/k_c$ where $k_c \equiv k(r_c)$.

With the effective potential discovered from the mapping scheme, we can now explain the dependence of orbital precession on initial conditions and system parameters. To begin, we introduce the definitions of E and L to eliminate $\dot{r}$ in $\mathcal{E} = \frac{1}{2}m\,\dot{r}^2 + V$ in favor of $dr/d\varphi$.

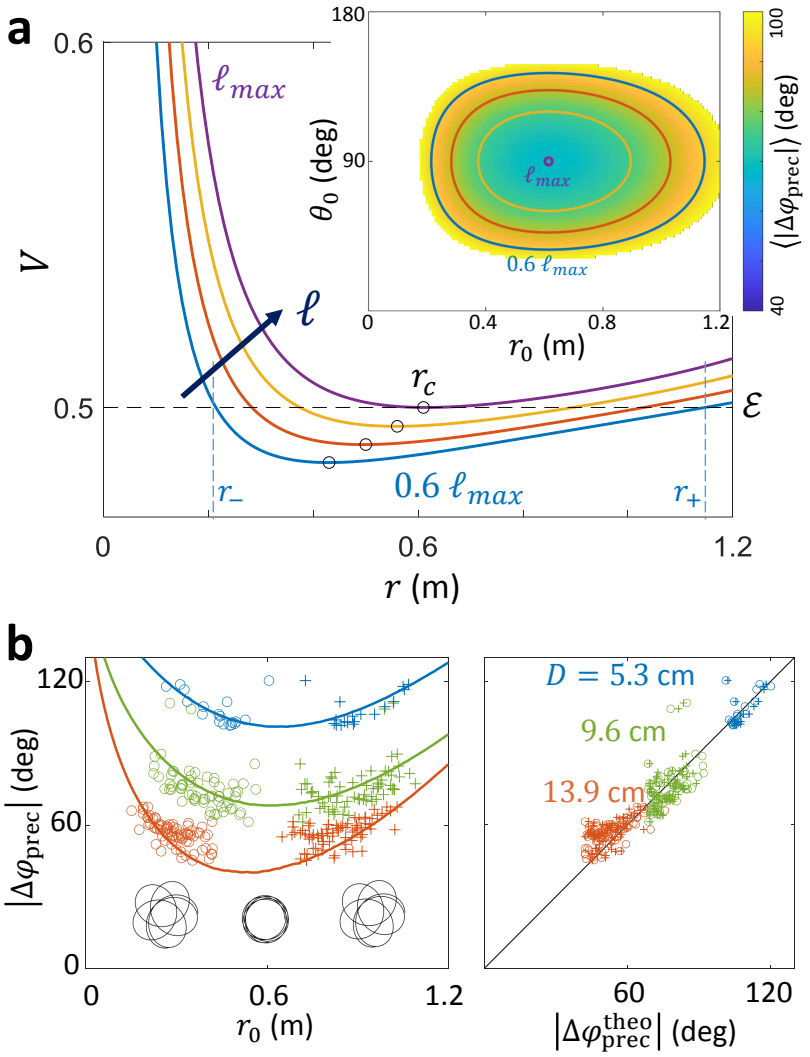

Figure 2.11: **The effective potential governing the orbital dynamics.** (a) Simulation data of V is shown for different values of ℓ with $D = 9.6$ cm. Black dots denote the minimum point of a given potential curve, and $r_c = v^2/k_c$ labels the case of a circular orbits when $\mathcal{E} = V_c$. The corresponding trajectories in the r-θ space are shown in the inset. (b) Precession angle $|\Delta\varphi_{\rm prec}|$ as a function of the effective initial radius r_0 for $\theta_0 = \pi/2$ and central depressions $D = 13.9$ cm (vermilion), 9.6 cm (green), and 5.3 cm (blue). Experimental data are open circles and plus signs. Solid lines are theoretical prediction using (Equation A.30a) and (Equation A.30b), or equivalently (Equation 2.42). The open dots show the r_- and the pluses show the r_+. The insets below the curves show the trajectories at different radii for $D = 9.6$ cm. Experimental observation of precession angle matches the theoretical value (from the solid lines in panel a) with a R^2 of 0.87.

This results in

$$\frac{\ell^2}{r^2}\left[\frac{1}{r^2}\left(\frac{dr}{d\varphi}\right)^2 + 1\right] = v^2\, e^{-2K/v^2}\,. \tag{2.42}$$

Next, we apply the change of variable $u = \ell/r$, and differentiate with respect to φ and get

$$\frac{d^2u}{d\varphi^2} + u = \frac{k\,\ell}{u^2} e^{-2K/v^2}\,. \tag{2.43}$$

As noted above, for circular orbits $r_c = v^2/k_c$, or equivalently $u_c = k_c\,\ell/v^2$. Perturbing (Equation 2.43) about a circular orbit, i.e. $u = u_c + \delta u$, we get

$$\frac{d^2\delta u}{d\varphi^2} + \left(1 + \frac{k_c'}{k_c} r_c\right) \delta u = 0\,. \tag{2.44}$$

Thus, $\delta u \propto \cos(\omega\,\varphi)$ with $\omega^2 \equiv 1 + r_c\,k_c'/k_c$ where $k_c' \equiv k'(r_c)$, and the perturbative solution to (Equation 2.43) is then given by $u = u_c[1 + e\,\cos(\omega\,\varphi)]$ where e is the eccentricity of the orbit. Notice from this solution that one radial cycle takes place over a $2\pi/\omega$ angular cycle. Therefore, the precession angle is given by $\Delta\varphi_{\text{prec}} = 2\pi/\omega_c - 2\,\pi \approx -\pi\,r_c\,k_c'/k_c$. Since $k_c > 0$, the sign of $\Delta\varphi_{\text{prec}}$, namely the direction of the precession, is given by the sign of k_c' . If $k_c' > 0$, we have $\Delta\varphi_{\text{prec}} < 0$, retrograde precession, with prograde precession if $k_c' < 0$. From Figure 2.9c, we have that $k_c' > 0$, which explains the observed retrograde precession. Further, the dependence of $\Delta\varphi_{\text{prec}}$ with r_c is consistent with our observation that the magnitude of the apsidal precession ($\Delta\varphi_{\text{prec}} < 0$) decreases as the radius of the orbits approaches the radius of the circular orbit r_c.

We now reexamine the dependence of precession angle $\Delta\varphi_{\text{prec}}$ on initial conditions (Figure 2.6c) in the mapping framework. We now can see that contours of constant color correspond to trajectories with the same angular momentum ℓ. And notably, the precession angle decreases as the orbits become more circular, with $\Delta\varphi_{\text{prec}} = -\pi\,r_c\,k_c'/k_c$ for the circular orbit. Figure 2.11b shows $\Delta\varphi_{\text{prec}}$ as a function of r_0 for initial heading angle $\theta_0 = 90^\circ$ with both the experimental data and the solution to (Equation 2.42). The minimum precession angle occurs for circular orbits.

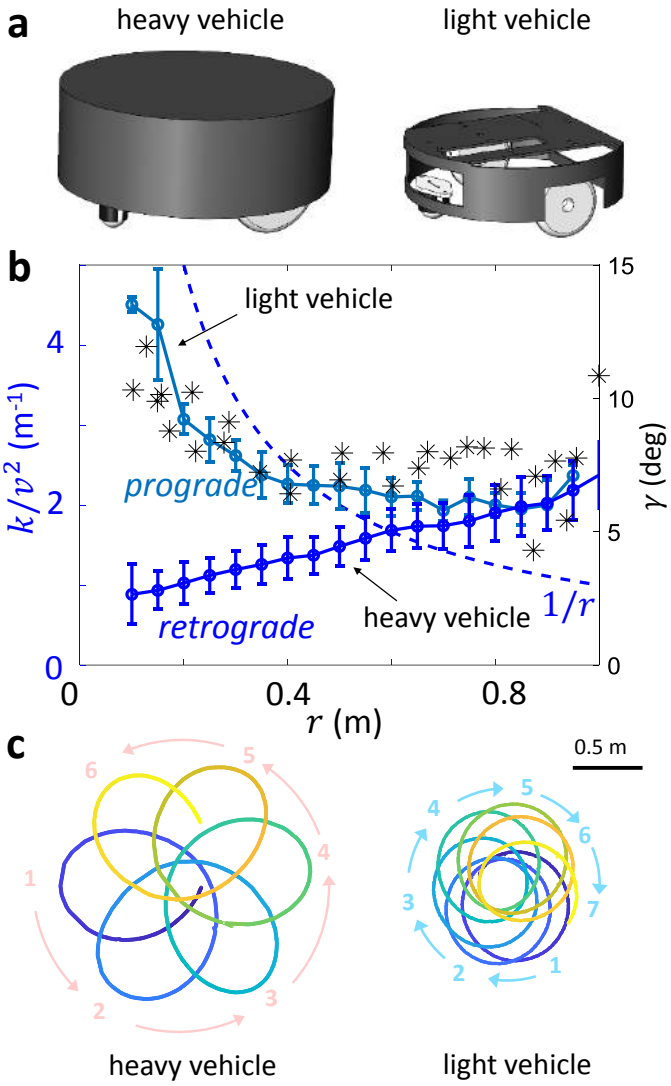

Figure 2.12: (a) The heavy ($m \approx 160$ g) vehicle and the light vehicle ($m \approx 45$ g). (b) Different $k(r)$ functions for prograde (light blue) and retrograde (dark blue) precession measured from experiments. The light vehicle has a negative k' at r_c (the intersect of $k(r)/v^2$ and $1/r$) while the heavy vehicle has a positive k' at such an intersect. The decreasing k has the same trend as the measured tilt angle $\gamma(r)$ (black stars). (c) Clockwise trajectories with retrograde (left) and prograde (right) precessions from experiments. Perihelia are marked in order. The prograde precession is made by a lightweight vehicle on the membrane with $D = 17$ cm central depression, for initial conditions $r_0 = 20$ cm, $\theta_0 = 90°$. The periapsides numbered in blue show a clockwise order while the orbit is precessing in the same direction. The magnitude of the precession for this trial is $\Delta\varphi_{\text{prec}} = 51°$.

2.2.4 Manipulating precession

As a consequence of $k' > 0$, our system generates retrograde orbits such that the vehicle's precession is opposite to that of GR in common situations. With our mapping, it is straightforward to understand how to obtain more GR-like prograde precession (like that of Mercury [111, 112])): we must change the sign of the slope of k so that $k' < 0$ over a significant range of the vehicle trajectory. Because k is connected to the tilting angle γ, we can achieve the desired change by increasing the tension of the membrane or decreasing the mass of the vehicle to enable the vehicle to more closely track the imposed membrane shape.

We chose to change the mass of the vehicle and constructed a smaller, lighter vehicle with mass 45 g (Figure 2.12a), approximately one quarter that of the original vehicle in Figure 2.5, a radius of 4 cm, and a speed $v = 0.11$ m/s. The vehicle produced trajectories (Figure 2.12c) demonstrating prograde precession over all sampled initial conditions (65 total experiments). For a particular initial condition ($r_0 = 69$ cm, $\theta_0 = 90°$), four out of five trials produced precessing orbits with significant eccentricity; here $\Delta\varphi_{\text{prec}} = +22° \pm 16°$. The theoretical prediction – with $k(r)$ (Figure 2.12b) deduced from such trajectories – $\Delta\varphi_{\text{prec}} = +33° \pm 7°$ mostly overlaps with the experimental range. For a given initial condition, the lightweight vehicle showed greater trajectory variability than that of the heavier vehicle. We posit such variability is related to the slight membrane anisotropy, which makes the dynamics of the lightweight vehicle sensitive to initial conditions. Here the change of precession sign with the vehicle's mass demonstrates how the matter reciprocally tells the local spacetime how to curve and influences its global dynamical properties.

2.3 Dynamics of multiple agents

2.3.1 Generalized dynamics

Thus far we have studied the interactions between a single vehicle and a central depression (which generates a time-independent imposed background) and have shown how we can understand the field-mediated orbital dynamics by mapping them to a "spacetime" using techniques from study of relativistically orbiting bodies. There are situations in which the deformation field experienced by a vehicle could be time-dependent; we have observed that a robot can be "guided" without contact via local deformation of the membrane alone. Further, in the case of swarms of vehicles moving on a curvature field, this sets up interesting dynamics such that (in the case of two robots for example) each robot carries its own depression field and affects another robot via this field alone, which could then affect the initial robot.

Therefore we next sought to develop a theory for the interaction of two agents via fields alone. The first element of the theory requires that we develop an equation of motion for the dynamics of a single vehicle experiencing an imposed deformation field that is not necessarily at the center of the membrane (the spacetime telling matter how to move component of the Wheeler encapsulation of the mechanics of GR). Thus, we need to first generalize the equations of motion (Equation A.30a,Equation A.30b) to a vehicle on an arbitrary terrain. The axi-symmetric model can be generalized for an arbitrary substrate by noticing that $a = k \sin\theta$ where θ is the angle between the velocity and the gradient of the slope and k is the magnitude of the gradient multiplied by a mechanical constant. In the symmetric case, the gradient is always along the radial direction so that only the magnitude of the gradient $k = C\,g\,\sin\gamma\cos\gamma \approx C\,g\,|\nabla z|$ is needed. In the general case, noticing the $\sin\theta$ is the cross product of the unit vectors of the arbitrary terrain gradient $\mathbf{d} = -\nabla z$ and the vehicle velocity, the generalized equation of motion (see section A.7 of the appendix

for derivation) is

$$\ddot{x} = C\, g\, \dot{y}\, (d_x \dot{y} - d_y \dot{x})/v^2 \tag{2.45}$$

$$\ddot{y} = -C\, g\, \dot{x}\, (d_x \dot{y} - d_y \dot{x})/v^2\,, \tag{2.46}$$

Conceptually, this is our "$F = ma$" with $\mathbf{d}$ playing the role of "F" (recall $d_i = -\nabla_i z$ with $i = x, y$).

To complete the field-mediated interaction picture, since a moving vehicle presents to another vehicle a time dependent deformation field, we require an equation to describe how a vehicle (the "matter") deforms the membrane curvature.

To characterize how the membrane responds to local perturbations, we use the wave equation, the simplest equation for a membrane assuming linear elasticity:

$$\ddot{Z} - v_m^2 \Delta Z = -P\,. \tag{2.47}$$

where v_m is the speed of propagation of disturbances in the membrane and $P = P_0\,(1 + \tilde{P})$ with $P_0 (> 0)$ the force load from the membrane and $\tilde{P}$ the additional load from the vehicles, which is the area density of the vehicles normalized by the area density of the membrane. Since P_0 is the stationary force load when the membrane is only deformed by its weight, the time dependence in the source in (Equation 2.47) arises from $\tilde{P}$ due to the moving vehicles. Experiments examining the membrane elasticity have found that the shape of a free stationary membrane where $\tilde{P} = 0$ and $\ddot{Z} = 0$ follows the Poisson equation reasonably well (subsection A.8.3 of the appendix).

The speed of propagation for the membrane in our experiment is $v_m \approx 400$ cm/s, which is significantly larger than the typical speed of our vehicles ($v \approx 20$ cm/s). Therefore, we neglect time derivatives in (Equation 2.47) and solve instead the Poisson equation $\Delta Z = P/v_m^2$.

Therefore, the evolution of the system proceeds as follows (Figure 2.13a): given the

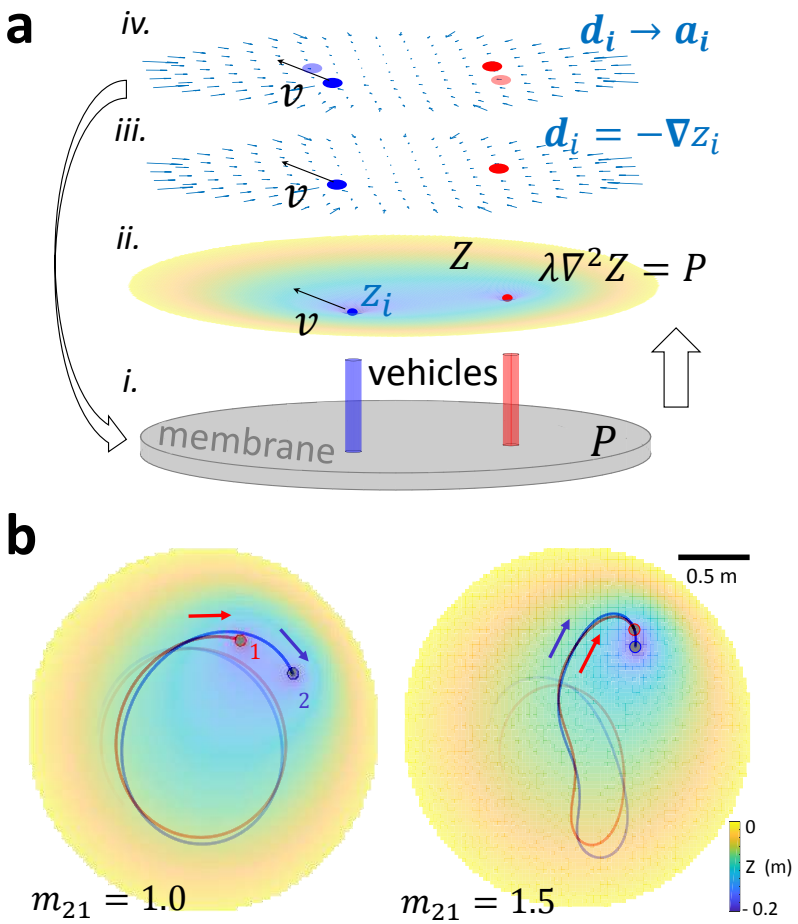

Figure 2.13: **Reciprocal interaction between the vehicle dynamics and curvature field.** (a) A sketch of the simulation procedure: (i) First, the shape of the membrane is solved from the Poisson equation with the load indicated in the bottom: gray disk for the membrane and two colored posts for the two vehicles in this example. (ii) Then, the height profile of the vehicle is evaluated at its position. (iii) Afterwards, the terrain gradient $\mathbf{d}$ is evaluated from the height profile of the vehicle. (iv) Finally, the acceleration determined by $\mathbf{d}$ using Equation 2.45,Equation 2.46 is integrated to update the new positions of the vehicles and the computation goes back to the first step again. (b) Theory and simulation predict larger leader mass ratio ($m_{21} \equiv m_2/m_1 = 1.5$) fosters a merger better than a smaller one ($m_{21} = 1.0$).

location of the vehicles, one first constructs the source P and solves $\Delta Z = P/v_m^2$ to obtain the membrane profile function Z (Figure 2.14c). After Z is obtained, naively one would use $Z(\mathbf{r})$ as the height of the vehicle $z(\mathbf{r})$. However, for a vehicle with a finite size, the actual physical contacts between the wheels and the membrane occur near the circumference of the disk. Thus, the vehicle height $z(\mathbf{r})$ can be approximated by the average membrane

height $Z(\mathbf{r})$ around the disk circumference ($z(\mathbf{r}) \approx \langle Z(\mathbf{r}')\rangle_{|\mathbf{r}'-\mathbf{r}|=R_v}$, see Figure 2.5c and subsection A.8.3 of the appendix). On our circular membrane, the analytical solution to Z evaluated in z yields the vertical position z_i for vehicle i with mass m_i as:

$$\begin{aligned} 2\pi\lambda z_i &= \frac{\pi}{2}(|\mathbf{r}_i|^2 - R^2) + \frac{m_i}{\sigma}\log\left(\frac{R_v R}{R^2 - |\mathbf{r}_i|^2}\right) \\ &+ \frac{1}{\sigma}\sum_{j\neq i} m_j \left(\log\frac{|\mathbf{r}_i - \mathbf{r}_j|}{|\mathbf{r}_i - \mathbf{r}'_j|} - \log\frac{|\mathbf{r}_j|}{R}\right), \end{aligned} \tag{2.48}$$

where $\mathbf{r}_i, \mathbf{r}'_i = (R/|\mathbf{r}_i|)^2\mathbf{r}_i$ are the planar position of the ith vehicle and its image charge [113], R and R_v are the radii of the membrane and the vehicle, σ is the area density of the membrane and $\lambda = v_m^2/P_0$ is a membrane constant. The three terms in the solution show respectively the contributions of the vehicle height field from the membrane, the weight of the vehicle of interest, and the other vehicles respectively. The last term conceptually acts as an attractive potential (like the Newtonian gravitational potential), whose gradient generates a pairwise attractive force between the vehicles.

With z and therefore the acceleration as a function of the terrain gradient $-\nabla z$ at hand, one obtains the new position of the vehicles by integrating (Equation 2.45,Equation 2.46).

While a full systematic study of interaction dynamics for arbitrary initial conditions of the two vehicles is beyond the scope of the work, integration of the above multi-body dynamical model reveals that surprisingly the simulation does not predict strong attraction between two vehicles with the same mass at the same speed (Figure 2.13b) unless they are started facing each other; experimental measurements of robot interaction are in accord with this prediction (see Figure 2.14b,c) such that two equally massed vehicles will undergo many transits around the membrane without cohering. This is analogous to the eccentric Kozai-Lidov mechanism, where the eccentricity excitation reduces when the masses become equal to each other and decreases the merger rate [**Naoz16**]. In contrast, the simulation predicts that in a situation where one vehicle trails another (Figure 2.14), increasing the mass of the leading vehicle can increase the attraction (Figure 2.13) and lead to vehicle

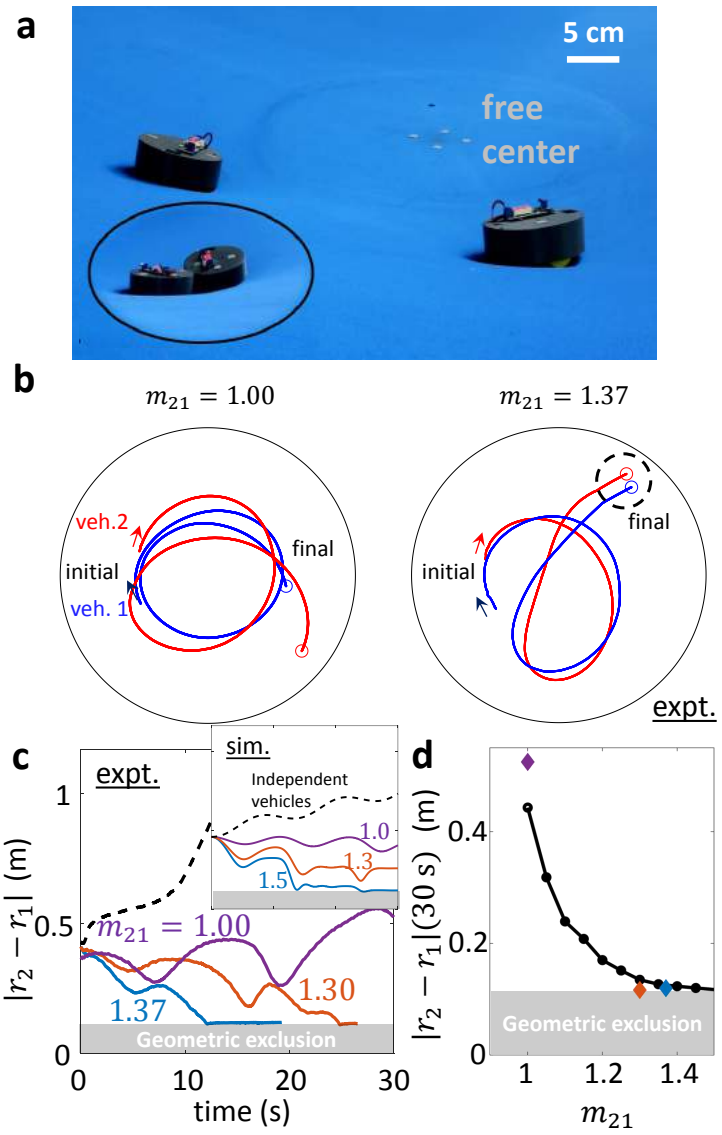

Figure 2.14: **Substrate deformation induced cohesion.** (a) Two vehicles moving on the elastic membrane merge due to the substrate-mediated attraction. The initial azimuth angle between the vehicles is $45°$. (b) Example trajectories of the two interacting vehicles with different mass ratio ($\frac{m_2}{m_1} = m_{21} = 1.00$ and 1.37) for a duration of 30 sec. (c) The evolution of the relative distance between the two interacting vehicles (solid) compared to the non-interacting case (dashed) where two vehicles with $m_{21} = 1.30$ were released individually from the same initial condition. The time to merge is shortened by the increased masses of the leading vehicle (vehicle 2, m_2). On the contrary, the distance between two independent vehicles from the same initial condition is non-decaying. The inset has the same axis ranges as the main figure. (d) Simulation shows the distance at 30 s between the two vehicles decays with the mass ratio m_{21}. Experiment results from (c) are shown in diamonds.

merger (cohesion).

To test the hypothesized merger enhancement with the increase of the leading vehicle's mass, we experimentally increased the mass of the leading mass vehicle (small weights were attached to the top of the vehicle without changing the center of mass), m_2, relative to the trailing vehicle, m_1 (characterized by the mass ratio $m_{21} = m_2/m_1$). For each experiment, both vehicles were placed at a radial distance of 60 cm from the center with azimuthal separation $\psi = 45^\circ$ and both with a heading of $\theta = 90^\circ$. Before each experiment, we set the speed of the two vehicles to 0.2 m/s by manually adjusting voltage of the motors. Due to the finite voltage, the speed slightly drops (< 10 %) as the separation between the two vehicles decreases. Figure 2.14b shows how the dynamics depend on the mass ratio. When $m_{21} = 1$, both vehicles execute nearly-circular orbits (left panel) and generally do not merge in a short time (see section A.9 of the appendix). As m_{21} is increased to 1.37, the trailing vehicle eventually becomes 'captured' by the leading vehicle leading to an effective cohesion such that the vehicles collide and then continue to move together for the duration of the experiment (right panel).

To quantify the attraction and cohesion dynamics, we measured the Euclidean distance between the vehicles projected onto the horizontal plane, $|\mathbf{r}_1 - \mathbf{r}_2|$, as a function of time. We find that the time to capture is reduced as the mass of the leading vehicle increases (Figure 2.14c). For instance, when $m_{21} = 1.30$, it took around 25 s for the trailing vehicle to become captured (i.e., the vehicles collide when $|\mathbf{r}_1 - \mathbf{r}_2| = 2R_v$). When $m_{21} = 1.37$, this capture occurred significantly faster, with the vehicles colliding in about 12 s. The coupling effects are highlighted by contrasting to the dynamics from independently conducted single-vehicle experiments, one with the initial conditions of the "leading" vehicle and the other with the initial conditions of the "trailing" vehicle. The distance evaluated from these two independent trajectories shows a non-decaying trend that differs from the cases with both vehicles on the membrane (dashed lines in Figure 2.14c). Simulations using the same setup as the experiments show qualitative match with the experiments and the distance be-

tween the two vehicles decreases with the mass ratio m_{21} (Figure 2.14d). We posit that the slight difference between simulation and experiment results from dynamic weight redistribution of the three contacts between the vehicle and membrane during locomotion; the simulation assumes the weight is always evenly distributed among contacts.

2.3.2 Speed feedback control to mitigate mergers

Given that unequal mass cars typically collide and cohere after some time, we next sought how we could *actively* mitigate such attraction. As demonstrated above, reducing vehicle mass can lessen the local deformation field to reduce cohesion, but active variation in this parameter is challenging. Intuitively, one could also control the vehicle to increase speed when it nears a high curvature region, thereby allowing the robot to accelerate out of such a region. We note that such a strategy is interesting because the robots could avoid (or potentially enhance) aggregation solely via local field measurements alone. Such dynamics could be useful for future swarms of sensory challenged robots [79] moving on highly deformable environments.

To test this cohesion mitigation strategy, we recall from the above section that as the distance between the two vehicles decreases, each 'feels' the membrane-induced deformation of the other more strongly and the tilt of both vehicles increases. To measure local tilt angle γ we added an IMU (Internal Measurement Unit) to the leading vehicle (Figure 2.15a) and implemented an adaptive speed controller that increased the speed of the leading vehicle as γ, the angle of inclination from the gravity vector measured by the IMU, increased in response to larger substrate deformations. Specifically, the speed of the leading vehicle was designated to be $(v_{\text{IMU}} - v_0)/v_0 = A \cdot (\gamma - \gamma_0)/\gamma_0$, where the tilt sensitivity A, sets the strength of the coupling between the leading vehicle and the local membrane deformation (Figure 2.15b).

The speed of the vehicle changes more quickly in response to the tilt when A is larger. We varied A from 0 (no control; constant speed) to 8 (speed sensitive to tilt angle) to

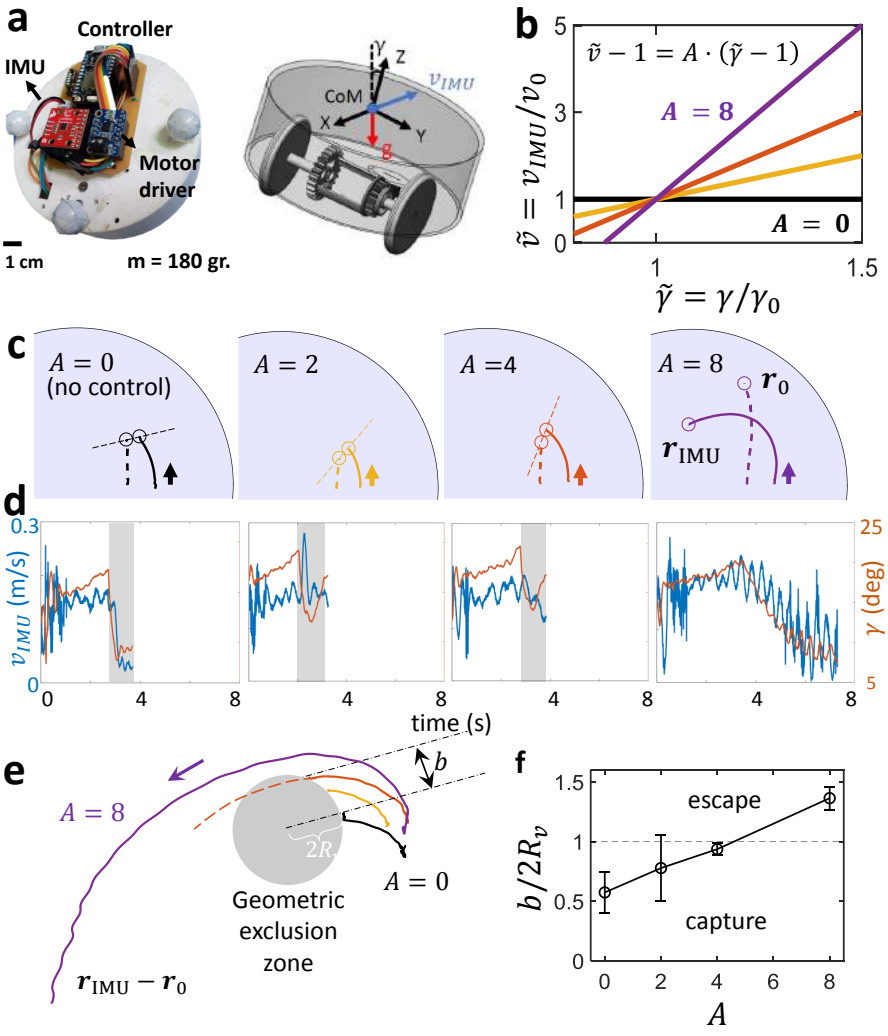

Figure 2.15: **Speed based on local tilt reduces substrate deformation induced cohesion.** (a) A controller, IMU and DC motor driver are mounted on the speed-controlled vehicle ($m \approx 180$ g) that changes speed according to the current tilt angle (right) with the same mechanics of the uncontrolled vehicle. (b) Control scheme of the controlled vehicle. The speed v increases with the tilt angle γ to avoid collision. The control parameter A increases from 0 (black, no control) to 8 (purple). (c) shows the trajectories of the controlled vehicle (solid line) and the uncontrolled vehicle (dashed line) when different magnitudes of control are applied. The relative angle between two vehicles upon collision (dotted line) increases with A. (d) shows the evolution of the speed and tilt of the controlled vehicle corresponding to panel c. The shaded regions denote the collisions. (e) shows the trajectories of the IMU-controlled vehicle in the frame of the uncontrolled vehicle. The geometric exclusion zone has a radius twice the radius of a vehicle. In an increasing order of tilt sensitivity $A = 0, 2, 4, 8$, the trajectories gets further and further away from the uncontrolled vehicle with an increasing margin b. (f) Mean and standard deviation of $b/2R_v$ over 3 trials for different A values. The vehicle eventually avoids the collision when $b/2R_v > 1$.

probe the effects of the speed-tilt coupling strength on potential collisions with the trailing vehicle. Figure 2.15c shows the trajectories of the vehicles starting from the same initial conditions ($r_{\text{IMU}}(0) = 0.6$ m, $r_{\text{passive}}(0) = 0.4$ m, $\theta_{\text{IMU}}(0) = \theta_{\text{passive}}(0) = 90°$, $v_{\text{passive}} = 0.11$ m/s, $v_{\text{IMU}}(0) = 0.15$ m/s, and $\gamma_0 = 15°$) for different A. From the recorded vehicle 3D position and orientation, we measured the speed and the tilt angle of the leading vehicle as a function of time; these measurements revealed that the controller generated the desired speed variation with tilt (Figure 2.15d).

The robot's strategy, based solely on local curvature, leads to an ability to avoid collisions without knowing the location of the other vehicle. We observed that when A was sufficiently large (≥ 4), the leading vehicle was able to successfully avoid collision. Figure 2.15e shows the relative trajectories of the controlled (leading) vehicle in the frame of the uncontrolled (trailing) vehicle ($\mathbf{r}_{\text{IMU}} - \mathbf{r}_0$). The geometric exclusion zone (with radius equal to $2R_v$) around the uncontrolled vehicle identifies the collision area. If the controlled vehicle enters this area, then a collision with the uncontrolled vehicle has occurred. As A increased, the margin b (i.e., the shortest distance between the controlled vehicle trajectory and the center of the uncontrolled vehicle) increased and eventually became larger than $2R_v$, indicating that the vehicles escaped the collision (Figure 2.15f). We note that the trajectory of the uncontrolled vehicle ended prematurely when a collision occurred; therefore, we fit it with an ellipse centered at the uncontrolled vehicle to extrapolate the margin b.

Inspired by the response of the vehicle to curvature, we developed controllers which can help avoid such cohesion via local measurements of tilt thus indeed generating global control over local forcing. We posit that the reciprocal coupling of the robot and the deformable substrate analyzed in detail here could be useful as a starting point for understanding field mediated locomotor dynamics in more complex environments.

We next sought to discover if the tilt-based speed control scheme could be effective in merger mitigation in a system consisting of a larger number of agents. Using the same vehicle ($m \approx 180$ g) and membrane as in the previous experiments, simulations of 5 vehicles

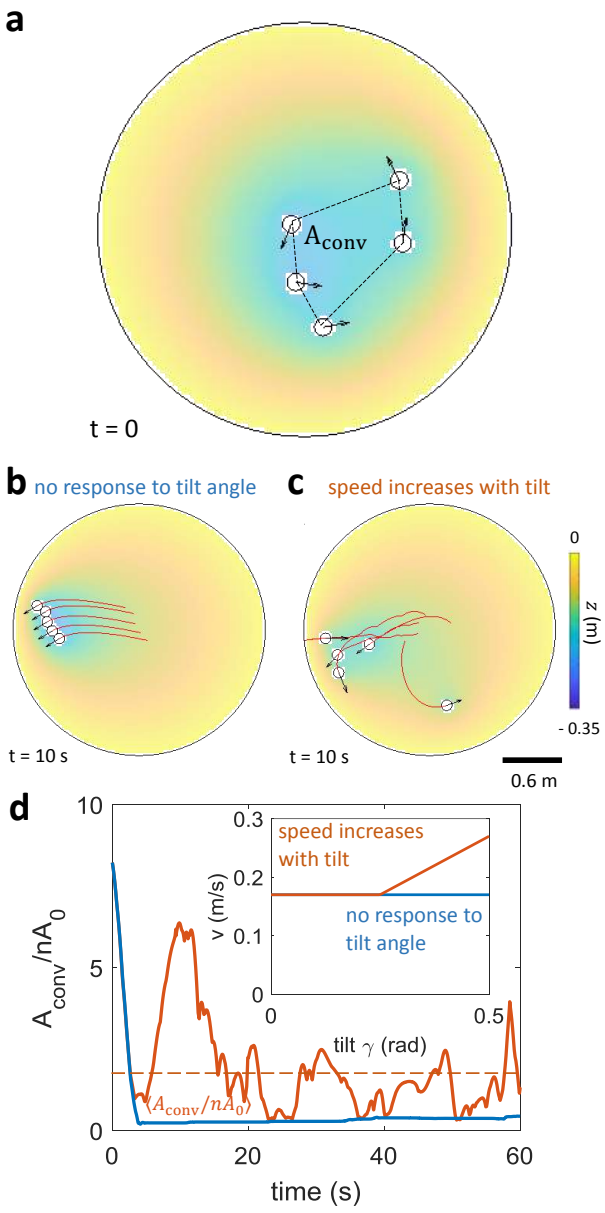

Figure 2.16: **Increasing speed with tilt helps to avoid mergers in swarms.** (a) The initial condition used for simulations of 5 vehicles shown in (b) and (c). The convex hull of the vehicles (shown by the dotted lines) is used to characterize the proximity of vehicles over time. (b) Without speed control, the vehicles attract and align with each other in a short time ($t < 10$ s) regardless of their different headings and positions at $t = 0$. (c) When the speed control is applied, the vehicles dynamically avoid each other. The snapshot of the vehicles' status at the same time as (b) show no mergers or alignment of headings. The red tails show the trajectories of the last 5 s. (d) The evolution of the convex-hull area of $n = 5$ vehicles. The evolution with vehicles under speed control is shown in orange. The response of the speed to the tilt angle is shown in the inset. The convex area A_{conv} is normalized by the total area of the n vehicles, each with an area of A_0. The orange dashed line shows the time-average of A_{conv}/nA_0 at steady-state for a single trial. A simulations of 5 vehicles without speed control is shown in blue.

without the tilt-based speed control (Figure 2.16) resulted in rapid collisions and mergers. However, if the speed of the vehicle responds rapidly to its tilt as in Figure 2.15, vehicles can dynamically avoid each other.

To characterize the dynamical cohesion among the vehicles, we tracked the convex-hull area (Figure 2.16a) of the collective. In the case with no speed-control, this area decreased to a value close to zero and maintained this value as the vehicles remained stuck to each other (Figure 2.16b,d). However, when sufficient control (tilt sensitivity $\Delta v/\Delta\gamma$) was applied, vehicles starting from the same initial condition as the case with no control (Figure 2.16a) increased their speed when approaching each other, resulting in time dependent convex area with a larger average mean (Figure 2.16c,d). The average area increased with tilt sensitivity $\Delta v/\Delta\gamma$ as shown in Figure 2.17a.

A full theory incorporating the interplay between the multi-body interactions and the vehicle's response to them would be useful in understanding the functional role of this mechanism, but is beyond the scope of this paper. However we can gain qualitative insight by analyzing a special but representative case. Here we consider the stable orbit of n bodies on a perfect ring (inset of Figure 2.17b). The vehicles can achieve this special mode due to the symmetry of the configuration. The black dashed line in Figure 2.17a shows that the convex-hull area of this characteristic mode $A_{\text{conv}}^{\text{ring mode}} = \pi r_{\text{ring}}^2$ captures the simulation result qualitatively well. Here, the radius of the stable ring r_{ring} follows $k(r_{\text{ring}}) = v(\gamma(r_{\text{ring}}))^2/r_{\text{ring}}$ where $\gamma = |\nabla z|$. Therefore, r_{ring} is determined by the intersection between the central attraction $k(r)$ and the centripetal acceleration $a_c(r) = v(\gamma(r))^2/r$. When there is no speed control scheme, one of two undesirable outcomes arises: either (1) $a_c(r)$ does not intersect with $k(r)$ and the vehicles cannot exhibit a stable ring orbit for any r or (2) $a_c(r)$ intersects with $k(r)$ within the geometric exclusion zone. One can find the critical tilt sensitivity $A \propto \Delta v/\Delta\gamma$ by making these two curved lines intersect outside the geometric exclusion zone. This minimal model thus rationalizes why tilt-based scheme can be used in systems with larger numbers of agents.

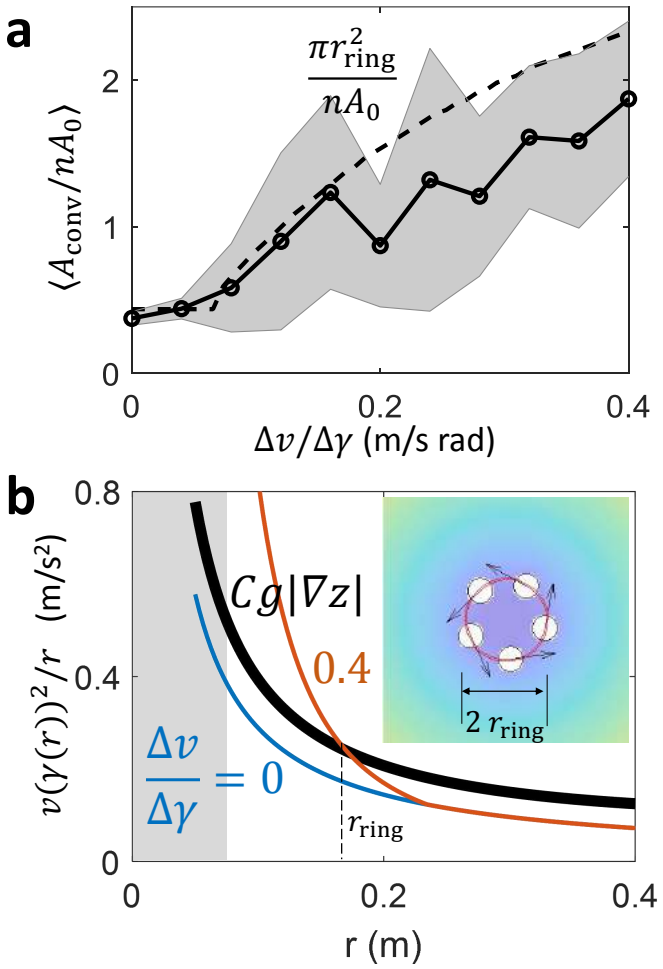

Figure 2.17: **Speed control and collective merger avoidance.** (a) Average convex area of the simulated 5 vehicle collective increases with the tilt sensitivity (see Figure 2.16); each point shows the average and standard deviation for 20 different random initial conditions. (b) A special mode, the ring mode in which all vehicles move on a circle at a steady state, is used to understand how the characteristic distance depends on the speed-control. The black thick line shows the attraction induced by membrane deformation, $Cg|\nabla z|$, and the colored lines show the centripetal acceleration $a_c(r) = v(\gamma(r))^2/r$ required to access the ring mode for cases with control (orange) and without control (blue). The radius of the ring which is given by the intersect of the black thick line and a colored line gives the characteristic area in panel (a) in a dotted line. The gray shade shade shows the geometric exclusion zone within which the vehicles collide with each other.

We can also interpret the speed control from the metric framework perspective. We first generalize the axi-symmetric substrate to a substrate with general landscape z such that a vehicle moving on top of it follows Equation 2.45, Equation 2.46 to obtain the temporal and spatial curvature of the metric $\alpha^2 = E^2(1-v^2e^{-Cgz/v^2})$, $\Phi^2 = E^2e^{-Cgz/v^2}(1-v^2e^{-Cgz/v^2})$.

The metric above reveals that the increase of speed v makes the metric approach (conformal) flatness since the ratio between the temporal curvature α^2 and spatial curvature Φ^2 approaches unity with a higher speed. The flatter spacetime implies smaller interaction between the vehicles. Thus our adopted strategy can be viewed as reduction of interaction by manipulating the effective spacetime metric. A fruitful future direction could be to use such insights to develop controllers for agents to mitigate effects of unexpected environmental perturbations.

2.3.3 Non-rigid body with internal structure and tidal effect

Besides the rigid active agents studied in the previous sections, more realistic cases could involve nonrigid (shape-changing) bodies. As we have learned earlier that the force emergent from the membrane varies with space, inspired by the tidal effect, we wonder have the gradient of the force would deform a non-rigid body. To gain insights into how a body with inner structure responds to the substrate-mediated interaction, we probed the dynamics of a nonrigid body composed of two rigid bodies on the elastic membrane [4].

To make this nonrigid body (vehicle pair), we connect the two vehicles which we have used in the previous sections with a spring (Figure 2.19AB). To avoid the transverse bending, we insert a metal rod inside of the spring to confine the spring on one dimension.

Before systematically running experiments to explore the tidal force, we needed to know what speed we should set for the two vehicles. Experiments and simulations (Figure 2.18) reveal three types of trajectories as we vary relative car speeds. The simulation uses the same setup as in Figure 2.13 except that we have included the spring force (spring constant $k \sim 1$ N/m) measured from experiments. To characterize the orbit, we looked at the spin angle, which is the winding angle of the two cars about their center of mass, and the orbital angle, which is the winding angle of the two cars about the center of the membrane.

[4] This is an unpublished work done with Hussain Gynai.

It is the direction of spin qualitatively distinguishes these orbits. It can be zero or with the same or opposite direction as the orbit. We refer them to the tidally locked regime, the prograde regimes and the retrograde regime.

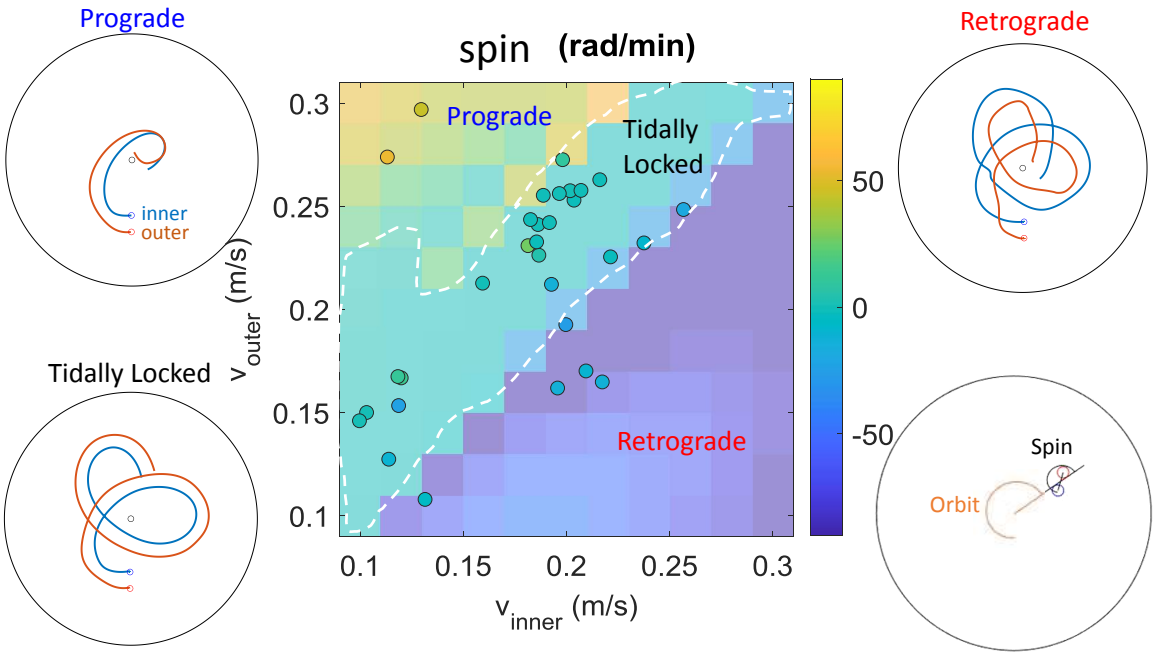

Figure 2.18: **Typical orbits of a vehicle pair depending on the vehicle speeds.** The orbit type depends on the speed of the inner and outer vehicle speeds (see the upper-left inset). Starting from the same initial condition, here we characterize the orbit by the self spin angle (see the lower-right inset) over different inner and outer speeds. When the two are close to each other, the spin does not grow systematically and two vehicles are tidally locked. When the two are quite different from each other, the spin has a trend to grow with the direction determined by the vehicle with higher speed. The colored solid dots in the main plot and the inset trajectories are from experiments.

We decided to further explore the tidally locked regime due to its similarity to the single vehicle which we have extensively studied in the previous sections so that we will see how a small change (the nonrigidity) could change the dynamics of an active agent on a deformable surface. In experiments, the distance between the two vehicles oscillates on the magnitude of several millimeters to several centimeters. To understand the effect from the force gradient, we measured the tilt angles of the two vehicles (Figure 2.19B) and evaluated their difference. The separation turns out to be positively correlated to this difference and therefore infers a tidal effect.

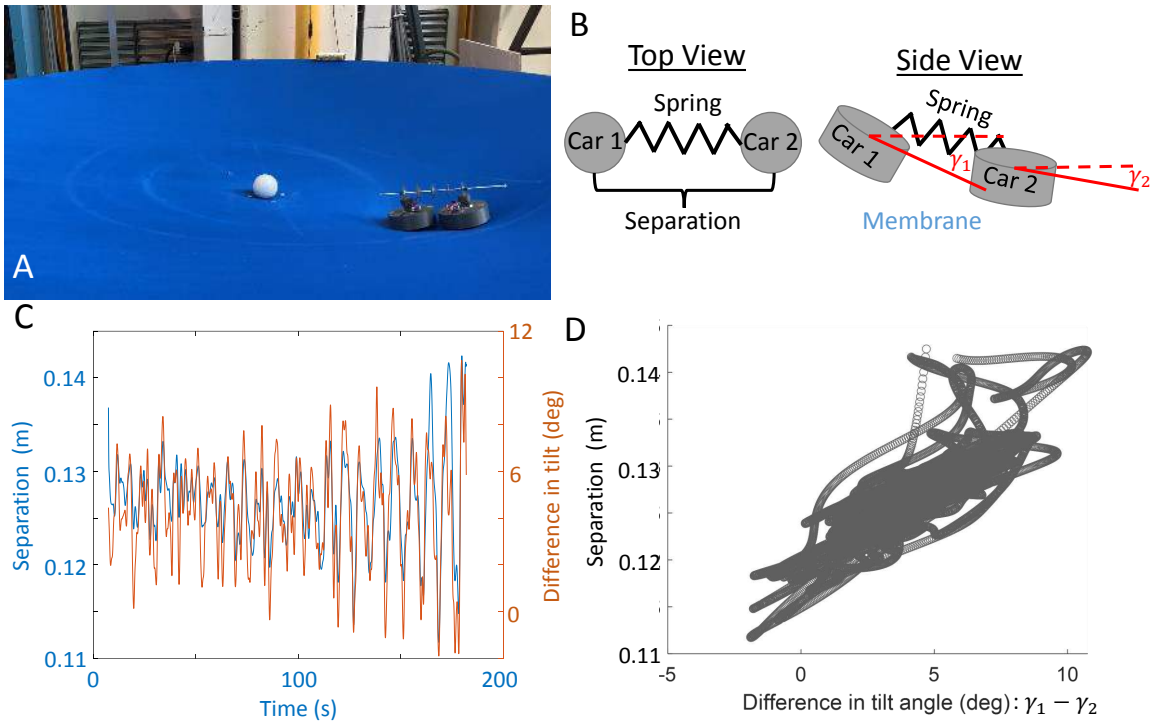

Figure 2.19: **Tidal effect from force gradient.** (A) A pair of vehicle connected moving on the elastic membrane with a central depression. (B) The top and side views of the vehicle pair. (C) The separation between the two vehicles and the tilt (γ_1, γ_2) difference, which infers the force gradient (shown in (B)) evolves with time. (D) That the separation increases with the tilt difference suggests the tidal effect.

Further, considering that the substrate is subjected to disturbance from external sources or other agents, we try to see how a time-varying substrate would alter the dynamics. To generate the external field, we oscillate the center of the membrane with an amplitude of 2 cm and a period $T_G = 2\pi/\omega_G$ to be determined in different experiments. We posited the vehicle pair might be excited when the center oscillates at periods close to the important time scales, such as the natural frequency from the spring and the orbital period of the vehicle pair. To characterize how much an orbit is resonated, we fit the evolution of radius to

$$r(t) = R_0 + \Delta R \cos(\omega_G t + \phi) \exp(\tau^{-1} t) \tag{2.49}$$

where τ^{-1} will be referred to as the pumping rate and used as the metric for resonance.

The larger τ^{-1} is, the more resonated the vehicle-pair is. Surprisingly, it turned out the orbital period is easier to be excited. As we oscillate the center of the substrate vertically, we find the case with zero spin responds to this field drive most and the orbit resonates with the field at the orbital period (Figure 2.20D).

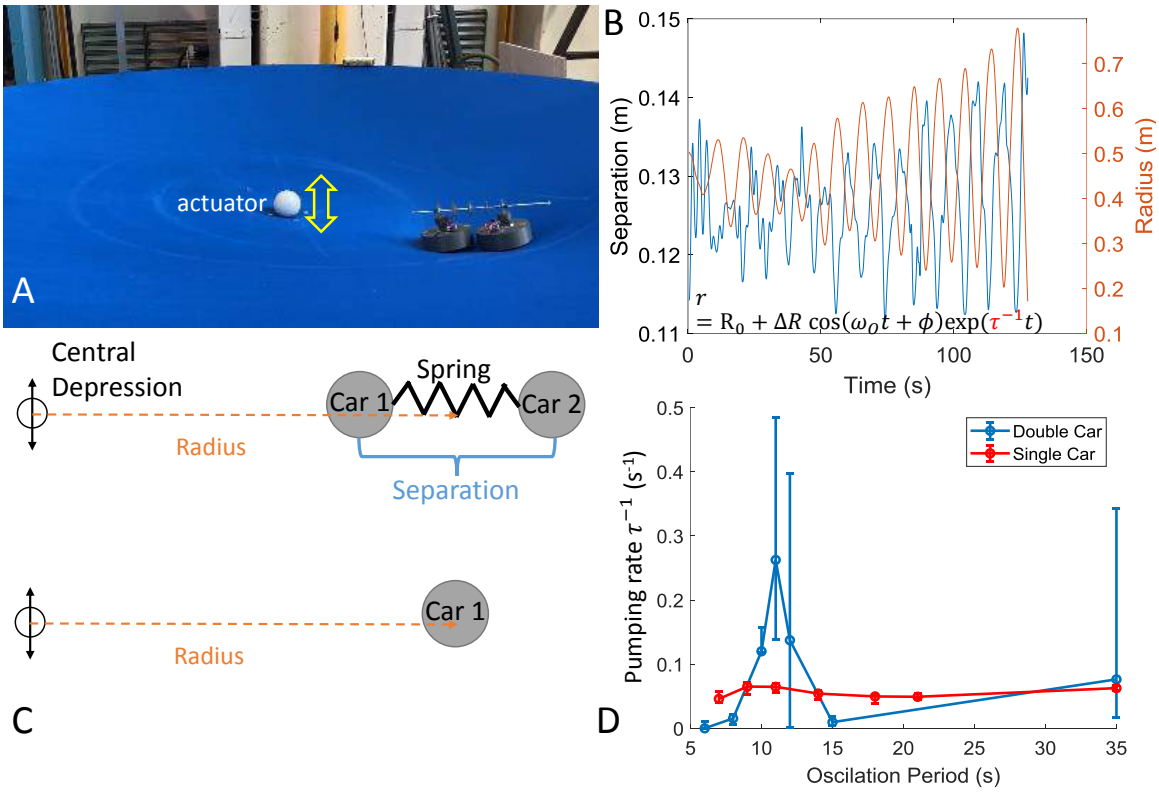

Figure 2.20: **Vehicles resonated by the central vibration.** (A) The central depression moves up and down with a prescribed oscillation period with an amplitude of 2 cm. (B) A typical evolution of the separation and the center-of-mass radius over time for a vehicle pair. (C) The upper and lower diagrams show a sketch of (A) and the single vehicle experiment respectively. (D) The characteristic pumping rate τ^{-1} by fitting the radius with model (ref) shows that both a vehicle pair and a single vehicle is resonated by the central oscillation at the orbital period, which is around 10 s.

If one looks at the motion's projection on the radial direction (Figure 2.20C) and regards the composite (vehicle pair) holistically, one might ask if a single vehicle also gets resonated. In the single vehicle experiments, we did find the vehicle resonated at a similar period (or frequency), but with smaller amplitude (Figure 2.20).

2.3.4 Conclusion

In this chapter, we performed the first study (to the best of our knowledge) of the locomotion dynamics of active agents on an elastic substrate with interactions mediated solely by local and global deformation (curvature fields). Experimentally, we studied the dynamics of a single vehicle on a centrally curved elastic surface, revealing nearly ubiquitous retrograde precessing orbits. Guided by the theoretical model based on experimental data, we observed that a reduction in vehicle weight leads to prograde precession. To further test our understanding of the vehicle dynamics and the emergent interactions, we next studied the interaction of two vehicles on a relatively flat membrane (without central depression) with the feature that the time-dependent curvature fields of the vehicle reciprocally govern the robot's trajectories. We observed how increasing the mass ratio between the vehicles led to increased curvature-field-mediated cohesion. We then developed a control scheme for the multibody system which mitigated cohesion by using only local sensing and interaction with the environment without knowing the positions of the robots on the membrane. The controller changes the vehicle's speed according to the vehicle's local tilt (indirect measurements of the local curvature field) without knowing the positions of the robots on the membrane. Extending the scheme to multiple vehicles interacting with each other on an arbitrary substrate revealed that our framework and control scheme could be generalized to active matter systems that consist of a larger number of agents.

Theoretically, to understand the single vehicle orbital dynamics, we constructed a minimal mechanical model which agreed well with the experimental results and revealed that the vehicle did not simply follow geodesics of the membrane. Inspired by the resemblance of dynamics in our system to those in General Relativity (GR), we wondered if a differential geometry framework could be of use to better understand features of the system. The active nature of the self-propelled robot allowed us to recast the robot's locomotion dynamics as geodesics of a test particle in an effective spacetime metric. This framework revealed how aspects of the system (e.g. retrograde precessing orbits) were related to system parameters

and allowed us to modify the vehicle mass to change orbital precession from retrograde to prograde; we explore the connections of our robophysical experiments to GR in more depth in [109]. To understand the reciprocal curvature-field-mediated interaction in a two-robot system, we first generalized the mapping to understand how individual vehicles responded to arbitrary curvature fields. We developed an equation for how the vehicles generated curvature by showing that the Poisson equation could approximate the shape of the membrane deformed by the masses on it. Solving the Poisson equation analytically demonstrated the origin of forces on the vehicles. Combining the equation of motion for a vehicle on a generalized deformed surface revealed the role of vehicle mass in attraction.

We posit that individuals and swarms of locomoting robots could benefit from discovery and utilization of principles by which agents can interact and communicate by exploiting environmental dynamics [62, 114]. Although our system is relatively simple compared to other locomotion and swarm situations in which agents experience field-mediated interactions, the simplicity (such as the linear elasticity in the Poisson equation for the membrane and the acceleration's linear dependence on the local gradient) could make our work serve as a starting point for other terrestrial (and even surface aquatic) systems with more complex rheological responses (e.g. media with viscous, plastic, and elastic responses). Study of active systems on elastic fields and the differential geometry framework could thus function as a model system and provide tools to robotic studies [115, 116, 117, 118, 119] of a broader class of physical[120, 72] systems. For instance, the local curvature could be used as an input in addition to other information such as vision [121, 122, 123] and stress sensing [124, 79, 14] in swarm robotics. Curvature field information could be exploited by robots with limited sensing and control, for example in lightweight water-walking robots [125, 118] or self-propelled microrobots [126] swarming on fluid membranes [37]. Finally, we note that our study is another example of the rich and under-exploited intersection of physics and robotics, adding to the list of tools and ideas– e.g. gauge theory [127, 128], diffraction and scattering [52, 129, 130], statistical mechanics [131, 79]. We expect that

such robophysical study can help transition robots and swarms from the factory floor into complex natural environments.

CHAPTER 3
ACTIVE AGENTS DRIVEN AND CONNECTED BY MUTUALLY CONSUMED RESOURCE

3.1 Field changing with speed similar to the active matter

In the previous chapter, the elastic substrate mediates the interaction between the active agents almost instantaneously, given the speed of the agents ($\sim$ 30 cm/s) is much smaller than the speed of the disturbance propagation (wave speed $\sim$ 400 cm/s). One would be curious to ask what will happen if these two speed are comparable in cases either the agents move faster or the substrate disturbance decays slower. In this chapter, we will explore this regime with an example reminiscent to ecology and show the richness of dynamics not seen in the previous chapter.

In this example, we investigate a unique form of active matter based on a combination of biological ecology [132] and robophysics [133, 91]. As autonomous robots become increasingly more adaptive, it is interesting to ask if adaptive robot swarms can achieve complex/dynamic behavior [48, 134].We present here a robot swarm that emulates natural collective ensembles in that they change their environment by their very presence, and observe collective state changes as a consequence of their ability to self-modify their environment and respond to that self-modification [1].

This ecology-inspired robot swarm rooted from more conventional active matter systems [135] move over a 4.0 meter by 4.0 meter light-emitting diode (LED) light board. Each robot can determine the local light intensities $I(x, y)$, which represents the amount of the local resource, and the gradient of the resource $\nabla I(x, y)$ (Figure 3.1). Positions here are given conveniently in terms of pixel coordinates, and speeds are given in pixels/second.

[1]This and the next section are adapted from a co-authored journal article 'Emergent field-driven robot swarm states,' Physical review letters, 2021, 126(10) where I contributed to the phase characterization.

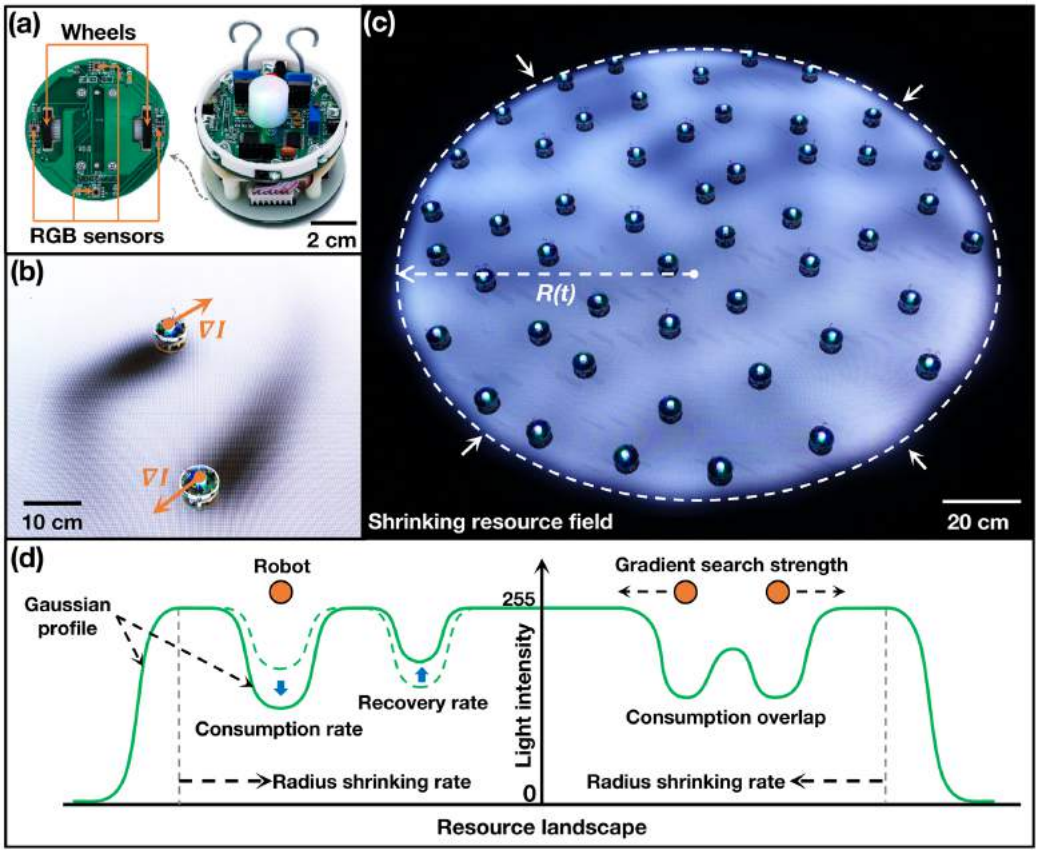

Figure 3.1: **Robots and the interactive LED light board environment.** (a) Each robot has one micro-controller. A robot base, of diameter of 65mm, has four RGB sensors for detection of light color from the LED light board. The movement of each robot is controlled by two independent pulse-width modulated gear motors. (b) The four RGB sensors are used to co-detect gradient vectors from the underneath resource landscape; (c) The LED light board of dimension 4.0m $\times$ 4.0m and 2.5mm pitch supplies complex and dynamic environment for the robot communities. (d) The rules and parameters that control landscape resource and agents consumption property. courtesy by Gao Wang and Trung Van Phan.

Each robot moves in response to the light intensity gradient $\nabla I(x, y)$ at their positions on the light board such that

$$\vec{v}_j = \frac{dx_j}{dt}\hat{x} + \frac{dy_j}{dt}\hat{y} = \kappa \nabla I(x_j, y_j; t) \ , \tag{3.1}$$

for robot j where $\hat{x}$, $\hat{y}$ are unit-vectors and κ is the robotic sensitivity to the landscape's local resource gradient.

Gradients in the intensity emerge from depletion (dimming) of the local intensity of the

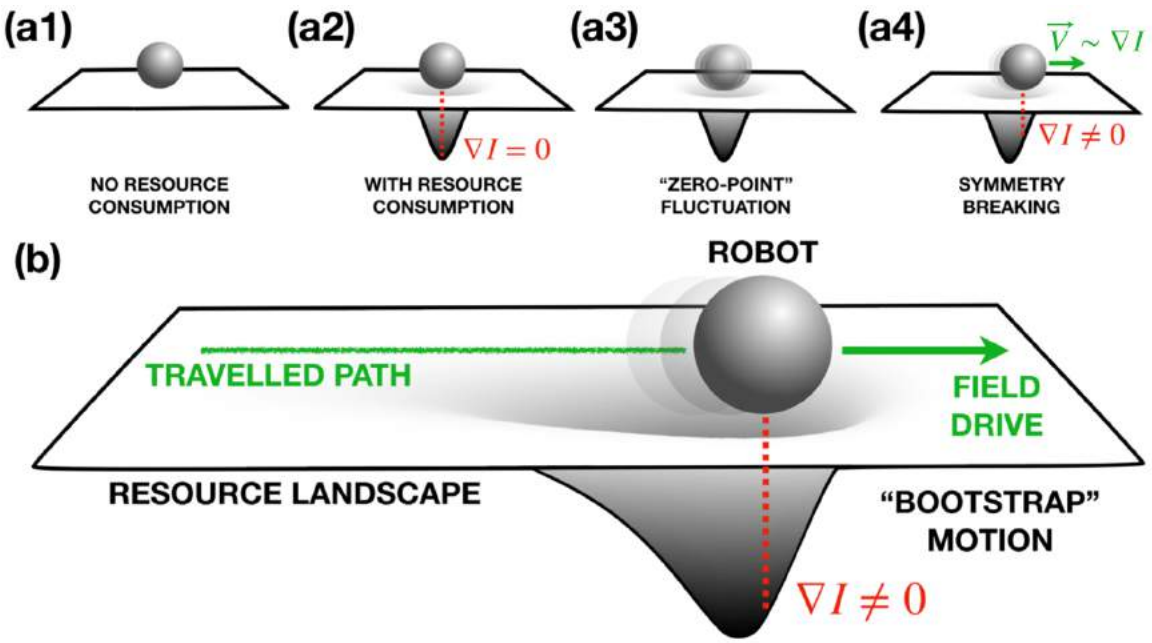

Figure 3.2: **Robotic field-drive emergent motion.** (a1)-(a2) Each robot consumes (dims) the light in a Gaussian circle around its position. (a3) Fluctuations give rise to transient intensity gradients which spontaneously give rise to a random velocity direction (a4). (b) Self-drive of a robot over an initially smooth resource field. courtesy by Trung Van Phan.

resource landscape by the robots. To achieve this resource consumption effect, an overhead camera is used to recognize the position of the robots and passes the dimming instruction to the LED board. A swarm of many field-driven robots creates an emergent complex resource field $I(x, y; t)$ which can be extremely time and space dependent. The presence of many robots $\{j\}$ at positions $\{(x_j, y_j)\}$ on the light board gives rise to a time dependent 2D light intensity landscape $I(x, y; t)$ across the light board:

$$\partial_t I = \frac{1}{\tau_R}\left(\tilde{I} - I\right) - \sum_j k_E e^{-\frac{(x-x_j)^2+(y-y_j)^2}{2\sigma^2}} \Theta(I) \tag{3.2}$$

where τ_R is the recovery time of a pixel intensity to the robot-free intensity $\tilde{I}$, k_E is the characteristic resource consumption rate of a robot, σ is the radius of resource consumption, and $\Theta(\zeta)$ is a Heaviside unit-step function $\Theta(\zeta > 0) = 1$, $\Theta(\zeta \leq 0) = 0$.

Symmetry in the depletion hole of the local intensity $I(x, y)$ created by a stationary

robot is spontaneously broken by digitization errors in the intensity detectors. This noise then bootstraps up an emergent field-drive motion. Each pixel of the local resource field shadow generated by the presence of a robot recovers with an exponential time constant τ_R once the robot moves away. The smaller τ_R is, the quicker the local resource shadow recovers. Figure 3.2 describes this field-drive of the robots and the decaying resource shadows they leave behind. In the realistic experiments, there is heterogeneity in the robot field drive sensitivity to mimic biological heterogeneity.

3.2 Emergent phases of matter on a single-type resource

The simplest resource landscape is a circle of light of radius R and a single resource color, namely "white" ($I_R = I_G = I_B$). In order to study how the robot swarm behavior changed with density we decreased the radius $R(t)$ linearly with time t:

$$R(t) = R_o(1 - \alpha t) \tag{3.3}$$

In order to provide gradients at the circle perimeter the perimeter is softened by a fixed Gaussian width $\sigma_o \ll R_o$.

The fundamental sign of the robot-robot field interaction is negative (repulsive) due to resource competition between two nearby robots as shown in Figure 3.3(a1). At relatively low robot densities the robots act like a gas of self-avoiding objects of finite size [Figure 3.3(a2)]. Familiar collective patterns emerge with increasing density, such as phenomenon related to phase transitions in soft-matter physics [136]. Figure 3.3(b1)-Figure 3.3(d1) shows that as the density increases, varieties of interaction modes emerge among the localized robots, thus leading to crystal, liquid and jammed states in sequence in overall community [Figure 3.3(b2)-Figure 3.3(d2)].

As the robot density increases, the resource landscape gets smoother since the average local consumption rate of resources increases with robot density, but the recovery rate

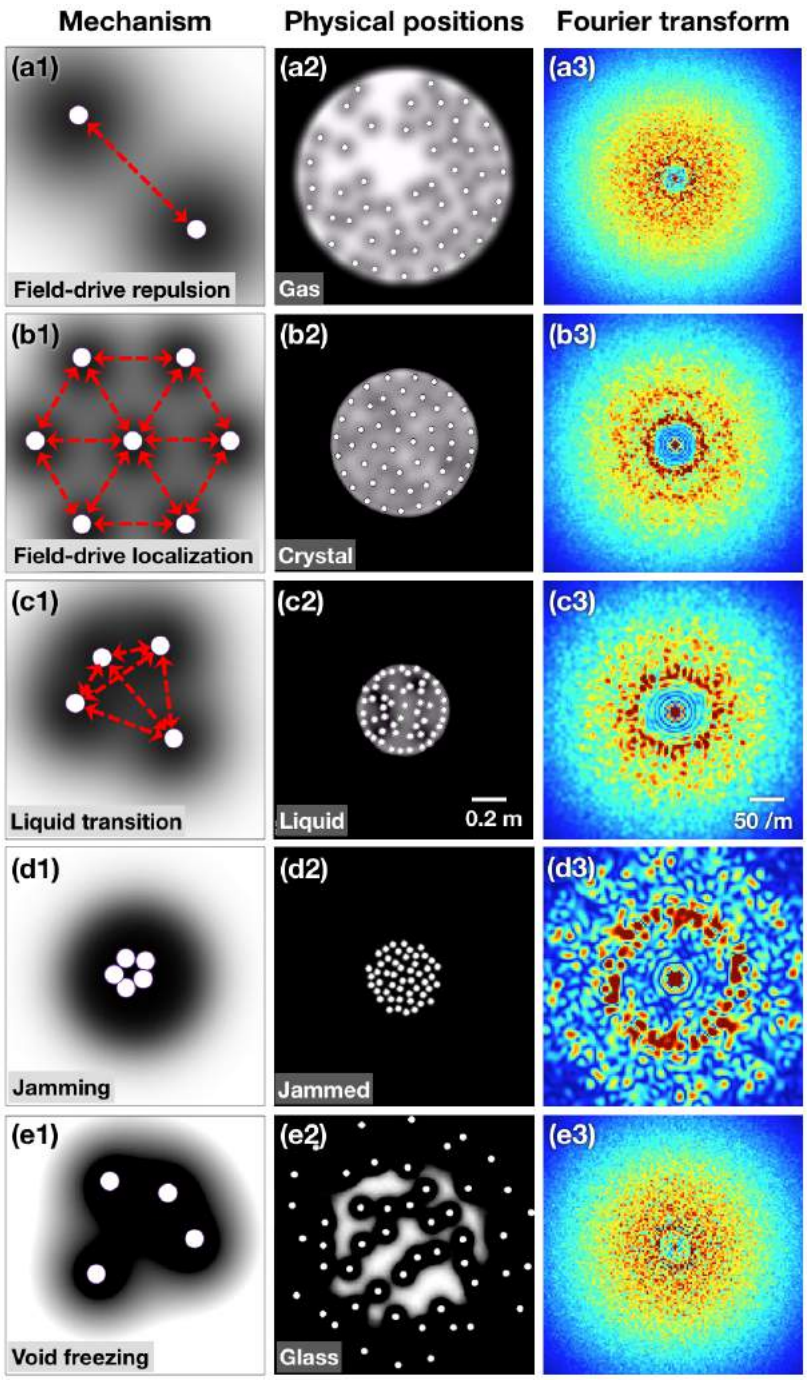

Figure 3.3: **The basic robot spatial distribution and the resource landscape field dynamic as the light environment radius shrinks.** Row (a1-e1) outlines how field drive results in robot different localized states, and row (a2-e2) shows snapshots of robot positions in five different phases. Row (a3-e3) shows the spatial Fourier transformation of the robot positions in row (a2-e2). courtesy by Gao Wang and Trung Van Phan.

per pixel does not. Figure 3.3(a3)-Figure 3.3(e3) shows the density dependent structure function $S(k_x, k_y)$ [137] we get from spatial Fourier transformation of robot positions as a function of robot density.

Since we can track individual robots, it is possible to quantitatively measure the position and velocity of each robot during a compression process. We use two different order parameters to characterize the emergent phases, ψ_6 for spatial ordering and τ^* for time ordering:

(1) ψ_6: Since circles close-pack to a hexagonal array [138], a natural order parameter to characterize the initial ordering of the robots with compression is the 6-fold index ψ_6 [139]:

$$\psi_6 = \left\langle \frac{1}{N_j} \sum_{j'} e^{i6\theta_{jj'}} \right\rangle_{\text{bulk}} \quad . \tag{3.4}$$

The value ψ_{6j} is the local bond-orientation order parameter, where the summation j' runs over all N_j nearest neighbor of robot j. $\theta_{jj'}$ is the angle between the vector connecting robots j to j' and an arbitrary fixed reference axis. $\langle\cdot\rangle_{\text{bulk}}$ denotes averaging over all robots excluding ones near the boundary of the environment. We use Voronoi tessellation [140] to define the nearness to the boundary.

(2) τ_*: The time-correlated spatial dynamics of the robots, as distinct from their time-independent spatial correlations ψ_6, can be captured by both the histogram of the robot kinetic energies $\langle \vec{v}_j^2 \rangle$ and the dynamic 4-point susceptibility order parameter χ_4 [141, 142]. χ_4 is calculated by first determining the dynamical overlap function $Q(t, \tau; a)$:

$$Q(t, \tau; a) = \frac{1}{N} \sum_{j=1}^{N} \Theta\big(a - |\vec{r}_j(t+\tau) - \vec{r}_j(t)|\big) \quad , \tag{3.5}$$

where the vector position of robot j at time t is given by

$$\vec{r}_j(t) = x_j(t)\hat{x} + y_j(t)\hat{y} \tag{3.6}$$

and a is a characteristic length which is usually chosen as the radius of an agent [143]. The function $\chi_4(\tau; a)$ is then computed as the variance of $Q(t, \tau; a)$ over the quasi steady-state time interval:

$$\chi_4(\tau; a) = N \text{ Var}_t\big(Q(t, \tau; a)\big) \tag{3.7}$$

Figure 3.4(c) shows the variance of Q(t,τ,a), i.e. χ_4, for an experiment. τ_*, as shown in Figure 3.4(c), can be intuitively viewed as the mean trapping *time* of a robot around a given position.

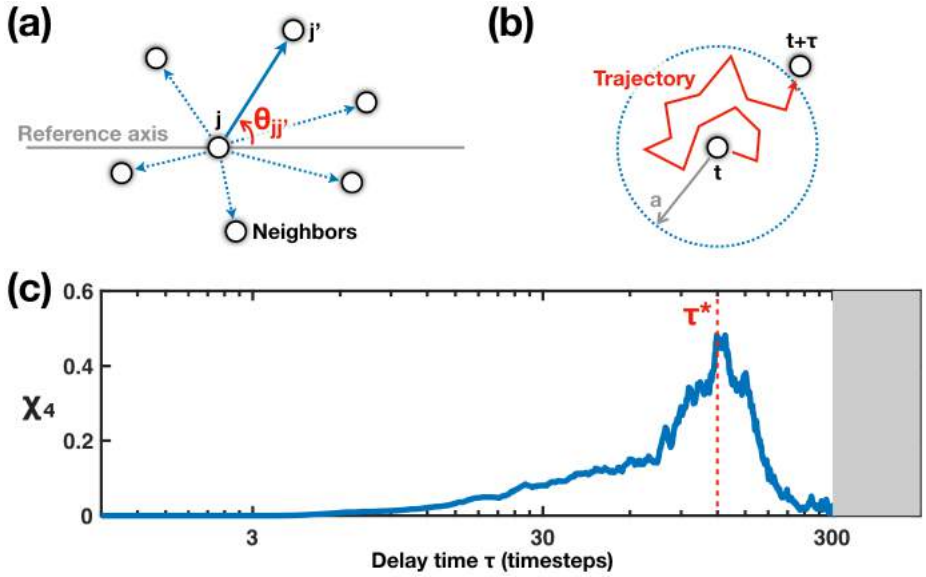

Figure 3.4: **Demonstration of the spatial and temporal characterization.** (a) Demonstration for ψ_6 calculation. (b) Demonstration for χ_4 calculation. (c) An example of characteristic time τ^* evaluated from the peak-position of $\chi_4(\tau, a)$.

There are three parameters which control the robot swarm field-drive matter states: the areal density of the robots σ and the two field relaxation processes: the shrinking rate of the light circle α in pixels/s and the environmental recovery time τ_R in seconds. If τ_R is set too slow and/or α is set too fast, the robots simply deplete (blacken) the resources and all motion freezes out. This phenomena that we call void freezing is a new form of glass-like state, showing in Figure 3.3(e2). Remarkably, even the gas state can directly transit to the void glass state if τ_R is sufficiently slow, something that does not occur in any other forms of active matter that we are aware of.

With decreasing values of τ_R for a fixed α different phases of the field-drive matter emerge, other robot phases emerge. With increasing compression, the robots first freeze into a hexagonal crystalline state, with high ψ_6, high τ^* and lowered $\langle \vec{v}_j^2 \rangle$. Note that this crystalline state is at relatively low robot densities and is not a jamming transition [144] because the robots are not in contact with each other.

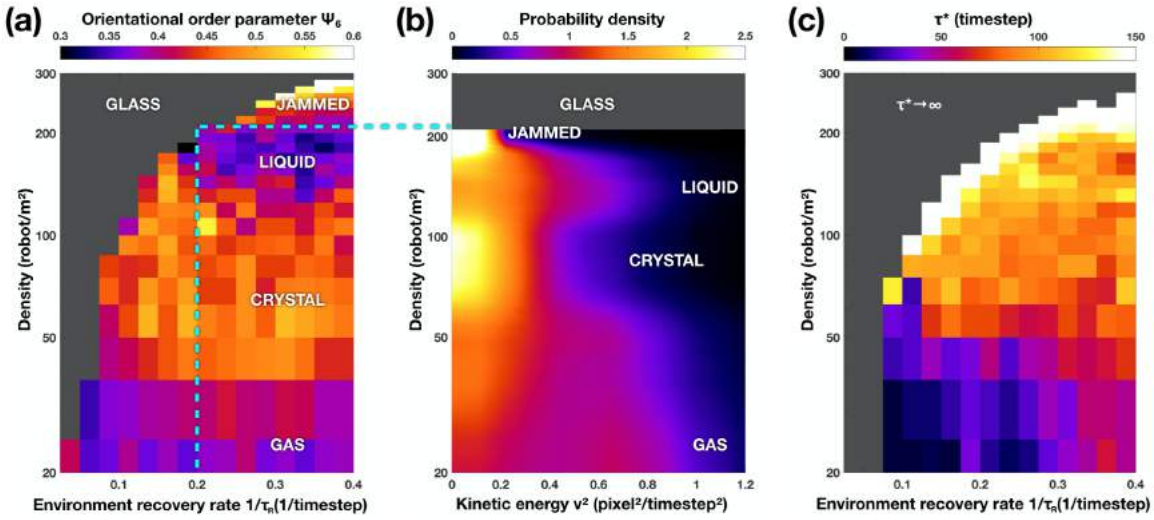

Figure 3.5: **Phase diagrams with respect to the density and resource recovery rate.** (a) ψ_6 as a function of robot density and resource recovery rate $1/\tau_R$. (b) Robot kinetic energy density $\vec{v}_j^2$ as a function of robot density for a fixed resource recovery time of $\tau_R =$ 5 time-steps. (c) τ_* as a function of robot density and resource recovery rate $1/\tau_R$.

The transition from a gas to a crystal state, not seen in inertially-driven systems [145], emerges since our robots have no physical inertia but rather a field-driven motion. By "no physical inertia", we mean that field drive (gradient searching of resources) gives the robots motility. In the absence of a gradient, they do not and cannot move. If we suddenly remove the gradient, the moving robots immediately stop by the next time step iteration. In that sense they have no physical inertial at all.

Due to the decreasing resource landscape roughness with increasing robot density, the crystalline state pressure melts into a liquid state, with a decrease in ψ_6, decrease in τ^* and increase in $\langle \vec{v}_j^2 \rangle$. Melting from a crystalline to a liquid state requires robot escape from local resource minima due to their ability in the field-drive mechanism to move against

a sufficiently weak resource gradient. Finally, the liquid state freezes in a jammed glass as the robot field drive moves the robots into contact with each other so that the state is incompressible, and the field again becomes depleted (black). The jammed state is however much different than the void glass freeze, the void glass state is due to the robots falling out of steady-state equilibrium. Figure 3.5(a), Figure 3.5(b) these results for the spatial order parameter ψ_6 and Figure 3.5(c) presents the dynamical order parameter χ_4 mean value τ^*. Information on $\langle \vec{v}_j^2 \rangle$ with different τ_R.

Since this biologically inspired robot swarm active matter does not have a well-defined temperature, it is difficult to draw the usual phase diagram to show the states. A plot of the states versus the ψ_6 oriental order parameter and the susceptibility characteristic timescale τ^* [143]:

$$\chi_4(\tau^*; a) = \text{Max}_\tau\big(\chi_4(\tau; a)\big) \tag{3.8}$$

is seen in Figure 3.4(c).

Our robot field-drive and emergent states present a biologically inspired active matter. The robots remodel a resource landscape and that remodeled landscape guides the robots' locomotion, even against resource gradients. The field drive also generates a field-analog multi-body interaction between the robots[146, 147]. We view robots as tools for a third way of modeling dynamical systems, complementing theoretical ideas, digital computation and now robophysical approaches. Thus robots (and robophysics [133]) provides another way to develop models of phenomena which can lead to insights in biological systems (locomotion, resource landscape utilization) as well as systems to explore interesting dynamics in physics (e.g. dynamical systems, active matter), and engineers in principle can take the robophysics insights and turn them into more interesting robots.

3.3 Evolution of active matter on multiple types of resource

In the previous section, though the LED screen is composed of red, green, and blue LEDs, we have constrained the resource to be effectively 'monochromatic' by enforcing the intensity of the three components equivalent to each other for every spatial point. One natural next step would be to explore the case where the three colors of the LEDs representing three different types of resources.[2].

Similar to the setup in the previous section, the robots move in response to local resource gradient created at their position on the light board, which together with the resource dynamics create a complex field-drive locomotion mechanism [148]. The many-body aspect of the resource landscape gradients are extremely dynamic since the robots locally deplete the resources, the result is that the gradients are a strong functions of both external drivers and the local density of the robots [149]. Figure 3.6 presents the basic flow of the robot swarm on the landscape.

The consumption of each of the three resources by the robots is also similar to the case in the previous section that the light intensity (resource) $[S]$ follows a relaxation dynamics:

$$\partial_t[S] = -\frac{1}{\tau}[S] + \sum^{\text{robots}} C \,, \tag{3.9}$$

where C is the consumption rate of each robot central around its position, τ is the fixed recovery rate of a resource. In our experiments, τ is a fixed value. The resource value is given by $I = I_{BG} - [S]$ so that when a robot consumes resources and leaves, the environment will slowly recover to the set background I_{BG}.

To exploit the feature of different resource types, we make the robots have different phenotype determined by a 6-byte diploid genome: (R1,G1,B1) and (R2,G2,B2). Each byte (gene) consists of 8 bits: 1 bit is reserved to flag if it is dominant (1:active) or recessive

[2]This section is adapted from a co-authored journal article 'Robots as models of evolving systems,' Proceedings of the National Academy of Sciences of the United States of America, 2022, 119(12) where I contributed to the entropic interpretation of the phenotype.

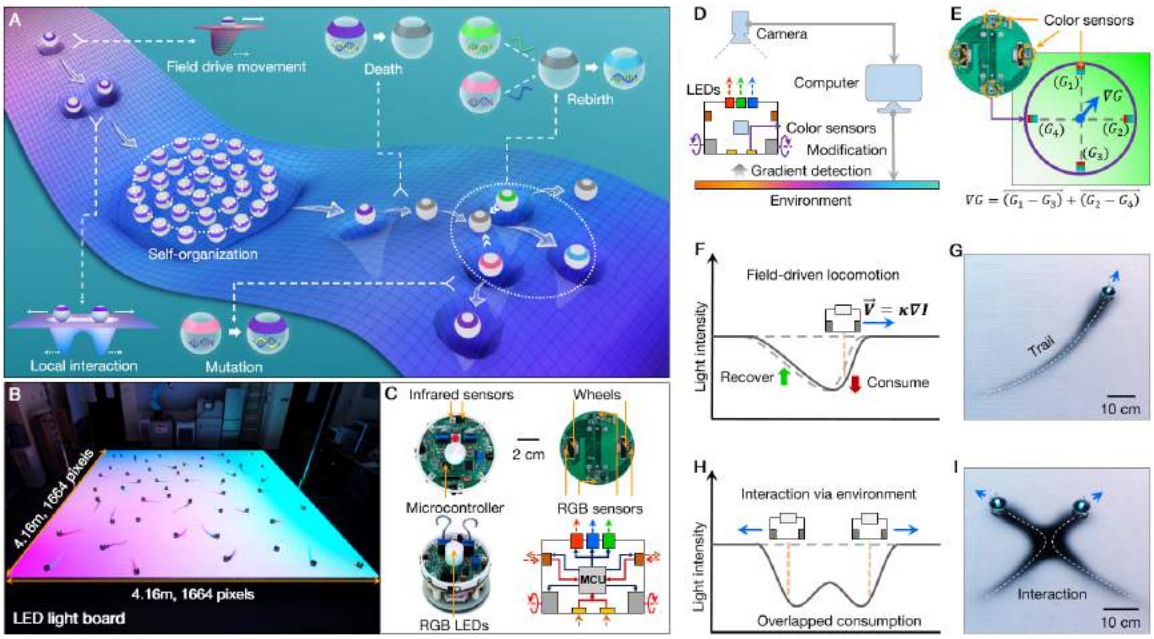

Figure 3.6: **Depiction of the robots.** (A) Depiction of the complex interactions of the robots. Ribbon: The robots move via self-generated field-drive on a resource landscape generated by an underlying LED light board, which the robots sense. Field drive is the self-generated movement of the robots in response to local resource depletion. (B) The 4.16 meter by 4.16 meter LED light board with robots across an RGB nested set of landscapes. (C) The hardware of a robot. Upper left: Infrared LEDs and sensors are used for gene exchange. Upper right: 2 wheels driven by independent motors move the robot over the LED light board, while 4 RGB downward looking sensors measure local light-board intensities. Lower left: RGB LEDs display the state of the 6-byte genome to an over-head camera. Lower right: Basic information flow: the downward looking sensors control while movement, the IR LEDs/sensors control gene exchange, the upward transmitting RGB LEDs sent genome state to the overhead camera. (D) The information logic flow for a given robot to determine resource consumption. The up-ward transmitting RGB LEDs are read by an overhead camera, which then sends information to a computer which dims the appropriate resource color(s) due to the dominate gene(s), and controls resource recovery. (E) Hard-wired computation of resource gradients by a robot. (F) The basic hard-wired manner in which a robot moves in response to resource gradients (field-drive). (G) The recovering resource "shadow" generated by a moving robot on a white homogeneous landscape due to field drive. (H) The basic repulsive interaction due to field-drive between 2 robots. (I) Soft resource driven "collision" between two field-drive robots on a white landscape. courtesy by Gao Wang and Trung Van Phan.

(0:non-responsive), as is shown in Figure 3.7. Only dominant genes can exhibit sensitivity to the corresponding resource gradients.

The remaining 7 bits (0000000 - 1111111) determine the sensitivity to the color associated with that gene and hence the velocity (a 2D vector) with which they climb out of a resource hole following resource gradients. The quantitative relationship between genes and robot velocities is as follows: three pairs of genomes respectively control robot sensitivity to three different resource (R/G/B), which are represented by R_{gene}, G_{gene}, B_{gene} :

$$\begin{aligned} R_{gene} &= \frac{R_1^{(flag)} R_1^{(value)} + R_2^{(flag)} R_2^{(value)}}{2 \times 127} , \\ G_{gene} &= \frac{G_1^{(flag)} G_1^{(value)} + G_2^{(flag)} G_2^{(value)}}{2 \times 127} , \\ B_{gene} &= \frac{B_1^{(flag)} B_1^{(value)} + B_2^{(flag)} B_2^{(value)}}{2 \times 127} . \end{aligned} \tag{3.10}$$

Here the quantities with superscript *(flag)* take value 0 for recessive gene and value 1 for dominant gene, the quantities with superscript *(value)* take the value of the remaining 7 bits, ranging 0 - 127 in decimal.

The vector velocity is determined then by the genotype and localized resource gradient:

$$\begin{aligned} \vec{V} = &\frac{V_{max}}{3} \times \\ &(R_{gene} \nabla I_{red} + G_{gene} \nabla I_{green} + B_{gene} \nabla I_{blue}) \ . \end{aligned} \tag{3.11}$$

Like the heterogeneity in the robot field drive in the system introduced in the previous section, there is an unexpected pleiotropy (one gene-multiple phenotypes) in our robot response. The pleiotropy in our genomes results from the finite spectral linewidths of the RGB LEDs in the light board which result in the RGB detectors in the robot base responding not only to the primary color (for example, red detector seeing only red but also blue and green).

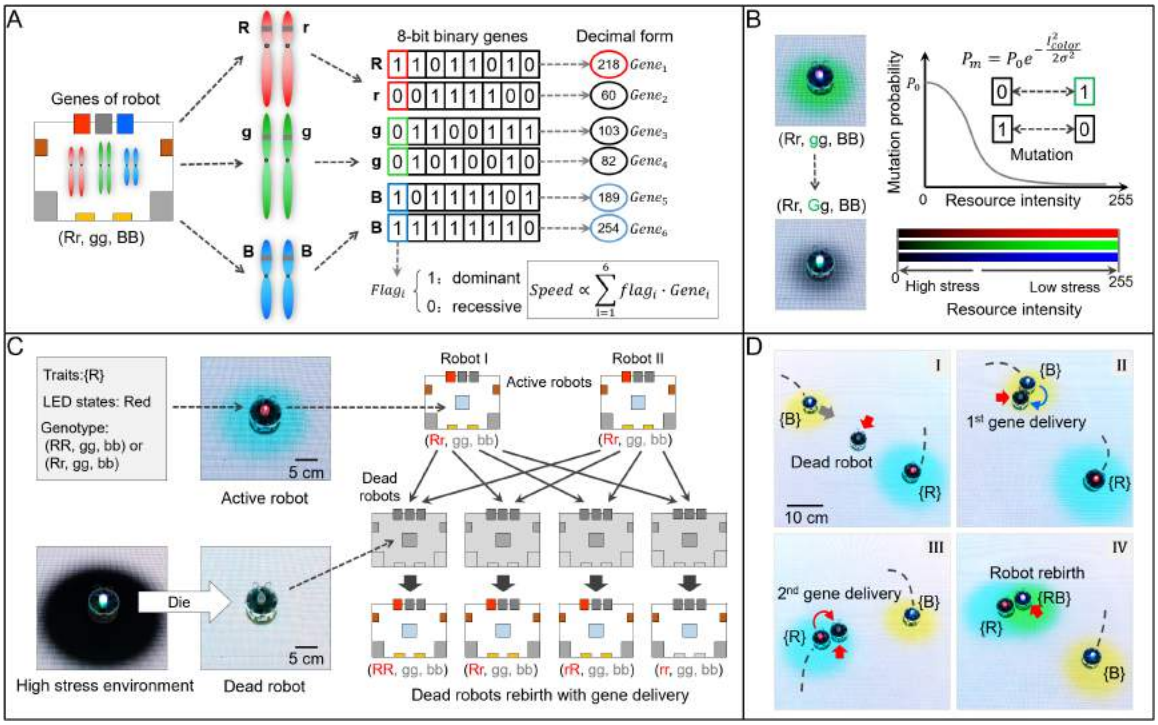

Figure 3.7: **Depiction of the robot genetic rules.** (A) Genes of the robots. Left: cartoon of the 6-byte genome and analogy to diploid human chromosomes. Right: The 6-byte genome. The first bit determines dominance or recessive nature, while the remaining 7 bits determine sensitivity to the underlying color on the LED light board. The translational speed of the robot is proportional to the 7-bit number times the state of the dominance/recessive flag. (B) Left: green resources untouched by a recessive green gene are consumed once a mutation makes the green gene dominant, giving rise to a black resource hole. Right: Mutation rates increase with lower levels of resources. (C) Pictorial gene exchange diagram as a dead robot (left) meets an active robot and haploid gene delivery occurs. (D) Images of the rebirth of a dead robot (center) due to 2 subsequent haploid gene deliveries. Courtesy by Gao Wang and Trung Van Phan.

There is no predetermined software algorithm to our robot phenotype [150]. Rather, the phenotype is collective, emergent and hardware driven, yet can be characterized as partly selfish and partly a form of altruism.

The selfish aspect is to exploit (consume) resources where you are, and move to find more resources as you deplete the ones you found by following the positive gradients of resources created by the robot and other nearby robots [148]. Robots which cannot escape from a resource hole die and lose their genes.

The altruism aspect is that if a living robot finds a dead robot, it copies 1/2 your genome to the dead robot. Two successive donations from non-identical robots gives rise to a re-birthed daughter robot. The altruism here is the survival of the robot species. Since our robots cannot unfortunately reconstruct themselves from basic materials [151], rebirth is our way to prevent inevitable extinction as Figure 3.7 shows. The re-birthed robot is thus genetically related to its parents. It is absolutely possible for us to design different reproduction modes, including asexual rebirth (one cell simply gives genes to a dead one), or just exchange genes between two alive robots, or any combination of these.

We correlate resource stress with mutation rates [152]: more resource stress gives rise to more mutations/time. Thus the stability of a gene in the robot is connected with the resource level: the dimmer the color intensity, the higher the mutation rate of the gene which is associated with that color. This allows a robot to escape in principle from a low resource dim region even if the 7 bit binary number associated with that color is low and hence there is a low sensitivity to light gradients: the enhanced mutation rate and the already low value of the gene implies a greater probability of drawing a high value and escaping. Likewise, a robot in a bright area will have a low mutation rate, in effect a robot with low sensitivity (low 7 bit binary number) is rewarded by being more likely to stay in that region until the inevitable depletion of resources happens. Then, there is always the risk of death.

The effective "metabolic" rate of resource consumption by the robots for a given color

is fixed to a level proportional to the local intensity of that color but is independent of the sensitivity of the robot to that color in terms of field drive. In principle only a robot with all "pure" recessive genes(rr,gg,bb) cannot consume any resource. It will stay still either mutate to a dominate gene, or it will die after 5 seconds. This is the reason why a robot with all recessive genes will die even in a white environment. They have no sensitivity to any resource, so they simply sit in one place, fatally. Thus a robot with more dominant genes will consume more resource, and it will move faster than a one with fewer dominant genes. A robot with only recessive genes will consume nothing, remain stationary, and die.

As we noted there is color leakage (pleiotropy) in this system: the RGB LEDs are not pure monochromatic light sources, so that for example a blue sensor on the robot will detect some fraction of the green light board even if no blue light is present: the net result is that robots do not necessarily die in an inappropriate environment. The biological equivalent for this is that recessive genes are not necessarily entirely recessive [153, 154].

Of course, if all the robots die, the population becomes extinct. Hence, breeding to produce an alive robot is essential. The genes of a reborn robot must come from two different alive robots (every robot has a unique ID).

We have carried out three different landscape evolution experiments to test to what extent our robot community is able to evolve and adapt to externally driven stresses.

1: No external time dynamics to resources. A white landscape with equal resources of red green and blue landscapes. This is the simplest possible landscape, with no explicit time -dependent external drive to the ecology, like the Earth's equatorial climate. However, with time the landscape will become spatially and temporally complex due to the heterogeneous nature of the robot genotypes, their motile resource exploitation, and their interactions, which result in locally preferential depletion of different resources.

Figure 3.8A shows the evolution of a survival landscape as a function of time for a fixed (white) landscape. As the theoretical guide predicted, there exists a mutational rate which leads to minimal survival and close to extinction of the robot community as time

progresses. Although some level of mutations are necessary for a population to evolve, presumably living systems would be driven to minimize mutation rates to the extent it is possible to avoid the mutational risk of extinction in a low-stress environment that occurs with increasing mutations [155].

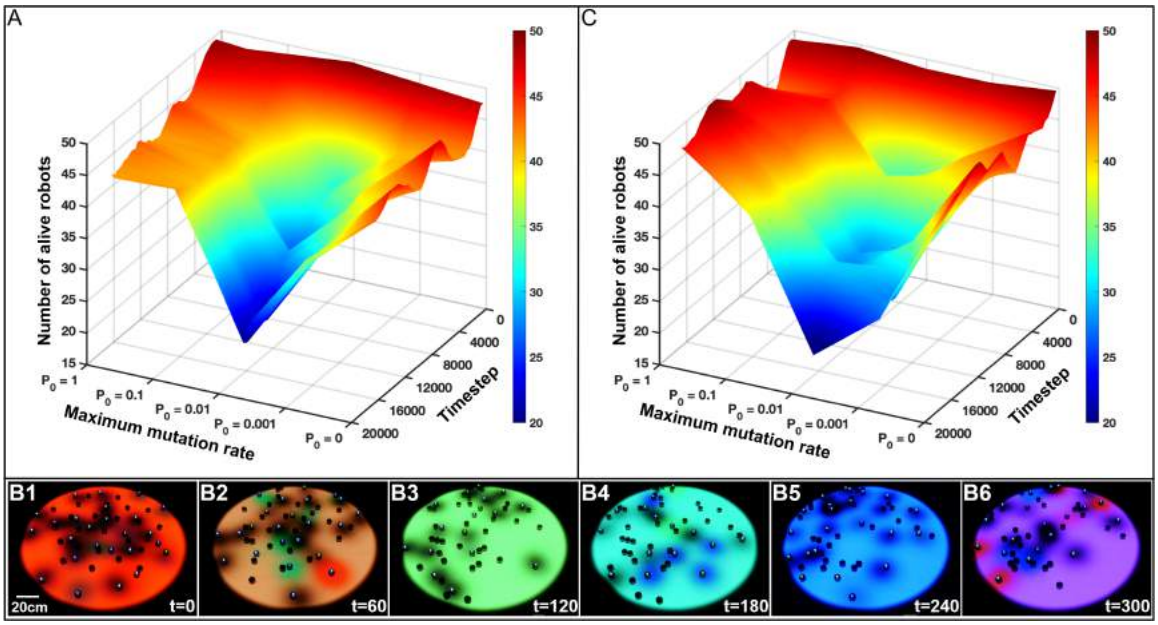

Figure 3.8: **Surviving rate in homogeneous and white landscapes.** (A) Surviving robot number versus time for a homogeneous white landscape which has no external time changes. (B) Images of robot positions for a periodically changing resource landscape: red - green - blue. (C) Surviving robot number versus time and mutation rate for a periodically changing environment. Courtesy by Gao Wang and Trung Van Phan.

2: Spatially Uniform but periodically changing landscape Here we drive the resource landscape with monotonically changing colors, representing in effect a well-mixed imposed landscape chemostat evolution experiment [156], but different from the classic chemostat experiment in that the initially homogeneous landscape can be locally modified by the robots. A fixed diameter circle of light homogeneously changes color from red to green to blue. The resource circle changed color with a 4320 time steps period for each color change, see Figure 3.8B.

As we have noted, it is only when robots have both mutations and gene exchange that a robust robot population can exist within a simple harmonically changing well-mixed

landscape. The robot's adaption to dynamic environment is revealed by the phenotypes responding to the detail RGB ingredients of the resource landscape. However, since the environment is changing with time, stress now opens up the mutational melt-down narrow valley and widens it.

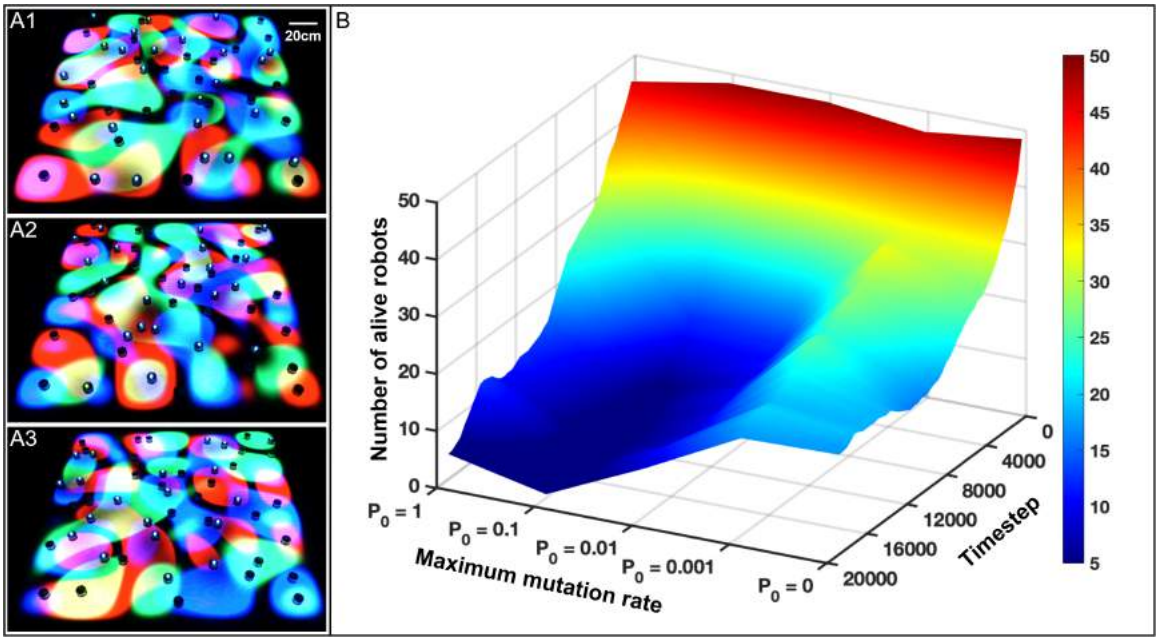

Figure 3.9: **Surviving rate in stochastic landscapes.** (A) Images of robot positions for a stochastic landscape which changes pattern randomly with time. (B) Surviving robot number versus time and mutation rate for a stochastic landscape with a stochastic time dependence.

3: Stochastic Spatial and Time Dependent Landscapes. To explore truly complex robot resource dynamics, unlike a typical biological laboratory well-mixed scenario, we created a stochastic, spatially fragmented complex landscape.

Figure 3.9 shows the number of surviving robots versus time on a stochastic, fragmented landscape. Clearly, as the stress imposed on the robots gets increasingly harder to predict versus time, it becomes increasingly harder for the robots to evolve. The valley of death increases dramatically in width as a function of mutation rate.

As we show in in Figure 3.9 for the case of pleiotropic genes $P_0 = 0$ is actually the sole optimum survival point in a stochastic environment with the parameters chosen. Pleiotropy inhibits chasing moving resources which vanish, but it can also result in a fragmented land-

scape in leaving robots isolated for too long a time and failing to undergo gene exchange, which is critical for survival.

In our toy robot organisms, the three genes are all equivalent in terms of phenotype, just respond basically to different colors. Yet the system evolves, so what is different in surviving populations that makes them successful since the phenotypes cannot evolve? We assumed that the evolutionary diversity must be in the relative numbers of bits set high within the genes. A useful metric for this kind of genetic diversity is the Shannon entropy of the dominant genes S [157, 158]:

$$S(t) = -\sum_{i}^{phenotype} p_i(t) \ln[p_i(t)] \tag{3.12}$$

where $p_i(t)$ is the time dependent probability of finding one of the 2^3 - 1 = 7 possible living phenotypes (red, green, blue, red + green = yellow, green + blue = cyan, red + blue = magenta, red + green + blue = white) as the landscape changes. If all the dominant genes in a collection of N robots are exclusively "green" eventually for example, then the final Shannon entropy is 0 and there is no dominant gene diversity on the resource landscape. The time dependence of the Shannon entropy is closely related to the Fisher information, since the Fisher information is basically the variance of the Shannon entropy [157]. We fit the measured time dependence of $S(t)$ to a logistic equation in Figure 3.10A. We choose the logistic equation primarily because of its close connection to ecological population dynamics, namely the role of the population growth rate R and carrying capacity K of an ecology [159], possibly related to our robot genome rate of change and limiting genomic diversity.

Under then the assumption that with time the initial Shannon genetic entropy $S(0)$ will evolve to a limiting entropy $S(\infty)$, we determined by curve fitting the Shannon genetic

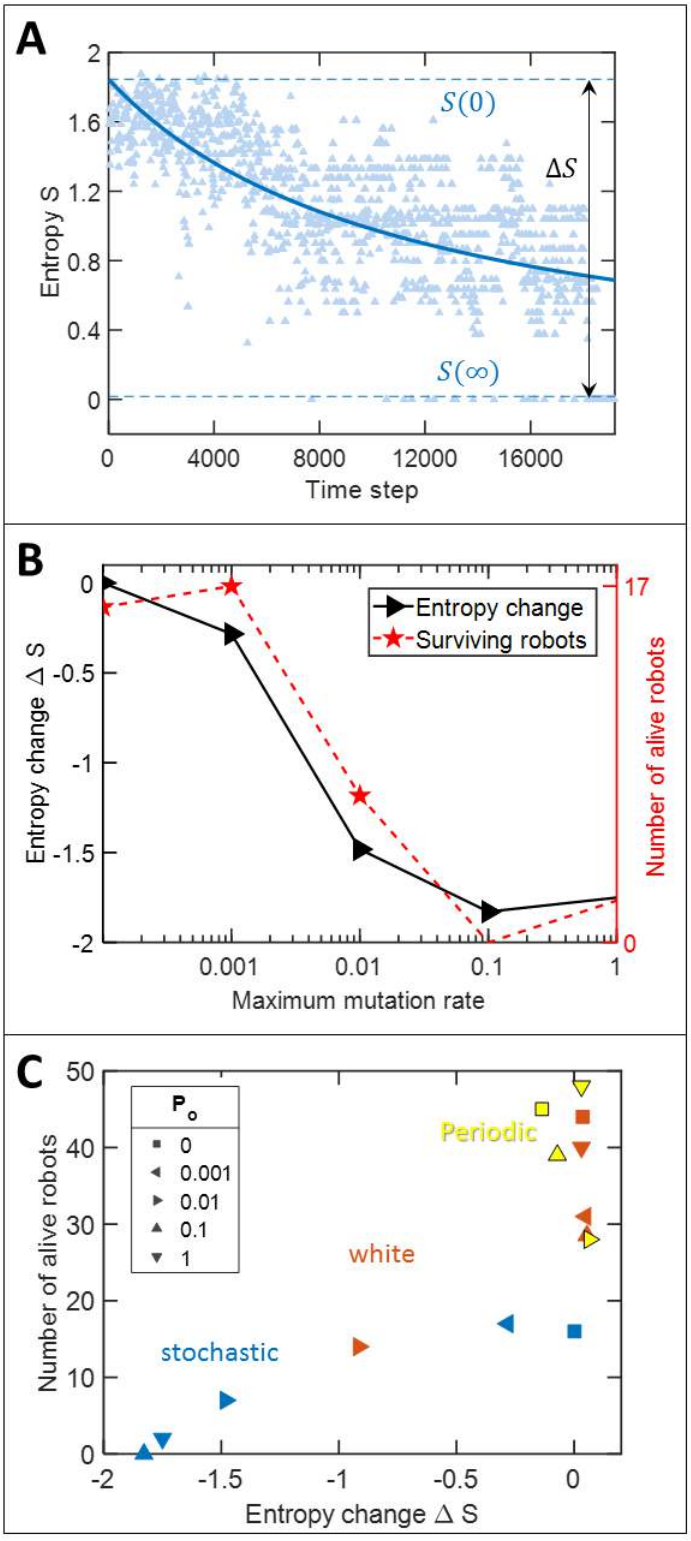

Figure 3.10: **Relation between genetic diversity and survival rate.** (A) Example of the logistic curve fit of the Shannon genetic entropy $S(t)$ versus time for $P_o = 0.1$. (B) Surviving robot population (red) and logistic curve fit of the total Shannon entropy change (black) ΔS as a function of basal mutation rate P_o for a stochastic landscape. (C) Correlation between Shannon entropy change $S(t)$ and robot survival for 3 different landscape dynamics, as a function of different intrinsic mutation rate P_o.

entropy change $\Delta S = S(\infty) - S(0)$

$$S(t) = \frac{S(0) \times S(\infty)}{S(0) + \Delta S \times e^{-t/\tau}} \tag{3.13}$$

where τ is the relaxation time of $S(t)$. Figure 3.10 presents the results primarily for the stochastic system. Note that, as would be expected, in the absence of mutations the Shannon entropy does not change.

Our evolution analysis indicates two important and surprising points connected to mutation rates: (1) the lower the final Shannon entropy, that is, the lower the genetic diversity, the lower is the survival probability of the robot population. (2) Static or periodically changing environments basically see no net change in genomic diversity with time even with changing intrinsic mutation rates P_o, but a stochastically changing environment drives genetic diversity down with time.

Our results suggest the basic hypothesis that while it is key for robots to mutate, exchange genes and breed to avoid extinction, high mutation rates can be a extinction driver in a sufficiently stochastic ecology. The numbers of robots is large ($N_{tot} = 50$) but not infinite, finite rather than infinite numbers of agents in biology is a meaningful and extremely important constraint in biology [160], especially in fragmented landscapes.

We have attempted to explore complicated bio-inspired resource dynamics with real physical robots instead of a more conventional digital approach (agent-based computer simulations), such as was used in the pioneering Sugarscape simulation [161, 162]. There are fundamental differences between these two methodologies, such as the overwhelming combinatoric load (at what point does the number of robots and their interactions become impossible to simulate?) [163], the distinctions between smooth analog time and discrete time in the flow of differential equations [164], and the general breakdown of algorithms in the presence of noise [165]. A concrete example is chronological ambiguity in digital operations, because combination of rules to represent simultaneous processes in discrete

time are intrinsically problematic: there usually is a specific order (non-parallel) to how the update of variable values is done. This results in the unsolved replication problem encountered in agent-based simulations, where observations cannot always be faithfully recreated based on just the physical analog description alone [166, 167].

From the success landscape, we conjecture that absorbing phase transitions [168] play an important role in the emergent behavior of this robotic system. In the extinction swamp, the system has crossed an absorbing phase transition boundary where the mutation-driven fluctuating state of some "alive" robots is no longer stable and get absorbed into the state of "dead" robots. Absorbing phase transitions are usually associated with strongly non-Gaussian behavior and diverging time scales [169, 170, 171], and there is of course room for more exploration here beyond the scope of this paper.

There is a potential clinical aspect to this work based upon our surprising results from stochastic landscapes. From the start of the design of this technology, we viewed our robots as cancer cells, and that the resource landscape over which they move represents changing nutrients and that chemotherapy is represented by changing the resource landscape in such a way that the cells, although they are capable of mutation and reproduction, cannot sustain a viable population.

From our results, we predict that a stochastic time and multiple-chemical chemotherapy rather than a periodic time and mono-drug course would target the high mutation rates of cancer cells [172] and be less punishing to cells that have the normal very low mutation rates that natural selection favors in the absence of high stress. At present this is based on a rather abstract stochastic resource landscape as is clear from Figure 3.9. Clearly, we will have to design our resource landscape to more closely resemble a solid tumor, with gradients in stress from an outside perimeter, and time-clocked flow of high stress chemotherapy at the perimeter.

CHAPTER 4

SHAPE-CHANGING ACTIVE PARTICLES

The previous two chapters are concerned with active matter in which agents interact with each other through a field with two spatial dimensions. In fact, active matter could also interact with each other through a one-dimensional substrate. Such substrate can be an elastic ring made of plastic [21] or paper[173]. This chapter introduces a type of shape-changing active particle that they can interact with each other through a confining moveable elastic ring. Most results have been published in a journal article [21] I have co-authored.

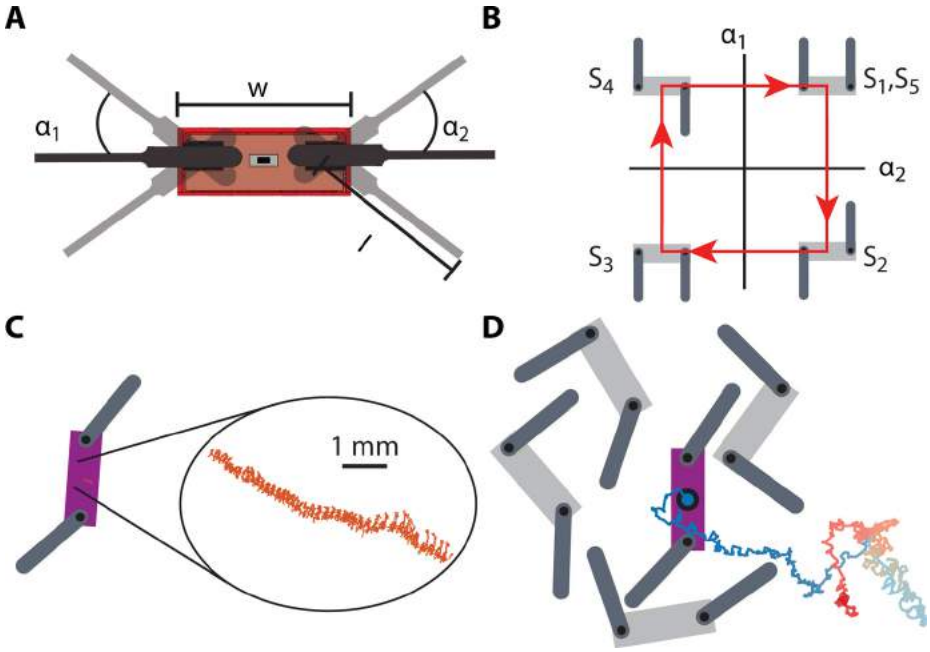

Figure 4.1: **Smarticle robot dynamics.** (A) Top view of a smarticle. (B) Clockwise square gait, with key configurations enumerated. (C) Drift of a single smarticle on a flat surface, executing a square gait over 38. (D) Tracked trajectory of a smarticle within an ensemble of other self-deforming smarticles; color gradient (blue to red) represents passage of time 47τ, with $\tau = 1.6$ s. Reproduced from [21].

4.1 Smarticle, a shape-changing active particle

Inspired by the entanglement of staples[174], William Savoie, a former Ph.D. student in Goldman's group has created a new type of active matter: smarticle, a customized robot that can change its shape between convex and concave configurations. This three-link centimeter-scale robotic object can be pre-programmed so that it will change shape with a particular sequence of maneuvers (gait) as we desire (Figure 4.1B). Bearing the feature of time-depending entanglement, it can move through the interaction with another smarticle, but an individual cannot translate on its own meaningfully(Figure 4.1C).

4.2 Supersmarticle, a collective of shape-changing active particles

To exploit the feature of entanglement, we investigated the behavior of a larger active system composed of these smaller active matter. Having observed that a collective of smarticles would typically disengage with each other after some time (though interesting long-lived pairs may show up depending on initial condition [175, 176]), we tried to use a moveable ring to enclose a few of them to make the interaction sustaining (Figure 4.2A). This ensemble diffuses when all smarticle execute the same gait.

Tracking the supersmarticle's motion for a ring of mass $m = 68$ g revealed no correlation between final angular position between trials (Figure 4.2D). The mean square displacement (MSD) of the ring, $\sigma^2(t) = \langle x^2(t)\rangle - \langle x(t)\rangle^2 \propto t^\gamma$ and γ specifies the type of diffusion the system undergoes. The supersmarticle exhibited different types of diffusion—normal ($0 < \gamma \leq 1$), superdiffusive ($1 < \gamma < 2$), and even approximately ballistic ($\gamma \geq 2$) — depending on the time scale observed. The short time scale regime was consistent with $\gamma = 1$ (Figure 4.2E), indicating normal diffusive motion. The long time scale regimes were best fit with $\gamma \approx 1.45$ representing directionally invariant superdiffusive motion.

Inspired by how cells composed of organelles and tissues composed of cells function, the way individual active matter work together as an ensemble could provide insights into

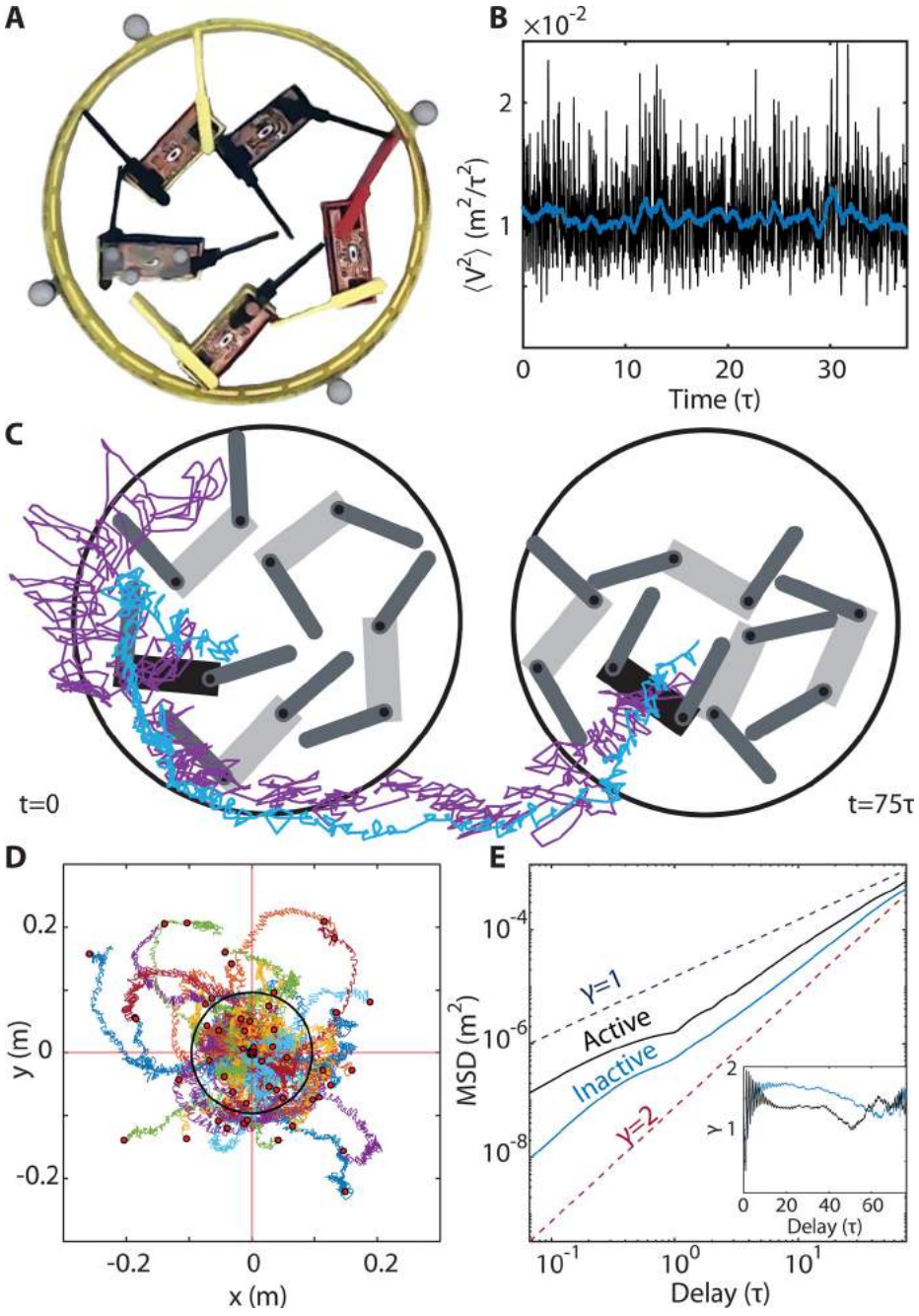

Figure 4.2: **Collective confined diffusion.** (A) Supersmarticle top view; ring inner radius is 9.6 cm. The four gray spheres were used to track the motion of the ring. (B) Granular temperature of five active smarticles confined in a ring; black line is raw data over 10 trials, and blue is a moving window mean with a window size of 1. (C) Trajectories, from an experiment, of a smarticle inside the ring (purple), and the ring's center of geometry (blue). (D) Experimental tracks of ring trajectory for 50 trials; m_{ring} = 68 g. The black circle represents the size and initial position of the ring. (E) MSD averaged over 50 and 80 trials, for the active and inactive systems, respectively, all lasting 75τ. The inset shows the average change of for active (black) and inactive (blue) systems. The oscillation seen in both the MSD and is related to the gait period τ (where $\tau = 1.6$ s). Reproduced from [21].

interesting biological questions such as how the robustness of living systems is achieved when some of the individual malfunction.

Interestingly, when one of the smarticles in the supersmarticle is turned off (inactive), the symmetry breaking leads to a drift of the ensemble. To understand the cause and the feature of this drift, such as how we can vary this drift by tuning the system parameters, I noticed two types of interaction fundamental in this system, being active→inactive→ring (type 1) and active→ring→inactive (type 2) Figure 4.3B.

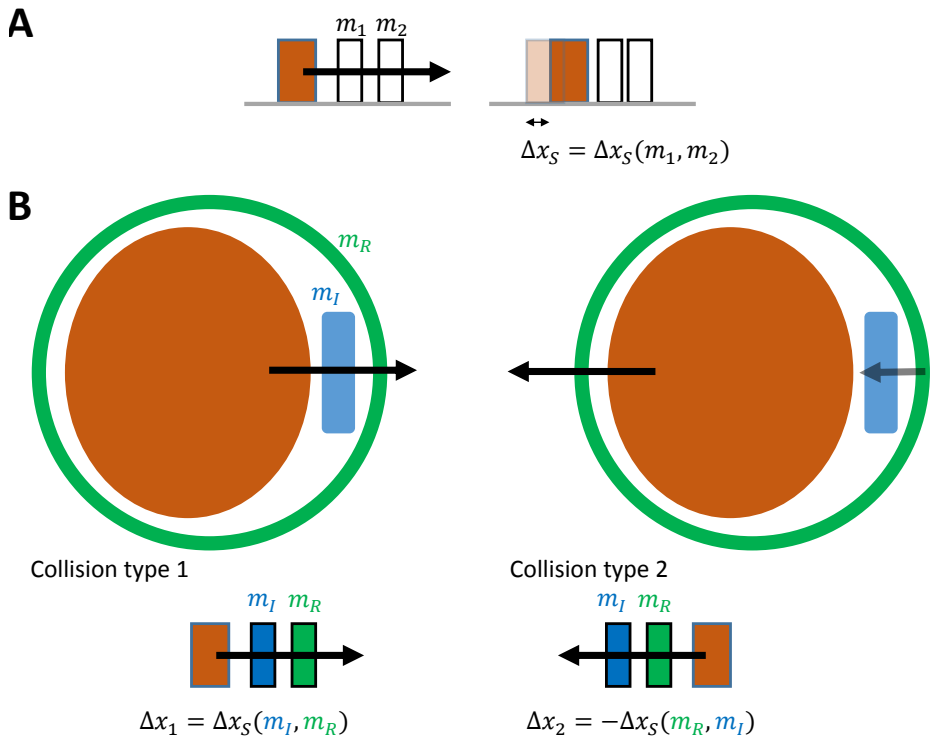

Figure 4.3: **Two basic collision types.** (A) Assume a system composed of three masses will move Δx_S after a collision and Δx_S is a function of the two masses ahead: m_1 and m_2. (B) shows the two basic types of collision. In type 1, the crowd of active smarticles (orange) first hit the inactive smarticle (blue) and then the inactive smarticle hits the ring (green) on the right side. In type 2, the active smarticles first hits the ring on the left side and then the right side of the ring hits the inactive smarticle to the left. The insets below show the corresponding abstract representations and the amount of the system displacement using the assumption in (A).

Before we investigate the interplay of these two types of collision, let us consider a mass M colliding onto two masses m_1 and m_2 in order and denoting the displacement of

the system, for instance denoted by the displacement of M, as Δx_S. Suppose Δx_S only depends on m_1 and m_2 for a particular M that $\Delta x_S = \Delta x_S(m_1, m_2)$, then the displacement of the system for a type 1 collision is $\Delta_1 = \Delta x_S(m_I, m_R)$ and that of a type 2 collision is $\Delta_2 = -\Delta x_S(m_R, m_I)$. Assuming these two types of collisions alternate with a frequency of f, the net velocity would be

$$v_{\text{drift}} = f \cdot (\Delta_1 + \Delta_2) \tag{4.1}$$

$$= f \cdot (\Delta x_S(m_I, m_R) - \Delta x_S(m_R, m_I)) \tag{4.2}$$

$v_{\text{drift}}(m_I, m_R)$ is anti-symmetric with respect to m_I and m_R such that $v_{\text{drift}}(m_a, m_b) = -v_{\text{drift}}(m_b, m_a)$. Therefore, a reversion of the inactive particle mass and the ring mass will cause a flip in the direction of the drift velocity.

Motivated by this, we found this to be true in an experiment with a very light ring, which was a regime we never touched when we first started the experiments with one inactive smarticle due to the manufacturing difficulty by then. This light ring carefully made by foam later proved my conjecture to be true[21].

When trajectories were examined in the frame of the inactive smarticle (Figure 4.4B), the bias in drift toward the inactive smarticle became clear. In Figure 4.4C, the cumulative displacements are shown in the continuously rotating frame attached to the center link of the inactive smarticle such that $S_\parallel = \Sigma_{t=0}^{t} \Delta \vec{s}^{\,i} \cdot \hat{R}_\parallel^i$ and $S_\perp = \Sigma_{t=0}^{t} \Delta \vec{s}^{\,i} \cdot \hat{R}_\perp^i$ where $\Delta \vec{s}^{\,i}$ denotes the vector connecting the center of the ring at consecutive instants in time, and $\hat{R}_\parallel^i, \hat{R}_\perp^i$ are the unit vectors specifying the local frame (Figure 4.4B). As with the fully active supersmarticle, the dynamics of the supersmarticle containing an inactive smarticle were superdiffusive and, at short time scales, approximately ballistic, as indicated by $\gamma \approx 2$. Besides the conceptual model introduced above, a detailed statistical model has shown quantitative match with the experiments.

Inspired by the drift caused by the inactive smarticle, we wondered if we can let the su-

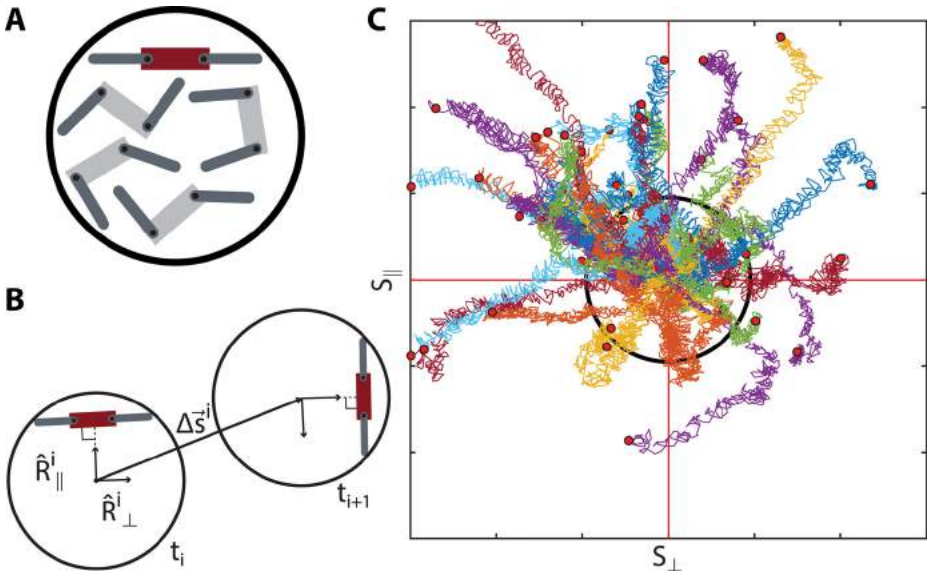

Figure 4.4: **Biasing supersmarticle transport.** (A) Supersmarticle schematic, with the inactive smarticle in red. (B) Supersmarticle trajectory frame transformation from laboratory to inactive smarticle frame. (C) Supersmarticle trajectories rotated into the laboratory frame, where axes are now the perpendicular and parallel components to the frame of the inactive particle. Reproduced from [21].

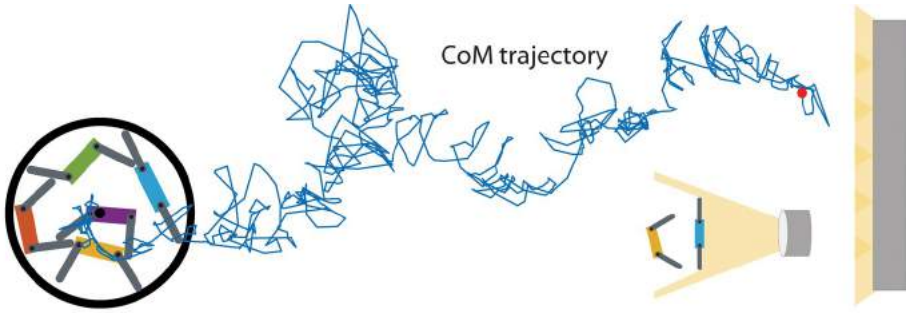

Figure 4.5: **Endogenous supersmarticle phototaxis.** Trajectory from an experiment of a self-directed (endogenously forced) photophilic supersmarticle tracking a static light source). Inset: Schematic showing how a smarticle in the straight configuration can occlude light from smarticle behind it. Reproduced from [21].

persmarticle respond to an external stimuli. In fact, without an external stimuli, the angular position of the inactive smarticle with respect to the ring, which also dictates the direction of the drift, typically migrate over time. Though this happens slowly, the drift direction does change over time without an external control. Therefore, we programmed smarticles to inactivate when light detected from its photosensor exceeded a threshold. When illuminated at low angles (i.e., in the plane of the smarticle light sensors), photoinactivated smarticles occlude light from neighbors further from the source (Figure 4.5A, inset). The inactivated smarticle occludes the light from its neighbors: The straightening and resulting occlusion of light serves as a decentralized and stigmergic directive. The inactive smarticle is affecting the motion of the ring by affecting the motion of the remaining smarticles. This decentralized strategy has been used in previous swarm robotic collectives to generate group movement and transport without requiring explicit communication between agents [177, 178].

4.3 Crawler

Although a single smarticle cannot translate when the two arms are perpendicular to the ground, by placing a single smarticle on its side, the sliding interaction with the ground caused by the shape change can enable locomotion as well[1].

We refer to a smarticle moving in this mode a crawler. Figure 4.6A shows the experiment setup where a crawler is constrained to move in only one direction. Figure 4.6 shows the simulation snapshots of a crawler locomoting on a flat ground. In the simulation, forces and torques are evaluated from normal forces, gravity, and frictions (both static and sliding) as the shape of the crawler is updated with the prescribed gait. The model for normal force uses a spring-dash model where the coefficients for the spring and dash are phenomenonlogically chosen such that the coefficient of restitution is on the magnitude of 10^{-4} as seen in the actual smarticles dropped to the ground. The mass of the center piece of a smarticle

[1]This section and the next section show unpublished works done by William Savoie and me where Will contributed to the experiments and I contributed to the simulation and theory.

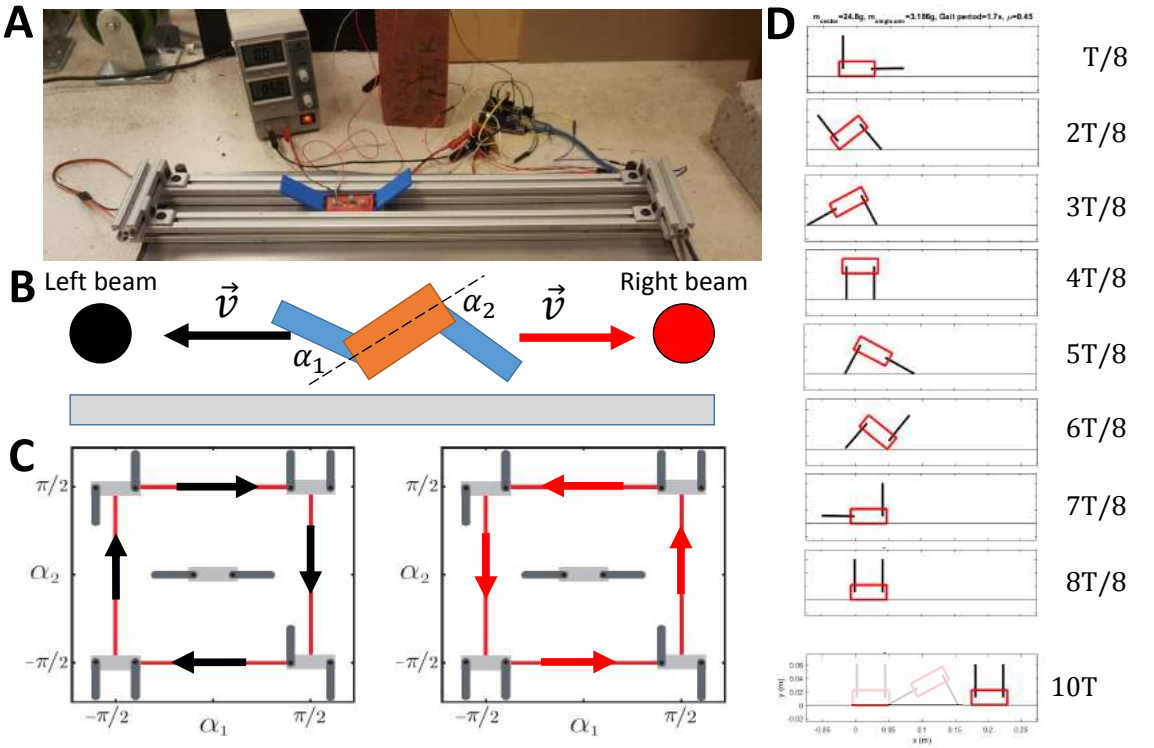

Figure 4.6: **A smarticle can craw when it sits on its side.** (A) A photo of the experiment setup. (B) The crawler moves to the left when executing a clockwise square gait and moves to the right with the same speed when executing a counterclockwise square gait as shown in (C). (D) Snapshots of a simulation where the crawler executes a square gait. T denotes the gait period.

is 24 g; the mass of arm is 3.6 g. The gait period is 1.7 s. The friction coefficient is 0.37.

Different gaits give the crawler different speeds and even different directions of locomotion. For instance, a counterclockwise square gait makes the crawler move to the left while a clockwise gait with the same shape would make it move to the right with the same speed (Figure 4.6B,C). To functionally understand how a gait dictates the locomotion, the framework of Geometric Mechanics (GM) could give us insights[128].

GM is a theory that assumes linear dependence of the body velocity on the velocities in shape space and gives a guidance for optimal trajectory in shape space for the body motion. For instance, in the crawler's case, I have found the body velocity in x direction, ξ^x, linearly depends on the angular speeds of the arms $\dot{\theta}_1, \dot{\theta}_2$ that $\xi^x = \mathbf{A}(\alpha)\dot{\alpha}$ where $\alpha = (\theta_1, \theta_2, 0)^T$ and $\mathbf{A}$ is the local connection (i.e. matrix) between the velocities in shape space and real

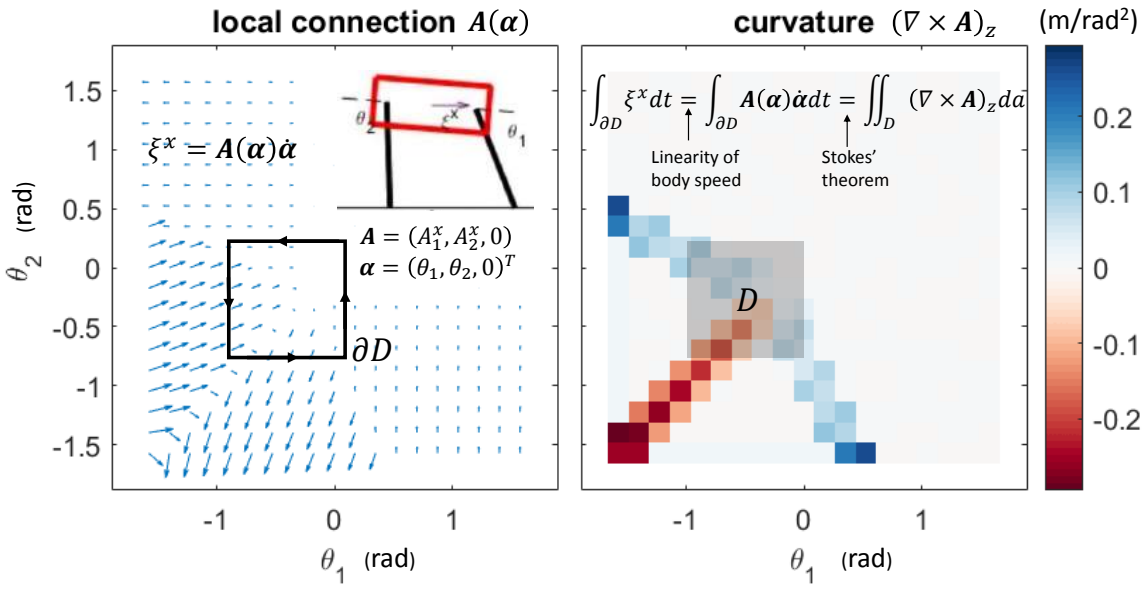

Figure 4.7: **Geometric mechanics of the crawler.** Left: The amount of displacement for a gait ∂D equals to the line integral along the gait on the local connection field $\mathbf{A}$, which is the linear coefficient between the body velocity ξ^x and shape velocities $\dot{\theta}_1, \dot{\theta}_2$. Right: By using Stokes' theorem, the line integral equals to the surface integral of the curl of the local connection field. This can guide one design optimal gaits by enclosing the domain with high curvature.

space. From simulations, I have found this linearity holds up until $\dot{\theta}_i \approx 1$ rad/s, which is considerably higher than the typical angular speed of θ_1, θ_2. The displacement of the body, which is the line integral along the gait ∂D in the connection field can be converted to the surface integral of the curl using Stokes' theorem:

$$\int_{\partial D} \xi^x dt = \int_{\partial D} \mathbf{A}(\alpha)\dot{\alpha} dt = \int_{\partial D} \mathbf{A}(\alpha) d\alpha = \iint_D (\nabla \times \mathbf{A})_z da \tag{4.3}$$

Here, $\xi^x dt$ is the infinitesimal displacement in x direction. Due to the fact that the body velocity in x direction ξ^x linearly depends on the shape velocity $\dot{\alpha} = (\dot{\theta}_1, \dot{\theta}_2, 0)^T$ so that $\xi^x = \mathbf{A}(\alpha)\dot{\alpha}$, we have the first equal sign in the equation above. The third equal sign holds due to the Stokes theorem where $da = d\theta_1 d\theta_2$ is the infinitesimal area in the shape space.

Figure 4.7 shows the connection field and the curl field (also referred to as the 'curvature') for the crawler. We see some high negative curvature concentrates on a diagonal in the third quadrant and high positive curvature somewhat perpendicular to it. The theoretical explanation to these can be found in section B.1 of the appendix. This kind of curvature field is commonly seen in locomotors that change contact states and one can optimized the locomotion using the curvature field with a potential field. See [179] which I have co-authored for details.

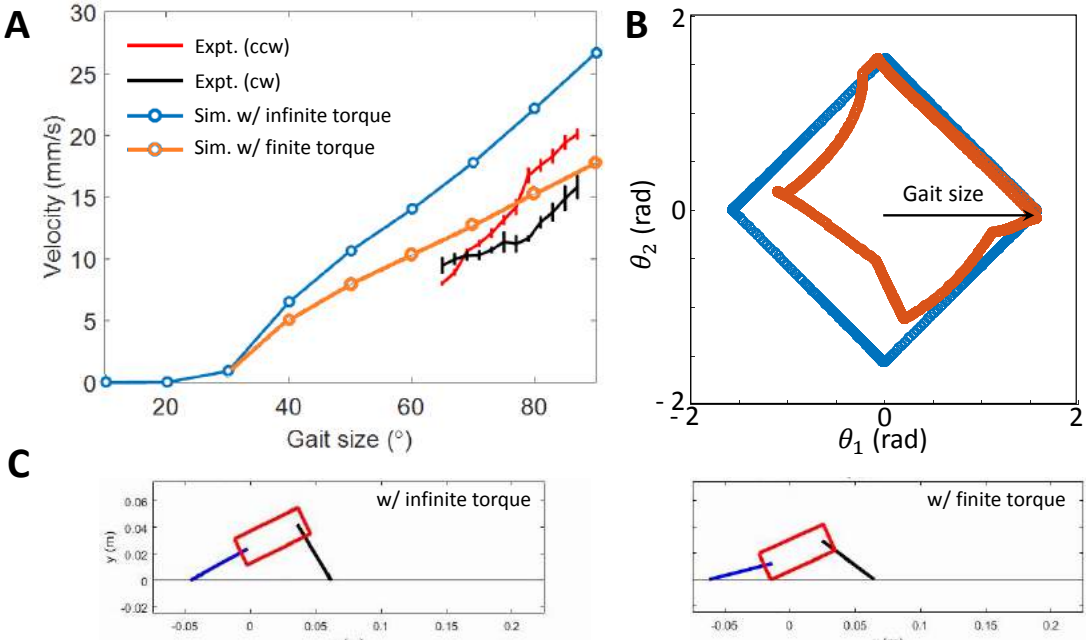

Figure 4.8: **Crawler with realistic finite torque.** (A) Theoretical prediction from GM or simulation (blue) is higher than the experiment results for diamonds gait with different gait sizes. A simulation with a motor having finite torques ($k_P = 240k_{P0}, k_D = 100k_{D0}$) matches better with the experiments. (B) The blue line shows an example diamond gait. The orange line shows the actually executed gait with a 'soft' motor using gain parameters $k_P = 10k_{P0}, k_D = 5k_{D0}$ where k_{P0} and k_{D0} gives the amount of torque that is just able to make the crawler lift itself. (C) The left shows the stance of a crawler when the motor is strong ($k_P = 240k_{P0}, k_D = 100k_{D0}$). The right shows the stance of crawler at the same moment when the motor is weak ($k_P = 10k_{P0}, k_D = 5k_{D0}$).

The blue line in Figure 4.8 shows the theoretical prediction of a diamond gait using the curl field in Figure 4.7 for various of gait size (size of the diamond gait). We then did experiments and found the performance is worse than the simulation and later realized the

finite torque might have played a role. To achieve this in simulation, I implemented a PD (proportional, differential) control for the crawler that the shape angles θ_i has

$$I\ddot{\theta}_i = \tau_{\text{controller}} + \tau_{\text{ground}} \tag{4.4}$$

where

$$\tau_{\text{controller}} = k_P(\Theta_i - \theta_i) + k_D \frac{d(\Theta_i - \theta_i)}{dt} \tag{4.5}$$

Here, Θ_i is the desired position prescribed by the gait for the ith joint and varies with time, whereas θ_i is the actually executed joint angle. τ_{ground} includes all the torques from the ground when we introduce the simulation at the beginning of this section.

When we choose the gain parameters (k_P and k_D) small, the crawler looks 'softer' (see the right figure of Figure 4.8C) than in the case where the gain parameters are larger. For some fitted gain parameters ($k_P = 240k_{P0}, k_D = 100k_{D0}$), the simulation can reproduce what we observe in experiments (Figure 4.8).

4.4 Smarticle train

In the early stage to find a simple model for supersmarticle, Will and I developed a one-dimensional mechanical model to study the motion of a moveable confinement enclosing shape-changing active particles. The model, i.e., the smarticle train, is composed of two shape-changing particles that can slide freely in a long linear moveable rectangular frame (Figure 4.9A, B). Each active particle inside the frame is a block with a harmonically-oscillating shaft, and we will refer them to the oscillators later. Although these active particles are not exactly the smarticle, this model might give us some intuition about a confinement with shape-changing particles inside.

In experiments, to restrict the motion only in one dimension, we used a ruler to confine the rectangular frame. One of the most interesting parameters in this system is the phase

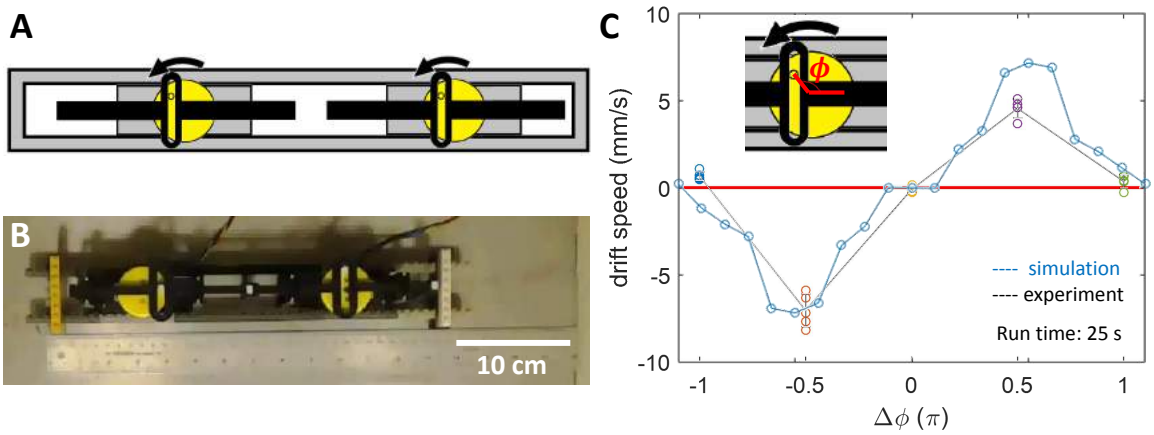

Figure 4.9: **Smarticle train.** (A) A sketch of the smarticle train (top view). (B) The smarticle train for experiment (top view). (C) The drift velocity as a function of the phase difference between the two oscillators $\Delta\phi = \phi_1 - \phi_2$ where the inset shows the phase ϕ of an individual oscillator. Credits to William Savoie for panels A and B.

difference between the two physically identical oscillators. The harmonic oscillation of the shaft on each oscillator is realized by the circular motion of a knob on a motor (Figure 4.9A and C inset). Therefore we use the rotation angle ϕ of the knob as the phase. We are curious how the motion of the smarticle train depends on the phase lag between the two phases $\Delta\phi = \phi_1 - \phi_2$. From the symmetry point of view, the rectangular frame should have no net motion since the two oscillators are moving symmetrically.

We also use this case as a calibration method in experiments to ensure there is no significant systematic error so that any drift for other $\Delta\phi$ will be convincing. We calibrated the system such that $\Delta\phi = 0$ will give us zero motion. We found that there were indeed net motions for general phase lags from experiments. The motion is antisymmetric about $\Delta\phi = 0$ and is zeros for $\Delta\phi = -\pi, \pi$, which are modes where the two oscillators move in phase.

To obtain some preliminary understanding, I performed simulations by integrating the interactions, including the oscillator-oscillator contact force, oscillator-frame contact force, and the ground-oscillator friction. The physical parameters were directly measured from experiments: The mass of each oscillator is 124 ± 2 g. The static and kinetic friction coefficients are 0.433 ± 0.018 and 0.374 ± 0.008, respectively. I used the spring-dash model

for the contact forces. The coefficients for the spring and dash are phenomenological that the coefficient of restitution is on the magnitude of 10^{-4}, and we posit the result should be largely irrelevant to the details of the contact model. The result matches the experiments (Figure 4.9C).

The result of the motion's dependence on phase is interesting in many aspects. First, this complements our study of supersmarticle in section 4.2 where all particles are started with the same phase. This complementary result on phase poses interesting questions such as if there are collective behavior emerging from some particular phase configuration and if we can utilize it. Secondly, considering the fact that an object cannot locomote when the friction is isotropic[180, 179], that the smarticle train can translate should be caused by the inertia effect. It will be interesting to see how the speed would qualitatively change the ability to move for an ensemble composed of shape-changing particles.

CHAPTER 5

LOCOMOTION OF SHAPE-CHANGING ACTIVE MATTER IN CURVED SPACE

5.1 Locomotion in flat and curved spaces

Curved surfaces are ubiquitous in physics, biology, engineering and mathematics but are defined by features that defy intuitions derived from flat space. For example, on a spherical surface the square of the hypotenuse is not the sum of the squares of the legs and "parallel" lines meet at the poles and the sum of the interior angles of a triangle grows with the triangle's area. Recently, the inability to form periodic crystals on spherical surfaces [181, 182] has given rise to lively dynamics of essential crystalline defects [183, 184]. And, of course, gravitational interactions themselves are derived from the fundamental curvature of four-dimensional spacetime [185] leading to explanations of dynamics such as precessing orbit of Mercury and gravitational lensing of light [1].

Less well known is the fact that curved surfaces permit locomotors embedded within them to self propel via translation without exchanging momentum with an environment [186, 187, 188] (as is done in swimming, flying and running in typical environments). How can this be? Consider, in particular, the prototypical swimmer confined to (or embedded within) the spherical surface depicted in Figure 5.1(a). By propelling masses along the vertical arms, the component of the moment of inertia that relates torque and momentum about the longitudinal axis can be altered, analogous to a process in flat space that somehow altered the mass of an object. By propelling an additional mass along the latitudinal arm on the sphere, angular momentum may be exchanged between this mass and the others during periods in which the robot has different moments of inertia. By pushing itself in one direction when it has low moment of inertia and the other when it has high, the robot

[1] This subsection is adapted from a co-first-authored arXiv preprint 'Locomotion without force, and impulse via dissipation: Robotic swimming in curved space via geometric phase' (2112.09740)

may attain a net movement in the first direction, even as the total robot structure maintains zero angular momentum. This is analogous to a falling cat, which instinctively exchanges angular momentum between different parts of its body while contorting itself to alter its moment of inertia.

This process relates to fundamental geometric properties: Whereas a flat plane is invariant under two translations and a rotation, leading to a two-dimensional conserved linear momentum and a one-dimensional conserved angular momentum, a spherical surface is invariant under the three rigid-body rotations of SO(3), leading to a conserved three-dimensional angular momentum. Crucially, these motions, which may be thought of as translations along the sphere, do not commute with each other as do translations in flat space. Consequently, when a robot changes its shape on a sphere as shown in Figure 5.1(a), it induces a series of incommensurate motions, so that a closed cycle of shapes induces a net displacement along the sphere, analogous to the rotation achieved by a falling cat.

This behavior is an example of a broader phenomenon in physics, in which dynamically varying patterns can induce a physical transformation known as a *geometric phase*. Geometric phase plays a crucial role in modern physics, from the general-relativistic curvature of spacetime that establishes closed orbits of planets around stars to the Berry curvature that underlies quantum-mechanical effects in graphene, topological insulators and cyclotron motion. And geometric phase even appears in locomotion. As pointed out by Shapere and Wilczek [189] and developed and applied over the past decades [190, 191, 128, 192, 193, 194] geometric phase describes how a self-deforming body locomotes in response to drag forces from viscous and frictional fluids to dry friction.

Here we demonstrate experimentally for the first time geometric phase driving dynamics solely induced by the curvature of space, resulting in self-propulsion without environmental force exchange. We do this by converting the abstract picture of the ideal spherical surface swimmer mentioned above to a precision robophysical model. The device's self-propulsion is determined by the geometrical phase induced by its shape changes as it slides

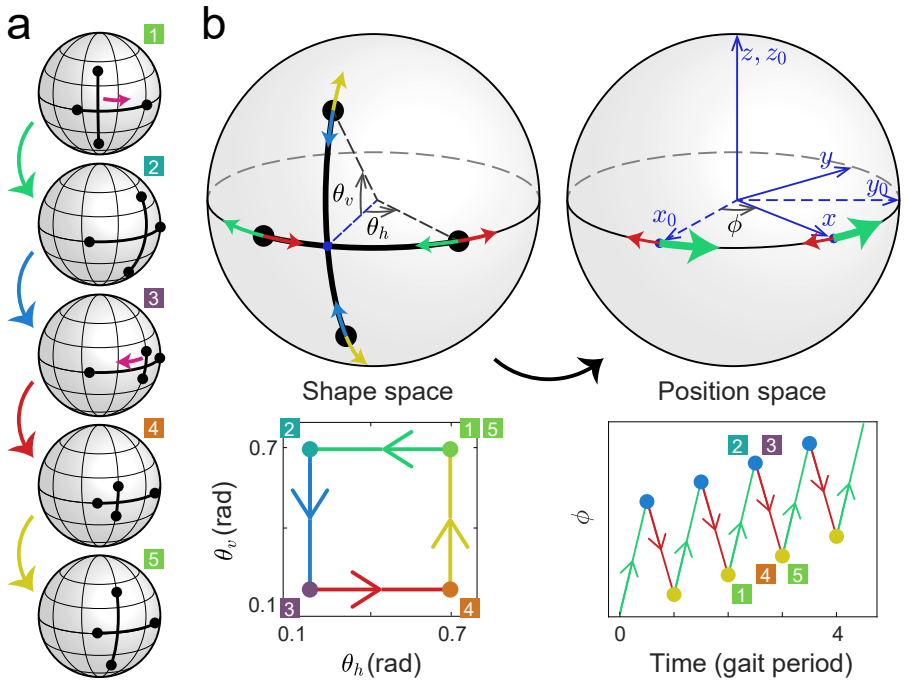

Figure 5.1: **Self-propulsion without reaction forces.** (a) A robot confined to a spherical surface executes a cyclic change of shape to generate net position change. (b) The cyclic change of shape described by the angles θ_h, θ_v of motorized weights (black dots) follows an order indicated by the gait diagram below. Due to the variable moment of inertia and the non-commutivity of these operations, this leads to a net change in the robot's position, represented by the rotation $\phi(t)$ applied to the coordinate axes in position space, even in the absence of momentum or external forces. The plot below shows the time evolution of $\phi(t)$ from each stroke of the gait shown in the same color as the gait diagram.

motorized masses along curved tracks. Further, under complex dissipative coupling to the environment, this geometric propulsion couples to friction in surprising ways, preventing decay into energy minima and capturing a finite-momentum state in a fixed position.

5.2 Ideal swimming

Testing the idea that self propulsion can occur in curved environments without forces requires confining the robophysical model to a curved surface while achieving control over its environmental coupling. While experiments often occur in flat planes whose dynamics approximate that of an ideal Euclidean plane, capturing the essence of a sphere is more challenging. In particular, no widely available method exists for placing particles on a

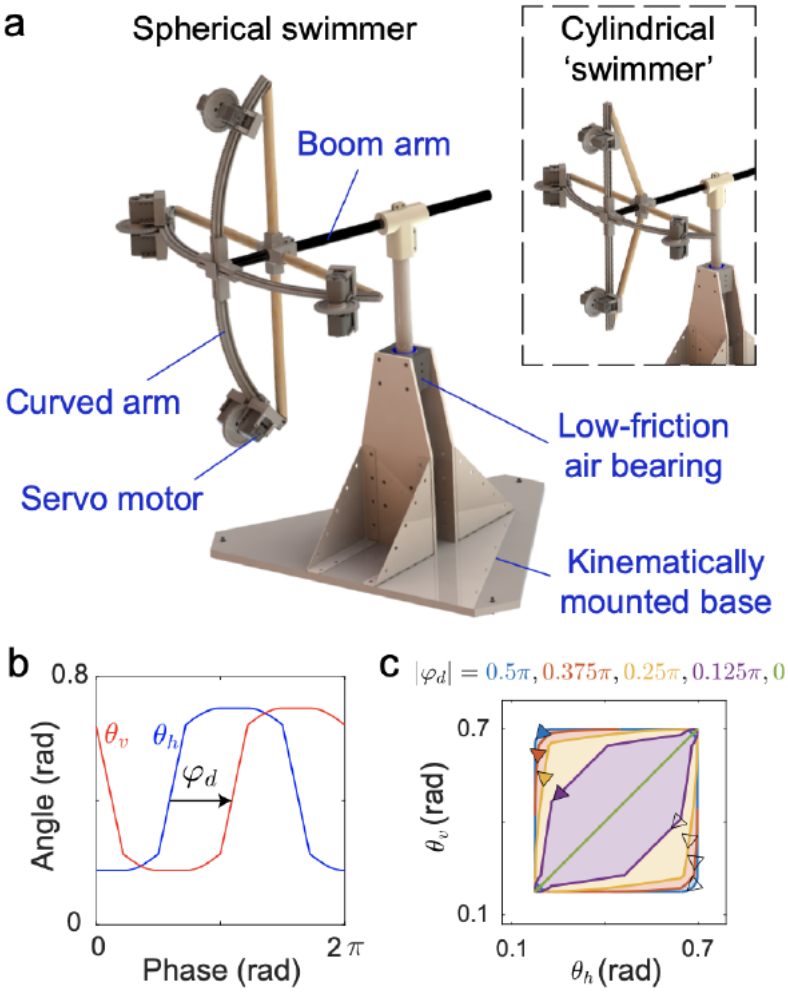

Figure 5.2: **Robophysical curved space swimmer.** (a) The experimental apparatus, rendered here schematically, confines the robot's active masses to a geometric (but not material) spherical surface of radius 46 cm via 3D-printed curved tracks along which servo motors (116 g for each of the four motors) propel masses of themselves and the tracks (388 g). The robot is free to rotate about a central pivot with a low-friction air bearing and mounted on a kinematically adjustable base used to minimize the torque induced by gravity. In contrast, the upper-right inset depicts a robot that, due to the straight arms, is confined to a cylindrical surface along which no corresponding motion can be induced via swimming. The lower-left inset shows the coupling between a motor and a curved track. (b) A phase difference φ_d between the robot's horizontal and vertical strokes breaks time-reversal and spatial inversion symmetry, as required for forward swimming. (c) The displacement of the robot per stroke, in the absence of external forces, is obtained as an integral of geometric phase over the shaded regions enclosed by the gaits in shape space. Credits to Tianyu Wang and Velin H. Kojouharov.

solid spherical shell while simultaneously minimizing both the effect of gravity (which would drive particles towards the bottom of the sphere) and friction (which would prevent

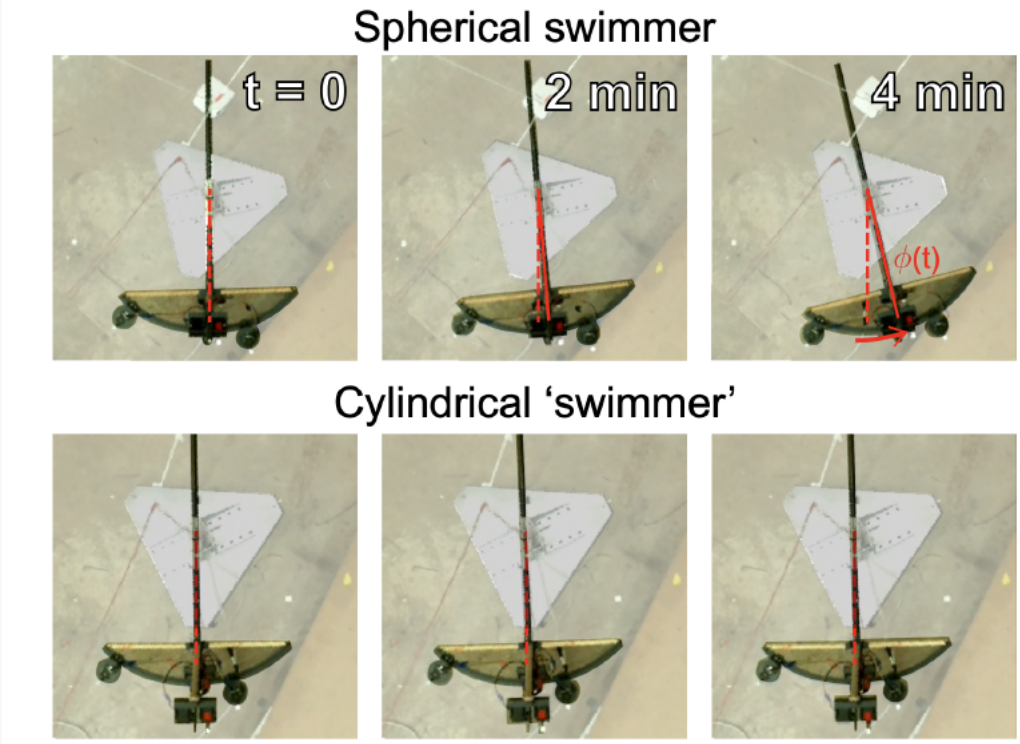

Figure 5.3: **Chronological snapshots of the spherical swimmer and the cylindrical 'swimmer'.** These snapshots show the swimming of the former is significant while the latter is vanishingly small. See the red trajectory in Figure 5.4, Figure 5.8(a) for the displacement over time.

us from isolating the novel curvature-induced motion from more conventional effects). Instead, we opt for a solution in which we attach the robot to a rigid boom arm free only to rotate about the vertical axis shown in Figure 5.2(a).

Masses are robotically propelled along curved tracks whose radius coincides with the length of the boom arm, ensuring that the robot's mass is confined to a spherical surface. The constraint of the boom arm ensures that all forces/torques would move the robot vertically or radially are negated, while freely permitting horizontal direction along the spherical surface. Consequently, the dynamics of the apparatus is well-described by that of an ideal sphere. Notably, the robot's ability to move does not violate the usual rule against movement without forces in three-dimensional space because the full three-dimensional dynamics in fact include normal forces on the robot supplied by the boom arm that confines it to the sphere.

This arrangement is achieved via precision servo motors connected to gears that move without slipping on the robot's 3D-printed toothed tracks that can be generated with arbitrary curvature profile. The tracks are connected to the central shaft, which rotates in air bushings with low friction. The base of the system is fixed on the hard ground via kinematic mount, which constrains motion of the base.

We control the motors' positions on the tracks to prescribe a "gait": a closed path in shape space parameterized by the position of the motor positions in horizontal (θ_h) and vertical (θ_v) directions, as shown in Figure 5.1(b). The swimmer is constrained to move angularly by the beam arm [Figure 5.2(a)]. This design can minimize environmental forces due to friction and gravity, although we also demonstrate that these couple to the geometric phase to generate additional exotic phenomena.

We test whether self-deformation in the presence of curvature can generate locomotion without significant environmental forces. We place the robot on the equator of the sphere and, for simplicity, restrict ourselves to shapes that are symmetrical under reflections across the equator. Such shape changes, combined with the apparatus design, constrain the robot to translate along the equator—i.e. to rotate about the north pole. The smooth trajectory through shape space, designed to minimize jerks and maximize motion, is shown in Figure 5.1(b).

In our primary result, as predicted by Wisdom [186] and indicated in Figure 5.1(a), the persistent cycling through shape space shown in Figure 5.2(b,c) leads the robot to translate back and forth, yet the effect of Gaussian (intrinsic) curvature permits a relatively small net motion [Figure 5.4(b)] which depends on the direction of the cycle in the configuration space. And, as predicted, because force-free propulsion relies on this curvature of the doubly-curved sphere, a robot confined to a singly-curved cylindrical surface [inset of Figure 5.2(a)] does not exhibit this propulsion [Figure 5.4(b) and Figure 5.8(a) inset]. Further, in contrast to Wisdom's force-free model, the robotic swimmer's motion saturates at a finite displacement, per Figure 5.8(a)'s main panel.

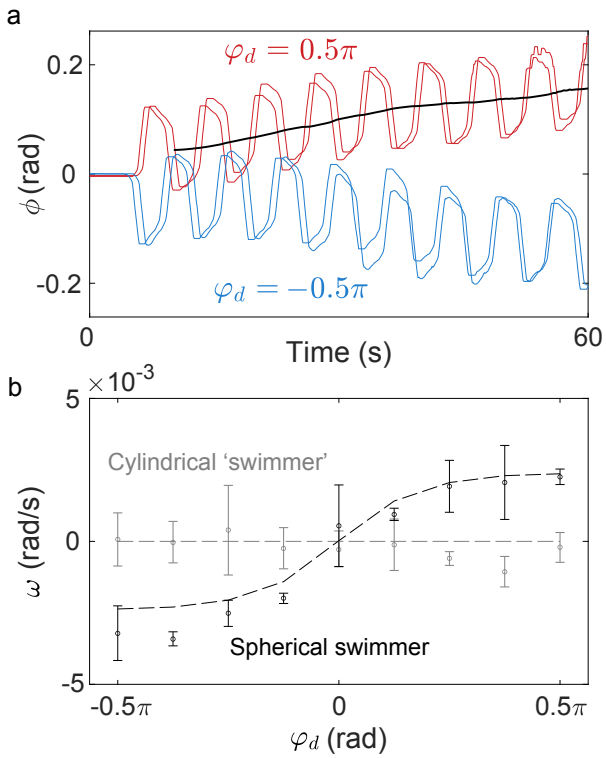

Figure 5.4: **Self propulsion via geometric phase.** (a) The robot, initially at rest, swims forward with an average initial angular velocity $\omega_i = \dot{\bar{\phi}}$ over the course of several strokes. The black thick line shows the time-averaged position $\bar{\phi}$. (b) The observed initial velocities match those predicted from the geometric phase, ω_g, (dashed lines) with variable gait controlling the speed and direction of the robot swimming on the sphere, in contrast to the robot on the cylinder, which cannot achieve significant net movement.

5.3 Realistic swimming

While we have now realized force-free swimming, as occurs over short times in Figure 5.4(a), the robophysical testing reveal more complex phenomena resulting from the interplay between this geometric phase and environmental effects, as in Figure 5.8(a).

5.3.1 Friction

To characterize and measure the friction, we tracked the decay rate of angular velocity as shown in Figure 5.5a. Figure 5.5b, an example of such experiment, shows the instantaneous decay rate a_C as a function of the angular velocity $\dot{\phi}$. We note that it is reasonably anti-symmetric about zero, giving a symmetric friction status such that the possible ratchet

effect, which could introduce unwanted swimming, is nominal. When reporting the friction in the main text, we use the acceleration evaluated for the range of angular velocity between 0.175 rad/s and 0.035 rad/s, which is the typical range of angular velocity in the swimmer's experiments. To average out the possible slight gravity residue effect, we performed experiments at 5 different azimuthal positions evenly spaced in $(0, 2\pi)$. To avoid the ratchet effect, we only performed swimmer experiments when the discrepancy of friction between the clockwise and counterclockwise value is less than 10 %.

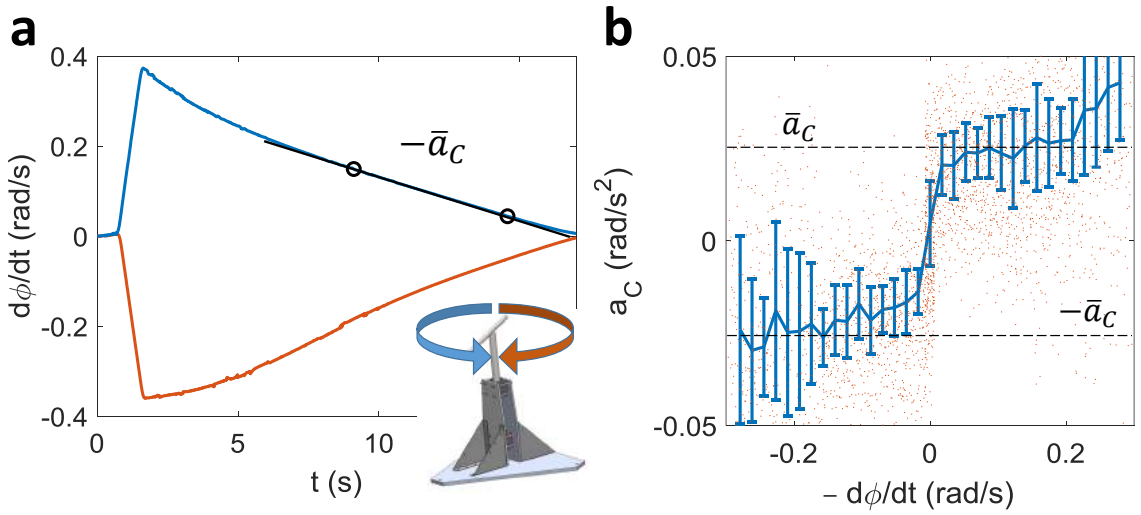

Figure 5.5: **Friction characterization.** (a) The decay of angular velocity $\dot{\phi}$ over time in experiment. (b) Angular acceleration over $\dot{\phi}$. The orange dots show the raw data. The blue error bars show the median and the middle quartiles of the binned data.

To convert the acceleration to the torque from friction τ_C, we multiply the average acceleration magnitude $\bar{a}_C$ by the total moment of inertia of the swimmer $I_0 = m_s R^2$ where m_s, R are the mass and the radius of the swimmer, respectively.

5.3.2 Residual potential

Since the gravity potential well from the slight tilting of the equator is so shallow that direct measurement from devices such as bubble meter or optic tracking does not have sufficient resolution due to possible error from the mounting of trackers, we infer its depth using the long oscillation period resulted from it.

Particularly, we perform a very long null gait in which only the horizontal motor moves. The averaged ϕ (i.e., the envelope $\bar{\phi}$) is given by Eq. (4) in the main text as

$$\langle I^{(0)}\rangle\ddot{\bar{\phi}} = -\frac{4\tau_C\langle I^{(0)}\rangle}{T|\ddot{\alpha}|}\left[\dot{\bar{\phi}} - \omega_g\right] - \tau_g\bar{\phi}. \tag{5.1}$$

where $\omega_g = 0$ since there is no geometric phase enclosed. Given that the moment of inertia is fixed as $I_0 = m_s R^2$ in the null gait and $\alpha = 2m_v R^2\theta_h$, the equation for the long-time envelope is, therefore

$$I_0\ddot{\bar{\phi}} = -\frac{2\tau_C m_s}{Tm_v|\ddot{\theta}_h|}\dot{\bar{\phi}} - \tau_g\bar{\phi}. \tag{5.2}$$

When τ_C is relatively small, the oscillation period of $\bar{\phi}$, T_{env}, is approximately $(2\pi/T_{\text{env}})^2 = \tau_g/I_0$ where $\tau_g = m_s g R\sin\theta_g$ and $I_0 = m_s R^2$. This implies

$$\theta_g \approx \sin\theta_g = \frac{R}{g}\left(\frac{2\pi}{T_{\text{env}}}\right)^2. \tag{5.3}$$

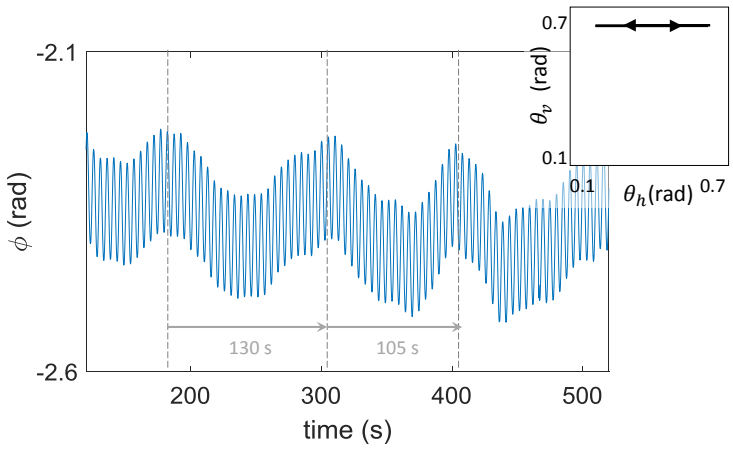

Figure 5.6: **Inferring the gravity residue.** The residual gravity angle is inferred from the long-time envelope of a null gait experiment with small friction ($\tau = 0.003$ kg m^2 s^{-2}).

With $R = 0.46$ m, from an experiment with null gait and small friction $\tau = 0.003$

kg m^2 s^{-2}, we can see the period of the envelope T_{env} is about 120 s and thus inferring a residual gravity of $\theta_g = 1.2 \times 10^{-4}$ rad.

5.3.3 Dynamics at long-time scale

We now develop an analytical theory and use numerical simulation to rationalize these results.

The total angular momentum of the swimmer is composed of three parts: the contribution from the vertical motors, the horizontal motors, and the track system supporting the motors together with the supporting rod.

$$\begin{aligned} L &= L_{\text{vertical}} + L_{\text{horizontal}} + L_{\text{track}} && (5.4) \\ &= 2m_v R^2 \cos^2\theta_v \dot{\phi} + 2m_h R^2(\dot{\theta}_h + \dot{\phi}) + I_{\text{track}}\dot{\phi} && (5.5) \end{aligned}$$

If we collect the terms with $\dot{\phi}$ together, we have (following the "shape dynamics" section of the Methods)

$$L = I\dot{\phi} + \dot{\alpha} \tag{5.6}$$

where now

$$\begin{aligned} I(t) &= 2m_v R^2 \cos^2\theta_v(t) + 2m_h R^2 + I_{track} R^2, && (5.7) \\ \alpha(t) &= 2m_h R^2 \theta_h(t). && (5.8) \end{aligned}$$

The torque that changes the angular momentum is composed of two parts, being the

contribution from the slight residual gravity and Coulomb friction.

$$\frac{dL}{dt} = \tau = A_g + A_C \tag{5.9}$$

The force from the residual gravity is caused by the mass of the swimmer on the equator, which normal slightly misaligns with the direction of Earth's gravity with an angle of θ_g. The residual gravity potential contributed by the two horizontal motors, two vertical motors, and the track compose a total residual potential energy of $V = -(2m_v + 2m_h + m_{\text{track}})gR\sin\theta_g\cos(\phi - \phi_0)$. This leads to a torque of

$$A_g = -\partial V/\partial\phi = -(2m_v + 2m_h + m_{\text{track}})gR\sin\theta_g\sin(\phi - \phi_0) \tag{5.10}$$

where ϕ_0 is the azimuthal position with the lowest potential energy. Without loss of generality, we set $\phi_0 = 0$ so the torque from gravity and assume ϕ is small and finally arrive at $A_g = -\tau_g\phi$ where $\tau_g = m_s gR\sin\theta_g$ where $m_s = 2m_v + 2m_h + m_{\text{track}}$.

The torque from friction has a constant magnitude τ_C and a direction opposite to the angular velocity so

$$M_C = -\tau_C \text{sgn}(\dot{\phi}) \tag{5.11}$$

Piecing all above, we have the equation of motion as

$$L = I\dot{\phi} + \dot{\alpha} \tag{5.12}$$

$$\dot{L} = -\tau_C \text{sgn}\dot{\phi} - \tau_g\phi \tag{5.13}$$

where $\tau_g = (2m_v + 2m_h + m_{\text{track}})gR\sin\theta_g$.

After some simplification, we have the simplified equation for the equatorial spherical

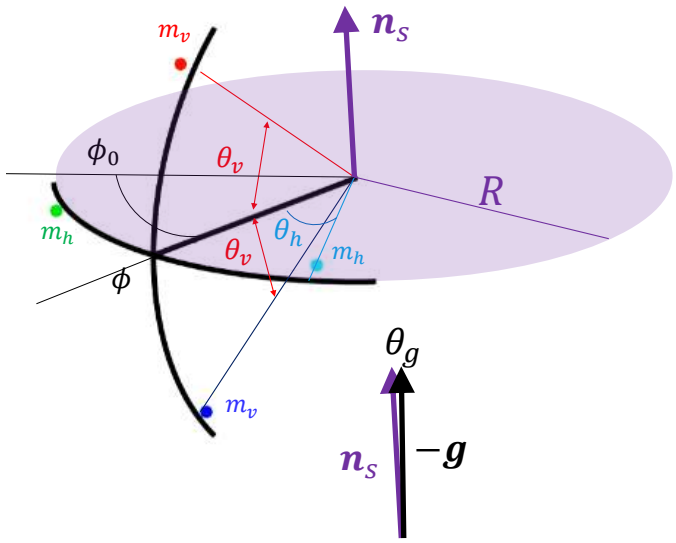

Figure 5.7: **Setup of the swimmer.** The swimmer with two horizontal motors (each with mass m_h) and two vertical motors (each with mass m_v) rotates about $\mathbf{n}_s$, the normal of the equator shown as the light purple plate. The position of the swimmer, ϕ, the azimuthal angle of the beam arm connecting the center and the curved track arms, evolves as the positions of the motors (θ_h, θ_v) move. Ideally, the normal of the equator $\mathbf{n}_s$ should be aligned with the opposite direction of gravity $-\mathbf{g}$. In realistic experiment, we characterize the small residual gravity by the angle θ_g ($\sim 10^{-4}$ rad) between $\mathbf{n}_s$ and $-\mathbf{g}$. We denote the minimal position of the gravity potential as ϕ_0.

swimmer to the scalar associations between the angular velocity, angular momentum and torque about the vertical axis:

$$\dot{\phi}(t) = \frac{L(t) - \dot{\alpha}(t)}{I(t)}, \tag{5.14a}$$

$$\dot{L}(t) = \tau(\phi, \dot{\phi}) = -\tau_C \operatorname{sgn}\dot{\phi} - \tau_g \phi. \tag{5.14b}$$

The moment of inertia $I(t)$ and the internal effective angular momentum $\dot{\alpha}(t)$ (the angular momentum induced by the shape change that the robot would have for $\dot{\phi} = 0$) both depend on time with period T via the shape-change gait. The torques due to friction and gravity are measured, rather than left as free model parameters, in additional experiments

as described in Secs. 4,5 of the Supplementary Information.

As a consequence of the dynamics of Eq. (Equation 5.14), even when angular momentum and torque vanish, the robot's gait causes it to advance at an average angular velocity

$$\omega_g = \frac{\Delta\phi}{T} = -\frac{1}{T}\int_0^T I^{-1}(t)\dot{\alpha}(t)dt = -\frac{1}{T}\oint \frac{d\alpha}{I}. \tag{5.15}$$

The final expression reflects the *geometric* nature of this movement as a Berry phase that depends on the path through shape space but not on the rate at which it is traversed.

As posited in Figure 5.1 and shown in Figure 5.4(a), in the absence of additional forces, a robot initially at rest would, upon initiating a particular series of shape changes, rotate around the equator of its spherical universe at a rate described by Eq. (Equation 5.15), a behavior analogous to the general-relativistic formulation of Wisdom [186]. Instead, we address the complex coupling between this geometrical phase and the robot's coupling to its environment reflected in the torques of Eq. (Equation 5.14).

Perhaps surprisingly, while the geometric phase is evaluated via a nonlinear numerical integration and the Coulomb friction is highly nonlinear, the interplay between the two can be treated analytically. This process, shown in the 'Two diverging friction models' section of the Methods section is done in the *rotating wave approximation* in which, drawing inspiration from techniques developed in optical physics [195] we decouple the rapid oscillations of the robot from the weaker influences of external torques:

$$\langle I^{(0)}\rangle\ddot{\bar{\phi}} = -\frac{4\tau_C\langle I^{(0)}\rangle}{T|\ddot{\alpha}|}\left[\dot{\bar{\phi}} - \omega_g\right] - \tau_g\bar{\phi}. \tag{5.16}$$

$$\dot{L} = -\frac{4\tau_C}{T|\ddot{\alpha}|}L - \tau_g\bar{\phi}. \tag{5.17}$$

Here, $\bar{\phi}(t)$ is the time-averaged position, removing the rapid, high-amplitude oscillations

due to the gait motion, as shown in Figs. Figure 5.4(a), Figure 5.8. $\langle I^{(0)} \rangle$ is the inverse of the time-averaging of the inverse moment of inertia. $\ddot{\alpha}$ is the rate of change of the internal angular momentum at the time in the gait at which it vanishes. This linear approximation relies on the smallness of the external angular momentum L relative to the internal angular momentum $\dot{\alpha}$ For larger angular momenta, higher-order terms become relevant.

We thus arrive at the effective dynamics of the curvature swimmer. Provided that the external torque does not vary significantly within a single stroke and the system remains in the linear force regime, the system attains an emergent form of the viscously damped linear harmonic oscillation, despite the nonlinearity of the Coulomb friction. The most striking feature is the uniform force field, proportional to both the geometric phase and the Coulomb friction. The periodic shape changes are reminiscent of a Floquet theory, yet the combination of a time-dependent force with a time-dependent inertia permits net forward motion.

The *low-torque* regime occurs when the swimmer, initially at the bottom of a shallow energy well engaged in a neutral swimming motion (which does not lead to self propulsion but maintains continuous self-deformation to prevent static friction), shifts into a forward swimming motion, as shown in Figure 5.8(a). The robot's motors drive its masses around the spherical surface in the trajectory shown in Figure 5.2(b). The parameter φ_d controls the offset between the motions of the horizontal and vertical arms, which is crucial to break time-reversal and spatial-inversion symmetries, as is necessary for a swimming gait. Here we refer to a gait with nonzero φ_d and thus nonzero swimming as a swimming gait and refer to a gait with zero φ_d as a null gait. The geometric phase ω_g is shown in Figure 5.4. Over short periods, the forces effect only a small change in the swimmer's momentum while the swimmer nevertheless advances at a measured initial angular rate $\omega_i = \dot{\tilde{\phi}}(0)$. As seen in Figure 5.4(b), the rate predicted (dashed line) by the calculated geometric phase ω_g (i.e., $\omega_i = \omega_g$) is in agreement with the observed initial rate, providing strong validation of the geometric theory.

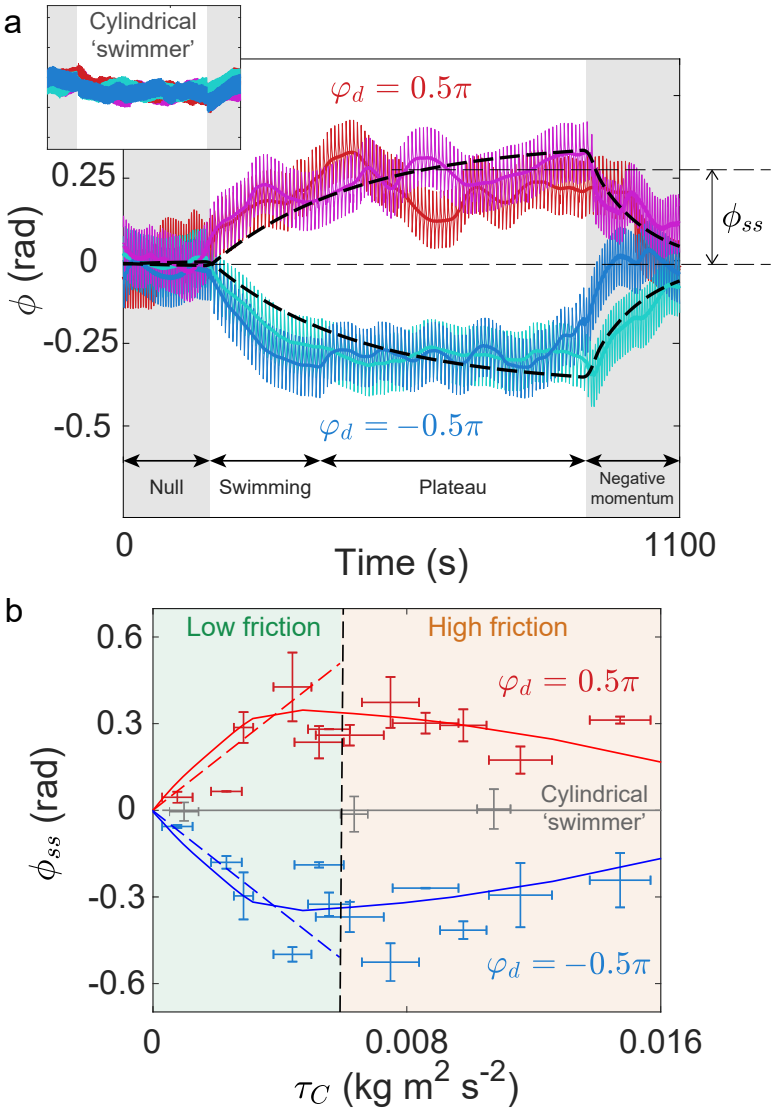

Figure 5.8: **Geometric swimming in the presence of environmental effects.** (a) Evolution of $\phi(t)$ of curved swimmer and cylindrical non-swimmer (inset) for Coulomb friction $\tau_C = 3.4 \times 10^{-3}$ kg m^2/s^2 and different φ_d's. There are two trials for each φ_d. (b) The steady-state plateau ϕ_{ss} as a function of τ_C. The dots with error bars, solid lines show the experiment and simulation [Eq. (Equation 5.14)] respectively. To understand how the plateau increases with small friction ($\tau_C < |\ddot{\alpha}|$), we show the first-order theory (Eq.Equation 5.18) with dashed lines until around the predicted cutoff friction ($\tau_C = |\ddot{\alpha}|$).

Over longer times, additional vibrations, resonances and nonlinearities preclude quantitative agreement between experiment and theory, yet qualitative agreement is nevertheless

observed throughout the trajectory in Figure 5.8(a). These trajectories contain a surprising feature: unlike the typical behavior of dissipative systems in flat space, the curvature drives the swimmer to plateau at a finite offset from the bottom of its potential well. The geometric theory of Eq. (Equation 5.16) predicts $\tau(\bar{\phi}_{ss}) = \frac{4\tau_C\langle I^{(0)}\rangle}{T|\ddot{\alpha}|}\omega_g$ and leads to a steady-state plateau of

$$\bar{\phi}_{ss} = \frac{4\tau_C\langle I^{(0)}\rangle}{\tau_g T|\ddot{\alpha}|}\omega_g. \tag{5.18}$$

This prediction of linear dependence between plateau height and friction strength is observed at low friction strength, as shown in Figure 5.8(b) and levels off at approximately the amount friction strength predicted by theory, which is $|\ddot{\alpha}|$.

The trajectory in Figure 5.8(a) naively suggests that the swimmer begins with a finite momentum that falls to zero as its position plateaues. As our analysis reveals, the reverse is true: at the beginning of the swimmer's journey, when its velocity is greatest, it lacks momentum. In contrast, once its average velocity in one direction vanishes, the momentum is maximal and points in the opposite direction. Because the swimmer advances without momentum the dissipative forces that arrest the swimmer's forward progress also impart an impulse that leaves it with nonzero momentum. To illustrate this, in Figure 5.8(a), Figure 5.9, we suspend the swimmer's forward stroke, replacing it with a null gait to prevent static friction. At this moment, normal classical physics, in which momentum and velocity are in proportion to one another, reasserts itself and the swimmer's negative momentum causes it to swing backwards towards its origin. We emphasize that this is not due to external forces: gravity is weak and friction opposes this motion. This is due purely to the momentum concealed by and compensated for in the swimmer's gait. The curvature swimmer thus displays the exotic behavior of using dissipative (frictional) forces to *increase* the magnitude of its momentum in the rest frame of its environment. This relationship between

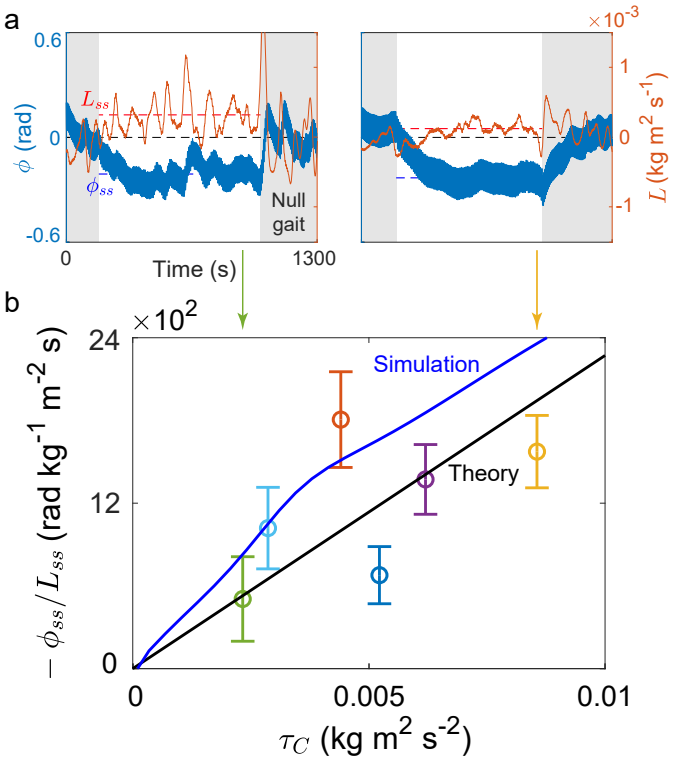

Figure 5.9: **Negative momentum in the steady state via environmental effects.** (a) Simultaneous evolution of ϕ and L for low and high friction ($\tau_C = 0.0023, 0.0089$ kg m^2 s^{-2}) for a swimmer conducting a swimming gait sandwiched by two null gaits. Note that the steady-state plateau ϕ_{ss} and angular momentum L_{ss} have opposite signs. (b) The ratio between the ϕ_{ss} and L_{ss} for various torques of friction τ_C. The black line shows the theory $-\phi_{ss}/L_{ss} = 4\tau_C/(T|\ddot{\alpha}|\tau_g)$ with all parameters measured from experiments. The blue line shows the simulation result.

steady-state displacement and momentum remains in qualitative agreement with simulation and theory (without free parameters) as friction is varied.

5.4 Conclusion and future work

In summary, we have experimentally realized and theoretically characterized the movement of a robot through a curved (spherical) space without relying on any momentum or reliance on environmental forces to translate, in contrast with all other observed systems. We demonstrated that this purely geometric effect couples to both conservative and dissipative forces present in real environments. In particular, we have shown how coupling between Coulomb friction and the geometric phase generates an effective force on the robot

that imparts an impulse that reduces its velocity while increasing its momentum in the opposite direction. This behavior sheds light both on Wisdom's proposed locomotion via spacetime curvature [186] and, more immediately, on a geometric effect always present when robots move on curved surfaces. As shown here, this effect can become dominant when the robot's body is comparable to the inverse curvature of the surface, which appears to extend to gravitational curvature of spacetime as well [186].

Further, the apparatus presented here can function as a test-bed for additional exotic behavior on curved surfaces, related to more complex and variable swimming gaits, nonlinear effects and collective behavior.

CHAPTER 6

CLUSTERING DYNAMICS OF ROBOTIC ACTIVE MATTER UNDER ATTRACTION

Self-organizing collective behaviors are found throughout nature, including shoals of fish aggregating to intimidate predators [196], fire ants forming rafts to survive floods [197], and bacteria forming biofilms to share nutrients when they are metabolically stressed [198]. Inspired by such systems, researchers in swarm robotics and programmable active matter have used many approaches towards enabling ensembles of simple, independent units to cooperatively accomplish complex tasks [199, 200, 201]. Both control theoretic and distributed computing approaches have achieved some success, but often rely critically on robots computing and communicating complex state information, requiring relatively sophisticated hardware that can be prohibitive at small scales [202, 203]. Alternatively, statistical physics approaches model swarms as systems being driven away from thermal equilibrium by robot interactions and movements (see, e.g., [124, 204]). Tools from statistical physics such as the Langevin and Fokker-Planck equations can then be used to analyze the mesoscopic and macroscopic system behaviors [205]. Current approaches present inherent tradeoffs, especially as individual robots become smaller and have limited functional capabilities [206, 207] or approach the thermodynamic limits of computing and power [208][1].

To apply to a general class of micro- or nano-scale devices with limited capabilities, we focus on systems of autonomous, self-actuated entities that utilize strictly local interactions to induce macroscale behaviors. Two behaviors of interest are *dynamic free aggregation*, where agents gather together without preference for a specific aggregation site (see Section 3.2.1 of [200]), and *dispersion*, its inverse. These problems are widely studied, but most

[1]This chapter is adapted from a co-first-authored journal article 'Programming active cohesive granular matter with mechanically induced phase changes,' Science Advances, 2021, 7(17)

work either considers robots or models with relatively powerful capabilities — e.g., persistent memory for complex state information [209, 210] or long-range communication and sensing [211, 212, 213] — or lack rigorous mathematical foundations explaining the generality and limitations of their results as sizes scale [214, 215, 216]. Recent studies on active interacting particles [217] and inertial, self-organizing robots [218] employ physical models to treat aggregation and clustering behaviors, but neither prove behavior guarantees that scale with system size and volume. Supersmarticle ensembles [21] are significantly more complex, exhibiting many transient behavioral patterns stemming from their many degrees of freedom and chaotic interactions, making them less amenable to rigorous algorithmic analysis.

Here we take a two-pronged approach to understanding the fundamental principles of programming task-oriented matter that can be implemented across scales without requiring sophisticated hardware or traditional computation that leverages the physics of local interactions. Motivated by a theoretical abstraction of *self-organizing particle systems* (SOPS, see section 6.2), we build a new system of deliberately rudimentary active "cohesive granular robots" (which, to honor granular physics pioneer Robert Behringer, we call "BOBbots" for Behaving, Organizing, Buzzing robots)

We will show that the interaction between the BOBbots qualitatively and quantitatively resembles that of the SOPS where we can design and rigorously analyze simple distributed algorithms to accomplish specific goals that are flexible and robust to errors. Remarkably, the lattice based equilibrium model quantitatively captures the aggregation dynamics of the robots.

With a provable algorithmic model and even simpler BOBbots capturing the algorithm's essential rules, we next explore how contact stress sensing — a capability that is readily available in the robotic platform but interestingly not easily computable by a strictly local, distributed algorithm — can enhance aggregation performance, as suggested by insights from the theoretical model.

This complementary approach demonstrates a new integration of the fields of distributed algorithms, active matter, and granular physics that navigates a translation from theoretical abstraction to practice, utilizing methodologies inherent to each field.

6.1 Physical description of BOBbots

Here we first introduce the *BOBbots* (Figure 6.1A–C) — Behaving, Organizing, Buzzing robots. Driven granular media provide a useful soft matter system to integrate features of the physical world into the toolkit for programming collectives. This builds upon three decades of work understanding how forced collections of simple particles interacting locally can lead to remarkably complex and diverse phenomena, not only mimicking solids, fluids, and gasses [219, 220] — e.g., in pattern formation [221, 222], supercooled and glassy phenomena [143, 223], and shock waves [224] — but also displaying phenomena characteristic of soft matter systems such as stress chains [225] and jamming transitions [226, 227]. While cohesive granular materials are typically generated in situations where particles are small (powders, with interactions dominated by electrostatic or even van der Waals interactions) or wet (with interactions dominated by formation of liquid bridges between particles) [228, 229], we generate our cohesive granular robots using loose magnets which can rotate to always achieve attraction.

Each BOBbot has a cylindrical chassis with a base of elastic "brushes" that are physically coupled to an off-center eccentric rotating mass vibration motor (ERM). The vibrations caused by the rotation of the ERM are converted into locomotion by the brushes (Figure 6.1C). Due to asymmetry in our construction of this propulsion mechanism, the BOBbots traverse predominantly circular trajectories [230] that are randomized through their initial conditions are inherently deterministic with some noise and occur at a constant speed per robot distributed as $v_0 = 4.8 \pm 2.0$ cm/s. While the individual trajectory is somehow deterministic, the system is very sensitive to initial conditions that a very small change in initial condition typically leads to huge difference in future trajectories (see Figure 6.6).

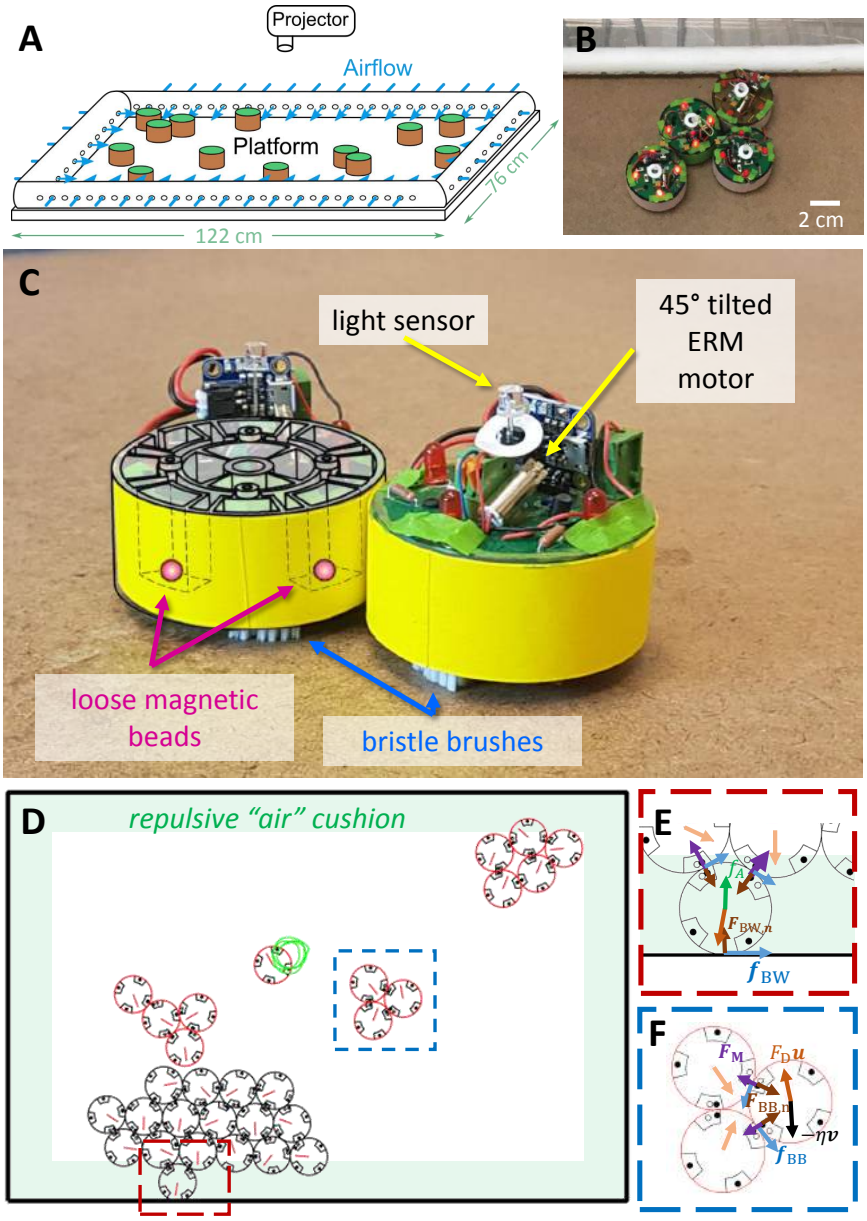

Figure 6.1: **BOBbots and their collective motion.** (**A**) Schematic of experimental setup. BOBbots are placed in a level arena with airflow gently repelling them from the boundaries. (**B**) A closeup of the experimental platform. (**C**) Mechanics of the BOBbots. Loose magnetic beads housed in the BOBbots' peripheries can reorient so BOBbots always attract each other. The vibration of the ERM motor and the asymmetry of bristles lead to the directed motion. The light sensor activates the motion. (**D**) Discrete element method simulation setup. (**E**) The BOBbot-boundary interactions: airflow repulsion f_A, BOBbot-boundary friction f_{BW}, and normal force $F_{\mathrm{BW,n}}$. (**F**) The inter-BOBbot interactions: attraction between magnetic beads F_M, inter-BOBbot friction f_{BB}, and sterical exclusion $F_{\mathrm{BB,n}}$. Photo Credit: Bahnisikha Dutta, Ram Avinery, Georgia Institute of Technology.

To allow for study of larger BOBbot ensembles and more comprehensive sweeps of parameter space, we also performed Discrete-Element Method (DEM) simulations of the BOBbots (see Figure 6.1D–F).

The motion of an individual BOBbot is modeled as a set of overdamped Langevin-type equations governing both its translation and rotation subject to its diffusion, drift [231], magnetic attraction, and sterical exclusion with other BOBbots. The translational drift corresponds to the speed from the equilibrium of the drive and drag forces while the rotational drift corresponds to the circular rotation. Similar methods have been used to understand macroscale phenomena emerging from collectives of microscopic elements [205] and to model particle motion in active matter [232].

The DEM simulation parameters are calibrated to match the physical BOBbot features. Many parameters such as the mass and dimensions of each BOBbot are easily measured. However, other parameters are better calculated by conducting simple experiments. The first such experiment (Figure 6.2) calculates the magnetic force F_{M0} between two magnets when their BOBbots' shells are touching. The first magnet is placed in a BOBbot shell attached to a rigid stand; a second shell is then tethered beneath the first by placing the second magnet inside it. Thus, the second shell falls once its weight exceeds F_{M0}. To leverage this insight, a cup is tethered to the second shell and BBs are added to the cup one-by-one until the second shell falls (Figure 6.2A). The weight of the shell, cup, and BBs are then measured to obtain a value of F_{M0} that is precise up to 0.1 g, the weight of a single BB (Figure 6.2B). On a log-linear plot of force, our measurements show exponential decay, which aligns closely with those reported by the magnet manufacturer (Figure 6.2C). A power law fit would gives an exponent of -18, which is far off from the -4 from dipole-dipole interaction, thus indicating an exponential decay as a better representation.

Each BOBbot's position $\vec{r}$ and orientation φ changes at a constant rate subject to noise. A BOBbot's constant translational speed v_0 comes from the competing driving force $F_D\hat{u}$ and the translational drag $-\eta\dot{\vec{r}}$. Similarly, each BOBbot's constant rotational speed ω_0

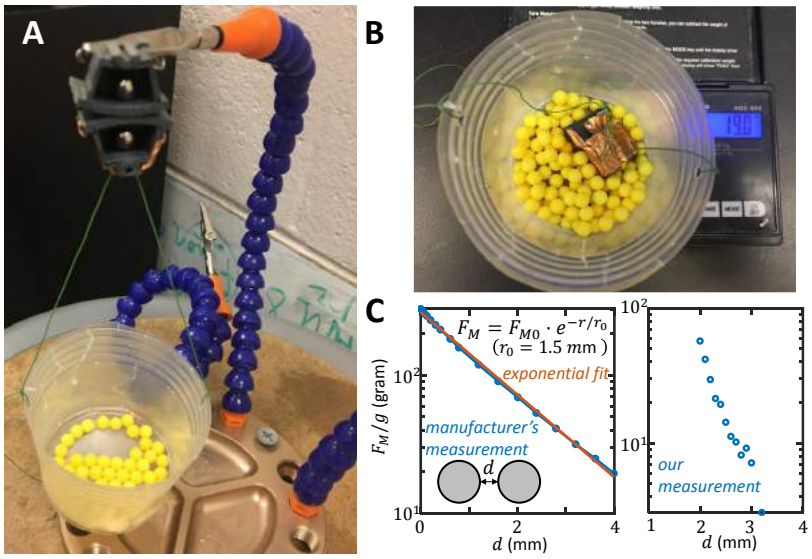

Figure 6.2: **Calibration experiment for calculating magnet force F_{M0}.** (**A**) The experimental setup for calculating F_{M0}. (**B**) Measuring the weight of the tethered apparatus once it falls gives a close approximation of F_{M0}. (**C**) Left: the magnetic force's decay with the separation d between two magnetic beads from the manufacturer for 4.6mm-diameter beads. Right: our measurement for 6.4mm-diameter beads.

comes from the competing driving torque τ_D and the rotational drag $-\eta_\varphi \dot{\varphi}$. The steady-state speeds therefore follow $v_0 = F_D/\eta$ and $\omega_0 = \tau_D/\eta_\varphi$. We again use simple experiments to determine the drive and drag. To measure the translational drag η, we compare a BOBbot's trajectory when it is on a 0° incline versus a tilted incline. In the former, the BOBbot circles regularly with some noise; in the latter, this regular circling is stretched towards the direction of gravity on the incline (Figure 6.3, top). Using the known gravitational force on the BOBbot, we can calculate the translational drag force and coefficient η. We then simulate a BOBbot's motion using different translational drag coefficients; the one that produces the trajectory most closely matching those in the experiments is chosen as the simulation η (Figure 6.3).

The measurement of the rotational drag η_φ exploits its balance with the driving torque. To measure the rotational torque exerted on a BOBbot, a very light rigid straw is attached across the diameter of a BOBbot (Figure 6.4). We then let the BOBbot use the straw to push objects at various arm lengths. For a given obstacle to push, the rotational torque is

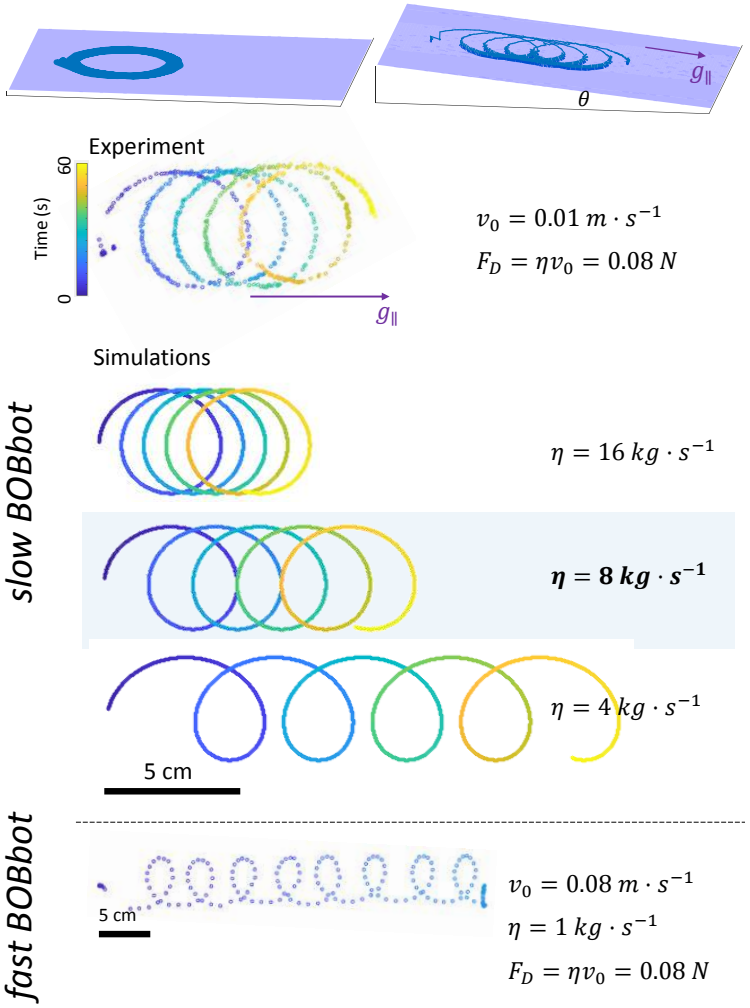

Figure 6.3: **Calibration experiment for calculating translational drag coefficient η.** When a BOBbot is driven on a level plane, it circles regularly with some noise. When placed on a tilted incline, its trajectory is stretched towards the direction of gravity on the incline. Using this known force, we measure the drag force by simulating BOBbot trajectories on a tilted incline using different drag coefficients, comparing each trajectory's stretch to that of the experiment. The correct drag produces a close approximate of the experimental trajectory. We find that viscosity varies between BOBbots, implying that the their speeds also vary. The first three trajectories are from a BOBbot with relatively slow velocity v_0; the last is from a fast BOBbot.

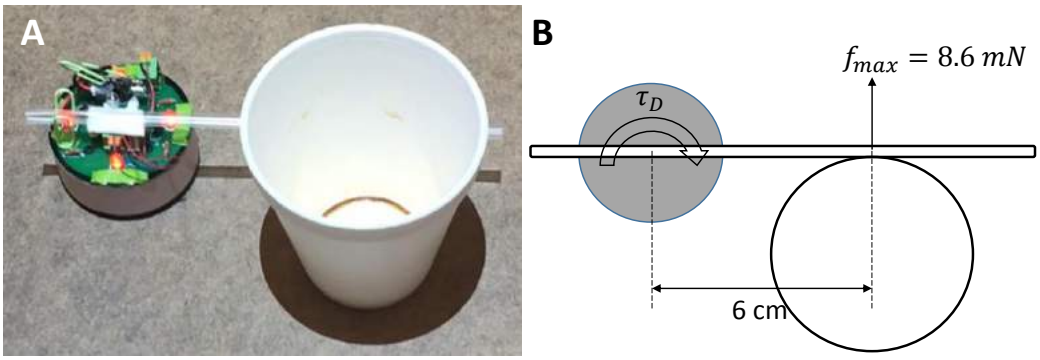

Figure 6.4: **Calibration experiment for calculating rotational drag coefficient η_φ.** (**A**) The experimental setup and (**B**) the corresponding force diagram, where f_{max} denotes the largest frictional torque that the driving torque τ_D can balance.

obtained by finding the largest torque of friction on an obstacle to balance. We decrease the arm length from a large value to a point the BOBbots can just push the obstacle. Given the measured saturated angular velocity ω_0, the rotational drag can be inferred as $\eta_\varphi = \tau_D/\omega_0$.

Many of our preliminary experiments were adulterated by boundary effects that caused small groups of BOBbots to collect at the edges and corners of the arena, affecting steady state properties. We mitigate these affects using airflow-based boundary repulsion. To characterize these airflow effects, a BOBbot is placed close to the boundary and its trajectory is tracked with and without airflow (Figure 6.5). The corresponding simulation parameters are then chosen to match the average characteristics of these experimental trajectories. The airflow force profile is chosen to match the decay length observed in the example experiment (which is $R_A = 6R_0$). The resting speed of the bot used in this experiment is $v_0 = 3$ cm/s. Note that the decay length chosen in the simulation runs throughout our study is $2R_0$ and $v_0 = 6$ cm/s.

Although the noise only causes small deviations in the individual trajectories, the combination of all the forces in the ensemble makes the system behavior very sensitive to initial conditions. Simulations with the same random seed started from almost exactly the same initial conditions except for a discrepancy of 0.5 mm of one robot's initial position deviate from each other significantly after 1 minute (Figure 6.6). We therefore regard this system

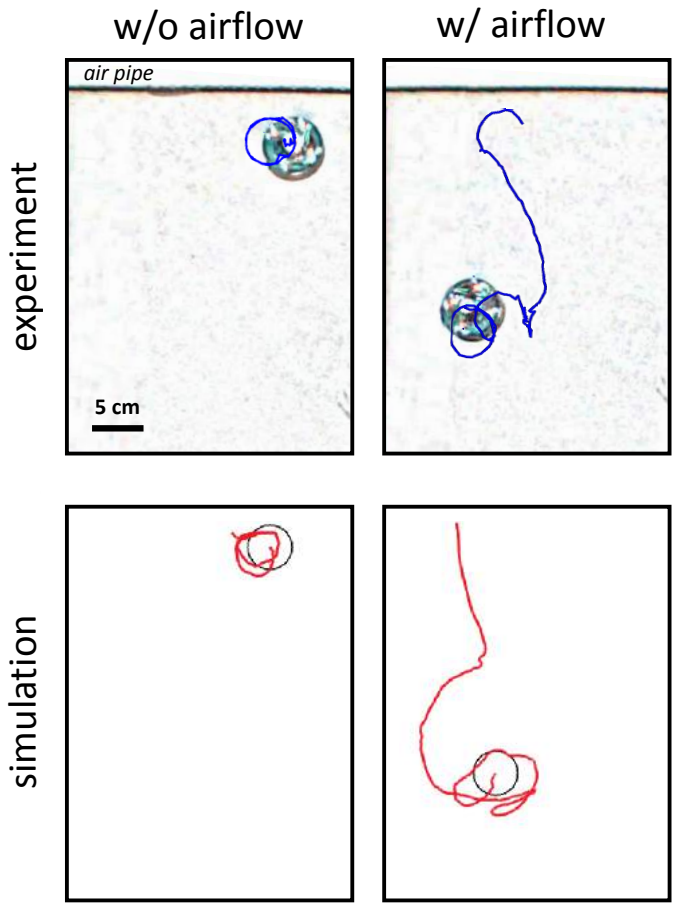

Figure 6.5: **Boundary airflow effects in experiment and simulation.** Here we show BOBbot trajectories with and without airflow effects.

as ergodic, yielding reasonable statistical sampling on longer time scales.

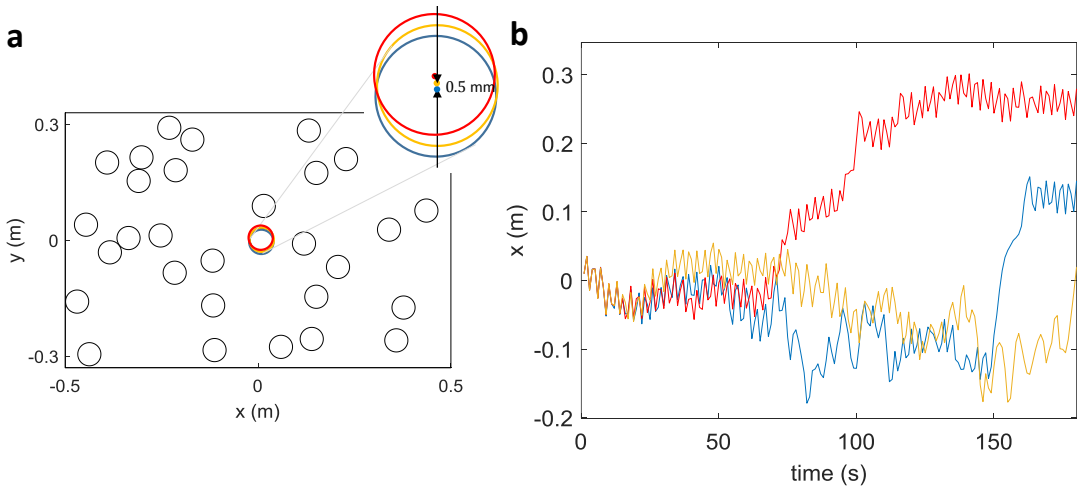

Figure 6.6: **Ensemble sensitivity to initial conditions.** (**A**) To measure the ensemble's sensitivity to initial conditions, we simulated three runs with the same random seeds and nearly identical initial conditions, with the exception of a spatial difference of 0.5 mm for the initial position of one BOBbot, shown in blue, yellow, and red. (**B**) The x-position over time of the perturbed BOBbot for different starting positions, where the curve color corresponds to the starting position in (A). The trials only coincide for roughly the first 30 s, and after one minute they diverge significantly.

Mitigating the effects of the arena's fixed boundaries in both experiments and simulations presented a significant design challenge. BOBbots can persist along the boundary or in corners, affecting system dynamics by, for example, enabling aggregates to form where they would not have otherwise or hindering multiple aggregates from integrating. To address these issues, uniform airflow was employed to gently repel BOBbots away from the boundary and similar effects were implemented in simulation.

Since the interaction strenght typically play a critical role in lattice gas model such as the SOPS model we will introduce later, we next investigated the degree to which collectives of BOBbots aggregate as a function of their peripheral magnet strength F_{M0} in both robotic experiments and DEM simulations. (For convenience, F_{M0} is normalized by the gravity of Earth $g = 9.81$ m/s^2 when using the unit of gram.)

The experimental protocol begins with placing magnets of a particular strength F_{M0} into the BOBbots' peripheral slots. The BOBbots are positioned and oriented randomly in

a rectangular arena and are then actuated uniformly for a fixed time during which the BOBbots' positions and the size of the largest connected component are tracked (Figure 6.7A–C). These trials are conducted for several F_{M0} values with repetition. We followed the same protocol in simulations.

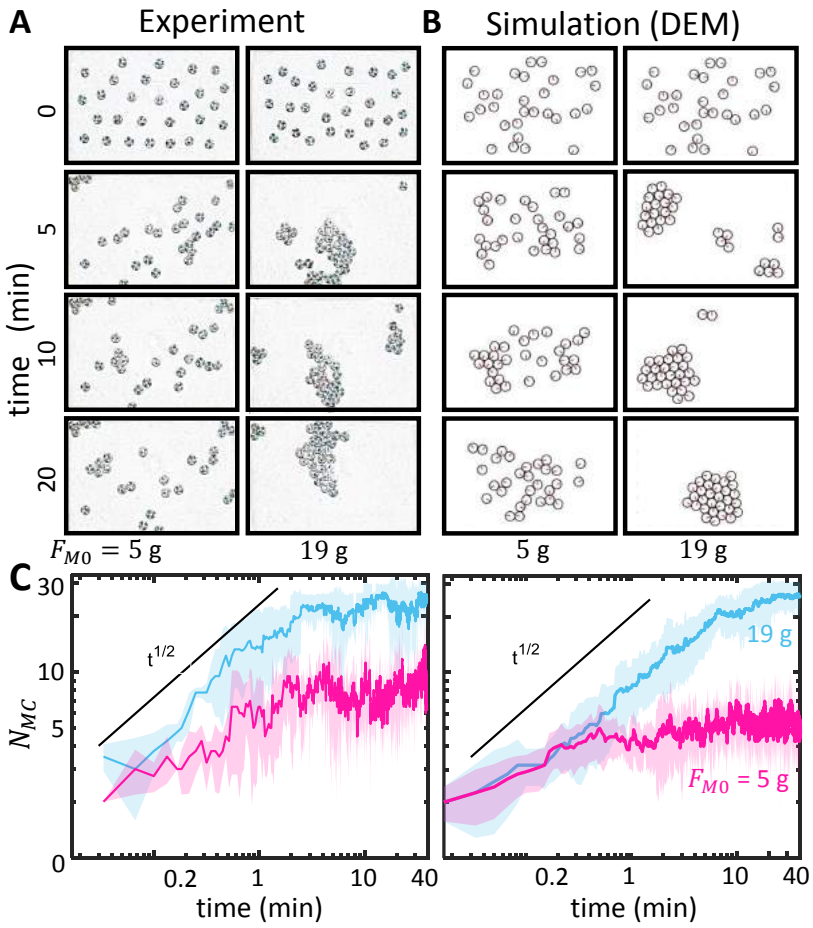

Figure 6.7: **Evolution of BOBbot clusters.** (**A**) Time evolution snapshots of both experiment and (**B**) simulation for a system of 30 BOBbots with different magnet strengths: $F_{M0} = 5$ g (left) where we observe dispersion, and $F_{M0} = 19$ g (right) where we observe aggregation. Experimental images have been processed with a low-pass filter for better visual clarity. (**C**) Time evolutions of the size of the largest component N_{MC} in experiment and simulation for a system of 30 BOBbots with $F_{M0} = 5$ g (magenta) and $F_{M0} = 19$ g (blue).

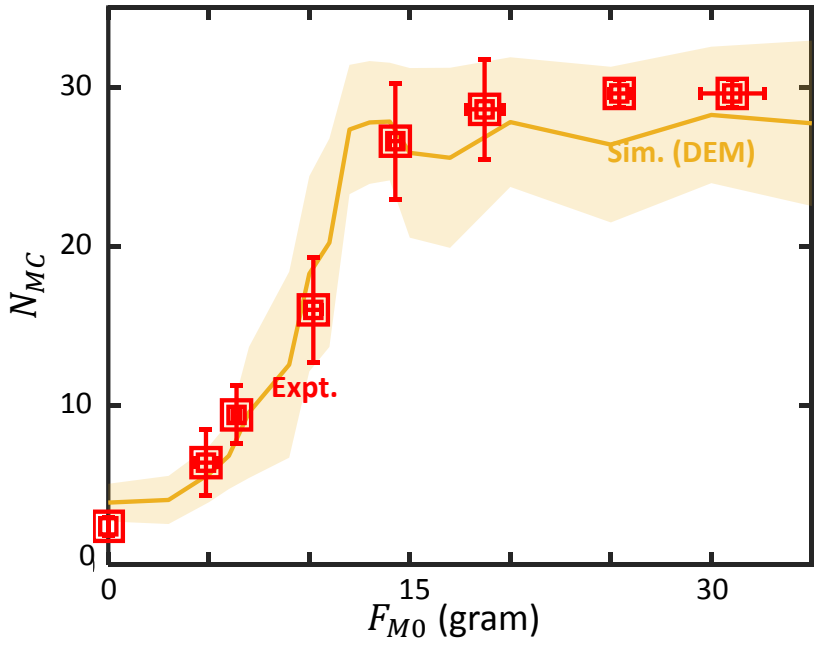

Figure 6.8: **Scaling of cluster size vs. magnetic strength.** This is for a system of 30 BOBbots showing an increase in N_{MC} as the magnet strength F_{M0} increases. The yellow plot line shows the mean and standard deviation of N_{MC} in the 150 simulation runs for each magnetic strength F_{M0} between 1–35 g, with a step size of 1 g. Experimental data is shown in red with error bars showing the standard deviation of largest cluster size N_{MC} and the uncertainty of F_{M0} due to empirical measurement.

6.2 Mapping onto lattice gas

In experiment and DEM simulation, we observe an abrupt, rapid rise and then saturation in the size N_{MC} of the largest connected component as the magnetic attraction F_{M0} increases (Figure 6.8). These curves resemble critical phenomena in lattice gas models [233]. Given this correspondence, we explored whether the equilibrium SOPS model could be used to make quantifiable predictions in the robot experiments.

While many systems use interparticle attraction and sterical exclusion to achieve system-wide aggregation and interparticle repulsion to achieve dispersion, these methods typically use some long-range sensing and tend to be nonrigorous, lacking formal proofs guaranteeing desirable system behavior. To better understand these collective behaviors, the abstract model of *self-organizing particle systems* (SOPS) allows us to define a formal distributed

algorithm and rigorously quantify long-term behavior. Particles in a SOPS exist on the nodes (or vertices) of a lattice, with at most one particle per node, and move between nodes along lattice edges. Each particle is anonymous (unlabeled), interacts only with particles occupying adjacent lattice nodes, and does not have access to any global information such as a coordinate system or the total number of particles.

In earlier work, Cannon et al. [234] analyzed a distributed SOPS algorithm for aggregation and dispersion under the assumption that the particle system remained simply connected (i.e., the system forms a single connected cluster with no holes). This SOPS algorithm defines a finite Markov chain with local moves that connect the state space of all simply connected configurations of particles. Moves are defined so that each particle, when activated by its own Poisson clock (i.e., after a delay chosen at random from a Poisson distribution with constant mean), chooses a random neighboring node and moves there with a probability that is a function of the number of neighbors in the current and new positions provided the node is unoccupied and the move satisfies local conditions that guarantee the configuration stays simply connected. In particular, for configurations σ and τ differing by the move of a single particle p along a lattice edge, the transition probability is defined as $P(\sigma, \tau) \propto \min(1, \lambda^{n'-n})$, where $\lambda > 0$ is a bias parameter that is an input to the algorithm, n is the number of neighbors of p in σ and n' is the number of neighbors of p in τ. These probabilities arise from the celebrated Metropolis–Hastings algorithm [235, 236] and are defined so that the Markov chain converges to a unique Boltzmann distribution π such that $\pi(\sigma)$ is proportional to $\lambda^{E(\sigma)}$, where $E(\sigma)$ is the number of nearest neighbor pairs in σ (i.e., those pairs that are adjacent on the lattice).

It was shown in [234] that the connected SOPS ensemble provably aggregates into a compact conformation when $\lambda > 3.42$ and expands to a conformation with nearly maximal (linear) perimeter when $\lambda < 2.17$ with high probability, i.e., with a probability of failure that is exponentially small in N, the number of particles. However, despite rigorously achieving both aggregation and dispersion, this distributed algorithm has two notable

drawbacks that make it infeasible for direct implementation in a physical system of simple robots: the connectivity requirement that tethers the particles together and the "look ahead" requirement used to calculate transition probabilities ensuring convergence to the desired Boltzmann distribution.

To address these issues, we define a modified aggregation and dispersion algorithm $\mathcal{M}_{\mathrm{AGG}}$ where particles can disconnect and moves rely only on the current state. Here, particles occupy nodes of a finite region of the triangular lattice, again moving stochastically and favoring configurations with more pairs of neighboring particles. Each particle has its own Poisson clock and, when activated, chooses a random adjacent lattice node. If that node is unoccupied, the particle moves there with probability λ^{-n}, where n is the number of current neighbors of the particle, for bias parameter $\lambda > 0$. Thus, rather than biasing particles towards nodes with more neighbors, we instead discourage moves away from nodes with more neighbors, with larger λ corresponding to a stronger ferromagnetic attraction between particles (Figure 6.9A). This new chain $\mathcal{M}_{\mathrm{AGG}}$ converges to the same Boltzmann distribution $\pi(\sigma) \propto \lambda^{E(\sigma)}$ over particle system configurations σ as the original SOPS algorithm.

By carefully analyzing the stationary distribution of $\mathcal{M}_{\mathrm{AGG}}$, which is just the desired Boltzmann distribution, we establish conditions that provably yield aggregation when the particles are confined to a compact region of the triangular lattice (Figure 6.9B). The proof uses arguments from [237]; see the Materials and Methods for details.

Let configuration σ be drawn from the stationary distribution of $\mathcal{M}_{\mathrm{AGG}}$ on a bounded, compact region of the triangular lattice, when the number of particles N is sufficiently large. If $\lambda > 5.66$, then with high probability there exist $\beta > 0$ and $0 < \delta < 1/2$ such that σ will be (β, δ)-aggregated. However, when $0.98 < \lambda < 1.02$, the configuration σ will be dispersed with high probability.

Varying values of λ in simulation gives strong indication that dispersion persists for larger values of λ and the aggregation algorithm undergoes a phase transition whereby

the macroscopic behavior of the system suddenly changes from dispersion to aggregation (Figure 6.9C–D), mimicking the fixed magnetization ferromagnetic Ising model which motivated our Markov chain algorithm. Nonetheless, our proofs demonstrate that our system has two distinct phases of behavior for different ranges of λ for any system with a sufficiently large number of interacting particles, which is enough for our purposes. From Figure 6.9D, we can see the magnetization F_{M0} plays a role analogous to the bias parameter λ.

First, we designed a test to examine how force and λ scale. Recall that in the SOPS algorithm, the force acting on each particle is proportional to λ^n, where n is the particle's current number of neighbors. In the experiments, BOBbots cannot count their neighbors, but the magnets are expected to provide a similar force that also increases geometrically when more magnets are engaged.

To estimate the relationship between force and λ, we investigate the rate at which a BOBbot loses or gains neighbors over a fixed amount of time. Viewing a BOBbot's completion of half its circular motion as analogous to a particle moving to a new lattice node in the SOPS algorithm and using this time interval to evaluate the transition, simulation data shows that a BOBbot's transition probability from having a higher number of neighbors n to a lower number n' closely follows the algorithm's $P(\sigma, \tau) \propto \min(1, \lambda^{n'-n})$ transition probabilities (Figure 6.11A). Further, we evaluated the BOBbots' effective bias parameter λ_{eff} as a function of F_{M0} and found an exponential relation $\lambda_{\text{eff}} = \exp(\beta F_{M0})$, where β is a constant representing inverse temperature (Figure 6.11B). The BOBbots' transition probabilities can then be approximated as $P(\sigma, \tau) = \exp(-\beta(\epsilon_n - \epsilon_{n'}))$, where β is the inverse temperature of the system and $\epsilon_n = n \cdot F_{M0}$ can be interpreted as the energy contributed by a BOBbot's n neighbors.

With the relation between F_{M0} and λ_{eff} established, we next compare the aggregation behaviors exhibited by the SOPS algorithm and the BOBbot ensembles. Figure 6.11C shows the fraction of particles/BOBbots in the largest component N_{MC}/N observed in

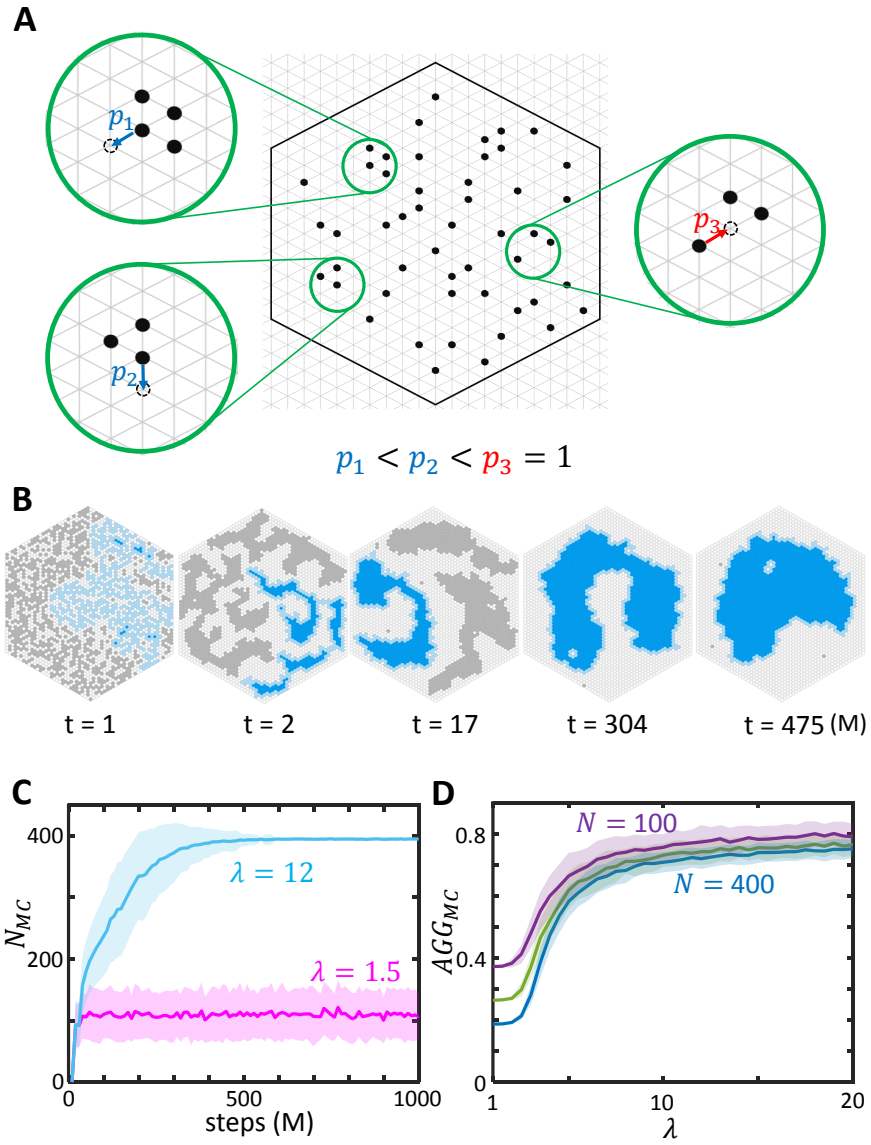

Figure 6.9: **The theoretical self-organizing particle system (SOPS).** (**A**) A particle moves away from a node where it has n neighbors with probability λ^{-n}, where $\lambda > 0$. Thus, moves from locations with more neighbors are made with smaller probability than those with fewer (e.g., in the insets, $p_1 = \lambda^{-3} < p_2 = \lambda^{-2} < p_3 = 1$). (**B**) Time evolution of a simulated SOPS with 1377 particles for $\lambda = 7.5$ showing progressive aggregation. The bulk of the largest connected component is shown in blue and its periphery is shown in light blue. (**C**) Time evolution of N_{MC}, the size of the largest connected component, showing dispersion for $\lambda = 1.5$ and aggregation for $\lambda = 12$. The simulations use 400 particles. (**D**) Phase change in λ-space for the aggregation metric $AGG_{MC} = N_{MC}/(k_0 P_{MC}\sqrt{N})$, where k_0 is a scaling constant, P_{MC} is the number of particles on the periphery of the largest component, and N is the total number of particles. This phase change is qualitatively invariant to the system's size.

both the SOPS algorithm and BOBbot simulations after converting with respect to λ_{eff}; the algorithm does indeed capture the maximum cluster fraction observed in the simulations. Notably, the aggregated and dispersed regimes in λ-space established by Theorem section 6.2 provide a rigorous understanding of these BOBbot collective behaviors. For instance, the proven dispersed regime $0.98 < \lambda < 1.02$ gives a clear explanation for why agents will not aggregate even in the presence of mutual attraction. Further, it also helps establish the magnitude of attraction needed to saturate the aggregation.

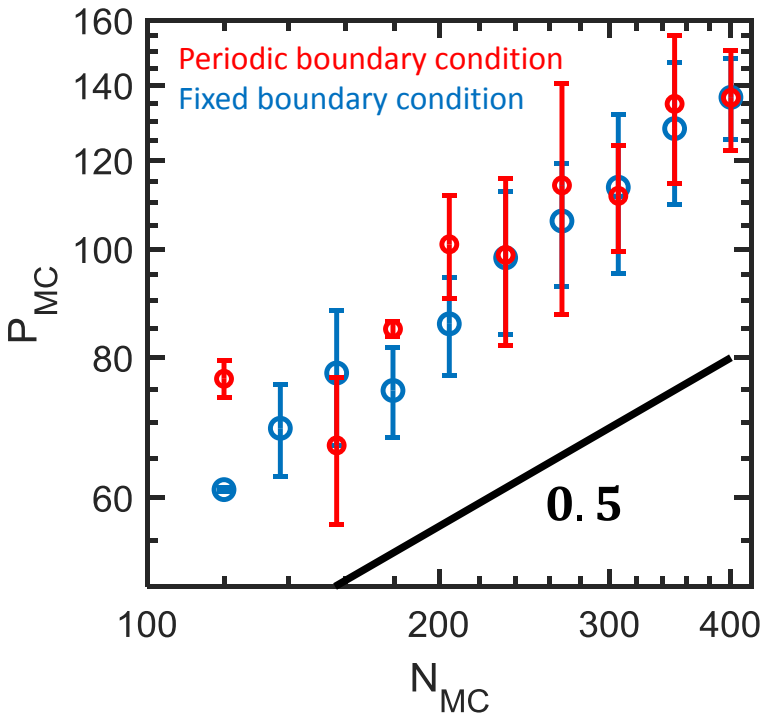

Figure 6.10: **Approaching $P_{MC} \propto N_{MC}^{1/2}$ with periodic boundary conditions.** Scaling between the largest component's size N_{MC} and perimeter P_{MC} in number of BOBbots for simulated systems of 100–400 BOBbots with $F_{M0} = 19$ gf using fixed boundary conditions (blue) and periodic boundary conditions (red). The fixed boundary conditions achieve a scaling power of 0.66 ± 0.07 while periodic boundary conditions achieve a scaling power of 0.59 ± 0.18.

We additionally test the SOPS prediction that the maximum cluster should not only be large but also compact, occupying a densely packed region. The results from [237] that we apply here for aggregation suggest the following relationship between the size of the

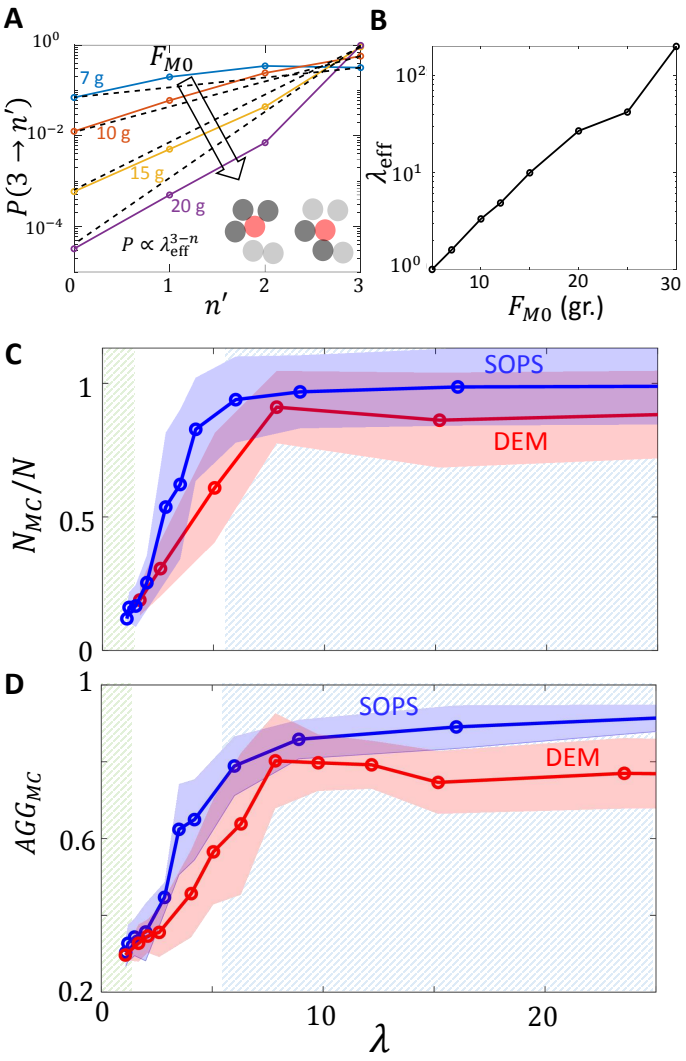

Figure 6.11: **Algorithmic interpretation of BOBbot clustering.** (**A**) A diagram showing how the effective bias parameter λ_{eff} is evaluated from the DEM simulation. (**B**) The dependence of λ_{eff} on the magnetic attraction force F_{M0}. The (**C**) maximum cluster fraction N_{MC}/N and (**D**) aggregation metric AGG_{MC} for different values of λ in both the SOPS algorithm (blue) and physical simulations (red). The green and blue shaded regions show the dispersed and aggregated regimes proved from theory, respectively.

largest component N_{MC} and its perimeter P_{MC}. In dispersed configurations, P_{MC} should scale linearly with N_{MC}, meaning that most BOBbots lie on the periphery of their components. In aggregated configurations, however, P_{MC} should scale as $N_{MC}^{1/2}$, approximating the minimal perimeter for the same number of BOBbots by at most a constant factor. We test these scaling relationships in simulations with 400 BOBbots (Figure 6.12A) and find

that the theory's predictions hold in the dispersed regime; however, the 0.66 ± 0.07 sublinear scaling power for the aggregated case is slightly higher than the theory's prediction of 0.5. This discrepancy may in part be due to boundary and finite-size effects — in fact, DEM simulations with periodic boundaries show a scaling power of 0.59 ± 0.18 that is closer to the SOPS theory (Figure 6.10) — but is also affected by non-reversibility inherent in the BOBbots' circular trajectories. To make a quantitative comparison that captures when components are both large and compact, we track $AGG_{MC} = N_{MC}/(k_0 P_{MC}\sqrt{N})$, where k_0 is a scaling constant defined such that $AGG_{MC} = 1$ when the system is optimally aggregated, achieving the minimum possible perimeter. Physically, AGG_{MC} is reminiscent of surface tension for which energy minimization leads to a smaller interface (in our setting, smaller perimeter P_{MC}), yielding an AGG_{MC} closer to 1. We obtain agreement between the SOPS and DEM simulations with respect to this metric as well (Figure 6.11D), further validating the theory's prediction, though the DEM simulations yield slightly smaller AGG_{MC} than the SOPS algorithm for large λ.

6.3 Mapping onto continuum model and universality

We noticed the size of the largest component N_{MC} grows roughly proportional to $t^{1/2}$ over time (Figure 6.7C). Since the perimeter of the largest cluster P_{MC} scales proportional to $N_{MC}^{0.66} \approx N_{MC}^{2/3}$ (Figure 6.12A), this implies the length scale grows like $t^{1/3}$. This is reminiscent of coarsening in a broad class of systems described by Cahn–Hilliard equation $\partial u/\partial t = \nabla^2(\Phi'(u) - \gamma\nabla^2 u)$ where order parameter u takes continuous values in $(-1, 1)$ where -1 and 1 are analogous to empty and occupied nodes in the SOPS lattice, respectively. To bridge the SOPS algorithm with the Cahn–Hilliard equation, we first observe that the SOPS algorithm with bias parameter λ can be exactly mapped to an Ising model with fixed magnetization [238, 239] with coupling strength $J = \frac{1}{2\beta}\log\lambda$, where β is inverse temperature.

Here we prove that the SOPS algorithm can be mapped to an fixed-magnetization Ising

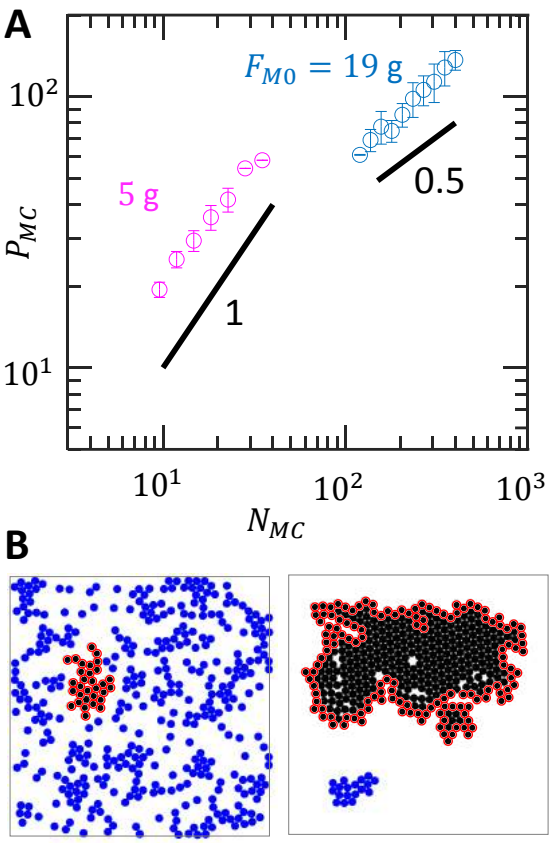

Figure 6.12: **Perimeter scaling of BOBbot clusters.** (**A**) Log-log plot showing the scaling relationship between the largest component's size N_{MC} and perimeter P_{MC} in number of BOBbots for simulated systems of 400 BOBbots with $F_{M0} = 5$ g (magenta) and 19 g (cyan) for fixed boundary conditions. Each data point is the average of 20 simulations. While the SOPS predicts a scaling power of 0.5 for the aggregated case (cyan), the data shows a slightly larger — but still sublinear — power of 0.66 ± 0.07. (**B**) Final snapshot of the collective motion of 400 BOBbots with $F_{M0} = 5$ g (left) and 19 g (right). BOBbots shown in black belong to the largest connected component; those outlined in red are on its periphery.

model with coupling strength $J = \frac{1}{2\beta} \log \lambda$. For a given SOPS configuration of particles in a bounded region of the lattice, construct a corresponding Ising lattice gas where the spin σ of an occupied (resp., unoccupied) node in the SOPS is $+1$ (resp., -1) in the gas. The SOPS algorithm has a transition probabilities $P_{\text{SOPS}} = \lambda^{-\Delta H_{\text{SOPS}}}$, where $H_{\text{SOPS}} = -n_{\text{move}}$ is its Hamiltonian and n_{move} is the number of neighbors that the moving particle is leaving. The Ising model has transition probabilities $P_{\text{Ising}} = \exp(-\beta \Delta H_{\text{Ising}})$, where $H_{\text{Ising}} = -\frac{1}{2} J \sum_{(i,j)} \sigma_i \sigma_j$ is its Hamiltonian and $\sigma_i \in \{-1, +1\}$ is the spin of site i.

Let H_{SOPS} be the Hamiltonian of the SOPS algorithm, H_{Ising} be the Hamiltonian of a fixed-magnetization Ising model, and J be the coupling strength of the Ising model. Then for any particle move in the SOPS algorithm and the corresponding spin updates in the Ising model, we have $\Delta H_{\text{Ising}} = 2J\Delta H_{\text{SOPS}}$. Consider a particle moving from node i to node j in the SOPS algorithm and let n_i (resp., n_j) be the number of neighbors the particle has at node i (resp., node j). It is easy to see that $\Delta H_{\text{SOPS}} = n_j - n_i$ for this move. To calculate ΔH_{Ising}, observe that the corresponding spin changes in the Ising model are $\sigma_i : +1 \to -1$ and $\sigma_j : -1 \to +1$. Let z be the coordination number (i.e., degree) of the lattice. Consider all sites k adjacent to i and j; we have four cases:

1. k is occupied and adjacent to i, so $\sigma_i\sigma_k : +1 \to -1$. There are n_i such sites.
2. k is occupied and adjacent to j, so $\sigma_j\sigma_k : -1 \to +1$. There are n_j such sites.
3. $k \neq j$ is unoccupied and adjacent to i, so $\sigma_i\sigma_k : -1 \to +1$. There are $z - n_i - 1$ such sites.
4. $k \neq i$ is unoccupied and adjacent to j, so $\sigma_j\sigma_k : +1 \to -1$. There are $z - n_j - 1$ such sites.

To calculate ΔH_{Ising}, we simply sum the spin changes of these cases; all other spins remain the same and thus cancel in the difference. We have:

$$\begin{aligned}
\Delta H_{\text{Ising}} &= -\frac{1}{2}J((n_i - (z - n_i - 1) - n_j + (z - n_j - 1)) \\
&\qquad\qquad - (-n_i + (z - n_i - 1) + n_j - (z - n_j - 1))) \\
&= -\frac{1}{2}J((2n_i - 2n_j) - (-2n_i + 2n_j)) \\
&= 2J(n_j - n_i) \\
&= 2J\Delta H_{\text{SOPS}}
\end{aligned}$$

This proves the lemma (Joshua Daymude has contributed to the formalism of this proof).

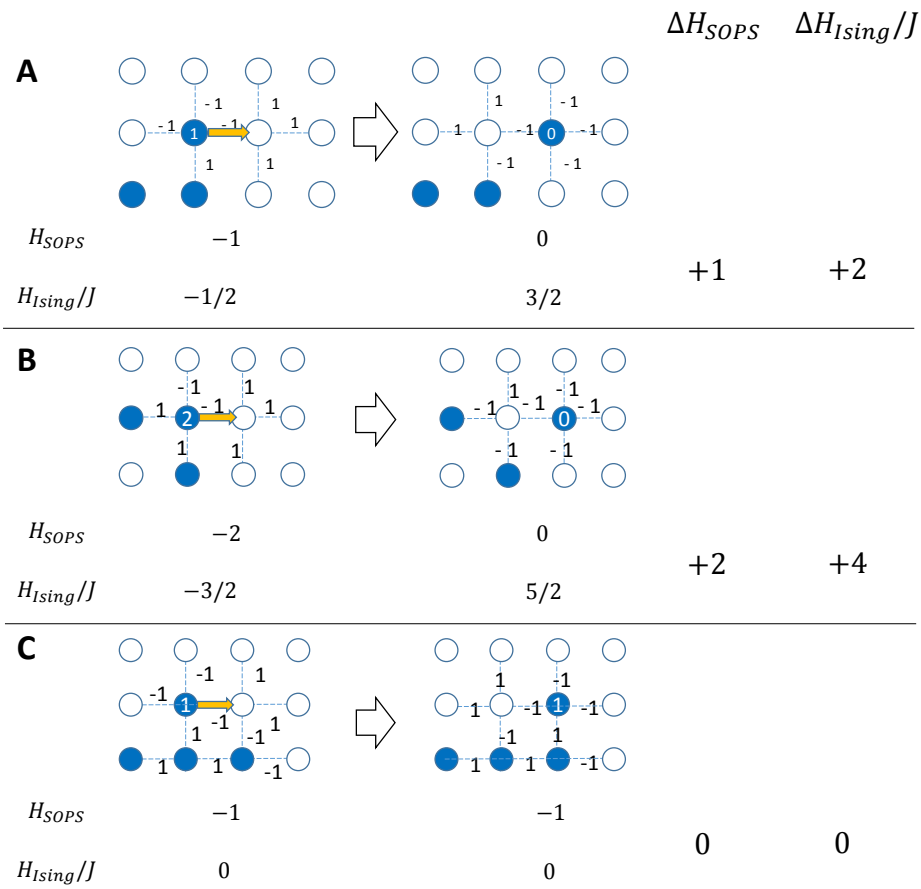

Figure 6.13: **Examples showing $\Delta H_{\text{Ising}} = 2J\Delta H_{\text{SOPS}}$.** A particle moves to the right with a decrease of (**A**) 1, (**B**) 2, and (**C**) 0 neighbors, illustrated by the graphs showing the local configuration before and after the move. The numbers in black between sites i and j are the value of $\sigma_i\sigma_j$. The number of neighbors of the moving particle is shown in white.

Figure 6.13 shows several examples of particle motions and their corresponding changes to the Ising Hamiltonian to illustrate the relationship established by Lemma section 6.3. Lemma section 6.3 shows that it is exactly when $J = \frac{1}{2\beta}\log\lambda$ that we achieve $P_{\text{SOPS}} = P_{\text{Ising}}$, which completes the mapping from the SOPS algorithm to the fixed-magnetization Ising model.

As shown by Penrose [240], the fixed magnetization Ising model with coupling strength J can be mapped to the surface tension γ of the Cahn–Hilliard equation as $\gamma = \beta J$. In particular,

$$\frac{\partial u}{\partial t} = M\nabla^2\{f'(u) - \epsilon\nabla^2 u\}$$

where $M = \beta$, $\epsilon = J$, $f(u) = \beta^{-1}g(u) - \frac{1}{2}(z+1)\epsilon u^2$, $g'(u) = \text{arctanh}(u)$, and the prime denotes d/du. Thus, we obtain:

$$\frac{\partial u}{\partial t} = \nabla^2\{\text{arctanh}(u) - (z+1)\beta\epsilon u - \beta\epsilon\nabla^2 u\}$$

which is the standard Cahn–Hilliard equation:

$$\frac{\partial u}{\partial t} = \nabla^2(\Phi'(u) - \gamma\nabla^2 u)$$

with surface tension $\gamma = \beta J$ and $\Phi'(u) = \text{arctanh}(u) - (z+1)\gamma u$. Here, z is the coordination number of the lattice: 4 for square and 6 for hexagonal. Along with $J = \frac{1}{2\beta}\log\lambda$ proved in the previous section, we arrive at the connection between the SOPS algorithm and the Cahn–Hilliard equation with surface tension $\gamma = \frac{1}{2}\log\lambda$.

When $\lambda = 1$, the Cahn–Hilliard equation has no surface tension as $\gamma = \frac{1}{2}\log 1 = 0$, $\Phi'(u)$ has only one zero, and Φ has only one minimum. As λ increases, the surface energy γ increases as well. When $\gamma > 1/(z+1)$, Φ' has three zeros and Φ has double wells (Figure 6.14), yielding a critical $\lambda_c = e^{2/7} \approx 1.33$ in the hexagonal lattice and $\lambda_c = e^{2/5} \approx 1.49$ in the square lattice. The critical value $\lambda_c \approx 1.33$ for the hexagonal lattice lies within the $\lambda_c \in (1.02, 5.66)$ range predicted by the SOPS theory and exhibited by the BOBbot experiments.

When the surface tension is above the critical point, the characteristic length ℓ grows as $t^{1/3}$ [60]. Growth rate proportional to $t^{1/3}$ is also seen in motility-induced phase separation [18] and entangled worms [26]. Figure 6.15 shows how ℓ grows with time when λ is above the critical point for square lattice. To deal with the singular behavior of arctanh, linear extension around ± 1 is used [61]. ℓ uses the first zero of the spatial correlation function $G(r)$, which is the Fourier transform of the structure factor [60]. Given the area scales as $N_{MC} \propto P_{MC}^{1/0.66} \approx P_{MC}^{3/2} = \ell^{3/2}$ for the aggregated case in $N \sim 100 \ll \infty$, cluster size grows with time as $t^{1/2}$.

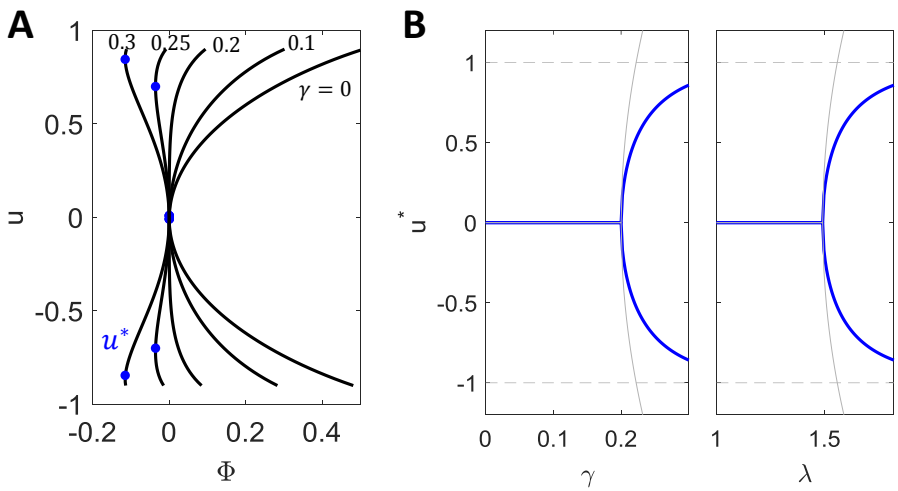

Figure 6.14: **Critical surface tension γ and bias parameter λ.** (**A**) Homogeneous free energy Φ for different surface tensions γ. (**B**) Position of the well for different surface tensions γ and its corresponding bias parameter λ. The solid gray line shows the value $u^* = \pm\sqrt{15(\gamma - 1/5)}$ from the Taylor expansion of Φ up until $\mathcal{O}(u^3)$.

Thus, the SOPS and BOBbot ensemble behaviors map to the Cahn–Hilliard equation with $\gamma = \frac{1}{2}\log\lambda \propto F_{M0}$. This suggests that in the limit, the SOPS and BOBbot aggregation behavior should display a second-order phase transition at a critical λ_c corresponding to the critical surface tension γ in the Cahn–Hilliard equation. The corresponding critical value $\lambda_c = e^{2/7} \approx 1.33$ on the hexagonal lattice lies within the $\lambda_c \in (1.02, 5.66)$ range proven by the SOPS theory. Thus, we obtain agreement between the SOPS theory for a finite lattice system and the Cahn–Hilliard equation for an active matter system at the continuum limit. This mapping gives further confirmation of the universality (Figure 6.16) of our results and provides another perspective for "programming" active collectives.

6.4 Control to manipulate the clustering

We have demonstrated that the BOBbot ensembles mimic a lattice model that can provably aggregate for large enough λ, corresponding physically to highly attractive interaction that favors large components with small perimeter. We now ask whether we can achieve rudimentary collective intelligence determining, for example, how robots could tune their

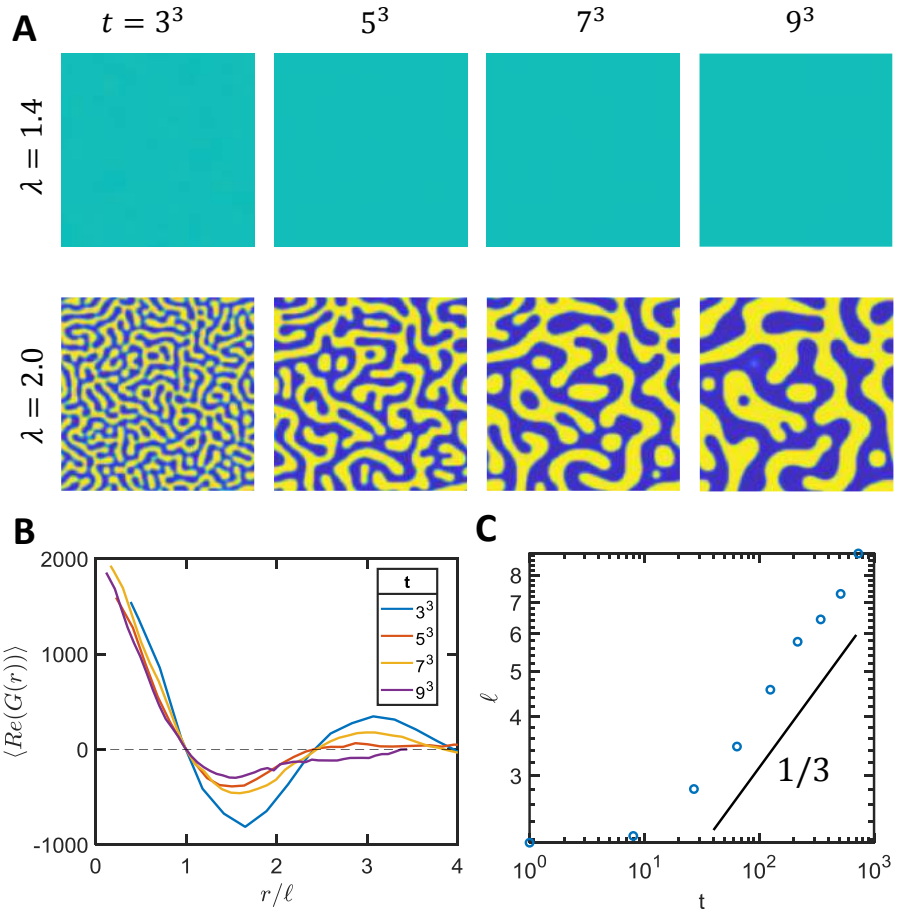

Figure 6.15: **Pattern formation below and above the critical λ.** (**A**) Simulation of the Cahn–Hilliard equation for $\lambda = 1.4$ below the critical point and $\lambda = 2.0$ above the critical point. Both simulations use a 128×128 grid and start with a uniform distribution of $u \sim \mathcal{U}[-0.1, 0.1]$. (**B**) Spatial correlation function normalized by the correlation length ℓ. (**C**) The increase of ℓ with time shows a power law with exponent $1/3$.

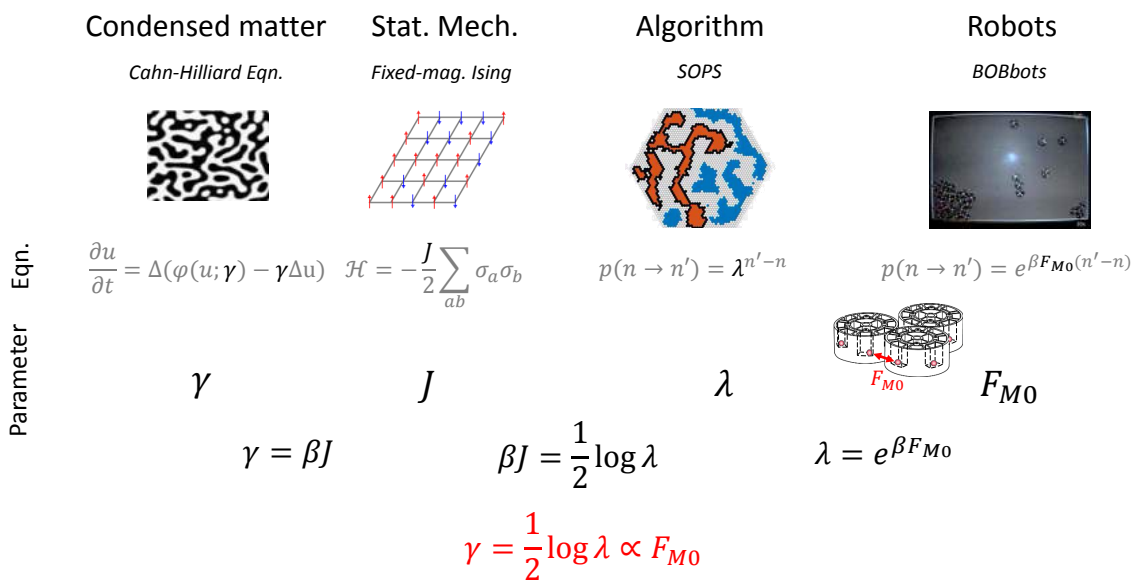

Figure 6.16: **Universality from the clustering of macroscopic active matter to phase separation of continuum.** With the mappings between the dynamics of robots, particles' motion on lattice, and continuum model, we can consequently show that the surface tension is proportional to the inter-particle attraction between macroscopic active matter.

responses to enhance or dampen aggregation, thereby achieving a more tightly clustered or dispersed state. In particular, we explore whether such tuning can help counteract some ways the system deviates from the theory, such as variations in the BOBbots' speeds and magnetic attraction, improving the fidelity to the original algorithm. While the BOBbots remain unable to count neighbors or estimate the Gibbs probabilities directly as prescribed by the algorithm, we take advantage of physical effects of the BOBbot ensembles to "program" desirable behavior without using any traditional computation.

The first effect relies on observations that for a fixed magnet strength, the size of the largest component N_{MC} decreases with increasing BOBbot speed v_0 (Figure 6.18). A full investigation of the behavior of BOBbot collectives at varying uniform speeds will be the subject of a separate study.

We further observe that N_{MC} scales linearly with z, the average number of neighbors per BOBbot at equilibrium (Figure 6.17A, inset). Thus, BOBbot speed v_0 is inversely correlated with the average number of neighbors per BOBbot z. This arises from v_0 being

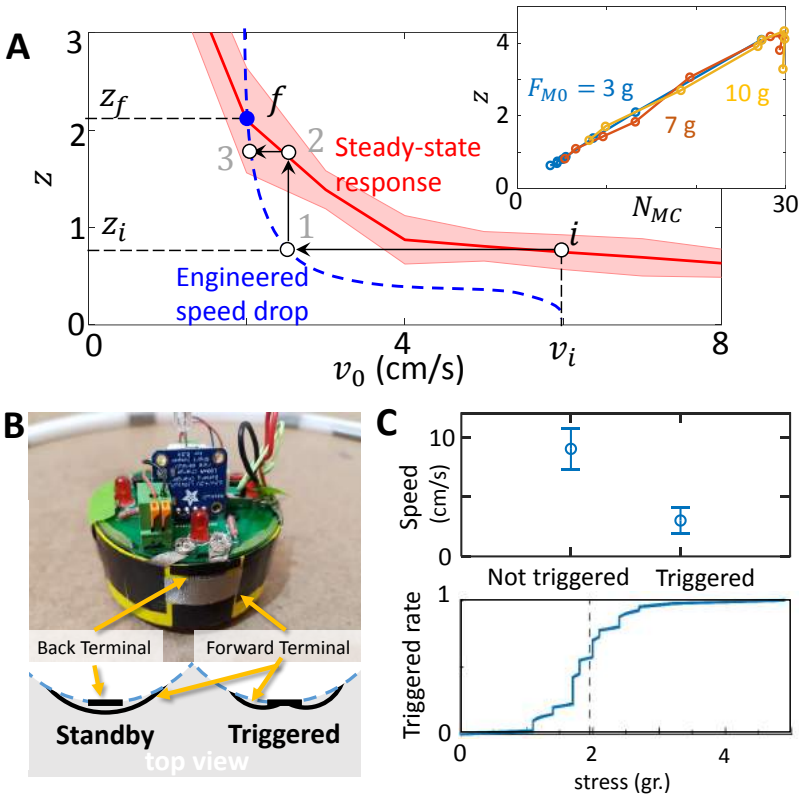

Figure 6.17: **Design and implementation of stress sensing for enhanced aggregation.** (**A**) The effect of the engineered, adaptive speeds (blue) on the steady-state average number of neighbors per BOBbot (red) for $F_{M0} = 3$ g. Without adapting speeds, BOBbots actuated at a given speed v_i would obtain an average of z_i neighbors per BOBbot at equilibrium (initial point i). With the adaptive speeds, an average of z_i neighbors per BOBbot causes the average speed to slow ($i \to 1$) which in turn enables convergence to the steady-state response with more neighbors per BOBbot ($1 \to 2$). This feedback iterates until the steady-state and engineered responses coincide at final point $f = (v_f, z_f)$, where $v_f < v_i$ and $z_f > z_i$. Inset: The mapping between maximum cluster size N_{MC} and the average number of neighbors per BOBbot z indicates the stress-sensing control strategy will increase component sizes. (**B**) A BOBbot equipped with a stress sensor and the schematic top-view sketch of the triggered and not-triggered states. (**C**) The BOBbot's response to stress. Top: the speed of a BOBbot when its sensor is and is not triggered. Bottom: The rate of sensor triggering as function of the stress applied. Photo Credit: Ram Avinery, Georgia Institute of Technology.

a proxy for β^{-1} in the effective attraction λ_{eff}. Consequently, we can mimic enhanced aggregation via increased magnet strength by reducing a BOBbot's speed as a function of its number of neighbors.

Without adapting a BOBbot's speed based on its number of neighbors, a BOBbot col-

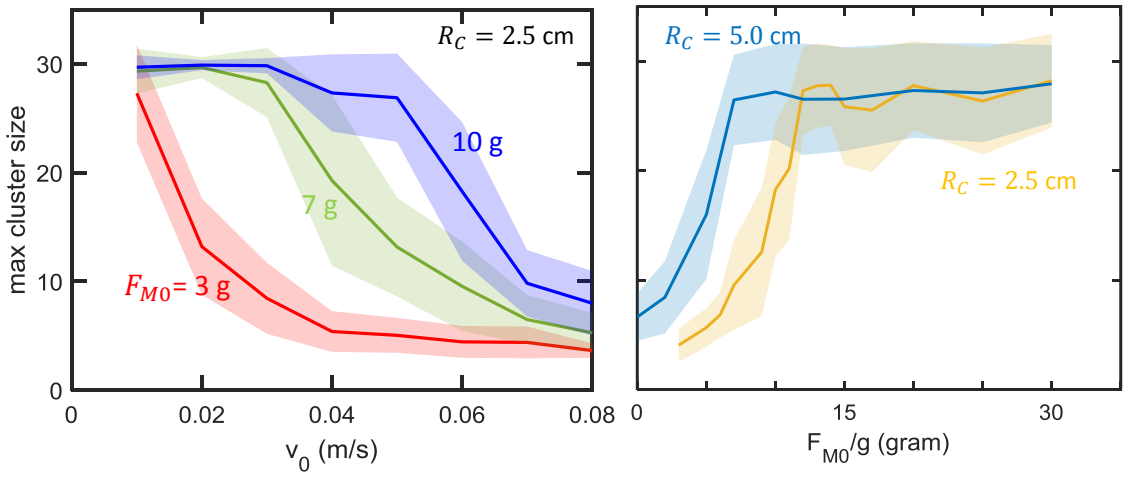

Figure 6.18: **Dependence of maximum cluster size N_{MC} on BOBbot speed v_0 and curvature R_C.** To investigate the effect of the BOBbots' individual speeds on the size of the maximum cluster, we run simulations for $F_{M0} = 3, 7, 10$ gf with 20 repetitions for 8 speeds equally spaced in range $v_0 = 1$–8 cm/s. Here we show how the maximum cluster size N_{MC} decreases as the BOBbots' individual speed is increased. We also find that N_{MC} increases with larger radii of curvature corresponding to decreased torque. The statistics shows the ensemble average from 20 simulations for each data point.

lective actuated uniformly at a speed v converges to an average of $z_{\text{std}}(v)$ neighbors per BOBbot at equilibrium (Figure 6.17A, red); any point in speed-neighbor space deviating from $z_{\text{std}}(v)$ is transient. To enhance aggregation, we engineer reduced speeds $v_{\text{eng}}(z)$ that a BOBbot with z neighbors should adapt to (Figure 6.17A, blue). These slowed speeds allow the collective to reconverge to a new steady-state with a larger number of average neighbors per BOBbot (Figure 6.17A, arrows). This feedback between the engineered speeds v_{eng} and the steady-state average number of neighbors z_{std} iterates until reaching the fixed point in speed-neighbor space where the steady-state and engineered behaviors meet as $z = z_{\text{std}}(v_{\text{eng}}(z))$.

While adapting speeds based on numbers of neighbors would be relatively straightforward to implement in more complex robots capable of counting neighbors (e.g., optically as in [241, 209, 242, 210]), implementing such a scheme in the deliberately simple BOBbots is challenging given their lack of such sensing. Here we utilize a second physical effect: inspired by the correlation of particle density and stress on individual particles in

granular systems [243], we propose that monitoring local contact stress can function as a proxy for counting numbers of neighbors. An immediate benefit of such a scheme is that it can be implemented on the existing robots via custom, low-cost, analog surface stress sensors (see Figure 6.17B and the Materials and Methods for details). The implemented stress sensors function such that for sufficiently large stress (e.g., when in a cluster), motor speed is decreased by 70% (Figure 6.17C).

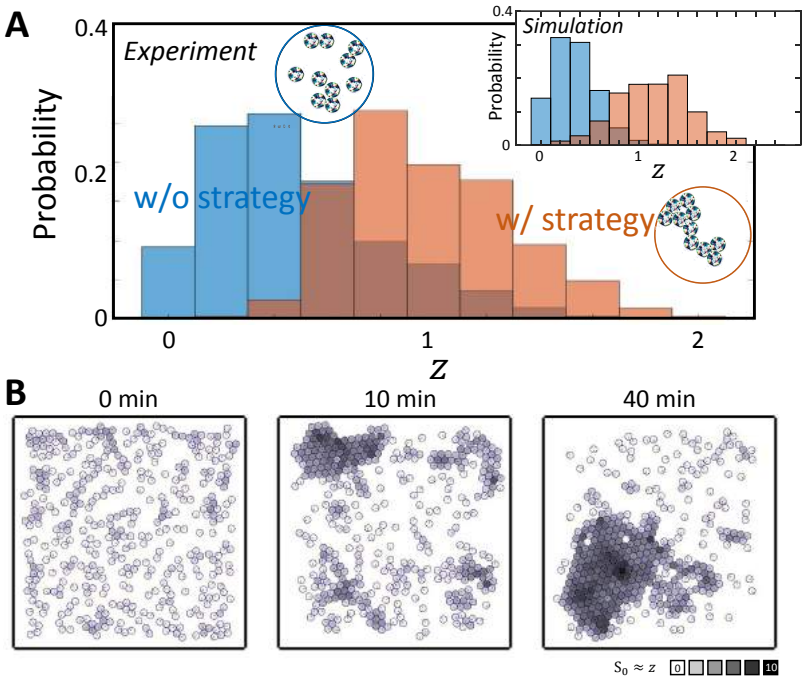

Figure 6.19: **Adapting speed via stress sensing enhances aggregation.** (**A**) The distribution of a BOBbot's number of contacts over six 10-minute experiments using $F_{M0} = 3$ g. Each sample is an average of number of contacts over 1 second. Inset: Simulation results using the same conditions as the experiment. (**B**) A simulation demonstrating enhanced aggregation in an ensemble of 400 BOBbots using a weak magnet strength of $F_{M0} = 7$ g. Each BOBbot's speed decreases from 6 cm/s to 1.2 cm/s as its stress $s_0 = \sum_{j \in \text{neighbors}} s_j / F_{M0} \approx z$ increases from 0 to 6, where z is its current number of neighbors. BOBbots in an aggregate's interior experience the most stress (dark gray) and thus have the slowest speeds, enabling larger aggregates to form. Without adapting speed in response to stress, the cluster sizes remain the same magnitude as in the 0 minute snapshot (left).

We implemented this "physical algorithm" on BOBbot ensembles with weakly attractive magnets. In experiments with ensembles of 10 BOBbots in a circular arena, adapting

BOBbot speeds in response to stress sensing significantly increases the average number of neighbors per BOBbot (Figure 6.19A). Further, there is a quantitative match in the final average number of neighbors per BOBbot between the experiments and the fixed points predicted in Figure 6.17A, validating our control strategy for enhancing aggregation. Simulations using the same arena and stress-mediated response reproduce the experimental results (Figure 6.19A, inset). In simulations of 400 BOBbots with $F_{M0} = 7$ g, we observe that BOBbots with more neighbors experience higher stress and thus have the slower speeds (Figure 6.19B). This stress-mediated decrease in speed enables large aggregates to form that would not have existed otherwise in the weakly attractive regime. The use of stress sensing opens an interesting avenue for collectives of rudimentary robots to incorporate higher-order information without complex vision systems; further, contact stress provides insights (e.g., closeness to a jamming transition) that could be valuable in densely packed clusters [9].

6.5 Stochastic non-robot transport

Encouraged by the close connections between the physical system and the underlying theoretical model along with the successful control scheme for enhanced aggregation using stress sensing, we sought to test whether aggregated BOBbots could collectively accomplish a task. In particular, could an aggregated BOBbot collective "recognize" the presence of a non-robot impurity in its environment and cooperatively expel it from the system? Typically, such collective transport tasks — e.g., the cooperative transport of food by ants [244, 245] — either manifest from an order-disorder transition or rely heavily on conformism between agents for concerted effort and alignment of forces. With our BOBbot collectives, we instead aim to accomplish transport via simple mechanics and physical interactions emergently controlling global behavior without any complex control, communication, or computation.

By maintaining a high magnetic attraction F_{M0}, we remain in the aggregated regime

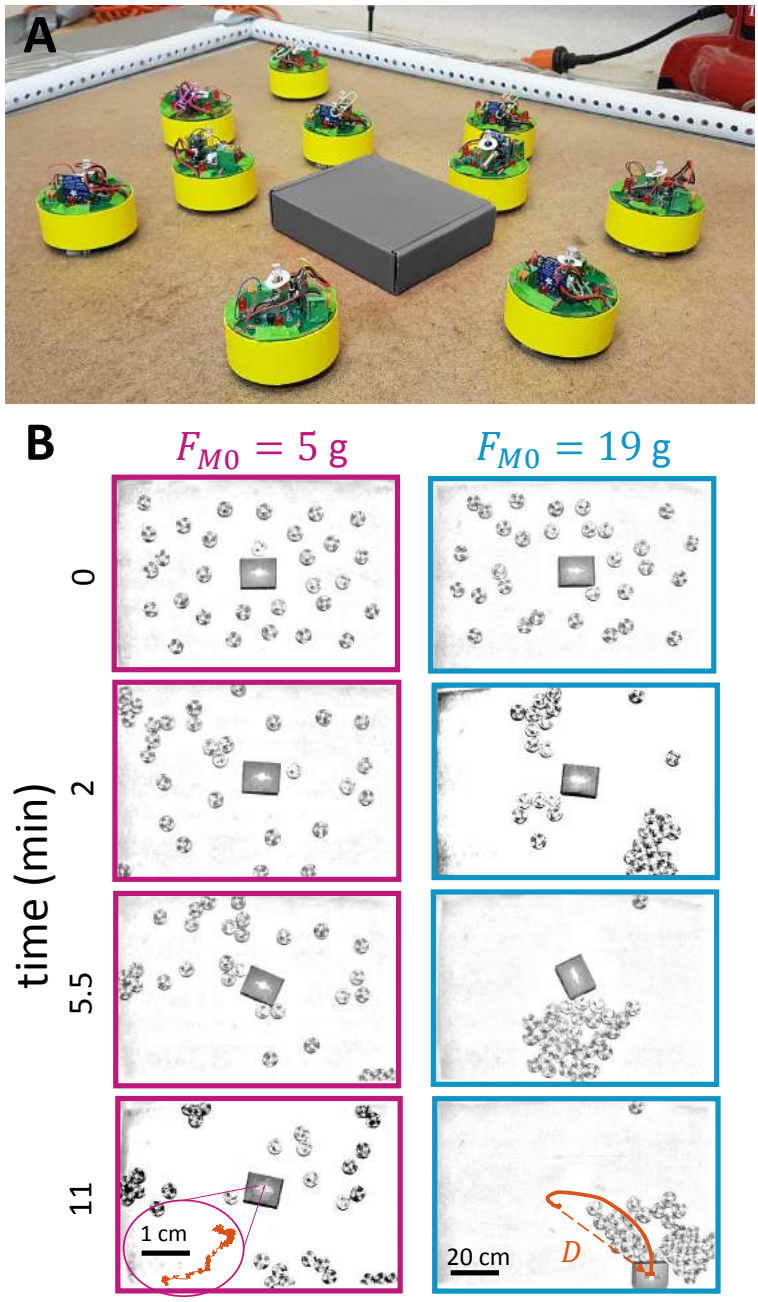

Figure 6.20: **Object transport using aggregation.** (**A**) Schematic of the experimental setup. (**B**) Time evolution snapshots of box transport by a system of 30 BOBbots with magnet strength $F_{M0} = 5$ g and 19 g. The box has a mass of 60 g. The final panel shows the object's complete trajectory, where D denotes the Euclidean distance of the final displacement. Photo Credit: Ram Avinery, Bahnisikha Dutta, Georgia Institute of Technology.

where most BOBbots connect physically and can cumulatively push against untethered impurities (e.g., a box or disk) introduced in the system (Figure 6.20A). The BOBbot

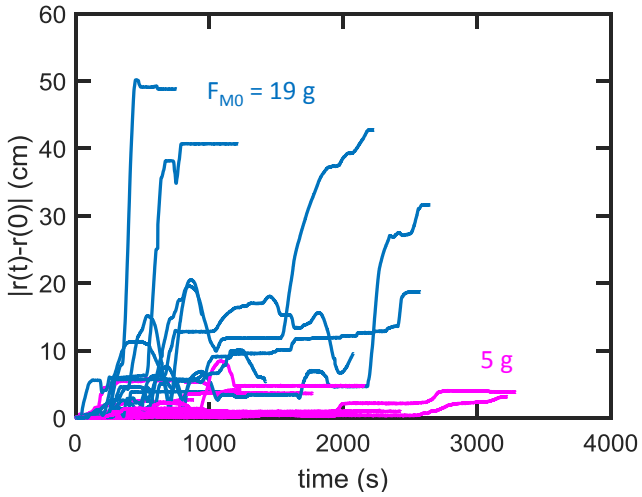

Figure 6.21: **Object transport trajectories.** Displacement of the box impurity over time for BOBbot collectives with $F_{M0} = 5$ g (magenta) and 19 g (blue).

collective's constant stochastic reconfiguration grants it the ability to envelop, grasp, and dislodge impurities as their individual forces additively overcome the impurities' friction, leading to large displacement in the aggregated regime (Figure 6.20B, right) with a median displacement of x7.9 cm over 12 minutes. On the contrary, we find that systems with weak magnetic attraction (i.e., those in the dispersed regime) can typically only achieve small impurity displacement (Figure 6.20B, left) with a median displacement of 0.9 cm over 12 minutes (see Figure 6.21 for distributions). We observe infrequent anomalies in which dispersed collectives achieve larger displacement than aggregated ones, but these outliers arise from idiosyncrasies of our rudimentary robots (e.g., an aggregated cluster of BOBbots may continuously rotate in place without coming in contact with an impurity due to the BOBbots' individual orientations in the aggregate.

Characterizing the impurity's transport dynamics as mean-squared displacement over time $\langle r^2(\tau)\rangle = v\tau^{\alpha}$ reveals further disparities between the aggregated and dispsered BOBbot collectives (Figure 6.23A). On a log-log plot, the intercept indicates $\log(v)$, where v is the characteristic speed of the impurity's transport; we observe that in all but one fringe case the strongly attractive collectives achieve transport that is orders of magnitude faster than those of the weakly attractive ones (Figure 6.23B). The slope of each trajectory indi-

cates the exponent α that characterizes transport as subdiffusive ($\alpha < 1$), diffusive ($\alpha = 1$), or superdiffusive ($\alpha > 1$). While all the strongly attractive collectives immediately achieve nearly ballistic transport (with $\alpha = 1.85 \pm 0.11$ for $\tau < 20$ s) indicating rapid onset of cluster formation and pushing, the weakly attractive collectives initially exhibit mostly subdiffusive transport (with $\alpha = 0.89 \pm 0.56$ for $\tau < 20$ s) caused by intermittent collisions from the dispersed BOBbots (Figure 6.23C). When the slight heterogeneous distribution of the dispersed BOBbots remains unchanged for a sufficiently long time, the accumulation of displacement in a persistent direction can cause a small drift, leading to ballistic transport at a longer time scale. These results align with the predictions of a simple model combining subdiffusive motion with small drift (Figure 6.22).

To validate this hypothesis, we developed a toy model in MATLAB where the subdiffusion $\mathbf{r}_H(t)$ with mean-squared displacement $\langle |\mathbf{r}_H(t+\tau) - \mathbf{r}_H(t)|^2 \rangle_t = Ct^{2H}$ (for $H < 1/2$) is generated by the fractional Brownian motion generator (from the MATLAB Wavelet Toolbox) and is added to a drift motion $\mathbf{r}_D(t) = \mathbf{v}_D t$. The relative magnitude difference between the subdiffusion and drift is chosen to match the experiments. When the drift is small (i.e., $|\mathbf{v}_D| = 0.005$), we observe two-stage transport dynamics consistent with the experiments (Figure 6.22, magenta). On the other hand, when the drift is dominant over the subdiffusion as in the strongly attractive collectives (i.e., $|\mathbf{v}_D| = 0.5$), the toy model reproduces the nearly ballistic trajectories observed in experiment (Figure 6.22, blue). In fact, the mean-squared displacement of this composed motion MSD$(\mathbf{r}_H + \mathbf{r}_D)$ is

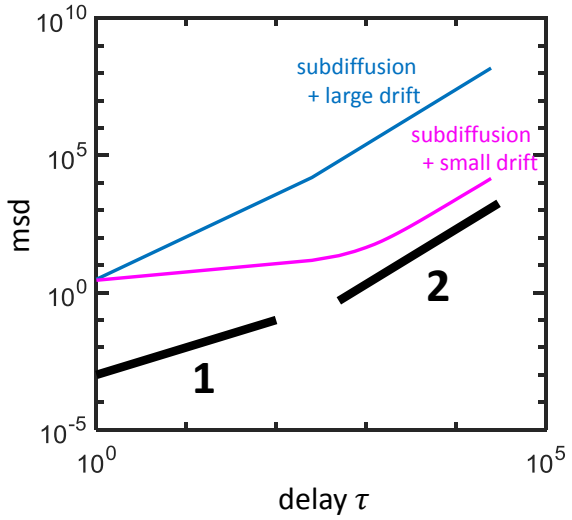

Figure 6.22: **Toy model for object transport.** Both trajectories include subdiffusive motion and drift. The blue curve has large drift while the magenta curve has small drift, representing transport by the strongly and weakly attractive BOBbot collectives, respectively. This model produces a qualitative match with the experiments, demonstrating the origin of the different types of mean-squared displacement over time in the transport experiments.

related to the purely subdiffusive $\mathrm{MSD}(\mathbf{r}_H)$ as:

$$
\begin{aligned}
\mathrm{MSD}(\mathbf{r}) &= \langle |\mathbf{r}(t+\tau) - \mathbf{r}(t)|^2 \rangle_t \\
&= \langle |\mathbf{r}_H(t+\tau) + \mathbf{r}_D(t+\tau) - \mathbf{r}_H(t) - \mathbf{r}_D(t)|^2 \rangle_t \\
&= \langle |(\mathbf{r}_H(t+\tau) - \mathbf{r}_H(t)) - \mathbf{v}_D t|^2 \rangle_t \\
&= \langle |(\mathbf{r}_H(t+\tau) - \mathbf{r}_H(t))|^2 \rangle_t + \langle 2\mathbf{v}_D \cdot (\mathbf{r}_H(t+\tau) - \mathbf{r}_H(t)) \rangle_t + \langle |\mathbf{v}_D|^2 t^2 \rangle_t \\
&= \mathrm{MSD}(\mathbf{r}_H) + 2\mathbf{v}_D \cdot \langle (\mathbf{r}_H(t+\tau) - \mathbf{r}_H(t)) \rangle_t + |\mathbf{v}_D|^2 t^2 \\
&= Ct^{2H} + |\mathbf{v}_D|^2 t^2
\end{aligned}
$$

where $\langle (\mathbf{r}_H(t+\tau) - \mathbf{r}_H(t)) \rangle_t$ vanishes due to the isotropy of subdiffusion. The final two equations demonstrate how the subdiffusive power is dominated by the ballistic power 2 when the drift speed $|\mathbf{v}_D|$ is large.

Nonetheless, the transport speeds achieved by the dispersed collectives are two orders of magnitude smaller than those of the strongly attractive ones.

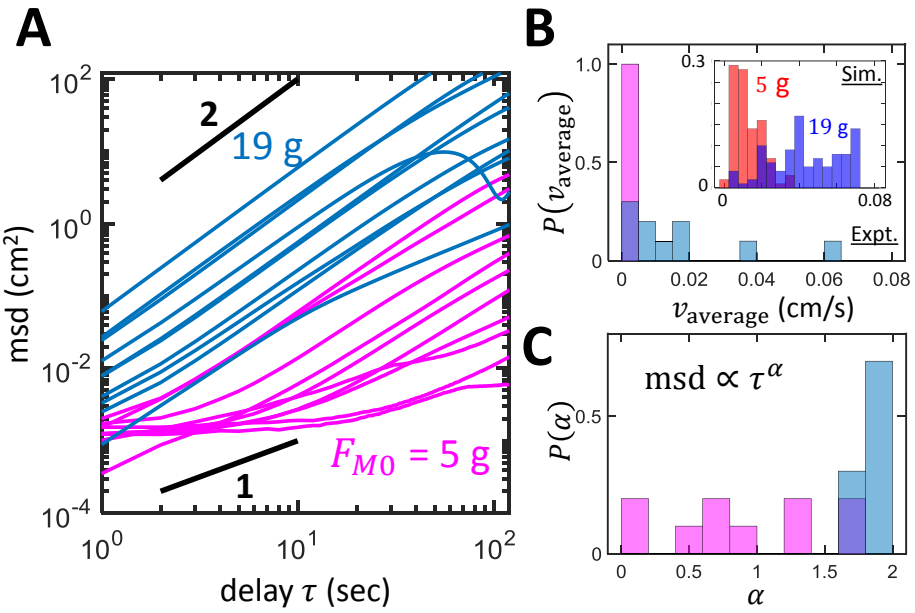

Figure 6.23: **Object transport using aggregation.** (**A**) Mean-squared displacement of the box over time in log-log scale for collectives with $F_{M0} = 5$ g (magenta) and 19 g (blue). (**B**) Distribution of the average speed, calculated as the final displacement D (as shown in Fig. Figure 6.20B) divided by total time. Inset: Simulation results for the overall transport speed. The two peaks for $F_{M0} = 19$ g correspond to pushing to the edges and corners. (**C**) Distributions of the mean-squared displacement exponent α at short time scale $\tau < 20$ s.

Simulations of impurity transport (see Figure 6.24 for details) reproduce the experimental results (Figure 6.23B, inset), including the rare anomalies. Seven of the 100 simulations of weakly attractive collectives succeeded in transporting the impurity to the arena boundary at slow speeds while 76 of the 100 simulations of strongly attractive collectives did so ballistically. The remaining 24 simulations of attractive collectives that did not achieve ballistic transport consistently formed an aggregate that never came into contact with the impurity. We found that disaggregating established aggregates by introducing time periods with no attraction enabled them to dissolve and reform for another attempt at transport. Using different disaggregating sequences, the attractive collectives achieved ballistic transport in 15–20% more simulations than without disaggregating (Figure 6.24).

In the additional DEM simulations with intermittent time periods with no attraction in order to dissolve and disaggregate formed aggregates. Our simulation demonstrates aggregates initially miss the obstacle to transport can find it successfully after disaggregating. All

three disaggregating sequences we investigated result in more successful transports to the boundary when compared to the base attractive case without disaggregating. As shown in Figure 6.24B, the remaining 24 cases out of the 100 where the transport used to be missed when no disaggregating sequences are applied can be partially remedied by the sequences.

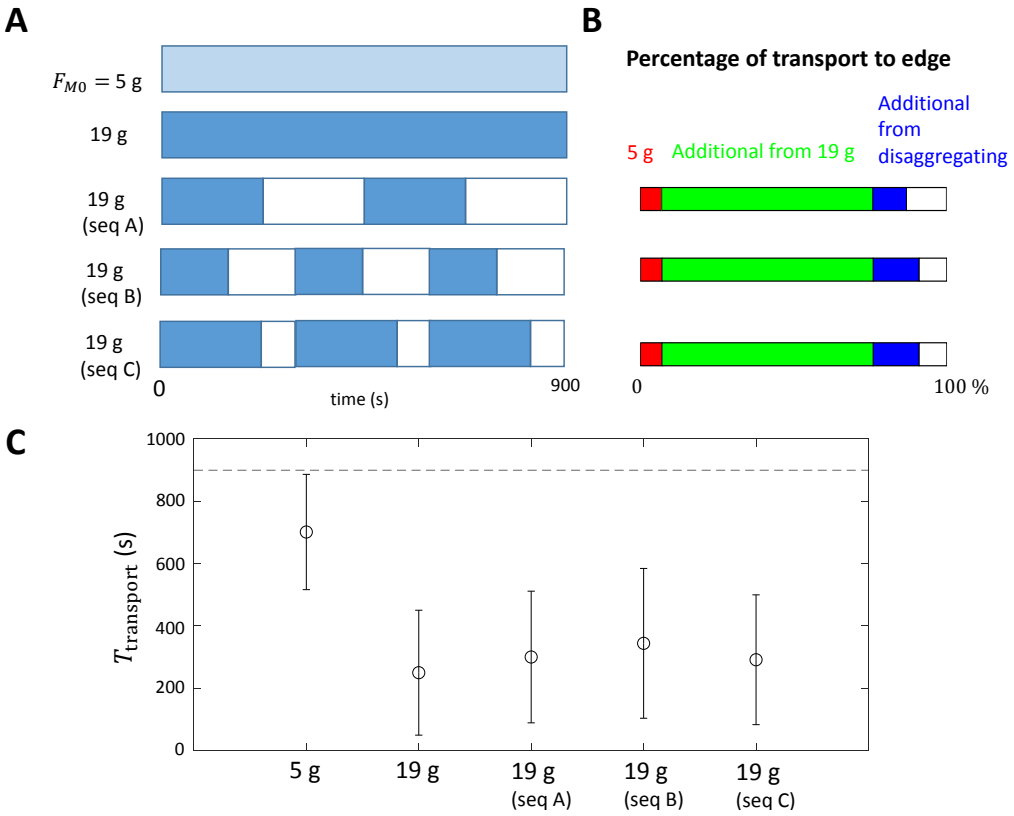

Figure 6.24: **Transport enhanced by disaggregating.** (**A**) Different patterns for magnetic strength over time used in simulations. The last three interleave periods of strong magnetic attraction with periods without any magnetic attraction (disaggregating). (**B**) The percentage of simulation runs achieved by weakly attractive collectives (red), strongly attractive collectives (green), and strongly attractive collectives with disaggregating (blue). The statistics use 100 simulations for each scenario. (**C**) Comparison of transport time to the boundary among collectives that are weakly attractive, strongly attractive, and strongly attractive with disaggregating.

Physically and interestingly, in the Cahn–Hilliard picture, impurity transport can be interpreted as the expulsion of an obstacle in a continuum mixture with sufficiently high surface tension to yield phase separation. If the obstacle occupies a position that is later occupied by the solid phase, the obstacle is expelled due to sterical exclusion; when its po-

sition is unvisited by the solid phase during the process of coarsening, however, it remains stagnant, similar to the anomalies for attractive collectives. In this interpretation, disaggregating effectively repeats the coarsening process to that the probability any given position is unvisited by the solid phase is significantly diminished.

6.6 Conclusions

In this chapter, we use mathematical ideas from distributed computing and statistical physics to create task-oriented cohesive granular media composed of simple interacting robots called BOBbots. As predicted by the theory, the BOBbots aggregate compactly with stronger magnets (corresponding to large bias parameter λ) and disperse with weaker magnets (or small λ). Simulations capturing the physics governing the BOBbots' motions and interactions further confirm the predicted phase change with larger numbers of BOBbots. The collective transport task then demonstrates the utility of the aggregation algorithm.

There are several noteworthy aspects of these findings. First, the *theoretical framework* of the underlying SOPS model can be generalized to allow many types of relaxations to its assumptions, provided its dynamics remain reversible and model a system at thermal equilibrium. For example, noting that the probability that a robot with n neighbors detaches may not scale precisely as λ^{-n} as suggested by the Boltzmann weights, we can generalize the SOPS model to be more sensitive to small variations in these weights: the proofs establishing the two distinct phases can be shown to extend to this setting, provided the probabilities p_n of detaching from n neighbors satisfy $c_1\lambda^{-n} \leq p_n \leq c_2\lambda^{-n}$, for constants $c_1, c_2 > 0$.

The *robustness* of the local, stochastic algorithms makes the macro-scale behavior of the collective resistant to many types of idiosyncrasies inherent in the BOBbots, including bias in the directions of their movements, the continuous nature of their trajectories, and nonuniformity in their speeds and magnet strengths. Moreover, our algorithms are inherently self-stabilizing due to their memoryless, stateless nature, always converging to a

desired system configuration — overcoming faults and other perturbations in the system — without the need for external intervention. In our context, the algorithm will naturally continue to aggregate, even as some robots may fail or the environment is perturbed.

We find agreement not only between the BOBbot ensembles and the discrete SOPS model, but also with *continuum models of active matter*. The SOPS algorithm for aggregation and dispersion was initially defined as a distributed, stochastic implementation of a fixed magnetization Ising model. In addition to showing that our experimental system follows guarantees established by the analysis of a discrete model, we also observe that the growth of its largest component matches the power-law derived for the Cahn–Hilliard equation, a continuous analog of the Ising model [240]. This mapping provides an intuitive understanding of how the SOPS bias parameter λ, the physical inter-BOBbot attraction F_{M0}, and the surface tension γ in the Cahn–Hilliard equation correspond; thus, as γ controls the phase change in the Cahn–Hilliard equation, so do λ and F_{M0} in their respective settings. This observation buttresses our confidence that the SOPS model provides a useful algorithmic framework capable of producing valid statistical guarantees for ensembles of interacting robots in continuous space.

Moreover, we find that the *nonequilibrium dynamics* of the BOBbots are largely captured by the theoretical models that we analyze at thermal equilibrium, which is in agreement with the findings of Stenhammar et al. [246]. For example, in addition to visually observing the phase change as the magnetic strengths increase, we are able to test precise predictions about the size and perimeter of the largest connected components based on the formal definitions of aggregation and dispersion from the SOPS model. We additionally use simulations to study the transition probability of a BOBbot from having n neighbors to having n' neighbors to see if the magnetic interactions conform to the theory, and indeed we see a geometric relation decrease in the probability of moving as we increase the number of neighbors, as predicted. The resultant correspondence between the magnetic attraction and effective bias in the algorithm confirms a quantitative connection between the physical

world and the abstract algorithm.

In terms of our contribution to active matter, we notice that very few active matter studies use robots more complicated than bristlebots in flat environments. Our study has extended this field first by introducing short-ranged attraction and then with active control. Active matter with active response to the environment could have practicality, such as mitigating mergers (subsection 2.3.2) and promoting clusters to perform tasks an individual cannot do.

In summary, the framework presented here using provable distributed, stochastic algorithms to inspire the design of robust, simple systems of robots with limited computational capabilities seems quite general. It also allows one to leverage the extensive amount of work on distributed and stochastic algorithms, and equilibrium models and proofs in guiding the tasks of inherently out of equilibrium robot swarms. Preliminary results show that we likely can achieve other basic tasks such as alignment, separation (or speciation), and flocking through a similar principled approach. We note that exploiting physical embodiment with minimal computation seems a critical step in scaling collective behavior to encompass many cutting edge settings, including micro-sized devices that can be used in medical applications and cheap, scalable devices for space and terrestrial exploration. Additionally, we plan to further study the important interplay between equilibrium and nonequilibrium dynamics to better solidify these connections and to understand which relaxations remain in the same universality classes.

CHAPTER 7
CONCLUSIONS AND FUTURE DIRECTION

7.1 Summary

In this dissertation, we have explored field-mediated interactions in active matter systems with three examples (chapter 2-chapter 4). In each example, we have observed phenomena not seen in conventional passive systems and understood some mechanisms with models constructed from experiment and theory. We have designed further experiments to utilize the active feature based on these mechanisms.

In Chapter 2, we extended the passive marbles in the mechanical gravity analog of marbles on a membrane with a differential driven vehicle. With this improvement, one can create steady-state orbits with more control parameters such as the speed. A mapping from the classical dynamics of a single vehicle to the motion in a curved spacetime allows one to design arbitrary spacetime by controlling these parameters. As an example, we show that one can create Schwarzschild metric by using this mapping. The established mapping has further allowed us to understand the precession sign of a single-vehicle orbit and helped us revert the precession sign by changing the vehicle mass. The generalization of the single vehicle dynamics and the Poisson equation for the elastic membrane allow us to model the interaction between multiple vehicles. The model is verified by double-vehicle mergers in experiments and helps design a control scheme which increases the vehicle speed with the instantaneous tilt angle to help the vehicles avoid mergers. The scheme works for both the two-vehicle case and the five-vehicle case. Based on the theoretical explanation to the five-vehicle case, we posit that the scheme will work for even larger systems.

In Chapter 3, we investigated another field-mediated case where the light intensity of a 2 m by 2 m LED screen represents the food resource for a swarm of cm-scale robots

which roam and consume the resource. At the same time, the resource also replenishes itself. The robots move along the resource gradient and consume resource where they pass through. Besides the drive force created by the gradient following, the cavities made by the resource consumption create field-mediated mutual repulsion between the robots. Depending on the density of the swarm and the resource replenishing rate, the swarm form various of states such as the gas state, the crystalline state, the liquid state, and the glass-like state. In the extended study of this system, the resource is composed of three components (R,G,B) at each position and each robot is equipped with 3 bytes of gene, either dominant or recessive, corresponding to the ability to consume the different resource (R,G,B), The robots exchange gene and the phenotype is determined by the Mendelian rule. A robot may die due to the non-fitting phenotype in the wrong type of resource and can be resurrected by two living robots coming to the rescue. Depending on the spatio-temporal pattern of the resource, the survival rate of the robots varies. We further find that the survival rate increases with the diversity of the phenotype.

In Chapter 4, we created a type of three-link shape-changing particle (*smarticle*) resembling a staple to investigate the role of articulated shape changes in active matter. While an individual could not move, a collective of smarticles (*supersmarticle*) confined in a moveable ring could move diffusively through their interaction with the substrate enabled by the inter-particle collisions. The ring acts a one-dimensional substrate and mediates the interactions between the smarticles. Additionally, when one of the individuals becomes inactive, not only the collective could still move, but as well the broken symmetry could be utilized to direct the motion. The drift direction and magnitude depend on the ratio between the inactive smarticle mass and the ring mass. This feature has allowed designing a phototaxis supersmarticle by making each smarticle respond to the light. For example, we have made each smarticle freeze when detecting light and obtained a phototaxis supersmarticle.

In addition to active systems under field-mediated interaction, this thesis also includes two studies on active matter with fixed or no environmental effect. Nonetheless, in the

future, it would be curious to extend these two research with field-mediated versions.

In Chapter 5, we created an individual shape-changing active matter (*swimmer*) constrained on a sphere to study how the curvature of the space affects the locomotion of active matter. The swimmer is composed of four masses that we are able to program their relative position over time (gait). By prescribing a gait that encloses geometric phase, the swimmer can locomote on the sphere (a curved smooth substrate) without exchanging momentum with the substrate by utilizing the geometric phase from the curvature. Additionally, we have found that in the realistic case with friction and residual potential, the geometric phase will generate a drive force proportional to it to help the swimmer get out of the potential well.

In Chapter 6, we studied the clustering dynamics of active matter with short-ranged attraction force realized by magnetic attraction. We have observed that the lab-brewed robots (BOBbots), which circle around individually in free space and attract each other through loose magnets in the peripheral, cluster as a collective over time. With a larger magnetic attraction, the final cluster size gets larger. DEM (discrete element method) simulations with physical parameters directly measurement have matched with the experiments and showed that the clustering behavior capture is captured the physics by Langevin-type equations. Based on the simulations, we discovered the dynamics can be mapped to a lattice gas model (SOPS), which is equivalent to the fixed-magnetization Ising model (FMI). Further, a bridge between FMI and Cahn-Hilliard model explains the critical strength of magnetic attraction to allow clustering and the growth rate of the clusters. Due to the algorithmic nature of lattice gas, this system provides us with a programmable matter, and we later showed that decreasing the robot speed could generate larger clusters, and the clusters could be used to clean obstacles in the arena.

7.2 Future directions

7.2.1 Analog models of field-mediated interaction

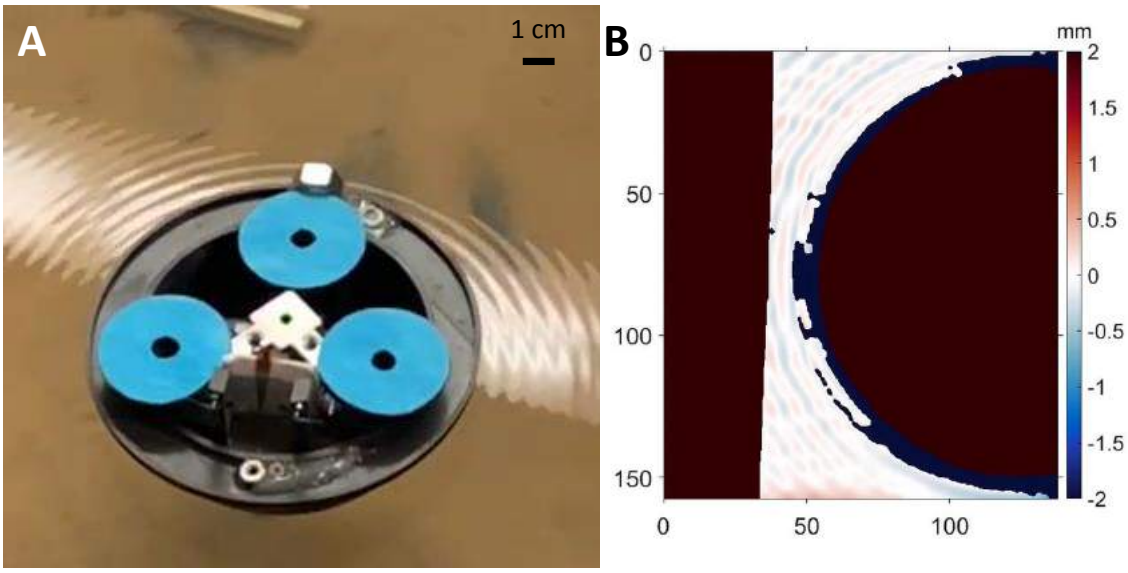

Figure 7.1: **Analog Casimir Force from a Self-propelling Vibrating Robot Boat.** (A) A vibrating boat floating on water generates wave that back reacts on the boat. (B) Schlieren imaging [247] of the wave around the boat. Credits to Steven Tarr.

As we have seen in the introduction (subsection 1.4.3), analog models can help us understand and explore physical phenomena by thinking about the similarity and differences between the two models and applying the findings back and forth. For instance, in chapter 2, we have shown that the tool from field theory, differential geometry has helped us understand the functional role of parameters in field-mediated interaction and guided us design useful control strategy to revert the orbital dynamics and avoid mergers. Given the extensive study of classical and quantum fields in the past few centuries, we are optimistic to see more inspiration be utilized in active matter under field-mediated interaction. For instance, A Ph.D. student, Steven Tarr from our lab has found that a vibrating boat in a water tank (Figure 7.1) can interact with the boundary in a fashion analogous to the Casimir effect explained by the Quantum Field Theory[53]. Depending on the vibration frequency of the boat and the initial distance from the boundary, the boat will either get attracted or

repelled by the boundary. If one could understand how this interaction depends on these conditions, we would have a control scheme to let an active floating object attract or avoid boundary.

7.2.2 Using lattice gas to understand living systems

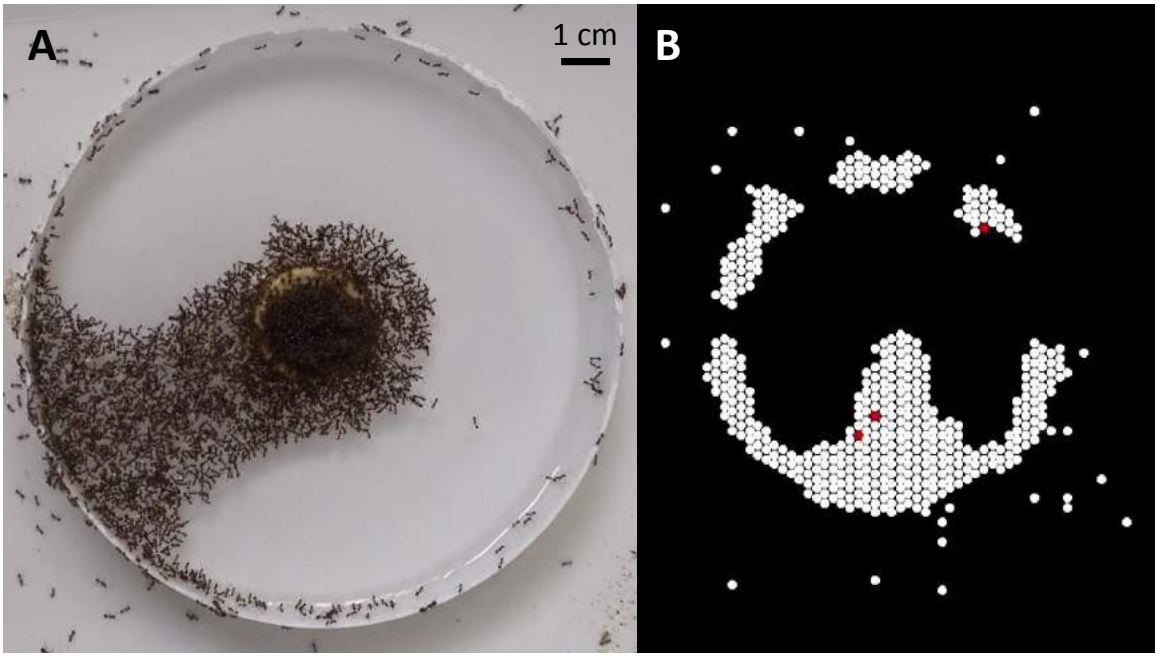

Figure 7.2: **Ants build a pontoon bridge across the water to fetch food.** (A) Top view of ants (*Solenopsis invicta*) building a pontoon bridge from the rim of a bowl filled with water to the peanut butter at the center of the bowl. Credit to Haolin Zeng. (B) A lattice gas algorithm that mimics the ant briding behavior. Credit to Noah Egan.

As we have seen in chapter 6 and other examples ([9, 248]), the lattice gas approach can be useful in modeling and understanding active matter and living systems. In chapter 6, we further benefited from the lattice model in that it can convert to continuum theory that helps us understand the functional role of the system parameters. Besides the Ising model - Cahn Hilliard equation correspondence we have seen in chapter 6, such tools exist in many other lattice models such as cellular automata[249]. It will be fruitful to explore more phenomena using this methodology. We have recently tried to understand ants building pontoon bridges to fetch food[250] (Figure 7.2A) with a lattice gas model. Having difficulty in equilibrium

lattice gas (Figure 7.2B), a non-equilibrium model has been found to capture some features of this process, and we look forward to analyzing it using this methodology.

7.2.3 Mechanical response to stress

In chapter 6, we find that the mechanical response to stress can be useful in controlling cluster formation. In this work, we have also found that when the robots cluster, they can clear the obstacles that a single robot cannot. However, in this case, the direction of obstacle cleaning is not directed. Nonetheless, if we can combine these two features together, it is possible we can direct the cluster to move an object as desired. To do so, we plan to apply stress sensors to each individual robot to recognize the obstacle while they roam around in the arena and then push together once the concerted force is satisfied. Besides this particular example, we believe the response to stress information would allow us to perform many more tasks given the rich spatio-temporal patterns one could get in granular material, which the active agents mimic.

7.2.4 Exploring more ecological systems with artificial active matter

In chapter 3, we have seen how a robotic active matter can help us understand the principle of an ecological system and provides us with insights into the control of living systems. In the future, we can continue to use this method to explore more ecological systems, even including the social dynamics of human society[39, 50]. Given the trend of human society that individuals are more distributed and can influence society much more than before while the society still has the power to affect individuals, this understanding might be helpful[251, 252].

Appendices

APPENDIX A

GR ROBOT

A.1 Probing the effective friction

Although the rolling friction can be complicated and the dissipation into the membrane could make it even more complicated, we probe the magnitude of an effective friction that absorbs all dissipative forces by doing the following experiment. We release the marble at the rim of the circular membrane with zero speed and thus zero kinetic energy. The marble then rolls radially towards the center, passes through the center, and stops before it reaches the other end of the diameter due to the effective rolling friction. Absorbing the loss of mechanical energy into the dissipation from the effective rolling friction f_{roll} for a distance of ℓ, we arrive at

$$f_{\text{roll}}\ell = mg\Delta h \tag{A.1}$$

The measurements from experiment that $\ell = 1.5$ m, $\Delta h = 0.1$ m give the effective friction coefficient $\mu = f_{\text{roll}}/mg = \Delta h/\ell = 0.07 \sim 0.1$.

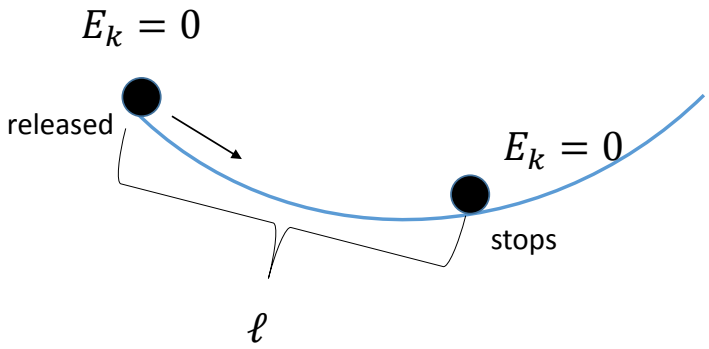

Figure A.1: **An experiment to probe the effective friction.**

A.2 Converting derivatives

With the help of $\mathring{q} \equiv \frac{dq}{d\lambda} = \frac{dt}{d\lambda}\frac{dq}{dt}$ and $\alpha^2 \mathring{t} = E, \Phi^2 r^2 \mathring{\varphi} = L$ in Eqs. Equation 2.11,Equation 2.12, we have

$$
\begin{aligned}
\mathring{t} &= \frac{E}{\alpha^2} && \text{(A.2)}\\
\mathring{\mathring{t}} &= \frac{dt}{d\lambda}\frac{d\mathring{t}}{dt} \\
&= \frac{E}{\alpha^2}\frac{d}{dt}(\frac{E}{\alpha^2}) \\
&= -\frac{E^2(\alpha^2)'}{(\alpha^2)^3}\dot{r} && \text{(A.3)}\\
\mathring{r} &= \frac{dt}{d\lambda}\frac{dr}{dt} = \frac{E}{\alpha^2}\dot{r} && \text{(A.4)}\\
\mathring{\mathring{r}} &= \frac{dt}{d\lambda}\frac{d\mathring{r}}{dt} \\
&= \frac{E}{\alpha^2}\cdot\frac{d}{dt}(\frac{E}{\alpha^2}\dot{r}) \\
&= \frac{E^2}{(\alpha^2)^2}\cdot\left(-\frac{(\alpha^2)'}{\alpha^2}\dot{r}^2 + \ddot{r}\right) && \text{(A.5)}\\
\mathring{\varphi} &= \frac{dt}{d\lambda}\frac{d\varphi}{dt} = \frac{E}{\alpha^2}\dot{\varphi} && \text{(A.6)}\\
\mathring{\mathring{\varphi}} &= \frac{dt}{d\lambda}\frac{d\mathring{\varphi}}{dt} \\
&= \frac{E}{\alpha^2}\frac{d}{dt}(\frac{E}{\alpha^2}\dot{\varphi}) \\
&= \frac{E^2}{(\alpha^2)^2}\cdot\left(-\frac{(\alpha^2)'}{\alpha^2}\dot{r}\dot{\varphi} + \ddot{\varphi}\right). && \text{(A.7)}
\end{aligned}
$$

A.3 Programming the metric

By eliminating the k in Eqs. Equation 2.27,Equation 2.28, we get

$$MV - V' = \frac{(\alpha^2)'}{\Phi^2} \tag{A.8}$$

where $M(r) = 2(\alpha^2)'(r)/\alpha^2(r) - (\Phi^2)'(r)/\Phi^2(r)$ and $V(r) = v^2(r)$.

We can multiply a function $f(r)$ to both sides of Equation A.8 to make the left hand

side exact. Noting $(fV)' = f'V + fV'$, we need $f'/f = -M$. Therefore,

$$f(r) = -e^{\int_{r_1}^{r} -M(r')dr'}. \tag{A.9}$$

With this f, we now have $(fV)' = f\ (\alpha^2)'/\Phi^2$. So,

$$V(r) = \left(\int_{r_1}^{r} f(r') \cdot \frac{(\alpha^2)'(r')}{\Phi^2(r')} dr'\right) \cdot \frac{1}{f(r)}. \tag{A.10}$$

By plugging in the Schwarzschild metric in isotropic coordinates $\alpha^2(r) = 1 - r_s/r$, $\Phi^2(r) = (1 - r_s/r)^{-1}$, we have

$$\begin{aligned} f(r) &= -e^{\int_{r_1}^{r} -\frac{3r_s}{r'(r'-r_s)} dr'} \\ &= -e^{(C_1 + 3\log(r/(r-r_s)))} \\ &= -C_2 \cdot \left(\frac{r}{r-r_s}\right)^3. \end{aligned} \tag{A.11}$$

Therefore,

$$\begin{aligned} V(r) &= \left(\int_{r_1}^{r} C_2 \cdot \left(\frac{r'}{r'-r_s}\right)^3 \cdot \frac{(r'-r_s)r_s}{r'^3} dr'\right) / f(r) \\ &= \left(\int_{r_1}^{r} C_2 \cdot \frac{r_s}{(r'-r_s)^2} dr'\right) / f(r) \\ &= (-C_2 \frac{r_s}{r-r_s} + C_3) / (-C_2 \cdot \left(\frac{r}{r-r_s}\right)^3) \\ &= r_s \frac{(r-r_s)^2}{r^3} + C\left(\frac{r-r_s}{r}\right)^3 \end{aligned} \tag{A.12}$$

$$\begin{aligned} k(r) &= -\frac{(\Phi^2)'V - (\alpha^2)'}{2\Phi^2} \\ &= \frac{(r-r_s)r_s(r + Cr + r_s - Cr_s)}{2r^4}. \end{aligned} \tag{A.13}$$

To program the active object physically, we want to prescribe the speed v_0 at a certain radius (say the inner radius r_0) so that $V(r_0) = v_0^2$, we need

$$C = \frac{v_0^2 r_0^3}{(r_0 - r_s)^3} - \frac{r_s}{r_0 - r_s}. \tag{A.14}$$

Further, a reasonable speed v_c at a characteristic orbit size (say the circular orbit r_c) will limit the size of the Schwarzschild radius r_s (the size of the black hole) with $\frac{V(r_c;r_s)}{r_c} = k(r_c)$.

A.4 Vehicle dynamics

The dynamics of the vehicle on an incline with slope γ, which is a localized representation of substrate under the vehicle helps explain the acceleration's dependence on the heading θ and local tilting angle γ (Figure A.2a) in experiments. On the incline, we denote the direction along the gravity as $\parallel$ and the direction perpendicular to it as $\perp$ so that the acceleration from the gravity field is $a_\perp^g = 0, \sim a_\parallel^g = g \sin\gamma$ (Figure A.2b). Considering this incline as a localized picture of the vehicle's immediate substrate, here $\hat{\perp}$ direction stands for the $\hat{\varphi}$ and $\hat{\parallel}$ direction stands for the $\hat{r}$[1].

Since the friction on the rolling caster is much smaller than the other friction forces, the vehicle rotates about the middle point of the wheel axis, M. The torque about M consists of the frictions on the two wheels and the caster, as well as the gravity component in the plane. Since the two wheels are connected to a differential drive, the torques generated by the friction parallel to the wheel $f_{L\parallel}, f_{R\parallel}$ are of same magnitude and opposite signs and therefore cancelled out. The torques generated by the friction perpendicular to the wheel are zero since the forces pass through M.

The non-zero torques left with us are the one generated by the gravity component in the

[1]The model in this section is a joint work with Charles Xiao.

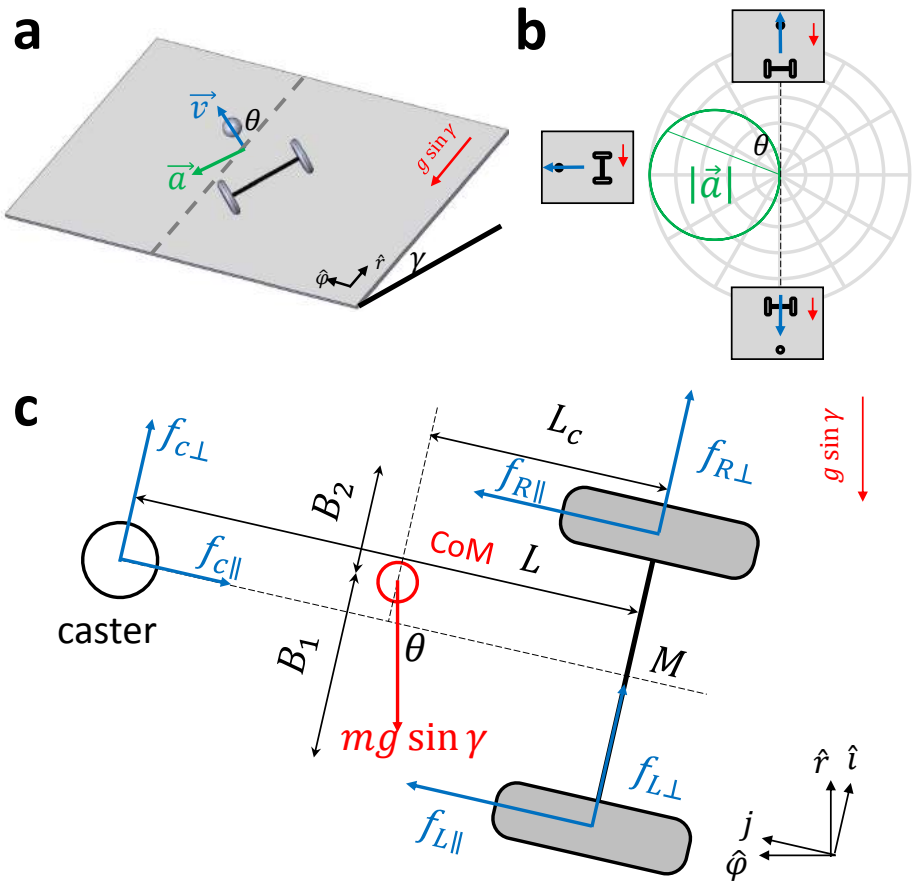

Figure A.2: **Vehicle dynamics of the robotic vehicle.** (a) Modelling the dynamics of the vehicle on a slope with incline angle equalled to its current tilt γ. (b) The magnitude of the acceleration changes with the heading angle θ and vanishes when going along the gradient of the incline. (c) The force diagram of the vehicle.

plane and the friction from the caster f_c:

$$\begin{aligned} \tau &= \left(\Delta B\,\hat{\imath} + L_c\,\hat{\jmath}\right) \times \\ &\quad mg\sin\gamma(-\sin\theta\,\hat{\imath} - \cos\theta\,\hat{\jmath}) + L\,\hat{\jmath} \times f_{c\perp}\,\hat{\imath} \qquad \text{(A.15)} \\ &= \left(mg\sin\gamma\,(-\Delta B\cos\theta + L_c\sin\theta) - f_{c\perp}L\right)\hat{k} \qquad \text{(A.16)} \end{aligned}$$

where $\Delta B \equiv \frac{1}{2}(B_2 - B_1)$.

The moment of inertia of the vehicle with respect to M is $I = I_{\text{vehicle}} + m(L^2 + \Delta B^2)$ where we approximate $I_{\text{vehicle}} = \frac{1}{2}mR_v^2$ with R_v being the radius of the vehicle since the

mass distribution is quite homogeneous. Therefore the magnitude of the angular acceleration ($\beta = \tau \cdot \hat{k}/I$) and the acceleration of the center of mass is

$$\begin{aligned} a &= \left| L_c\, \hat{j} + \Delta B\, \hat{i} \right| \cdot \beta && \text{(A.17)} \\ &\approx L_c \cdot \frac{\tau \cdot \hat{k}}{I} && \text{(A.18)} \\ &= \frac{mg \sin\gamma (L_c \sin\theta - \Delta B \cos\theta) - f_c L}{\frac{1}{2} m R_v^2 + m L_c^2 + m \Delta B^2} L_c && \text{(A.19)} \end{aligned}$$

For the ideal case that the center of mass is not biased to the left or right so that $B_1 = B_2$, the acceleration is

$$\begin{aligned} a &= \frac{mg L_c \sin\gamma \sin\theta - f_c L}{\frac{1}{2} m R_v^2 + m L_c^2} L_c \\ &= \frac{L_c^2}{\frac{1}{2} R_v^2 + L_c^2} g \sin\gamma \sin\theta - \frac{f_c L}{\frac{1}{2} m R_v^2 + m L_c^2} && \text{(A.20)} \end{aligned}$$

When $\theta = \pi/2$ and f_c being very small since this is a rolling friction, the acceleration projected onto the horizontal plane is

$$a(\theta = \pi/2) \approx \frac{L_c^2}{\frac{1}{2} R_v^2 + L_c^2} g \sin\gamma \cos\gamma \qquad \text{(A.21)}$$

The actual numbers in the experiment $R_v = 5$ cm, $L_c \approx 1$ cm give the theoretical prediction

$$a_{\text{theo}}(\theta = \pi/2) \approx 0.074\ g \sin\gamma \cos\gamma \qquad \text{(A.22)}$$

which is quite close to the experimental measurement

$$a_{\text{expt}}(\theta = \pi/2) = (0.073 \pm 0.001)\ g \sin\gamma \cos\gamma \qquad \text{(A.23)}$$

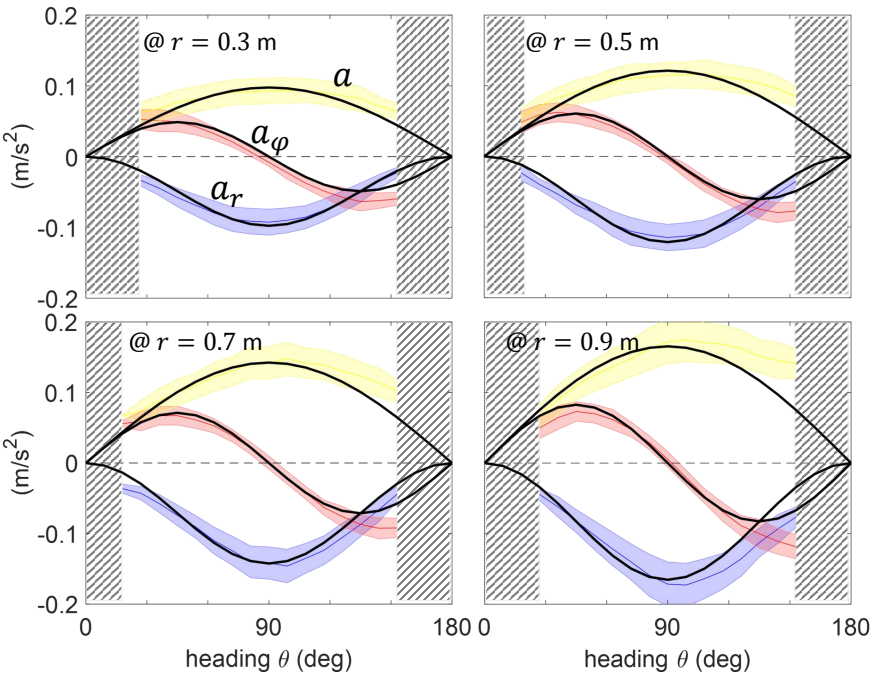

Figure A.3: **Acceleration at different radii.** The shading colored in yellow, red and blue are the magnitude a, and the azimuthal, radial components a_φ, a_r of the acceleration respectively from experiments. The black lines are the theory $a = k(r) \cdot \sin\theta$, $a_r = -a\sin\theta$, and $a_\varphi = a\cos\theta$ where $k(r)$ takes the mean value shown in 4c in the main text.

In reality, there is always a small bias between B_1 and B_2, this small correction from the CoM (center of mass) offset that breaks the symmetry of acceleration with respect to the heading gives the attraction to the circular orbit and will is discussed in Section S3.

This bias is

$$a_{\text{bias}} = -g\,\sin\gamma\cos\theta\,\frac{L_c\Delta B}{\frac{1}{2}R^2 + L_c^2 + \Delta B^2} \tag{A.24}$$

where ΔB can be measured by weighing the normal force on the left and right wheels and given by

$$\Delta B = \frac{L_w}{2}\frac{N_R - N_L}{N_R + N_L} \tag{A.25}$$

where N_L, N_R are the normal forces on the two wheels and $L_w = 6$ cm. For an imbalance

of $(N_R - N_L)/(N_R + N_L) \approx 20\ \%$ thus $\Delta B \approx 0.6$ cm. Thus, the maximum bias ($\theta = 0°, 90°$) when driving on a typical local slope of $\gamma = 10°$ is $a_{\text{bias}} = 0.074$ m/s^2, which is about $40\ \%$ of the maximum magnitude of the acceleration in the system. Figure A.4 shows how this bias causes the slight dependence on θ.

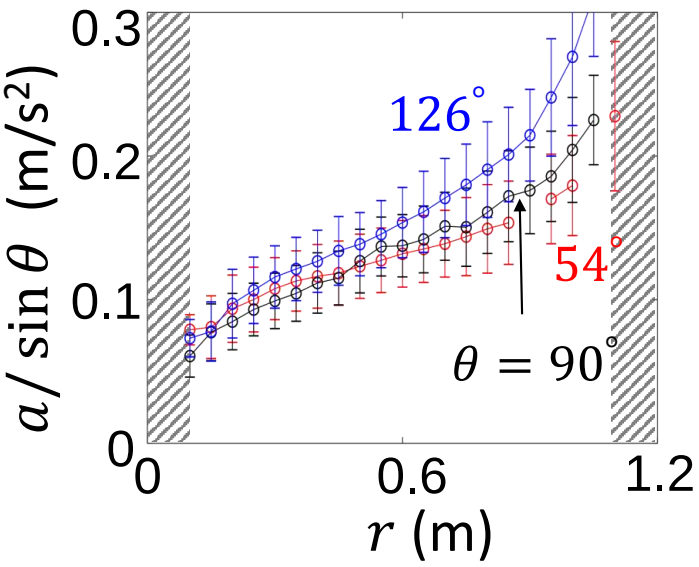

Figure A.4: Plots of k as a function of r for various values of θ using $a/\sin\theta$. The gray shaded regions refer to regions which are forbidden due to steric exclusion.

A.5 Transient Dynamics of a Vehicle with Slight Chirality

A.5.1 Result

The transient behavior of some trajectories that decay into circular orbits is caused by the slight asymmetry in the mechanical structure that the center of mass (CoM) deviates slightly from the center-line. As shown in Section S1, the acceleration magnitude $|a|$ for a vehicle with slight asymmetry with respect to the heading is given by

$$|a| = k(r) \cdot (\sin\theta + \epsilon \cdot \cos\theta) \tag{A.26}$$

where $\epsilon = -\frac{\Delta B}{L_c}$ increases with the CoM's deviation from the center-line being ΔB.

Following the treatment shown in the main text, the polar equation of the trajectory is

$$r_{,\varphi\varphi} = \frac{2r_{,\varphi}^2}{r} + r - \tilde{k}(r) \cdot (r^2 + r_{,\varphi}^2) \\ -\epsilon \cdot \tilde{k}(r) \cdot (r_{,\varphi} r + \frac{r_{,\varphi}^3}{r}) \tag{A.27}$$

where $\tilde{k} \equiv k/v^2$.

Let $r = r_c + \rho$ where ρ is the perturbation and r_c is the radius of the circular orbit that $k(r_c) = v^2/r_c$. After discarding the $O(\rho^2)$ terms, the differential equation is reduced to

$$\rho_{,\varphi\varphi} = -(1 + r_c k_c'/k_c)\rho - \epsilon \rho_{,\varphi} \tag{A.28}$$

where $k_c \equiv k(r_c), k_c' \equiv k'(r_c)$.

The solution to this damped oscillator gives the solution as

$$\rho(\varphi) = \rho(0)\ \cos\left(\sqrt{1 + r_c k_c'/k_c - (\epsilon/2)^2}\varphi\right) e^{-\epsilon\varphi/2} \tag{A.29}$$

with an exponentially decaying envelope with a half-life $(2\log 2)/\epsilon$ that degrades with the bias; that is, the larger the imperfection is, the faster the trajectory is attracted a circular orbit.

On the other hand, when the vehicle has an acceleration bias towards the orbit direction, ϵ will be negative, then ρ will expand and leads the orbit to either crash to the center or escape from the membrane. From this example with counterclockwise trajectory, we see that the orbit is attracted to a circular orbit when $\epsilon \propto (B_2 - B_1) > 0$, that is when the CoM is biased to the left wheel. The data listed in the previous section shows an estimate $\epsilon \approx 0.5$, indicating a half life of $(2\log 2)/0.5 \approx 3$. This qualitatively matches with our experimental observation of the transient orbits when the vehicle tested on a leveled ground does not drive sufficiently straight. We posit the quantitative difference may come from the

inaccuracy of the ΔB and L_c estimate.

In summary, a counterclockwise (clockwise) orbit will get attracted to a circular orbit when the CoM is biased to the right (left) while the eccentricity increases to escape or crash when the CoM is biased to the left (right).

A.5.2 Derivation

We consider a slightly simpler case where the membrane is rather flat that $\Psi^2 = 1 + (\partial z/\partial r)^2 \approx 1$. The acceleration components in radial and azimuthal directions are given by Equation A.30a,Equation A.30b in the main text as

$$\begin{cases} r\ddot{\varphi} + 2\dot{r}\dot{\varphi} = a_\varphi = f & \text{(A.30a)} \\ \ddot{r} - r\dot{\varphi}^2 = a_r = -f \cdot \tan\theta & \text{(A.30b)} \end{cases}$$

where $f = k(r) \cdot (\sin\theta + \epsilon\cos\theta)\cos\theta$ for a vehicle with bias ϵ.

The definition of the heading θ gives

$$\tan\theta \equiv \frac{v_\varphi}{v_r} = \frac{r\dot{\varphi}}{\dot{r}}. \tag{A.31}$$

Using $\dot{\varphi} = \dot{r}\tan\theta/r$, we get the time derivatives of azimuth φ as

$$\dot{\varphi} = \frac{\dot{r}\tan\theta}{r}, \qquad \ddot{\varphi} = \frac{\ddot{r}\tan\theta}{r} + \frac{\dot{r}\dot{\theta}\sec^2\theta}{r} - \frac{\dot{r}^2\tan\theta}{r^2}. \tag{A.32}$$

Substitute the $\dot{\varphi}$ and $\ddot{\varphi}$ in (Equation A.30) with (Equation A.32) and eliminate $\ddot{r}$ by (Equation A.30a)-(Equation A.30b)$\cdot\tan\theta$, we have

$$\dot{r}\dot{\theta} + \frac{\dot{r}^2}{r}\tan\theta = f. \tag{A.33}$$

Consider the radial speed as the velocity's projection on the radial direction $\dot{r} = v \cdot \cos\theta$, we arrive at the vector field description:

$$\begin{cases} \dot{r} = v \cdot \cos\theta & \text{(A.34a)} \\ \dot{\theta} = \dfrac{f(r,\theta)}{v \cdot \cos\theta} - \dfrac{v \cdot \sin\theta}{r}. & \text{(A.34b)} \end{cases}$$

Plug in $f = k(r) \cdot (\sin\theta + \epsilon\cos\theta)\cos\theta$, we have

$$\begin{cases} \dot{r} = v \cdot \cos\theta & \text{(A.35a)} \\ \dot{\theta} = (k/v - v/r)\sin\theta + (k/v)\epsilon\cos\theta. & \text{(A.35b)} \end{cases}$$

Divide (Equation A.35a) by (Equation A.35b), we have

$$\frac{dr}{d\theta} = \frac{v \cdot \cos\theta}{(k(r)/v - v/r + (k(r)/v)\epsilon\cos\theta) \cdot \sin\theta}. \tag{A.36}$$

As we want r to be a function of the azimuth φ, we convert all θ to φ. We use the definition of heading again $\tan\theta = r\dot{\varphi}/\dot{r} = (rd\varphi/dt)/(dr/dt) = rd\varphi/dr = r/r_{,\varphi}$, $\sin\theta = r/\sqrt{r^2 + r_{,\varphi}^2}$, and $\cos\theta = r_{,\varphi}/\sqrt{r^2 + r_{,\varphi}^2}$. The left hand side of (Equation A.36) can thus be converted to

$$LHS = \frac{dr}{d\theta} = \frac{1}{\theta_r} = \frac{1}{\frac{d(\arctan(r/r_{,\varphi}))}{d(r/r_{,\varphi})} \cdot \frac{d(r/r_{,\varphi})}{dr}} = \frac{1}{[1 + (r/r_{,\varphi})^2]^{-1} \cdot \left[\frac{1}{r_{,\varphi}} - \frac{r \cdot r_{,\varphi\varphi}}{r_{,\varphi}^3}\right]} \tag{A.37}$$

The right hand side can be converted to

$$RHS = \frac{r_{,\varphi}}{(\tilde{k} - 1/r) \cdot r + \epsilon\tilde{k}r_{,\varphi}}. \tag{A.38}$$

where $\tilde{k}(r) \equiv k(r)/v^2$.

Equate the LHS (Equation A.37) and the RHS (Equation A.38), we finally arrive at

$$r_{,\varphi\varphi} = \frac{2r_{,\varphi}^2}{r} + r - \tilde{k}(r) \cdot (r^2 + r_{,\varphi}^2) - \epsilon \cdot \tilde{k}(r) \cdot (r_{,\varphi}r + \frac{r_{,\varphi}^3}{r}). \tag{A.39}$$

A.6 Conserved quantities

The metric $ds^2 = -\alpha^2 dt^2 + \Phi^2(\Psi^2 dr^2 + r^2 d\varphi^2)$ gives

$$-1 = -\alpha^2 \mathring{t}^2 + \Phi^2(\Psi^2 \mathring{r}^2 + r^2 \mathring{\varphi}^2) \tag{A.40}$$

where $dq/d\lambda \equiv \mathring{q}$ and we specify the affine parameter λ to be s. To convert the $\mathring{q}$ to $\dot{q}$, we use $\mathring{t} = E/\alpha^2$ and $\mathring{\varphi} = L/\Phi^2 r^2$ from Equation 2.11 and Equation 2.12. Using $\mathring{t} = E/\alpha^2$ again in $\mathring{r}$, we have $\mathring{r} = dr/d\lambda = (dr/dt)(dt/d\lambda) = \dot{r}\mathring{t} = (E/\alpha^2)\dot{r}$. Plug these into Equation A.40, we have

$$-1 = -\frac{E^2}{\alpha^2} + \Phi^2\Psi^2\frac{E^2\dot{r}^2}{\alpha^4} + \frac{L^2}{\Phi^2 r^2} \tag{A.41}$$

Multiply both sides with $-\alpha^2/E^2$ and rearrange the terms, we arrive at

$$1 = \frac{\Phi^2}{\alpha^2}\Psi^2\dot{r}^2 + \frac{1}{r^2}\frac{\alpha^2}{\Phi^2}\frac{L^2}{E^2} + \frac{\alpha^2}{E^2} \tag{A.42}$$

which leads to Equation 2.40 in the main text.

To show the maximum of ℓ is obtained at r_0, we plug the derived metric into Equation 2.11,Equation 2.12,

$$\ell \equiv \frac{L}{E} \;\; = \;\; e^{-K(r_0)/v^2} r_0 \cdot v \tag{A.43}$$

The maximum of ℓ is obtained at r_0 that

$$\frac{\partial \ell}{\partial r_0} \;\; = \;\; e^{-K(r_0)/v^2}\left(1 - \frac{r_0 k(r_0)}{v^2}\right) = 0, \tag{A.44}$$

showing r_0 coincides with the circular orbit radius r_c such that $k(r_c) = v^2/r_c$.

A.7 Generalization from axi-symmetric substrate to general substrate

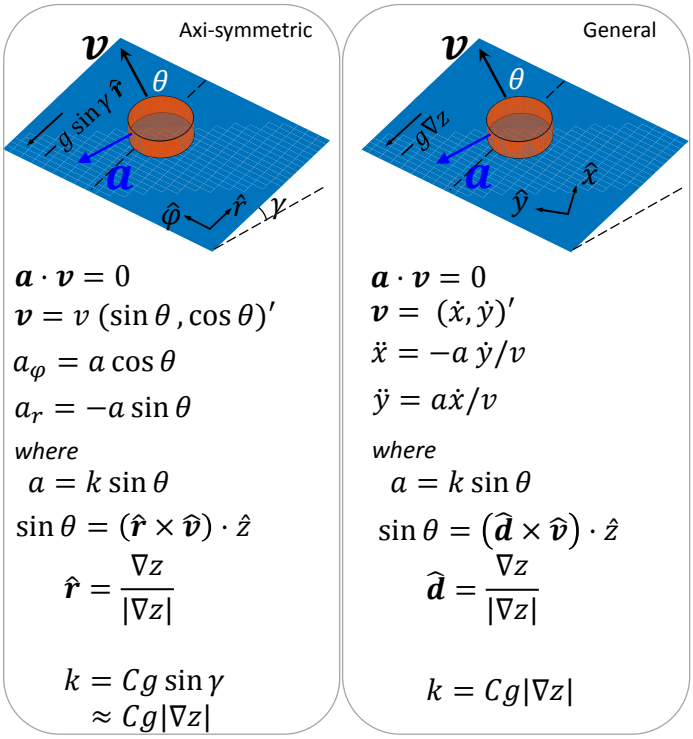

Figure A.5: **Generalization of the vehicle dynamics on an arbitrary terrain.**

We construct the general dynamics by making analogy such that the axi-symmetric case is a special case of the general case. The analogies can be found in Figure A.5.

If we plug the generalized direction and magnitude into the acceleration components, we get

$$
\begin{aligned}
\ddot{x} &= -a\,\frac{\dot{y}}{v} && \text{(A.45)}\\
&= k\sin\theta\,\frac{\dot{y}}{v} && \text{(A.46)}\\
&= k(\hat{d}\times\hat{v})\cdot\hat{z}\,\frac{\dot{y}}{v} && \text{(A.47)}\\
&= Cg|\nabla z|\left(\frac{\nabla z}{|\nabla z|}\times\hat{v}\right)\cdot\hat{z}\,\frac{\dot{y}}{v} && \text{(A.48)}\\
&= Cg(\nabla z\times\frac{v}{v})\cdot\hat{z}\,\frac{\dot{y}}{v} && \text{(A.49)}\\
&= \frac{Cg}{v^2}(z_{,x}\dot{y}-z_{,y}\dot{x})\dot{y} && \text{(A.50)}\\
&= C\,g\,\dot{y}\,(d_x\dot{y}-d_y\dot{x})/v^2 && \text{(A.51)}
\end{aligned}
$$

Similarly, we have $\ddot{y} = -C\,g\,\dot{x}\,(d_x\dot{y} - d_y\dot{x})/v^2$.

In both cases, the acceleration magnitude vanishes when the velocity us along the radial (gradient) direction and the acceleration direction is perpendicular to the velocity.

A.8 Membrane Measurement

A.8.1 Membrane constant

To model the membrane deformation, we consider a free circular membrane with radius R only deformed by its self weight and pressed by a cap in the center with depth D and cap radius $R_0 < R$. When the load from self weight is uniform, the height of the membrane z follows

$$\Delta Z = \lambda^{-1} \tag{A.52}$$

where λ absorbed the elasticity and the mass density.

Applying the axi-symmetry ($\partial Z/\partial\varphi = 0$) and boundary conditions $Z(R) = 0, Z(R_0) = -D$ for a membrane without a load such as the robotic vehicle, the general solution to a

membrane deformed by only self weight is

$$Z(r) = \frac{1}{4\lambda} r^2 + C_1 \log r + C_2 \tag{A.53}$$

where

$$C_1 = \frac{D - \frac{1}{4\lambda}(R^2 - R_0^2)}{\log(R/R_0)}, \tag{A.54}$$

$$C_2 = \frac{\frac{1}{4\lambda}(R^2 \log R_0 - R_0^2 \log R) - D \log R}{\log(R/R_0)} \tag{A.55}$$

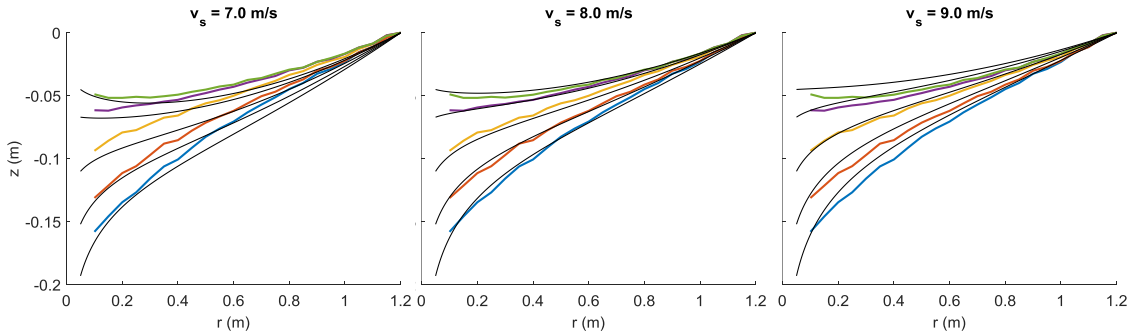

Figure A.6: **Membrane constant measurement.** The black lines show the radial profiles of the free membrane from Poisson equation Equation A.53. The colored lines show the measurement from experiments.

We measured the cross sections of the membrane with various central depressions D's and compare them with solution Equation A.53 for various λ. The value of λ is chosen such that the solutions match with experiments the best. In our setup, λ is measured to be 6.5 m (Figure A.6).

A.8.2 Membrane isotropy

Ideally, the height of the membrane at a particular radius should be the same for any azimuthal angle in terms of the axi-symmetry. To understand how the membrane deviates from the ideal, the variation of this height is evaluated with the data taken from the Optitrack cameras for three different central depressions. The variation is found to be smaller

than 5% of the central depression.

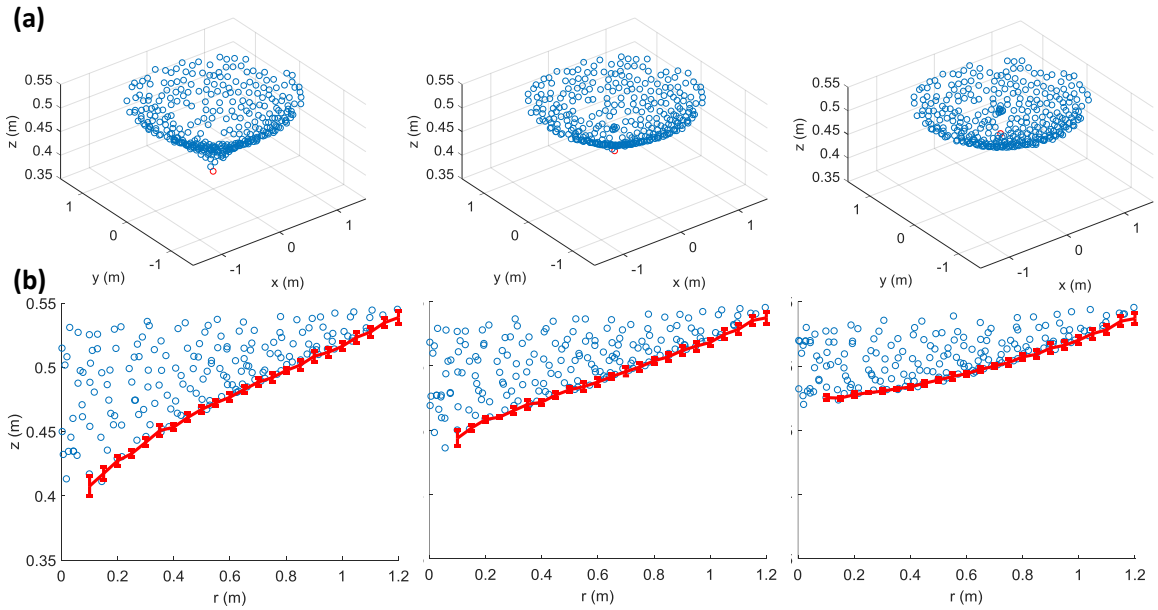

Figure A.7: **Shapes of the membrane with different central depressions.** (a) The perspective views of the membrane profile measured from the optical tracking system. (b) The red curves show the heights averaged over the azimuthal angles.

A.8.3 Analytic solution to the membrane

As shown in the previous section, the deformation of the membrane by its self weight can be well characterized by $\Delta Z = \lambda^{-1}$. To model the additional load from the vehicles besides the weight of the membrane itself, we evaluate the area density of vehicle and scaled it by that of the membrane so that $\Delta Z = \lambda^{-1}(1 + \tilde{P})$ with $\tilde{P} = \sigma_v/\sigma$ where σ_v and σ are the density of the vehicle ($\approx 20,000$ g/m^2) and the membrane (137 g/m^2) respectively. For simplicity, we assume the load is a uniform distribution on a disc centered at the ith vehicle's position $\mathbf{r}_i$ and with the radius of the vehicle R_v so that $\sigma_{v,i} = \frac{m_i}{\pi R_v^2} 1(\mathbf{r} \in \Omega_i)$ and $\sigma_v = \sum_i \sigma_{v,i}$ where $\Omega_i = \{\mathbf{r} : |\mathbf{r} - \mathbf{r}_i| < R_v\}$.

To solve the Poisson equation, we integrate the Green function $G(\mathbf{r}, \mathbf{s})$ of Poisson equa-

tion with the source.

$$\begin{aligned} \lambda Z(\mathbf{r}) &= \int G(\mathbf{r},\mathbf{s})(1+\tilde{P}(\mathbf{s}))d\mathbf{s}^2 && \text{(A.56)} \\ &= \int G(\mathbf{r},\mathbf{s})d\mathbf{s}^2 + \frac{1}{\sigma}\sum_i \int_{\Omega_i} G(\mathbf{r},\mathbf{s})\sigma_{v,i}(\mathbf{s})d\mathbf{s}^2 && \text{(A.57)} \\ &\equiv I_1 + I_2 && \text{(A.58)} \end{aligned}$$

where the Green function on a disc with radius R is

$$\begin{aligned} G(\mathbf{r},\mathbf{s}) &= \frac{1}{2\pi}\log|\mathbf{r}-\mathbf{s}| \\ &- \frac{1}{2\pi}\log\left(\frac{|\mathbf{s}|}{R}\cdot\left|\mathbf{r}-R^2\frac{\mathbf{s}}{|\mathbf{s}|^2}\right|\right) && \text{(A.59)} \\ G(\mathbf{r},\mathbf{0}) &= \frac{1}{2\pi}\log|\mathbf{r}| - \frac{1}{2\pi}\log R && \text{(A.60)} \end{aligned}$$

Let us consider a field point that is not covered by the vehicles $\mathbf{r} \notin \cup_i \Omega_i$. I_1 is the solution to the case with uniform load that $I_1 = \frac{1}{4}(|\mathbf{r}|^2 - R^2)$. For I_2, the source is effectively a point source since the field point is outside the source, so

$$\begin{aligned} I_2 &= \frac{1}{\sigma}\sum_i \int_{\Omega_i} G(\mathbf{r},\mathbf{s})\frac{m_i}{\pi R_v^2}\pi R_v^2\delta(\mathbf{s}-\mathbf{r}_i)d\mathbf{s}^2 && \text{(A.61)} \\ &= \frac{1}{\sigma}\sum_i m_i G(\mathbf{r},\mathbf{r}_i) && \text{(A.62)} \end{aligned}$$

Up till so far, we have solved the shape of the membrane $Z(\mathbf{r})$. Next, we evaluate the height of the ith vehicle. Since the vehicle is not a point object, we average the membrane height Z on the rim of the vehicle to approximate the height of the vehicle z_i.

$$\begin{aligned} z_i &= \langle Z \rangle_{\partial\Omega_i} && \text{(A.63)} \\ \lambda z_i &= \langle I_1 + I_2 \rangle = \langle I_1 \rangle + \langle I_2 \rangle && \text{(A.64)} \end{aligned}$$

$\langle I_1 \rangle$ is contributed by the self weight of the entire membrane so that we approximate it

by just the value at the center of the vehicle $\mathbf{r}_i$: $\langle I_1 \rangle = \frac{1}{4}(|\mathbf{r}_i|^2 - R^2)$.

For $\langle I_2 \rangle$, there are two different types of contributions. The first ones are the patches of domain from the vehicles other than the ith vehicle, the one of concern that contribute as far field. The second type is the contribution from the load of vehicle i itself.

For the first type, we still use the point source approximation:

$$\langle I_{2,j\neq i} \rangle = \frac{m_j}{\sigma} G(\mathbf{r}_i, \mathbf{r}_j) \tag{A.65}$$

For the second type:

$$\begin{aligned}
\langle I_{2,i} \rangle &= \frac{m_i}{\sigma} \langle G(\mathbf{r}, \mathbf{r}_i) \rangle_{\mathbf{r}\in\Omega_i} && \text{(A.66)} \\
&= \frac{m_i}{2\pi\sigma} \left(\langle \log|\mathbf{r} - \mathbf{r}_i| \rangle - \left\langle \log\left(\frac{|\mathbf{r}_i|}{R} \cdot \left| \mathbf{r} - R^2 \frac{\mathbf{r}_i}{|\mathbf{r}_i|^2} \right| \right) \right\rangle \right) \\
&= \frac{m_i}{2\pi\sigma} \left(\log R_v - \log\left(\frac{|\mathbf{r}_i|}{R} \cdot \left| \mathbf{r}_i - R^2 \frac{\mathbf{r}_i}{|\mathbf{r}_i|^2} \right| \right) \right) \\
&= \frac{m_i}{2\pi\sigma} \log\left(\frac{R_v R}{R^2 - |\mathbf{r}_i|^2} \right) && \text{(A.67)}
\end{aligned}$$

Piecing all these terms together, we arrive at the z position of the ith vehicle is

$$\begin{aligned}
2\pi\lambda z_i &= \frac{\pi}{2}(|\mathbf{r}_i|^2 - R^2) + \frac{m_i}{\sigma} \log\left(\frac{R_v R}{R^2 - |\mathbf{r}_i|^2} \right) \\
&+ \frac{1}{\sigma} \sum_{j\neq i} m_j \left(\log \frac{|\mathbf{r}_i - \mathbf{r}_j|}{|\mathbf{r}_i - \mathbf{r}'_j|} - \log \frac{|\mathbf{r}_j|}{R} \right) && \text{(A.68)}
\end{aligned}$$

where $\mathbf{r}' = (R/|\mathbf{r}|)^2\mathbf{r}$ is conventionally regarded as the position of the image charge. $\mathbf{r}_j$'s are the positions of the other vehicles.

Despite the fact that some approximations are made, the analytical solution matches with the numerical result (FEM) with a relative error smaller than 10^{-3} (Figure A.8).

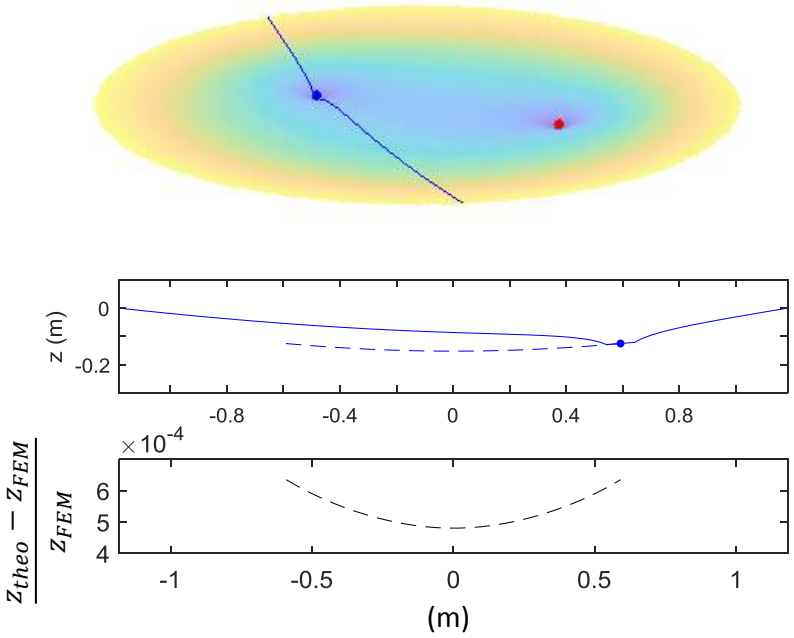

Figure A.8: **Numerical verification of the analytical solution.** We show a test with the blue vehicle put at different y positions while the x position is fixed (0.2 m). The solid blue line shows the membrane shape and the dotted line shows the vertical position of the vehicle z when placed at different positions. The bottom panel shows the relative error of z between the analytical (Equation A.68) and numerical (FEM) solution.

A.9 Dynamics of two vehicles with the same mass

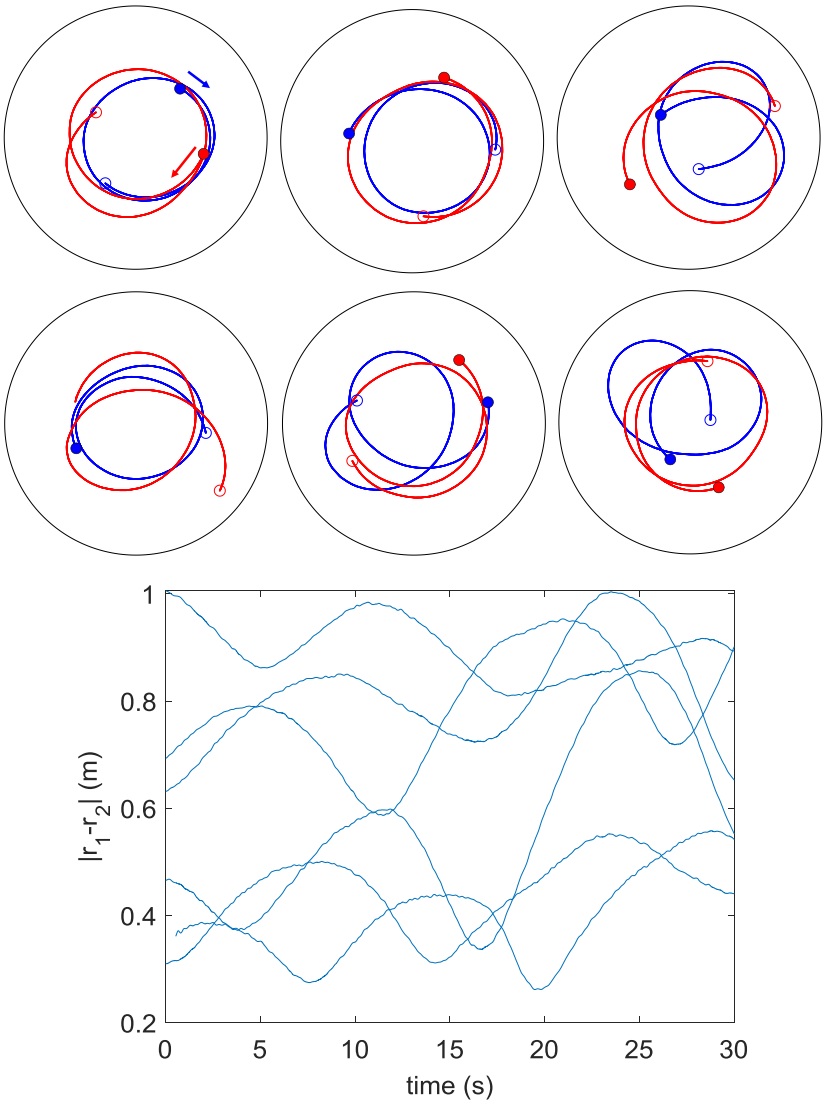

Figure A.9: **Dynamics of two vehicles with the same mass** (a) Trajectories of vehicles with the same mass started at different initial conditions. (b) The relative distance of the two vehicles in (a).

APPENDIX B

SMARTICLE

B.1 Geometric Mechanics of the crawler

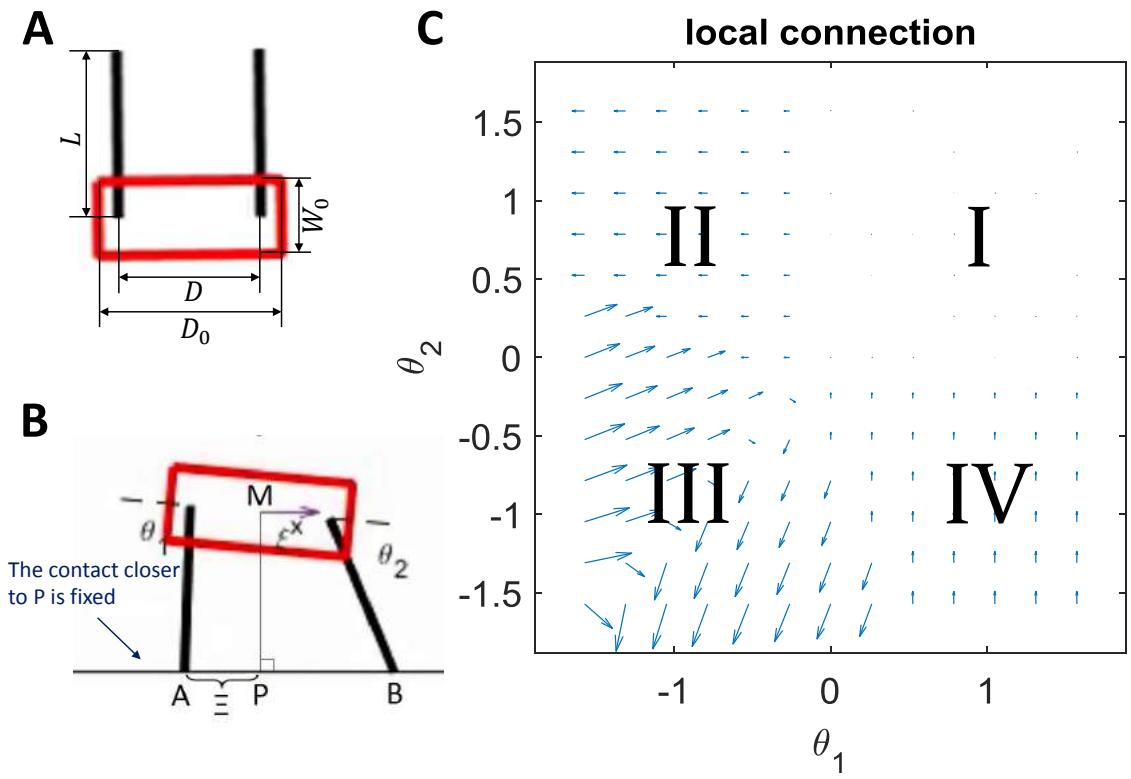

Figure B.1: **Basic information of a smarticle crawler.** (A) The dimensions of a smarticle crawler. (B) A crawler with the arm angled in quadrant III of the shape space. (C) The local connection measured from simulation.

Here we show a minimal model for the connection field of a smarticle crawler. In this model, we assume the tip closer to the projection of the center of mass (CoM) of the crawler always freezes given that this tip has a larger normal force and thus a larger maximum static friction. For instance, Figure B.1, in tip A and B, A is closer to P, the projection of the CoM, M since $AP < BP$. At this moment, we assume the A will be fixed and only B will slide as θ_1 and θ_2 change according to the gait.

If we denote $AP = \Xi$, we have

$$\Xi(\theta_1, \theta_2) = \frac{D^2 + 2L^2 + L(3D\cos\theta_1 + D\cos\theta_2 + 2L\cos(\theta_1 + \theta_2))}{2\sqrt{D^2 + 2L^2 + 2L(D\cos\theta_1 + D\cos\theta_2 + L\cos(\theta_1 + \theta_2))}} \tag{B.1}$$

An approximate Ξ to the first order gives us

$$d\Xi = \frac{\partial \Xi}{\partial \theta_1} d\theta_1 + \frac{\partial \Xi}{\partial \theta_2} d\theta_2. \tag{B.2}$$

Geometric mechanics assumes linear relation between the velocity in shape space (θ_1, θ_2) and real space (ξ^x). This gives

$$\xi^x = \frac{d\Xi}{dt} \equiv a_1 \dot{\theta}_1 + a_2 \dot{\theta}_2. \tag{B.3}$$

By comparing Equation B.2 and Equation B.3, we have

$$a_1 = \frac{\partial \Xi}{\partial \theta_1}, \quad a_2 = \frac{\partial \Xi}{\partial \theta_2}. \tag{B.4}$$

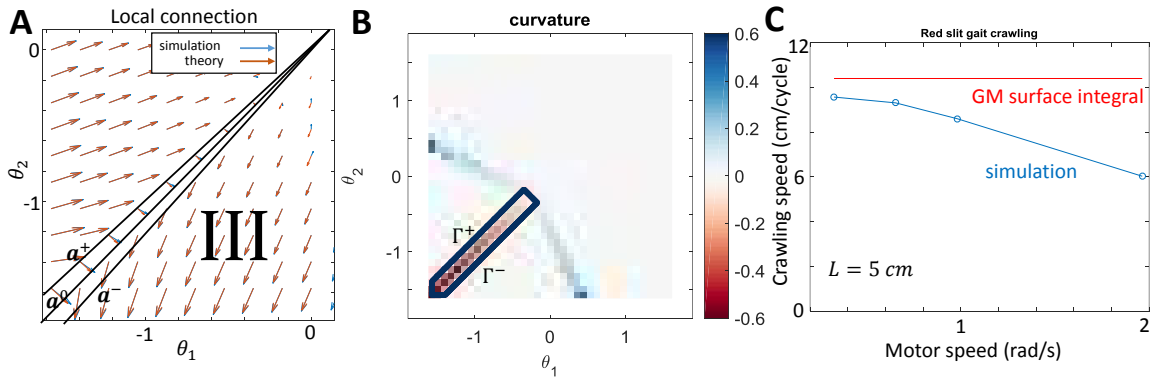

Figure B.2: **Connection field in quadrant III.** (A) Simulation and theory connection are shown in orange and blue arrows in quadrant III. The black lines are the boundary of a red slit gait. (B) The curl of the connection field (curvature) for the entire shape space. (C) The crawling speed from simulation (blue) deviates from the geometric approximation (red) as the motor speed gets higher and the system gets less and less kinetic where the GM works.

Figure B.2A shows the result by Equation B.4 with orange arrows are close to the blue arrows from numerical simulations. In these simulations, to get the connection at (θ_1, θ_2), the smarticle starts from a point in the close neighborhood of (θ_1, θ_2) and ends at (θ_1, θ_2). There is no dependence on the neighborhood point one choose as we expect.

Now that we have the connection field in quadrant III, we wonder if the efficient gait enclosing the most sufficient part of the shape space would produce a crawling as we expect. If we consider a gait around the diagonal slit $\Gamma^+ \cup \Gamma^-$ and denote the corresponding connection field as $\mathbf{a}^+$ and $\mathbf{a}^-$, we have

$$\mathbf{a}^+ \equiv \lim_{\epsilon \to 0} \mathbf{a}(\theta_0, \theta_0 + \epsilon) \tag{B.5}$$

$$= \begin{pmatrix} \frac{LD\sin\theta_0 + L^2\sin\theta_0\cos\theta_0}{D+2L\cos\theta_0} \\ \frac{L^2\sin\theta_0\cos\theta_0}{D+2L\cos\theta_0} \end{pmatrix} \tag{B.6}$$

$$\mathbf{a}^- \equiv \lim_{\epsilon \to 0} \mathbf{a}(\theta_0, \theta_0 - \epsilon) \tag{B.7}$$

$$= \begin{pmatrix} \frac{L^2\sin\theta_0\cos\theta_0}{D+2L\cos\theta_0} \\ \frac{LD\sin\theta_0 + L^2\sin\theta_0\cos\theta_0}{D+2L\cos\theta_0} \end{pmatrix} \tag{B.8}$$

The crawling along this gait (counterclockwise) per cycle is therefore

$$S_{\text{red slit}} = \int_{\Gamma^+} \mathbf{a}^+ \cdot d\theta + \int_{\Gamma^-} \mathbf{a}^- \cdot d\theta \tag{B.9}$$

$$= 2\int_{-\pi/2}^{0} \mathbf{a}^+ \cdot (d\theta_0, d\theta_0) \tag{B.10}$$

$$= 2\int_{-\pi/2}^{0} \frac{LD\sin\theta_0 + 2L^2\sin\theta_0\cos\theta_0}{D+2L\cos\theta_0} d\theta_0 \tag{B.11}$$

$$= -2L \tag{B.12}$$

This matches our intuition that a gait fully expanding the two arms with length L produces a crawling of $2L$.

Now, let us consider another two important slits of the connection field in quadrants II and IV.

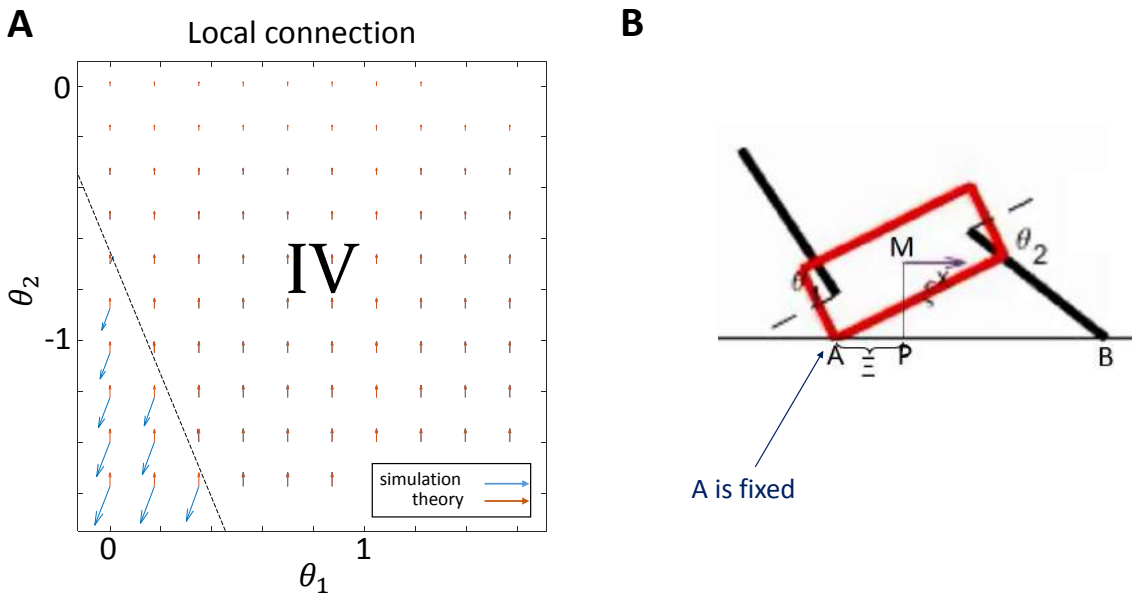

Figure B.3: **Connection field in quadrant IV.** (A) simulation and theory connection in quadrant IV. (B) A typical snapshot of the crawler in quadrant IV.

Using the same treatment as quadrant III. As shown in Figure B.3B, now the fixed tip is the lower left corner of the body segment A. The motion in x direction is denoted as $AP = \xi$ where

$$\Xi(\theta_1, \theta_2) = \frac{D_0 D + D_0^2 + W_0^2 + 2D_0 L\cos\theta_2 - 2W_0 L\sin\theta_2}{2\sqrt{(D+D_0)^2 + 4L^2 + W_0^2 + 4(D+D_0)L\cos\theta_2 - 4W_0 L\sin\theta_2}} \tag{B.13}$$

Therefore, the connection field is

$$a_1 = 0, \quad a_2 = \frac{\partial \Xi}{\partial \theta_2}. \tag{B.14}$$

We can see the match between the theoretical and the simulation values in Figure B.3A.

Finally, let us see if we understand the boundary between these domains.

The boundary between the 'two hands up' domain in quadrant I and 'one arm touching

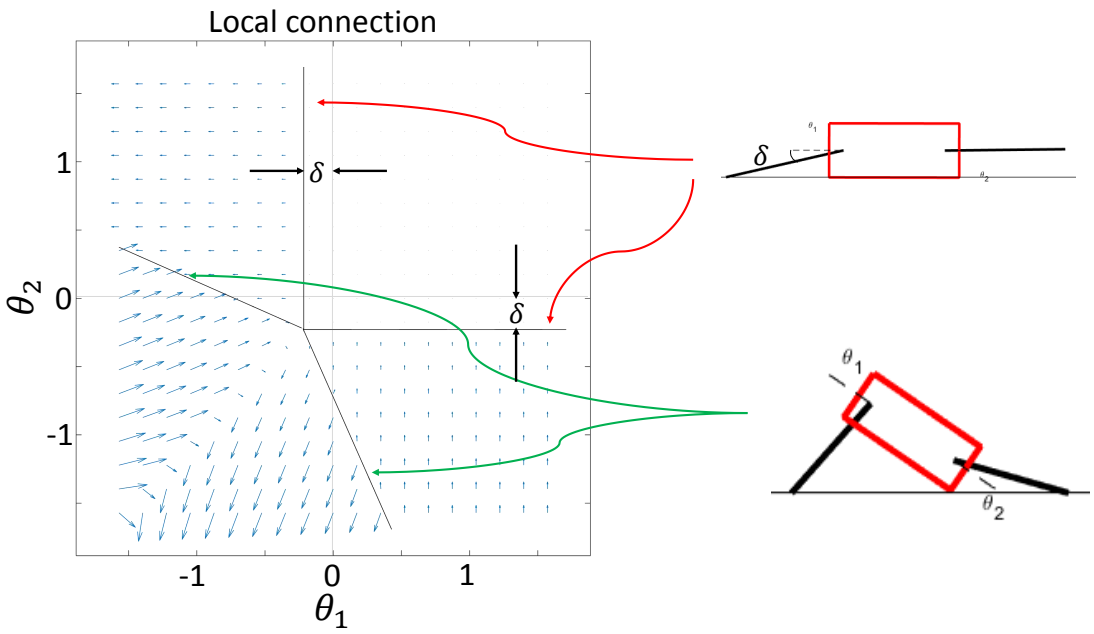

Figure B.4: The boundary of the domains are set by the different contact modes.

the ground' is given by the angle δ as shown in the upper-right inset of Figure B.4.

$$\delta = \arcsin\left(W_0/2L\right). \tag{B.15}$$

The boundary between the 'one arm touching the ground' and 'belly off the ground' is given by the geometric constraint

$$\begin{aligned} 0 &= F(\theta_1, \theta_2) = DW_0 + L(W_0(\cos\theta_1 + \cos\theta_2) \\ &+ (-D + D_0)\sin\theta_1 - (D + D_0)\sin\theta_2 - 2L\sin\left(\theta_1 + \theta_2\right)). \end{aligned} \tag{B.16}$$

A linear approximation of these two boundaries can be computed as

$$
\begin{aligned}
k_1 &= \frac{d\theta_2}{\theta_1}|_{(\theta_1,\theta_2)=(-\delta,\delta)} && \text{(B.17)}\\
&= -\frac{\partial F/\partial\theta_1}{\partial F/\partial\theta_2}|_{(-\delta,-\delta)} && \text{(B.18)}\\
&= \frac{1}{2} && \text{(B.19)}\\
k_2 &= 1/k_1. && \text{(B.20)}
\end{aligned}
$$

In Figure B.4, we can see this approximation (black line) captures the simulation result reasonably well.

APPENDIX C

SWIMMER

C.1 Numerical integration

To obtain the equation for numerical integration, we plug the angular momentum Equation 5.6 into the equation of motion Equation 5.13, so

$$
\begin{aligned}
-\tau_C \text{sgn}(\dot{\phi}) - \tau_g \phi &= \frac{dL}{dt} && \text{(C.1)} \\
&= \frac{dI}{dt}\dot{\phi} + I\ddot{\phi} + \ddot{\alpha} && \text{(C.2)} \\
&= \frac{\partial I}{\partial \theta_v}\dot{\theta}_v\dot{\phi} + I\ddot{\phi} + \ddot{\alpha} && \text{(C.3)}
\end{aligned}
$$

Plugging in the $I(\theta_v(t))$ in Equation 5.7 and the α in Equation 5.8, we finally arrive at

$$
\ddot{\phi} = I(\theta_v)^{-1}\left(2m_v R^2 \sin(2\theta_v)\,\dot{\theta}_v\dot{\phi} - 2m_h R^2\ddot{\theta}_h - \tau_C \text{sgn}(\dot{\phi}) - \tau_g\theta\right) \qquad \text{(C.4)}
$$

The numerical simulation integrates Equation C.4. The initial position $\phi(0) = 0$ such that the swimmer starts from the bottom of the slight potential well from the residual gravity. The initial angular velocity $\dot{\phi}$ is chosen that the initial angular momentum $L(0) = I(0)\dot{\phi}(0) + \dot{\alpha}(0)$ is zero.

The motor positions $\theta_v(t)$ and $\theta_h(t)$ use the commanded signal sent to the motor (see S1). The sign function in the Coulomb friction is smoothed by the arctan function with characteristic angular speed 0.01 rad/s $\ll$ the typical speed of the swimmer to avoid the numerical singularity. There are two motors on the horizontal track and two motors on the vertical track. The mass of each motor is 0.116 kg $= m_v = m_h$. The radius of the swimmer is $R = 0.46$ m. The mass the track is $m_{\text{track}} = 0.388$ kg.

For the convenience of implementing the same gait as the commanded shape change sent to the motors, which are discrete signals requiring interpolation in the differential equations to be integrated, we use a numerical scheme with fixed steps (forward Euler) so that the interpolation of the input signal is time-economic. The test of convergence with step size h shows a global (i.e. position ϕ) error of $O(h)$ (and therefore local error of $O(h^2)$) as expected for a first-order scheme. We use the step size $h = 3.1 \times 10^{-4}$ s such that the relative error is 1.8 %.

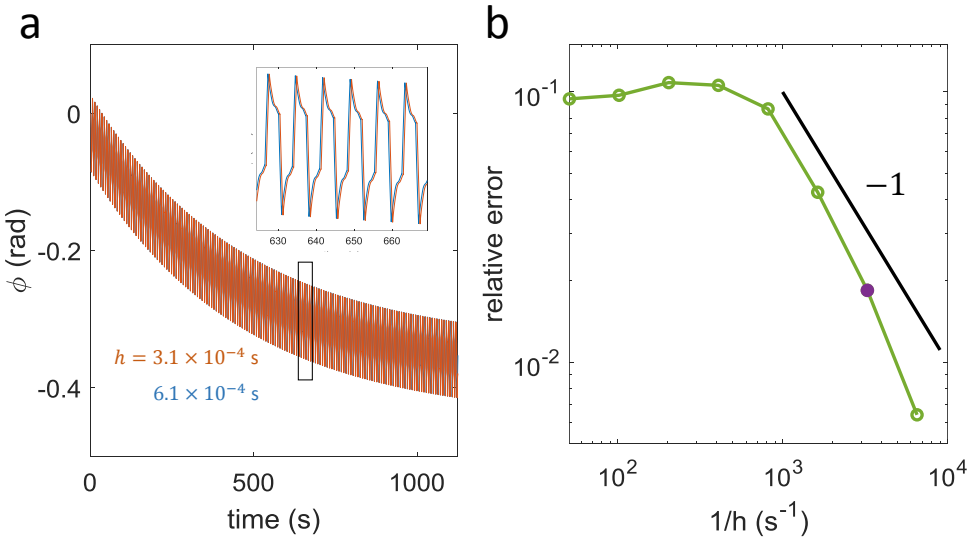

Figure C.1: **Numerical convergence check.** (a) Numerical integration of a swimmer driven by a square swimming gait and subjected to a friction of $\tau_C = 8.6 \times 10^{-3}$ kg m^{2}s^{-2} and residual gravity $\tau_g = 4.0 \times 10^{-4}$ kg m^{2}s^{-2} with step sizes $h = 3.1 \times 10^{-4}$ s and 6.1×10^{-4} s. The inset shows a close-up at around 650 s. (b) The relative error from numerical integration improves with the decrease of step size h. The improvement largely follows a trend of $O(h)$, which can be seen by a comparison with the black line that has a power of -1. Here the relative error is defined as the average of $|\phi_{\text{num}} - \phi_{\text{truth}}|/|\phi_{\text{num}}|$ where we use $h = 7.7 \times 10^{-5}$ s to approximate ϕ_{truth}. The step size we use in this study, $h = 3.1 \times 10^{-4}$, is shown in a solid purple dot.

REFERENCES

[1] H. F. Mccreery, Z. A. Dix, M. D. Breed, and R. Nagpal, "Collective strategy for obstacle navigation during cooperative transport by ants," *Journal of Experimental Biology*, vol. 219, no. 21, pp. 3366–3375, Nov. 2016.

[2] C. Anderson, G. Theraulaz, and J. L. Deneubourg, *Self-assemblages in insect societies*, 2002.

[3] C. K. Hemelrijk and H. Hildenbrandt, *Schools of fish and flocks of birds: Their shape and internal structure by self-organization*, 2012.

[4] M. Brambilla, E. Ferrante, M. Birattari, and M. Dorigo, "Swarm robotics: A review from the swarm engineering perspective," *Swarm Intelligence*, vol. 7, no. 1, pp. 1–41, Jan. 2013.

[5] M. Schranz, M. Umlauft, M. Sende, and W. Elmenreich, *Swarm Robotic Behaviors and Current Applications*, Apr. 2020.

[6] S. J. Chung, A. A. Paranjape, P. Dames, S. Shen, and V. Kumar, "A Survey on Aerial Swarm Robotics," *IEEE Transactions on Robotics*, vol. 34, no. 4, pp. 837–855, Aug. 2018.

[7] F. Berlinger, M. Gauci, and R. Nagpal, "Implicit coordination for 3d underwater collective behaviors in a fish-inspired robot swarm," *Science Robotics*, vol. 6, no. 50, 2021. eprint: https://robotics.sciencemag.org/content/6/50/eabd8668.full.pdf.

[8] M. C. Marchetti, J. F. Joanny, S. Ramaswamy, T. B. Liverpool, J. Prost, M. Rao, and R. A. Simha, "Hydrodynamics of soft active matter," *Rev. Mod. Phys.*, vol. 85, pp. 1143–1189, 3 Jul. 2013.

[9] J. Aguilar, D. Monaenkova, V. Linevich, W. Savoie, B. Dutta, H.-S. Kuan, M. Betterton, M. Goodisman, and D. Goldman, "Collective clog control: Optimizing traffic flow in confined biological and robophysical excavation," *Science*, vol. 361, no. 6403, pp. 672–677, 2018.

[10] P. Chvykov, T. A. Berrueta, A. Vardhan, W. Savoie, A. Samland, T. D. Murphey, K. Wiesenfeld, D. I. Goldman, and J. L. England, "Low rattling: A predictive principle for self-organization in active collectives," *Science*, vol. 371, no. 6524, pp. 90–95, 2021.

[11] J. W. Bush, "Pilot-wave hydrodynamics," *Annual Review of Fluid Mechanics*, vol. 47, pp. 269–292, 2015.

[12] D. L. Hu, B. Chan, and J. W. Bush, "The hydrodynamics of water strider locomotion," *Nature*, vol. 424, no. 6949, p. 663, 2003.

[13] M. Fruchart, R. Hanai, P. B. Littlewood, and V. Vitelli, "Non-reciprocal phase transitions," *Nature*, vol. 592, no. 7854, pp. 363–369, 2021.

[14] G. Wang, T. V. Phan, S. Li, M. Wombacher, J. Qu, Y. Peng, G. Chen, D. I. Goldman, S. A. Levin, R. H. Austin, *et al.*, "Emergent field-driven robot swarm states," *Physical review letters*, vol. 126, no. 10, p. 108 002, 2021.

[15] B. Cowan, *Topics in statistical mechanics*. World Scientific, 2021.

[16] C. Jarzynski, "Nonequilibrium equality for free energy differences," *Physical Review Letters*, vol. 78, no. 14, p. 2690, 1997.

[17] S. Jiang, Q. Chen, M. Tripathy, E. Luijten, K. S. Schweizer, and S. Granick, "Janus particle synthesis and assembly," *Advanced materials*, vol. 22, no. 10, pp. 1060–1071, 2010.

[18] M. N. Van Der Linden, L. C. Alexander, D. G. Aarts, and O. Dauchot, "Interrupted motility induced phase separation in aligning active colloids," *Physical review letters*, vol. 123, no. 9, p. 098 001, 2019.

[19] K. Copenhagen, R. Alert, N. S. Wingreen, and J. W. Shaevitz, "Topological defects promote layer formation in myxococcus xanthus colonies," *Nature Physics*, vol. 17, no. 2, pp. 211–215, 2021.

[20] N. Gravish, G. Gold, A. Zangwill, M. A. Goodisman, and D. I. Goldman, "Glass-like dynamics in confined and congested ant traffic," *Soft matter*, vol. 11, no. 33, pp. 6552–6561, 2015.

[21] W. Savoie, T. A. Berrueta, Z. Jackson, A. Pervan, R. Warkentin, S. Li, T. D. Murphey, K. Wiesenfeld, and D. I. Goldman, "A robot made of robots: Emergent transport and control of a smarticle ensemble," *Science Robotics*, vol. 4, no. 34, eaax4316, 2019.

[22] G. S. Redner, A. Baskaran, and M. F. Hagan, "Reentrant phase behavior in active colloids with attraction," *Physical Review E*, vol. 88, no. 1, p. 012 305, 2013.

[23] D. Mandal, K. Klymko, and M. R. DeWeese, "Entropy production and fluctuation theorems for active matter," *Physical review letters*, vol. 119, no. 25, p. 258 001, 2017.

[24] N. Yamaguchi, T. Mizutani, K. Kawabata, and H. Haga, "Leader cells regulate collective cell migration via rac activation in the downstream signaling of integrin β1 and pi3k," *Scientific reports*, vol. 5, no. 1, pp. 1–8, 2015.

[25] H.-P. Zhang, A. Be'er, E.-L. Florin, and H. L. Swinney, "Collective motion and density fluctuations in bacterial colonies," *Proceedings of the National Academy of Sciences*, vol. 107, no. 31, pp. 13 626–13 630, 2010.

[26] A. Deblais, A. Maggs, D. Bonn, and S. Woutersen, "Phase separation by entanglement of active polymerlike worms," *Physical Review Letters*, vol. 124, no. 20, p. 208 006, 2020.

[27] A. Cavagna, A. Cimarelli, I. Giardina, G. Parisi, R. Santagati, F. Stefanini, and M. Viale, "Scale-free correlations in starling flocks," *Proceedings of the National Academy of Sciences*, vol. 107, no. 26, pp. 11 865–11 870, 2010.

[28] J. L. Silverberg, M. Bierbaum, J. P. Sethna, and I. Cohen, "Collective motion of humans in mosh and circle pits at heavy metal concerts," *Physical review letters*, vol. 110, no. 22, p. 228 701, 2013.

[29] B. Liebchen and H. Löwen, "Synthetic chemotaxis and collective behavior in active matter," *Accounts of chemical research*, vol. 51, no. 12, pp. 2982–2990, 2018.

[30] T. Vicsek, A. Czirók, E. Ben-Jacob, I. Cohen, and O. Shochet, "Novel type of phase transition in a system of self-driven particles," *Physical review letters*, vol. 75, no. 6, p. 1226, 1995.

[31] D. Helbing, A. Johansson, and H. Z. Al-Abideen, "Dynamics of crowd disasters: An empirical study," *Physical review E*, vol. 75, no. 4, p. 046 109, 2007.

[32] M. Rubenstein, A. Cornejo, and R. Nagpal, "Programmable self-assembly in a thousand-robot swarm," *Science*, vol. 345, no. 6198, pp. 795–799, 2014.

[33] F. Berlinger, M. Gauci, and R. Nagpal, "Implicit coordination for 3d underwater collective behaviors in a fish-inspired robot swarm," *Science Robotics*, vol. 6, no. 50, eabd8668, 2021.

[34] A. Brugués, E. Anon, V. Conte, J. H. Veldhuis, M. Gupta, J. Colombelli, J. J. Muñoz, G. W. Brodland, B. Ladoux, and X. Trepat, "Forces driving epithelial wound healing," *Nature physics*, vol. 10, no. 9, pp. 683–690, 2014.

[35] P. Friedl, Y. Hegerfeldt, and M. Tusch, "Collective cell migration in morphogenesis and cancer," *International Journal of Developmental Biology*, vol. 48, no. 5-6, pp. 441–449, 2004.

[36] A. Senoussi, J.-C. Galas, and A. Estévez-Torres, "Programmed mechano-chemical coupling in reaction-diffusion active matter," *Science advances*, vol. 7, no. 51, eabi9865, 2021.

[37] T. A. T. Liu, "Colloidal electronics," Ph.D. dissertation, Massachusetts Institute of Technology, 2020.

[38] Z. Zhao and D. Randall, "Socioeconomic clustering and racial segregation on lattices with heterogeneous sites," *arXiv preprint arXiv:2108.01657*, 2021.

[39] N. Bredeche and N. Fontbonne, "Social learning in swarm robotics," *Philosophical Transactions of the Royal Society B*, vol. 377, no. 1843, p. 20 200 309, 2022.

[40] P. Galajda, J. Keymer, P. Chaikin, and R. Austin, "A wall of funnels concentrates swimming bacteria," *Journal of bacteriology*, vol. 189, no. 23, pp. 8704–8707, 2007.

[41] A. Cavagna and I. Giardina, "Bird flocks as condensed matter," *Annu. Rev. Condens. Matter Phys.*, vol. 5, no. 1, pp. 183–207, 2014.

[42] J. K. Parrish and W. M. Hamner, *Animal groups in three dimensions: how species aggregate*. Cambridge University Press, 1997.

[43] C. Li, T. Zhang, and D. I. Goldman, "A terradynamics of legged locomotion on granular media," *science*, vol. 339, no. 6126, pp. 1408–1412, 2013.

[44] J. Aguilar, T. Zhang, F. Qian, M. Kingsbury, B. McInroe, N. Mazouchova, C. Li, R. Maladen, C. Gong, M. Travers, *et al.*, "A review on locomotion robophysics: The study of movement at the intersection of robotics, soft matter and dynamical systems," *Reports on Progress in Physics*, vol. 79, no. 11, p. 110 001, 2016.

[45] T. Li, G. Li, Y. Liang, T. Cheng, J. Dai, X. Yang, B. Liu, Z. Zeng, Z. Huang, Y. Luo, *et al.*, "Fast-moving soft electronic fish," *Science advances*, vol. 3, no. 4, e1602045, 2017.

[46] G.-K. Lau, "A stunt flying hawk-inspired drone," *Science Robotics*, vol. 5, no. 47, 2020.

[47] S. Berman, Q. Lindsey, M. S. Sakar, V. Kumar, and S. C. Pratt, "Experimental study and modeling of group retrieval in ants as an approach to collective transport in swarm robotic systems," *Proceedings of the IEEE*, vol. 99, no. 9, pp. 1470–1481, 2011.

[48] M. Rubenstein, A. Cornejo, and R. Nagpal, "Programmable self-assembly in a thousand-robot swarm," *Science*, vol. 345, no. 6198, pp. 795–799, 2014. eprint: https://science.sciencemag.org/content/345/6198/795.full.pdf.

[49] V. Narayan, S. Ramaswamy, and N. Menon, "Long-lived giant number fluctuations in a swarming granular nematic," *Science*, vol. 317, no. 5834, pp. 105–108, 2007.

[50] T. Van Phan, "Swarm intelligence in natural and synthetic lives," Ph.D. dissertation, Princeton University, 2021.

[51] T. V. Phan, R. Morris, M. E. Black, T. K. Do, K.-C. Lin, K. Nagy, J. C. Sturm, J. Bos, and R. H. Austin, "Bacterial route finding and collective escape in mazes and fractals," *Physical Review X*, vol. 10, no. 3, p. 031 017, 2020.

[52] P. E. Schiebel, J. M. Rieser, A. M. Hubbard, L. Chen, D. Z. Rocklin, and D. I. Goldman, "Mechanical diffraction reveals the role of passive dynamics in a slithering snake," *Proceedings of the National Academy of Sciences*, vol. 116, no. 11, pp. 4798–4803, 2019.

[53] S. Tarr, E. Aydin, and D. Goldman, "Surface wave and transport dynamics of a self-propelling vibrating robot fan boat," in *APS Division of Fluid Dynamics Meeting Abstracts*, 2021, A27–002.

[54] T. Majmudar, E. E. Keaveny, J. Zhang, and M. J. Shelley, "Experiments and theory of undulatory locomotion in a simple structured medium," *Journal of the Royal Society Interface*, vol. 9, no. 73, pp. 1809–1823, 2012.

[55] S. C. Takatori, R. De Dier, J. Vermant, and J. F. Brady, "Acoustic trapping of active matter," *Nature communications*, vol. 7, no. 1, pp. 1–7, 2016.

[56] BBC. (2002). "'wobbly' millennium bridge fixed," (visited on 03/07/2022).

[57] S. H. Strogatz, D. M. Abrams, A. McRobie, B. Eckhardt, and E. Ott, "Crowd synchrony on the millennium bridge," *Nature*, vol. 438, no. 7064, pp. 43–44, 2005.

[58] Y. Lan and P. Cvitanović, "Unstable recurrent patterns in kuramoto-sivashinsky dynamics," *Physical review E*, vol. 78, no. 2, p. 026 208, 2008.

[59] E. Wei, E. W. Justh, and P. Krishnaprasad, "Pursuit and an evolutionary game," *Proceedings of the Royal Society A: Mathematical, Physical and Engineering Sciences*, vol. 465, no. 2105, pp. 1539–1559, 2009.

[60] S. Saha, J. Agudo-Canalejo, and R. Golestanian, "Scalar active mixtures: The nonreciprocal cahn-hilliard model," *Physical Review X*, vol. 10, no. 4, p. 041 009, 2020.

[61] Brown. (2019). "Researchers directly measure 'cheerios effect' forces for the first time," (visited on 03/08/2022).

[62] D. Vella and L. Mahadevan, "The "cheerios effect"," *American journal of physics*, vol. 73, no. 9, pp. 817–825, 2005.

[63] I. Ho, G. Pucci, and D. M. Harris, "Direct measurement of capillary attraction between floating disks," *Physical review letters*, vol. 123, no. 25, p. 254 502, 2019.

[64] A. J. Spence, S. Revzen, J. Seipel, C. Mullens, and R. J. Full, "Insects running on elastic surfaces," *Journal of Experimental Biology*, vol. 213, no. 11, pp. 1907–1920, 2010. eprint: https://jeb.biologists.org/content/213/11/1907.full.pdf.

[65] T. A. McMahon and P. R. Greene, "The influence of track compliance on running," *Journal of biomechanics*, vol. 12, no. 12, pp. 893–904, 1979.

[66] D. L. Hu, M. Prakash, B. Chan, and J. W. Bush, "Water-walking devices," in *Animal Locomotion*, Springer, 2010, pp. 131–140.

[67] S. H. Suhr, Y. S. Song, S. J. Lee, and M. Sitti, "Biologically inspired miniature water strider robot.," in *Robotics: Science and Systems*, vol. 1, 2005, pp. 319–325.

[68] C. Roh and M. Gharib, "Honeybees use their wings for water surface locomotion," *Proceedings of the National Academy of Sciences*, 2019.

[69] S. Shrivastava, A. Karsai, V. Paez, W. Bluethmann, R. Ambrose, D. Goldman, *et al.*, "A robophysical analysis and gait development for the nasa resource prospector rover," *Bulletin of the American Physical Society*, 2019.

[70] E. Palsson and H. G. Othmer, "A model for individual and collective cell movement in dictyostelium discoideum," *Proceedings of the National Academy of Sciences*, vol. 97, no. 19, pp. 10 448–10 453, 2000. eprint: https://www.pnas.org/content/97/19/10448.full.pdf.

[71] F. Ziebert and I. S. Aranson, "Effects of adhesion dynamics and substrate compliance on the shape and motility of crawling cells," *PLOS ONE*, vol. 8, no. 5, pp. 1–14, May 2013.

[72] Y. Couder, S. Protiere, E. Fort, and A. Boudaoud, "Dynamical phenomena: Walking and orbiting droplets," *Nature*, vol. 437, no. 7056, p. 208, 2005.

[73] D. Bohm, "A suggested interpretation of the quantum theory in terms of" hidden" variables. i," *Physical review*, vol. 85, no. 2, p. 166, 1952.

[74] L. de Broglie, "Interpretation of quantum mechanics by the double solution theory," in *Annals of the Louis de Broglie Foundation*, vol. 12, 1987, pp. 1–23.

[75] J. W. Bush and A. U. Oza, "Hydrodynamic quantum analogs," *Reports on Progress in Physics*, 2020.

[76] J. Toner and Y. Tu, "Flocks, herds, and schools: A quantitative theory of flocking," *Physical review E*, vol. 58, no. 4, p. 4828, 1998.

[77] A. U. Oza, S. Heidenreich, and J. Dunkel, "Generalized swift-hohenberg models for dense active suspensions," *The European Physical Journal E*, vol. 39, no. 10, pp. 1–8, 2016.

[78] S. Kole, G. P. Alexander, S. Ramaswamy, and A. Maitra, "Layered chiral active matter: Beyond odd elasticity," *Physical Review Letters*, vol. 126, no. 24, p. 248 001, 2021.

[79] S. Li, B. Dutta, S. Cannon, J. J. Daymude, R. Avinery, E. Aydin, A. W. Richa, D. I. Goldman, and D. Randall, "Programming active cohesive granular matter with mechanically induced phase changes," *Science Advances*, vol. 7, no. 17, 2021.

[80] B. P. Abbott, R. Abbott, T. Abbott, M. Abernathy, F. Acernese, K. Ackley, C. Adams, T. Adams, P. Addesso, R. Adhikari, *et al.*, "Observation of gravitational waves from a binary black hole merger," *Physical review letters*, vol. 116, no. 6, p. 061 102, 2016.

[81] W. G. Unruh, "Experimental black-hole evaporation?" *Physical Review Letters*, vol. 46, no. 21, p. 1351, 1981.

[82] S. Patrick, A. Coutant, M. Richartz, and S. Weinfurtner, "Black hole quasibound states from a draining bathtub vortex flow," *Physical review letters*, vol. 121, no. 6, p. 061 101, 2018.

[83] J. Steinhauer, "Observation of quantum hawking radiation and its entanglement in an analogue black hole," *Nature Physics*, vol. 12, no. 10, p. 959, 2016.

[84] J. Zhu, Y. Liu, Z. Liang, T. Chen, and J. Li, "Elastic waves in curved space: Mimicking a wormhole," *Physical review letters*, vol. 121, no. 23, p. 234 301, 2018.

[85] T. G. Philbin, C. Kuklewicz, S. Robertson, S. Hill, F. König, and U. Leonhardt, "Fiber-optical analog of the event horizon," *Science*, vol. 319, no. 5868, pp. 1367–1370, 2008.

[86] F. Belgiorno, S. L. Cacciatori, M. Clerici, V. Gorini, G. Ortenzi, L. Rizzi, E. Rubino, V. G. Sala, and D. Faccio, "Hawking radiation from ultrashort laser pulse filaments," *Physical review letters*, vol. 105, no. 20, p. 203 901, 2010.

[87] C. A. Middleton and D. Weller, "Elliptical-like orbits on a warped spandex fabric: A theoretical/experimental undergraduate research project," *American Journal of Physics*, vol. 84, no. 4, pp. 284–292, 2016.

[88] G. D. White, "On trajectories of rolling marbles in cones and other funnels," *American Journal of Physics*, vol. 81, no. 12, pp. 890–898, 2013.

[89] G. D. White and M. Walker, "The shape of "the spandex" and orbits upon its surface," *American Journal of Physics*, vol. 70, no. 1, pp. 48–52, 2002.

[90] Y. O. Aydin, J. M. Rieser, C. M. Hubicki, W. Savoie, and D. I. Goldman, "Physics approaches to natural locomotion: Every robot is an experiment," in *Robotic Systems and Autonomous Platforms*, Elsevier, 2019, pp. 109–127.

[91] S. Li, Y. Ozkan Aydin, C. Xiao, G. Small, H. N. Gynai, G. Li, J. M. Rieser, P. Laguna, and D. I. Goldman, "Field-mediated locomotor dynamics on highly deformable surfaces," *arXiv preprint arXiv:2004.03549*, 2021.

[92] J. A. Wheeler and K. W. Ford, *Geons, Black Holes, and Quantum Foam*. Norton & Company, 2000.

[93] C. A. Middleton and M. Langston, "Circular orbits on a warped spandex fabric," *American Journal of Physics*, vol. 82, no. 4, pp. 287–294, 2014.

[94] R. H. Price, "Spatial curvature, spacetime curvature, and gravity," *American Journal of Physics*, vol. 84, no. 8, pp. 588–592, 2016.

[95] P. Batlle, A. Teixidó, J. Llobera, I. Medrano, and L. C. Pardo, "Exploring the rubber sheet spacetime analogy by studying ball movement in a bent trampoline," *European Journal of Physics*, vol. 40, no. 4, p. 045 005, 2019.

[96] *An anonymous additional manuscript 'Field-mediated locomotor dynamics on highly deformable surfaces' is attached with this submission to AJP*,

[97] Y. O. Aydin, J. M. Rieser, C. M. Hubicki, W. Savoie, and D. I. Goldman, "6 - physics approaches to natural locomotion: Every robot is an experiment," in *Robotic Systems and Autonomous Platforms*, ser. Woodhead Publishing in Materials, S. M. Walsh and M. S. Strano, Eds., Woodhead Publishing, 2019, pp. 109–127, ISBN: 978-0-08-102260-3.

[98] C. Barceló, S. Liberati, and M. Visser, "Analogue gravity," *Living Reviews in Relativity*, vol. 14, no. 1, p. 3, May 2011.

[99] J. W. M. Bush, "Quantum mechanics writ large," *Proceedings of the National Academy of Sciences*, vol. 107, no. 41, pp. 17 455–17 456, 2010. eprint: https://www.pnas.org/content/107/41/17455.full.pdf.

[100] S. Gart, D. Vella, and S. Jung, "The collective motion of nematodes in a thin liquid layer," *Soft Matter*, vol. 7, no. 6, pp. 2444–2448, 2011.

[101] D.-G. Lee, P. Cicuta, and D. Vella, "Self-assembly of repulsive interfacial particles via collective sinking," *Soft matter*, vol. 13, no. 1, pp. 212–221, 2017.

[102] B. Szabo, G. Szöllösi, B. Gönci, Z. Jurányi, D. Selmeczi, and T. Vicsek, "Phase transition in the collective migration of tissue cells: Experiment and model," *Physical Review E*, vol. 74, no. 6, p. 061 908, 2006.

[103] F. B. Hoogterp and W. R. Meldrum, "Differential torque steering for future combat vehicles," in *SAE 2000 World Congress*, SAE International, Nov. 1999.

[104] Y. Chung, C. Park, and F. Harashima, "A position control differential drive wheeled mobile robot," *IEEE Transactions on Industrial Electronics*, vol. 48, no. 4, pp. 853–863, 2001.

[105] "Independent wheel torque control of 4wd electric vehicle for differential drive assisted steering," *Mechatronics*, vol. 21, no. 1, pp. 63–76, 2011.

[106] J. J. Uicker, G. R. Pennock, J. E. Shigley, *et al.*, *Theory of machines and mechanisms*. Oxford University Press New York, NY, 2011, vol. 1.

[107] A. Gauthier, D. van der Meer, J. H. Snoeijer, and G. Lajoinie, "Capillary orbits," *Nature communications*, vol. 10, no. 1, pp. 1–5, 2019.

[108] M. Pössel, "Relatively complicated? using models to teach general relativity at different levels," *arXiv preprint arXiv:1812.11589*, 2018.

[109] S. Li, H. N. Gynai, S. Tarr, P. Laguna, G. Li, and D. I. Goldman, "Robophysical modeling of spacetime dynamics," *arXiv preprint arXiv:2202.04835*, 2022.

[110] J. B. Hartle, *Gravity : an introduction to Einstein's general relativity*. 2003.

[111] T. Clifton and J. D. Barrow, "The power of general relativity," *Phys. Rev. D*, vol. 72, p. 103 005, 10 Nov. 2005.

[112] G. M. Clemence, "The relativity effect in planetary motions," *Reviews of Modern Physics*, vol. 19, no. 4, p. 361, 1947.

[113] S. Sarkar, M. Čebron, M. Brojan, and A. Košmrlj, "Method of image charges for describing deformation of bounded two-dimensional solids with circular inclusions," *Physical Review E*, vol. 103, no. 5, p. 053 004, 2021.

[114] W. Liu, A. F. Winfield, J. Sa, J. Chen, and L. Dou, "Towards energy optimization: Emergent task allocation in a swarm of foraging robots," *Adaptive behavior*, vol. 15, no. 3, pp. 289–305, 2007.

[115] D. L. Hu, B. Chan, and J. W. M. Bush, "The hydrodynamics of water strider locomotion," *Nature*, vol. 424, pp. 663–666, 2003.

[116] S. Floyd, T. Keegan, J. Palmisano, and M. Sitti, "A novel water running robot inspired by basilisk lizards," in *Intelligent Robots and Systems, 2006 IEEE/RSJ International Conference on*, IEEE, 2006, pp. 5430–5436.

[117] K. Suzuki, H. Takanobu, K. Noya, H. Koike, and H. Miura, "Water strider robots with microfabricated hydrophobic legs," in *2007 IEEE/RSJ International Conference on Intelligent Robots and Systems*, Oct. 2007, pp. 590–595.

[118] J.-S. Koh, E. Yang, G.-P. Jung, S.-P. Jung, J. H. Son, S.-I. Lee, P. G. Jablonski, R. J. Wood, H.-Y. Kim, and K.-J. Cho, "Jumping on water: Surface tension–dominated jumping of water striders and robotic insects," *Science*, vol. 349, no. 6247, pp. 517–521, 2015. eprint: https://science.sciencemag.org/content/349/6247/517.full.pdf.

[119] Y. Chen, N. Doshi, B. Goldberg, H. Wang, and R. J. Wood, "Controllable water surface to underwater transition through electrowetting in a hybrid terrestrial-aquatic microrobot," *Nat Commun*, vol. 9, p. 2495, 2018.

[120] J. W. Bush and D. L. Hu, "Walking on water: Biolocomotion at the interface," *Annu. Rev. Fluid Mech.*, vol. 38, pp. 339–369, 2006.

[121] S.-J. Chung, A. A. Paranjape, P. Dames, S. Shen, and V. Kumar, "A survey on aerial swarm robotics," *IEEE Transactions on Robotics*, vol. 34, no. 4, pp. 837–855, 2018.

[122] A. Weinstein, A. Cho, G. Loianno, and V. Kumar, "Visual inertial odometry swarm: An autonomous swarm of vision-based quadrotors," *IEEE Robotics and Automation Letters*, vol. 3, no. 3, pp. 1801–1807, 2018.

[123] O. Y. Sergiyenko and V. V. Tyrsa, "3d optical machine vision sensors with intelligent data management for robotic swarm navigation improvement," *IEEE Sensors Journal*, vol. 21, no. 10, pp. 11 262–11 274, 2021.

[124] S. Mayya, P. Pierpaoli, G. Nair, and M. Egerstedt, "Localization in densely packed swarms using interrobot collisions as a sensing modality," *IEEE Transactions on Robotics*, vol. 35, no. 1, pp. 21–34, 2019.

[125] J. Zhao, X. Zhang, and Q. Pan, "A water walking robot inspired by water strider," in *2012 IEEE International Conference on Mechatronics and Automation*, IEEE, 2012, pp. 962–967.

[126] A. T. Liu, J. F. Yang, L. N. LeMar, G. Zhang, A. Pervan, T. D. Murphey, and M. Strano, "Autoperforation of two-dimensional materials to generate colloidal state machines capable of locomotion," *Faraday Discuss.*, pp. -, 2020.

[127] A. Shapere and F. Wilczek, "Geometry of self-propulsion at low reynolds number," *Journal of Fluid Mechanics*, vol. 198, pp. 557–585, 1989.

[128] R. L. Hatton, Y. Ding, H. Choset, and D. I. Goldman, "Geometric visualization of self-propulsion in a complex medium," *Physical review letters*, vol. 110, no. 7, p. 078 101, 2013.

[129] J. M. Rieser, P. E. Schiebel, A. Pazouki, F. Qian, Z. Goddard, K. Wiesenfeld, A. Zangwill, D. Negrut, and D. I. Goldman, "Dynamics of scattering in undulatory active collisions," *Physical Review E*, vol. 99, no. 2, p. 022 606, 2019.

[130] F. Qian and D. Goldman, "Anticipatory control using substrate manipulation enables trajectory control of legged locomotion on heterogeneous granular media," in *Micro-and Nanotechnology Sensors, Systems, and Applications VII*, International Society for Optics and Photonics, vol. 9467, 2015, 94671U.

[131] S. Mayya, G. Notomista, D. Shell, S. Hutchinson, and M. Egerstedt, "Non-uniform robot densities in vibration driven swarms using phase separation theory," in *2019 IEEE/RSJ International Conference on Intelligent Robots and Systems (IROS)*, IEEE, 2019, pp. 4106–4112.

[132] M. Cenzer and L. K. M'Gonigle, "Local adaptation in dispersal in multi-resource landscapes," *Evolution*, vol. 73, no. 4, pp. 648–660, 2019.

[133] J. Aguilar, T. N. Zhang, F. F. Qian, M. Kingsbury, B. McInroe, N. Mazouchova, C. Li, R. Maladen, C. H. Gong, M. Travers, R. L. Hatton, H. Choset, P. B. Umbanhowar, and D. I. Goldman, "A review on locomotion robophysics: The study of movement at the intersection of robotics, soft matter and dynamical systems," *Reports on Progress in Physics*, vol. 79, no. 11, 2016.

[134] A. Deblais, T. Barois, T. Guerin, P. H. Delville, R. Vaudaine, J. S. Lintuvuori, J. F. Boudet, J. C. Baret, and H. Kellay, "Boundaries control collective dynamics of inertial self-propelled robots," *Phys. Rev. Lett.*, vol. 120, p. 188 002, 18 May 2018.

[135] J. Seo, J. Paik, and M. Yim, "Modular reconfigurable robotics," *Annual Review of Control, Robotics, and Autonomous Systems, Vol 2*, vol. 2, pp. 63–88, 2019.

[136] S. R. Nagel, "Experimental soft-matter science," *Rev. Mod. Phys.*, vol. 89, p. 025 002, 2 Apr. 2017.

[137] P. M. Chaikin, T. C. Lubensky, and T. A. Witten, *Principles of condensed matter physics*. Cambridge university press Cambridge, 1995, vol. 10.

[138] S. Atkinson, F. H. Stillinger, and S. Torquato, "Existence of isostatic, maximally random jammed monodisperse hard-disk packings," *Proceedings of the National Academy of Sciences of the United States of America*, vol. 111, no. 52, pp. 18 436–18 441, 2014.

[139] D. Nelson, *Bond-orientational order in condensed matter systems*. Springer Science & Business Media, 2012.

[140] D. Debnath, J. S. Gainer, C. Kilic, D. Kim, K. T. Matchev, and Y. P. Yang, "Identifying phase-space boundaries with voronoi tessellations," *European Physical Journal C*, vol. 76, no. 11, 2016.

[141] T. Reisz, "Advanced linked cluster-expansion - scalar fields at finite-temperature," *Nuclear Physics B*, vol. 450, no. 3, pp. 569–602, 1995.

[142] J. J. Godina, Y. Meurice, M. B. Oktay, and S. Niermann, "Guide to precision calculations in dyson's hierarchical scalar field theory," *Physical Review D*, vol. 57, no. 10, pp. 6326–6336, 1998.

[143] A. S. Keys, A. R. Abate, S. C. Glotzer, and D. J. Durian, "Measurement of growing dynamical length scales and prediction of the jamming transition in a granular material," *Nature physics*, vol. 3, no. 4, pp. 260–264, 2007.

[144] G. Briand and O. Dauchot, "Crystallization of self-propelled hard discs," *Physical Review Letters*, vol. 117, no. 9, 2016.

[145] A. Deblais, T. Barois, T. Guerin, P. H. Delville, R. Vaudaine, J. S. Lintuvuori, J. F. Boudet, J. C. Baret, and H. Kellay, "Boundaries control collective dynamics of inertial self-propelled robots," *Physical Review Letters*, vol. 120, no. 18, 2018.

[146] G. S. Fulcher, "Analysis of recent measurements of the viscosity of glasses," *Journal of the American Ceramic Society*, vol. 8, no. 6, pp. 339–355, 1925.

[147] M. P. Brenner, L. S. Levitov, and E. O. Budrene, "Physical mechanisms for chemotactic pattern formation by bacteria," *Biophysical journal*, vol. 74, no. 4, pp. 1677–1693, 1998.

[148] T. V. Phan, G. Wang, L. Liu, and R. H. Austin, "Bootstrapped motion of an agent on an adaptive resource landscape," *Symmetry*, vol. 13, no. 2, p. 225, 2021.

[149] G. Wang, T. V. Phan, S. Li, M. Wombacher, J. Qu, Y. Peng, G. Chen, D. I. Goldman, S. A. Levin, R. H. Austin, and L. Liu, "Emergent field-driven robot swarm states," *Phys. Rev. Lett.*, vol. 126, p. 108 002, 10 Mar. 2021.

[150] L. J. Fogel, A. J. Owens, and M. J. Walsh, *Artificial Intelligence Through Simulated Evolution*. John Wiley and Sons Inc., 1966.

[151] A. Dneprov, *Crabs on the Island*. Moscow: Mir Publishers, 1968.

[152] D. M. Fitzgerald, P. J. Hastings, and S. M. Rosenberg, "Stress-induced mutagenesis: Implications in cancer and drug resistance," *Annual Review of Cancer Biology, Vol 1*, vol. 1, pp. 119–140, 2017.

[153] D. Monies, S. Maddirevula, W. Kurdi, M. H. Alanazy, H. Alkhalidi, M. Al-Owain, R. A. Sulaiman, E. Faqeih, E. Goljan, N. Ibrahim, F. Abdulwahab, M. Hashem, M. Abouelhoda, R. Shaheen, S. T. Arold, and F. S. Alkuraya, "Autozygosity reveals recessive mutations and novel mechanisms in dominant genes: Implications in variant interpretation," *Genetics in Medicine*, vol. 19, no. 10, pp. 1144–1150, 2017.

[154] R. Levins and R. Lewontin, *The Dialectical Biologist*. Cambridge, MA 02138, USA: Harvard University Press, 1987.

[155] M. Lynch, "The lower bound to the evolution of mutation rates," *Genome Biol Evol*, vol. 3, pp. 1107–18, 2011.

[156] L. Rindi, M. Dal Bello, L. Dai, J. Gore, and L. Benedetti-Cecchi, "Direct observation of increasing recovery length before collapse of a marine benthic ecosystem," *Nature Ecology and Evolution*, vol. 1, no. 6, 2017.

[157] S. A. Frank, "Natural selection maximizes fisher information," *J Evol Biol*, vol. 22, no. 2, pp. 231–44, 2009.

[158] E. V. Koonin, "The meaning of biological information," *Philosophical Transactions of the Royal Society A: Mathematical, Physical and Engineering Sciences*, vol. 374, no. 2063, p. 20 150 065, 2016.

[159] R. S. Cantrell and C. Cosner, "On the effects of spatial heterogeneity on the persistence of interacting species," *Journal of Mathematical Biology*, vol. 37, no. 2, pp. 103–145, 1998.

[160] S. Wright, *Evolution: selected papers*. University of Chicago Press, 1986.

[161] J. M. Epstein and R. Axtell, *Growing artificial societies: social science from the bottom up*. Brookings Institution Press, 1996.

[162] A. Bigbee, C. Cioffi-Revilla, and S. Luke, "Replication of sugarscape using mason," in *Agent-Based Approaches in Economic and Social Complex Systems IV*, Springer, 2007, pp. 183–190.

[163] S. M. Reia, A. C. Amado, and J. F. Fontanari, "Agent-based models of collective intelligence," *Physics of Life Reviews*, vol. 31, pp. 320–331, 2019.

[164] A. Litman and S. Moran-Schein, "Smooth scheduling under variable rates or the analog-digital confinement game," *Theory of Computing Systems*, vol. 45, no. 2, pp. 325–354, 2009.

[165] F. Antenucci, S. Franz, P. Urbani, and L. Zdeborová, "Glassy nature of the hard phase in inference problems," *Phys. Rev. X*, vol. 9, p. 011 020, 1 Jan. 2019.

[166] B. Edmonds and D. Hales, "Replication, replication and replication: Some hard lessons from model alignment," *Journal of Artificial Societies and Social Simulation*, vol. 6, no. 4, 2003.

[167] C. Sansores and J. Pavón, "Agent-based simulation replication: A model driven architecture approach," in *Mexican International Conference on Artificial Intelligence*, Springer, 2005, pp. 244–253.

[168] C. Reichhardt and C. J. O. Reichhardt, "Absorbing phase transitions and dynamic freezing in running active matter systems," *Soft Matter*, vol. 10, no. 38, pp. 7502–7510, 2014.

[169] H. Hinrichsen, "Non-equilibrium critical phenomena and phase transitions into absorbing states," *Advances in physics*, vol. 49, no. 7, pp. 815–958, 2000.

[170] G. Ódor, "Universality classes in nonequilibrium lattice systems," *Reviews of modern physics*, vol. 76, no. 3, p. 663, 2004.

[171] K. A. Takeuchi, M. Kuroda, H. Chaté, and M. Sano, "Directed percolation criticality in turbulent liquid crystals," *Physical review letters*, vol. 99, no. 23, p. 234 503, 2007.

[172] D. Hanahan and R. A. Weinberg, "The hallmarks of cancer," *Cell*, vol. 100, no. 1, pp. 57–70, 2000.

[173] J.-F. Boudet, J. Lintuvuori, C. Lacouture, T. Barois, A. Deblais, K. Xie, S. Cassagnere, B. Tregon, D. Brückner, J.-C. Baret, *et al.*, "From collections of indepen-

dent, mindless robots to flexible, mobile, and directional superstructures," *Science Robotics*, vol. 6, no. 56, eabd0272, 2021.

[174] N. Gravish, S. V. Franklin, D. L. Hu, and D. I. Goldman, "Entangled granular media," *Physical review letters*, vol. 108, no. 20, p. 208 001, 2012.

[175] A. Vardhan, S. Li, Y. Zhang, K. Wiesenfeld, and D. Goldman, "Smarticle glider: Locomoting, spontaneous excitations in a shape changing active matter system," *Bulletin of the American Physical Society*, vol. 65, 2020.

[176] A. Vardhan, R. Avinery, H. Kedia, K. Wiesenfeld, and D. Goldman, "Physical gliders produced from smarticle clouds," in *APS March Meeting Abstracts*, vol. 2021, 2021, P06–010.

[177] J. Chen, M. Gauci, W. Li, A. Kolling, and R. Groß, "Occlusion-based cooperative transport with a swarm of miniature mobile robots," *IEEE Transactions on Robotics*, vol. 31, no. 2, pp. 307–321, 2015.

[178] R. Groß and M. Dorigo, "Towards group transport by swarms of robots," *International Journal of Bio-Inspired Computation*, vol. 1, no. 1-2, pp. 1–13, 2009.

[179] B. Chong, T. Wang, B. Lin, S. Li, G. Blekherman, H. Choset, and D. I. Goldman, "Moving sidewinding forward: Optimizing contact patterns for limbless robots via geometric mechanics,"

[180] S. Alben, "Efficient sliding locomotion with isotropic friction," *Physical Review E*, vol. 99, no. 6, p. 062 402, 2019.

[181] R. E. Guerra, C. P. Kelleher, A. D. Hollingsworth, and P. M. Chaikin, "Freezing on a sphere," *Nature*, vol. 554, no. 7692, pp. 346–350, 2018.

[182] T. Lopez-Leon, V. Koning, K. Devaiah, V. Vitelli, and A. Fernandez-Nieves, "Frustrated nematic order in spherical geometries," *Nature Physics*, vol. 7, no. 5, pp. 391–394, 2011.

[183] Y.-H. Zhang, M. Deserno, Z.-C. Tu, *et al.*, "Dynamics of active nematic defects on the surface of a sphere," *Physical Review E*, vol. 102, no. 1, p. 012 607, 2020.

[184] P. W. Ellis, D. J. Pearce, Y.-W. Chang, G. Goldsztein, L. Giomi, and A. Fernandez-Nieves, "Curvature-induced defect unbinding and dynamics in active nematic toroids," *Nature Physics*, vol. 14, no. 1, pp. 85–90, 2018.

[185] C. W. Misner, K. S. Thorne, and J. A. Wheeler, *Gravitation*. Macmillan, 1973.

[186] J. Wisdom, "Swimming in spacetime: Motion by cyclic changes in body shape," *Science*, vol. 299, no. 5614, pp. 1865–1869, 2003.

[187] J. Avron and O. Kenneth, "Swimming in curved space or the baron and the cat," *New Journal of Physics*, vol. 8, no. 5, p. 68, 2006.

[188] E. Guéron, "Adventures in curved spacetime," *Scientific American*, vol. 301, no. 2, pp. 38–45, 2009.

[189] A. Shapere and F. Wilczek, "Gauge kinematics of deformable bodies," *American Journal of Physics*, vol. 57, no. 6, pp. 514–518, 1989.

[190] J. E. Marsden and J. Ostrowski, "Symmetries in motion: Geometric foundations of motion control," 1998.

[191] S. D. Kelly and R. M. Murray, "Geometric phases and robotic locomotion," *Journal of Robotic Systems*, vol. 12, no. 6, pp. 417–431, 1995.

[192] R. L. Hatton and H. Choset, "Nonconservativity and noncommutativity in locomotion," *The European Physical Journal Special Topics*, vol. 224, no. 17, pp. 3141–3174, 2015.

[193] H. C. Astley, J. R. Mendelson III, J. Dai, C. Gong, B. Chong, J. M. Rieser, P. E. Schiebel, S. S. Sharpe, R. L. Hatton, H. Choset, *et al.*, "Surprising simplicities and syntheses in limbless self-propulsion in sand," *Journal of Experimental Biology*, vol. 223, no. 5, jeb103564, 2020.

[194] B. Chong, T. Wang, J. M. Rieser, B. Lin, A. Kaba, G. Blekherman, H. Choset, and D. I. Goldman, "Frequency modulation of body waves to improve performance of sidewinding robots," *The International Journal of Robotics Research*, vol. 40, no. 12-14, pp. 1547–1562, 2021.

[195] E. T. Jaynes and F. W. Cummings, "Comparison of quantum and semiclassical radiation theories with application to the beam maser," *Proceedings of the IEEE*, vol. 51, no. 1, pp. 89–109, 1963.

[196] A. E. Magurran, "The adaptive significance of schooling as an anti-predator defence in fish," *Annales Zoologici Fennici*, vol. 27, no. 2, pp. 51–66, 1990.

[197] N. J. Mlot, C. A. Tovey, and D. L. Hu, "Fire ants self-assemble into waterproof rafts to survive floods," *Proceedings of the National Academy of Sciences*, vol. 108, no. 19, pp. 7669–7673, 2011.

[198] J. Liu, A. Prindle, J. Humphries, M. Gabalda-Sagarra, M. Asally, D.-Y. D. Lee, S. Ly, J. Garcia-Ojalvo, and G. M. Süel, "Metabolic co-dependence gives rise to

collective oscillations within biofilms," *Nature*, vol. 523, no. 7562, pp. 550–554, 2015.

[199] M. Brambilla, E. Ferrante, M. Birattari, and M. Dorigo, "Swarm robotics: A review from the swarm engineering perspective," *Swarm Intelligence*, vol. 7, no. 1, pp. 1–41, 2013.

[200] L. Bayindir, "A review of swarm robotics tasks," *Neurocomputing*, vol. 172, pp. 292–321, 2016.

[201] M. Dorigo, G. Theraulaz, and V. Trianni, "Reflections on the future of swarm robotics," *Science Robotics*, vol. 5, no. 49, eabe4385, 2020.

[202] K. Elamvazhuthi and S. Berman, "Mean-field models in swarm robotics: A survey," *Bioinspiration & Biomimetics*, vol. 15, no. 1, p. 015 001, 2019.

[203] P. Flocchini, G. Prencipe, and N. Santoro, Eds., *Distributed Computing by Mobile Entities*. Switzerland: Springer International Publishing, 2019.

[204] G. Notomista, S. Mayya, A. Mazumdar, S. Hutchinson, and M. Egerstedt, "A study of a class of vibration-driven robots: Modeling, analysis, control and design of the brushbot," in *2019 IEEE/RSJ International Conference on Intelligent Robots and Systems*, 2019, pp. 5101–5106.

[205] H. Hamann, *Swarm Robotics: A Formal Approach*. Springer, 2018.

[206] L. Hines, K. Petersen, G. Z. Lum, and M. Sitti, "Soft actuators for small-scale robotics," *Advanced Materials*, vol. 29, no. 13, p. 1 603 483, 2017.

[207] H. Xie, M. Sun, X. Fan, Z. Lin, W. Chen, L. Wang, L. Dong, and Q. He, "Reconfigurable magnetic microrobot swarm: Multimode transformation, locomotion, and manipulation," *Science Robotics*, vol. 4, no. 28, eaav8006, 2019.

[208] D. H. Wolpert, "The stochastic thermodynamics of computation," *Journal of Physics A: Mathematical and Theoretical*, vol. 52, no. 19, p. 193 001, 2019.

[209] M. Rubenstein, A. Cornejo, and R. Nagpal, "Programmable self-assembly in a thousand-robot swarm," *Science*, vol. 345, no. 6198, pp. 795–799, 2014.

[210] B. Piranda and J. Bourgeois, "Designing a quasi-spherical module for a huge modular robot to create programmable matter," *Autonomous Robots*, vol. 42, no. 8, pp. 1619–1633, 2018.

[211] N. Fatès and N. Vlassopoulos, "A robust aggregation method for quasi-blind robots in an active environment," in *ICSI 2011*, 2011.

[212] M. Gauci, J. Chen, W. Li, T. J. Dodd, and R. Groß, "Self-organized aggregation without computation," *International Journal of Robotics Research*, vol. 33, no. 8, pp. 1145–1161, 2014.

[213] A. Özdemir, M. Gauci, A. Kolling, M. D. Hall, and R. Groß, "Spatial coverage without computation," in *2019 IEEE International Conference on Robotics and Automation*, ser. ICRA 2019, IEEE, 2019, pp. 1346–1353.

[214] S. Garnier, J. Gautrais, M. Asadpour, C. Jost, and G. Theraulaz, "Self-organized aggregation triggers collective decision making in a group of cockroach-like robots," *Adaptive Behavior*, vol. 17, no. 2, pp. 109–133, 2009.

[215] N. Correll and A. Martinoli, "Modeling and designing self-organized aggregation in a swarm of miniature robots," *The International Journal of Robotics Research*, vol. 30, no. 5, pp. 615–626, 2011.

[216] S. Li, R. Batra, D. Brown, H.-D. Chang, N. Ranganathan, C. Hoberman, D. Rus, and H. Lipson, "Particle robotics based on statistical mechanics of loosely coupled components," *Nature*, vol. 567, pp. 361–365, 2019.

[217] M. Agrawal, I. R. Bruss, and S. C. Glotzer, "Tunable emergent structures and traveling waves in mixtures of passive and contact-triggered-active particles," *Soft Matter*, vol. 13, no. 37, pp. 6332–6339, 2017.

[218] A. Deblais, T. Barois, T. Guerin, P. H. Delville, R. Vaudaine, J. S. Lintuvuori, J. F. Boudet, J. C. Baret, and H. Kellay, "Boundaries control collective dynamics of inertial self-propelled robots," *Phys. Rev. Lett.*, vol. 120, p. 188 002, 18 2018.

[219] B. Andreotti, Y. Forterre, and O. Pouliquen, *Granular media: between fluid and solid*. Cambridge University Press, 2013.

[220] M. X. Lim, A. Souslov, V. Vitelli, and H. M. Jaeger, "Cluster formation by acoustic forces and active fluctuations in levitated granular matter," *Nature Physics*, vol. 15, no. 5, pp. 460–464, 2019.

[221] F. Melo, P. B. Umbanhowar, and H. L. Swinney, "Hexagons, kinks, and disorder in oscillated granular layers," *Physical review letters*, vol. 75, no. 21, p. 3838, 1995.

[222] P. Eshuis, K. Van Der Weele, D. Van Der Meer, R. Bos, and D. Lohse, "Phase diagram of vertically shaken granular matter," *Physics of Fluids*, vol. 19, no. 12, p. 123 301, 2007.

[223] D. I. Goldman and H. L. Swinney, "Signatures of glass formation in a fluidized bed of hard spheres," *Physical review letters*, vol. 96, no. 14, p. 145 702, 2006.

[224] E. C. Rericha, C. Bizon, M. D. Shattuck, and H. L. Swinney, "Shocks in supersonic sand," *Physical review letters*, vol. 88, no. 1, p. 014 302, 2001.

[225] D. Howell, R. Behringer, and C. Veje, "Stress fluctuations in a 2d granular couette experiment: A continuous transition," *Physical Review Letters*, vol. 82, no. 26, p. 5241, 1999.

[226] E. I. Corwin, H. M. Jaeger, and S. R. Nagel, "Structural signature of jamming in granular media," *Nature*, vol. 435, no. 7045, pp. 1075–1078, 2005.

[227] D. Bi, J. Zhang, B. Chakraborty, and R. P. Behringer, "Jamming by shear," *Nature*, vol. 480, no. 7377, pp. 355–358, 2011.

[228] N. Mitarai and F. Nori, "Wet granular materials," *Advances in Physics*, vol. 55, no. 1-2, pp. 1–45, 2006.

[229] A. Hemmerle, M. Schröter, and L. Goehring, "A cohesive granular material with tunable elasticity," *Scientific Reports*, vol. 6, no. 1, p. 35 630, 2016.

[230] F. Kümmel, B. ten Hagen, R. Wittkowski, I. Buttinoni, R. Eichhorn, G. Volpe, H. Löwen, and C. Bechinger, "Circular motion of asymmetric self-propelling particles," *Physical review letters*, vol. 110, no. 19, p. 198 302, 2013.

[231] S. Jahanshahi, H. Löwen, and B. Ten Hagen, "Brownian motion of a circle swimmer in a harmonic trap," *Physical Review E*, vol. 95, no. 2, p. 022 606, 2017.

[232] S. Ramaswamy, "Active matter," *Journal of Statistical Mechanics: Theory and Experiment*, vol. 2017, p. 054 002, 2017.

[233] B. A. Cipra, "An introduction to the ising model," *The American Mathematical Monthly*, vol. 94, no. 10, pp. 937–959, 1987.

[234] S. Cannon, J. J. Daymude, D. Randall, and A. W. Richa, "A Markov chain algorithm for compression in self-organizing particle systems," in *Proceedings of the 2016 ACM Symposium on Principles of Distributed Computing*, ser. PODC '16, New York, NY, USA: ACM, 2016, pp. 279–288.

[235] N. Metropolis, A. W. Rosenbluth, M. N. Rosenbluth, A. H. Teller, and E. Teller, "Equation of state calculations by fast computing machines," *Journal of Chemical Physics*, vol. 21, pp. 1087–1092, 1953.

[236] W. K. Hastings, "Monte carlo sampling methods using Markov chains and their applications," *Biometrika*, vol. 57, pp. 97–109, 1970.

[237] S. Cannon, J. J. Daymude, C. Gokmen, D. Randall, and A. W. Richa, "A local stochastic algorithm for separation in heterogeneous self-organizing particle systems," *arXiv preprint arXiv:1805.04599*, 2018.

[238] M. Jerrum and A. Sinclair, "Polynomial-time approximation algorithms for the ising model," *SIAM Journal on computing*, vol. 22, no. 5, pp. 1087–1116, 1993.

[239] D. Randall and D. Wilson, "Sampling spin configurations of an Ising system," in *Proceedings of the Tenth Annual ACM-SIAM Symposium on Discrete Algorithms, 17-19 January 1999, Baltimore, Maryland, USA*, ser. SODA '99, ACM/SIAM, 1999, pp. 959–960.

[240] O. Penrose, "A mean-field equation of motion for the dynamic Ising model," *Journal of Statistical Physics*, vol. 63, no. 5-6, pp. 975–986, 1991.

[241] L. Bayindir and E. Sahin, "Modeling self-organized aggregation in swarm robotic systems," in *2009 IEEE Swarm Intelligence Symposium*, 2009, pp. 1–8.

[242] G. Valentini, D. Brambilla, H. Hamann, and M. Dorigo, "Collective perception of environmental features in a robot swarm," in *International Conference on Swarm Intelligence*, Springer, 2016, pp. 65–76.

[243] T. Majmudar, M. Sperl, S. Luding, and R. P. Behringer, "Jamming transition in granular systems," *Physical review letters*, vol. 98, no. 5, p. 058 001, 2007.

[244] S. Wilson, T. P. Pavlic, G. P. Kumar, A. Buffin, S. C. Pratt, and S. Berman, "Design of ant-inspired stochastic control policies for collective transport by robotic swarms," *Swarm Intelligence*, vol. 8, pp. 303–327, 2014.

[245] O. Feinerman, I. Pinkoviezky, A. Gelblum, E. Fonio, and N. S. Gov, "The physics of cooperative transport in groups of ants," *Nature Physics*, vol. 14, pp. 683–693, 2018.

[246] J. Stenhammar, A. Tiribocchi, R. J. Allen, D. Marenduzzo, and M. E. Cates, "Continuum theory of phase separation kinetics for active brownian particles," *Phys. Rev. Lett.*, vol. 111, p. 145 702, 14 Oct. 2013.

[247] S. Wildeman, "Real-time quantitative schlieren imaging by fast fourier demodulation of a checkered backdrop," *Experiments in Fluids*, vol. 59, no. 6, pp. 1–13, 2018.

[248] M. Andrés Arroyo, S. Cannon, J. J. Daymude, D. Randall, and A. W. Richa, "A stochastic approach to shortcut bridging in programmable matter," *Natural Computing*, vol. 17, no. 4, pp. 723–741, 2018.

[249] X.-S. Yang and Y. Young, "Cellular automata, pdes, and pattern formation," *arXiv preprint arXiv:1003.1983*, 2010.

[250] N. Egan, S. Li, R. Avinery, H. Zeng, T. Sasaki, and D. Goldman, "Modeling ant pontoon bridging using a robophysical active matter system," *Bulletin of the American Physical Society*, 2022.

[251] R. Axelrod and D. S. Bennett, "A landscape theory of aggregation," *British Journal of Political Science*, vol. 23, pp. 211–233, 1993.

[252] T. Balch, F. Dellaert, A. Feldman, A. Guillory, C. L. Isbell, Z. Khan, S. C. Pratt, A. N. Stein, and H. Wilde, "How multirobot systems research will accelerate our understanding of social animal behavior," *Proceedings of the Ieee*, vol. 94, no. 7, pp. 1445–1463, 2006.

VITA

Shengkai Li was born and raised in Shanghai, China. He graduated from Gezhi High School in 2011 and Shanghai Jiao Tong University in 2015. After receiving his Bachelor of Science degree in the latter, he continued to pursue physics in Georgia Institute of Technology as a Ph.D. student. His research resulted in several peer-reviewed publications including *Science Advances*, *Science Robotics*, *Physical Review Letters*, and *PNAS*. On the way towards the Ph.D. degree, he earned Masters of Science in Physics in 2017 and Masters of Engineering in Computational Science and Engineering in 2020, and was awarded the STAMI fellowship in 2020. After obtaining the Ph.D. degree, he expects to work at Princeton University as a CPBF postdoctoral fellow.